

**Design, Synthesis and DNA Interaction Studies
with Novel Photosensitizer Molecules as Efficient
Photodynamic Therapeutic Agents**

**Thesis Submitted to AcSIR for the Award of the Degree
of**
DOCTOR OF PHILOSOPHY
In Chemical Science



(Academy of Scientific and Innovative Research)

By
Vadde Ramu
(Reg.No. 10CC12A26084)

Under the guidance of
Dr. Amitava Das

**CSIR-National Chemical Laboratory
Pune, Maharashtra, India – 411008**

CANDIDATE'S STATEMENT

I hereby declare that the work incorporated in the present thesis is original and has not been submitted to any University/Institution for the award of a Diploma or a Degree. Research material obtained from other sources has been duly acknowledged in the thesis. Any text, illustration, table etc., used in the thesis from other sources, have been duly cited and acknowledged." further declare that the results presented in the thesis and the considerations made therein, contribute in general to the advancement of knowledge in chemistry and in particular to "**Design, Synthesis and DNA Interaction Studies with Novel Photosensitizer Molecules as Efficient Photodynamic Therapeutic Agents".**

Vadde Ramu

CERTIFICATE BY SUPERVISOR

This is to certify that the contents of this thesis entitled "**Design, Synthesis and DNA Interaction Studies with Novel Photosensitizer Molecules as Efficient Photodynamic Therapeutic Agents**" is the original research work of **Mr. Vadde Ramu**, carried out under my supervision at CSIR-National Chemical Laboratory, Pune, India.

Further, I hereby certify that the work has not been submitted either partly or fully to any other University or Institution for the award of any degree.

Amitava Das
Ph.D. Supervisor

Acknowledgement

Acknowledgements

It is a great pleasure to express my deep sense of gratitude and thanks to my supervisor **Dr. Amitava Das** for his insightful comments and encouragement, but also for the hard question, which incited me to widen my research from various perspectives. I am extremely grateful to him for the freedom that I have enjoyed during my research career as a Ph.D. student. I dedicate all my success, whatever I have achieved as a Ph.D. student, to this wonderful person and his family members.

I am also thankful to **Prof. Jim A Thomas** for giving me the opportunity to associate with his research group at University of Sheffield (United Kingdom) under the DST-UKIERI project. The experiences and memories gained while working with **Prof. Carl G Smythe, Dr. Martin Gill, Dr. Mike G. Walker** during my visit to University of Sheffield for three months are extremely rewarding. I am thankful to the DST-UKIERI for funding this work.

I wish to convey my gratefulness to **Dr. Biswajit Ganguly** and **Dr. Samit Chattopadhyay** for fruitful discussions on research problems, appreciative comments, and continuous guidance whenever I approached.

My special thanks to **Dr. Sayam Sen Gupta** and **Dr. B.L.V. Prasad** for their help in providing me the fellowship during the end of my tenure. I wish to express my word of thanks to **Dr. P. K. Ghosh**, Director, Central Salt and Marine Chemicals Research Institute for providing me infrastructure to carry out my research work. I wish to convey my gratefulness to **Dr. Parimal Paul**, Discipline Coordinator, for providing me all analytical facilities and all other institutional supports.

I wish to express my word of thanks to **Prof. Sourav Pal**, (Ex-Director, National Chemical Laboratory) and **Prof. Ashwini Kumar Nangia** (Director, National Chemical Laboratory, Pune) for providing me the necessary facilities for carrying out my research work at NCL. I wish to convey my gratefulness to **Dr. Pradeep Kumar Tripathi** Divisional Chairperson of Organic Chemistry Division of National Chemical Laboratory.

My special thanks to my Doctoral Advisory Committee members **Dr. D. Srinivas, Dr. Sayam Sen Gupta** and **Dr. B.L.V. Prasad** for their valuable suggestions during my course work presentations. I also thank to **Dr. Khureshy** and **Dr. Chetan Gadgil** for their support and advices during my AcSIR course work period and completion of thesis.

I would like to extend my special thanks to **Dr. Sakya Sen**, for helping me while writing one of the manuscripts. I wish to express thanks to **Dr. A.K. Siddhanta, and Dr. Adimurthy** for their guidance and valuable advices during my AcSIR class course work.

I wish to express my sincere thanks to **Dr. Vinod Boricha** for recording NMR, **Mr. Vinod Agarwal** for recording FTIR, **Mr. Arun Kumar Das** for Mass Spectrometry, **Harsad Brambhatt** for elemental analysis and HPLC measurements at CSMCRI.

Acknowledgement

I would like to express my Special thanks to **Dr. Prasenjit Kar, Dr. Amrita Ghosh, Dr. Moorthy Suresh, Dr. Prasenjit Mahato, Dr. Amal Kumar Mandal, Dr. Priyadip Das, Dr. Sukdeb Saha, Dr. Tanmay Banerjee**, my seniors. They all have been so successful in their own way. They all taught me initial days of my research carrier and took me along with them until their final days at CSMCRI.

I feel fortunate enough to have, **Dr. Upendar Reddy, Dr. L. Praveen, Dr. Sovan Roy, Dr. Suman Pal, Dr. Ajoy Pal, Dr. Shilpi Kushwaha, Hridesh Agarwalla, Arunava Maity, Monalisa Gangopadhyay, Firoj Ali, Sunil Aute, Anila H.A, Anantha Dey and Sanjukta Pahar** as my research colleagues, with whom I worked all these years in my lab 101 & 182. Each one of them has contributed in different way in fulfilling my goal.

I am sincerely thankful to **Dr. Muni Swamy, Dr. Shafee** and **Dr. V. Ramakrishna**, who took care of mine in the initial days of my joining CSMCRI, also their effort which brought me to CSMCRI and for enormous helps during in my whole PhD journey.

I am extremely thankful to my beloved friends **Sadu Nageswara Rao, Dr. Chandramohan, Bhanu Chandar, Subba Rao, Dr. Stalin, Sandeep, Sampath, Rabin, Kalam, Dr. K. Srinivas, Dr. Pankaj** who shared my joy and happiness while playing sports as well in doing the research.

I am very glad to have nice room partners **Sandeep Nadella, N. Vishwanath, Bhuma Naresh, Battu Satish**, and for their friendly and moral support in day to day life at CSMCRI & NCL.

My sincere thanks to all my friends and well-wishers and colleagues **Nandaraj Taye, and Aftab Alam** for their fruitful discussion about the cell biology experiments. I sincerely thank all other scientists, Technician and other staff Members of **CSMCRI** and **NCL** for their keen help and co-operation.

I would like to acknowledge **DBT, UKIERI and DAE-BRNS**, Government of India for financial assistance in the form of a research fellowship.

Finally, I thank the most important people in my life, my parents **Mr. Govindu, Mrs. Ramalakshmi** for their unconditional love and affection on me. I am also very lucky to have unlimited support & love from my wife **Deepika** who has waited and still waiting for my arrival for the last 7 years.

There are inevitably people I have missed out. If you are not mentioned, it is not because you didn't contribute. Thank you.

Vadde Ramu

ABBREVIATIONS

Cdk	Cyclin dependant kinase
CD ₂ Cl ₂	Deuterated dichloromethane
CDCl ₃	Deuterated chloroform
CD ₃ OD	Deuterated Methanol
DMF-d ₇	Deuterated N, N'-dimethylformamide
DMSO-d ₆	Deuterated Dimethyl sulfoxide
CD ₃ CN	Deuterated acetonitrile
DMF	N,N'-dimethylformamide
DNA	Deoxyribonucleic acid
DMSO	Dimethyl sulfoxide
EDTA	Ethylenediaminetetraacetate
ESI	Electrospray Ionization
LED	Light Emitting Diode
(λ _{exc})	Excitation Wavelength
(λ _{emi})	Emission Wavelength
MLCT	Metal to Ligand Charge Transfer
ns	Nanosecond
PDT	Photodynamic Therapy
TCSPC	Time Correlated Single Photon Counting
mM	Mill molar
µL	Micro litre
ITC	Isothermal Titration Calorimeter
PBS	Phosphate buffered saline

SD	Standard deviation
PAGE	Polyacrylamide gel electrophoresis
NMR	Nuclear Magnetic Resonance
FTIR	Fourier transform infrared
ppm	Parts per million
CT-DNA	Calf-thymus deoxyribonucleic acid
CLSM	Confocal laser scanning microscope
ER	Endoplasmic reticulum
MTT	3-(4,5-dimethylthiazol-2-yl)-2,5-diphenyltetrazolium bromide
RNO	N, N-Dimethyl-4-nitrosoaniline
LC	Ligand-centered
K _r	Radiative rate constant
K _{nr}	Non radiative rate constant
IC ₅₀	Inhibitory concentration to kill 50% cells
HEPES	4-(2-hydroxyethyl)-1-piperazineethanesulfonic acid
D ₂ O	Deuterium oxide
rpm	Revolutions per minute
ICP-MS	Inductively coupled plasma mass spectrometry
MP-AES	Microwave Plasma - Atomic Emission Spectroscopy
Chk2	Checkpoint kinase 2
amp	Aminomethyl pyridine
fs	Femto second
ROS	Reactive oxygen species
HpD	Hematoporphyrins

CHAPTER	SECTION	TITLE	PAGE No
Chapter 1	1	DESIGN, SYNTHESIS AND DNA INTERACTION STUDIES WITH NOVEL PHOTOSENSITIZER MOLECULES AS EFFICIENT PHOTODYNAMIC THERAPEUTIC AGENTS	1
	1.1	Introduction	1
	1.2	Cellular uptake and localization	4
	1.3	Small molecules binding to DNA	6
	1.3.1	Irreversible binding to DNA	7
	1.3.2	Reversible binding to DNA	8
	1.4	Characterization of metal complexes binding to DNA	11
	1.5	Ruthenium complexes as anti-cancer drugs	13
	1.5.1	Hypotheses on the mechanism of action of Ru(II) complexes	14
	1.5.2	Existing Ru(II) anticancer compounds: State of the art	15
	1.5.3	Polynuclear Ruthenium-Platinum complexes	17
	1.6	Aim of the thesis	18
	1.7	Ruthenium(II) complexes as cellular imaging agents	20
	1.8	Photo induced cytotoxicity of Ru(II)-polypyridyl complexes	24
	1.8.1	Active components of PDT	24
	1.8.2	Ruthenium complexes as photosensitizers in PDT	26
	1.9	References	28

Chapter 2	SYNTHESIS, CHARACTERIZATION AND CYTOSTATIC ACTIVITY OF Ru(II)-Pt(II) BIS(TERPYRIDYL) COMPLEX THAT BLOCKS ENTRY INTO S-PHASE	33
2.1	Introduction	33
2.2	Experimental section	36
2.2.1	Materials and methods	36
2.2.2	General experimental procedures for interaction studies with CT-DNA	37
2.2.3	Calculation of lipophilicities of metal complexes (Partition coefficients/logP)	38
2.2.4	Isothermal Titration Calorimetry (ITC) studies with CT-DNA	38
2.3	Experimental procedures for various cell biology studies	39
2.3.1	Cell culture studies	39
2.3.2	Cell proliferation assay	39
2.3.3	Nuclear morphology	39
2.3.4	Cell growth and cell viability (Trypan Blue)	40
2.3.5	Cellular uptake quantification (ICP-MS)	40
2.3.6	Sub-cellular fraction	40
2.3.7	Cell cycle analysis Flow cytometry studies	41
2.3.8	Immunoblot analysis (western Blotting)	41
2.4	Design, synthesis and characterization of Ru(II)-Pt(II) complex	42
2.4.1	Synthesis and characterization	43
2.4.2	Synthesis of L ₁ : 4-([2,2':6',2"-terpyridin]-4'-yl)aniline: (tpyA)	44
2.4.3	Synthesis of Ru(tpy)Cl ₃	44

2.4.4	Synthesis of [Ru(tpy)(tpy-a)](PF ₆) ₂ (1)	45
2.4.5	Synthesis of [Ru(tpy)(tpypma)](PF ₆) ₂ (2)	46
2.4.6	Synthesis of [Ru(tpy)(tpypma)Pt(Cl) ₂]Cl ₂ (3)	47
2.4.7	Synthesis of [Ru(tpy)(tpypma)Pt(Cl)(DMSO)](PF ₆) ₃ (4)	47
2.4.8	Synthesis of [Pt(amp)(Cl)(DMSO)] ⁺ (5)	48
2.5	Results and discussion	49
2.5.1	Photophysical properties	49
2.5.2	DNA-binding studies: UV-Visible titration with CT-DNA	50
2.5.3	Viscosity Measurements	51
2.5.4	¹ H NMR titration studies with guanosine	52
2.5.5	Isothermal titration calorimetry studies with CT-DNA	55
2.5.6	Partition coefficient measurement	56
2.5.7	The impact of complex 4 on cancer cell proliferation	56
2.5.8	Cellular uptake properties of 2, 4, 5 and cisplatin	59
2.5.9	Complex 4 does not induce apoptosis or necrosis	62
2.5.10	Complex 4 induces G1 cell cycle arrest	64
2.5.11	Complex 4 does not activate the DNA damage response network	65
2.5.12	Complex 4 up-regulates p ²⁷ and inhibits Rb phosphorylation	67
2.6	Conclusion	69
2.7	References	71

Chapter 3	3	PHOTO-INDUCED CYTOTOXICITY AND ANTI-METASTATIC ACTIVITY OF Ru(II)-POLYPYRIDYL COMPLEXES	73
3.1	Introduction	73	
3.2	Experimental section	76	
3.2.1	N,N-Dimethyl-4-nitrosoaniline/histidine assay	76	
3.2.2	Cytotoxicity and confocal studies	77	
3.2.3	Wound healing (scratch motility) assay	78	
3.2.4	Comet assay	78	
3.2.5	Cellular uptake & quantification of 1, 2, by MP-AES	79	
3.2.6	Cell cycle analysis	79	
3.2.7	Invasion assay	79	
3.2.8	Western blotting	80	
3.3	Synthesis and characterization	81	
3.3.1	Synthesis of L ₁ : Ethyl (4'-methyl-[2,2'-bipyridine]-4-carbonyl)tyrosinate	81	
3.3.2	Synthesis of L ₂ : Ethyl (4'-methyl-[2,2'-bipyridine]-4-carbonyl)tryptophanate	82	
3.3.3	Synthesis of complex 1	82	
3.3.4	Synthesis of complex 2	83	
3.4	Results and discussion	84	
3.4.1	UV-Visible and fluorescence titration studies with CT-DNA	84	
3.4.2	Isothermal titration calorimetry studies with CT-DNA	86	
3.4.3	Viscosity studies	87	
3.4.4	Light induced cytotoxicity: MTT assay	88	

3.4.5	DNA photo-cleavage: Gel electrophoresis studies	90	
3.4.6	Single-Cell Gelectrophoresis (SCGE) or Comet assay	93	
3.4.7	Evaluation of $^1\text{O}_2$ production ability of 1 and 2	94	
3.4.8	Cellular uptake and confocal imaging studies	96	
3.4.9	Partition coefficient logP measurement	98	
3.4.10	Anti-metastatic activity test	99	
3.4.11	Invasion assay	100	
3.4.12	Cell cycle analysis studies	101	
3.4.13	Complex 1 and 2 induces apoptosis by caspase-3 and caspase-9 activation	102	
3.5	Conclusions	103	
3.6	References	104	
Chapter 4	4	SYNTHESIS, CHARACTERIZATION AND DNA INTERACTION STUDIES OF HETERODINUCLEAR Ru(II)-Pt(II) BIPYRIDYL COMPLEX	107
4.1	Introduction	107	
4.2	Experimental section	109	
4.2.1	Confocal microscopy and MTT assay	109	
4.3	Synthesis and characterization	110	
4.3.1	Synthesis of L ₁ : 1-(4'-methyl-[2,2'-bipyridin]-4-yl)ethan-1-one	110	
4.3.2	Synthesis of L ₂ : 1-(4'-methyl-[2,2'-bipyridin]-4-yl)-N-(pyridin-2-ylmethyl)methanamine	111	
4.3.3	Synthesis of [Ru(bpy) ₂ (bpy-amp)] ²⁺ 1	112	
4.3.4	Synthesis of [Ru(bpy) ₂ (bpy-amp)PtCl ₂] ²⁺ 2	113	

4.4	Results and Discussion	113	
4.4.1	Photophysical characterization	113	
4.5	DNA-binding studies	114	
4.5.1	UV-Visible and fluorescence titration with CT-DNA	114	
4.5.2	Isothermal titration calorimetry studies	116	
4.5.3	Viscosity studies	118	
4.5.4	Gelectrophoresis studies	119	
4.5.5	Cytotoxicity studies: MTT assay	121	
4.5.6	Cellular uptake and confocal imaging studies	122	
4.6	Conclusions	123	
4.7	References	124	
Chapter 5	5	Ru(II)-POLYPYRIDYL BASED IMAGING REAGENTS FOR LIPID DENSE REGIONS IN LIVE CELLS AND THE NUCLEUS IN FIXED MCF-7 CELLS	127
5.1	Introduction	127	
5.2	Experimental section	129	
5.2.1	Crystallographic study of complex 1	129	
5.2.2	MTT assay and confocal studies	129	
5.2.3	Cellular uptake and quantification of 1, 2, and 3 by (MP-AES)	130	
5.3	Synthesis and characterization	131	
5.3.1	Synthesis of L₁ and L₂	132	
5.3.2	Synthesis of L₁: 1-((4'-methyl-[2,2'-bipyridin]-4-yl)methyl)pyrimidine-2,4(1H,3H)-dione	133	
5.3.3	Synthesis of L₂: 5-Fluoro-1-((4'-methyl-[2,2'-bipyridin]-4-yl)methyl)pyrimidine-2,4(1H,3H)-dione	133	

5.3.4	Synthesis of [Ru(bpy) ₂ (L ₁)](PF ₆) ₂ (1), [Ru(bpy) ₂ (L ₂)](PF ₆) ₂ (2) and [Ru(bpy) ₂ (L ₃)](PF ₆) ₂ (3)	134
5.3.5	Single crystal X-Ray diffraction studies and crystal structures of complex 1	136
5.4	Results and discussion	138
5.4.1	Photophysical characterization of complexes 1 and 2	138
5.4.2	Isothermal titration calorimetry studies	140
5.4.3	Viscosity measurements	142
5.4.4	pBR322 plasmid DNA cleavage studies	143
5.4.5	Cytotoxicity studies	144
5.4.6	Live cellular imaging studies	144
5.4.7	Correlation between the lipophilicity and cellular uptake	146
5.4.8	Fixed cell staining studies	148
5.4.9	Photostability test	150
5.6	References	153
	Conclusion & Future scope of the work	157
	Appendix	161
	List of Publications/patents	179
	List of conferences/workshops attended	180

CHAPTER 1

INTRODUCTION



1. Design, synthesis and DNA interaction studies with novel photosensitizer molecules as efficient photodynamic therapeutic agents

1.1. Introduction

In all eukaryotic and prokaryotic organisms the storage of genetic information is encoded almost entirely in the biopolymer called deoxyribonucleic acid (DNA).¹ The “genetic code” within DNA is contained in the cells of the organism and provides the blueprint for the formation of ribonucleic acid (RNA) and proteins, which are the functional components of cells. The flow of biological information, whereby a section of DNA is transcribed into RNA, which in turn is responsible for the synthesis of specific proteins (translation), is set forth in “the central dogma of molecular biology”, as formalized by Crick (Figure 1.1).²

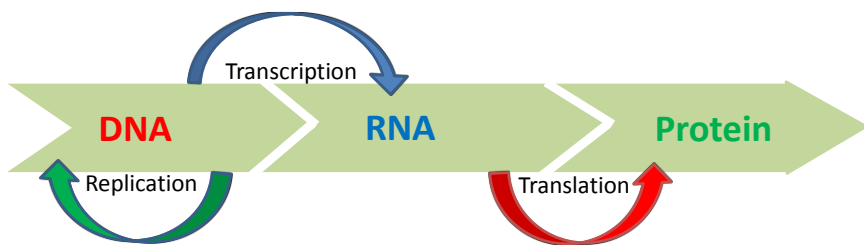


Figure 1.1. The central dogma of molecular biology.

The process of DNA replication that allows organisms to make duplicates of their genomes. Along with the ability of cells to replicate themselves, this assists each new generation of the cell (and therefore the organism) to undergo the exact transfer of information encoded by the cell's DNA and this serves as the basis of biological inheritance and genetics.³

DNA is a linear bio-polymer composed of repeating nucleotide units, each included of a nitrogen heterocyclic base, a pentose sugar and a phosphate group (Figure 1.2). The four nitrogenous bases in DNA can be adenine (A), guanine (G), cytosine (C) and thymine (T) and it is through sequences of these bases that the genetic information of the organism is contained and then expressed via translation and

transcription.⁴ Each nucleotide in the DNA molecule is linked by a phosphodiester bond between the 3' and 5' carbon atoms on adjacent sugar rings and sequences of DNA are written in the 5' → 3' direction.

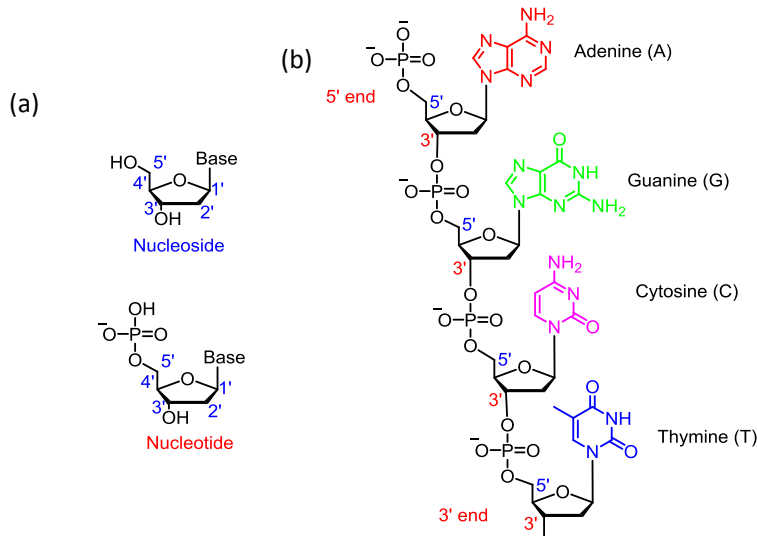


Figure 1.2. (a) Structure of the DNA nucleoside and nucleotide, (b) nucleotides of DNA connected by phosphodiester linkage bonds.

The most energetically favorable form of DNA is the right-handed double helix B-DNA, which was first described by Watson and Crick using Franklin's crystal structure.⁴ The structure of B-DNA consists of two strands of DNA running in opposite directions organized by hydrogen bonding between pairs of bases on opposing strands;

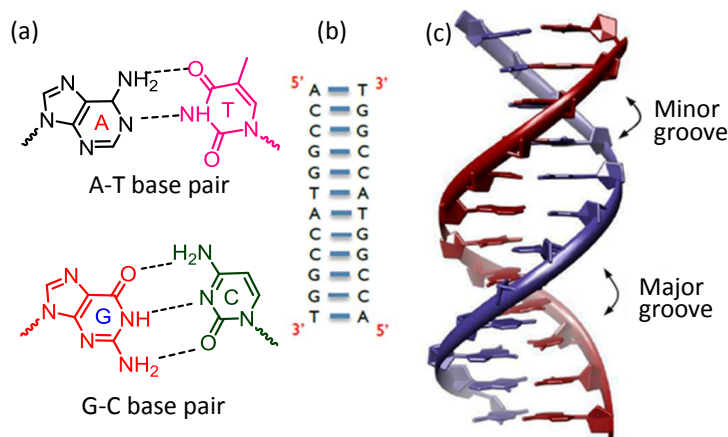


Figure 1.3. (a) DNA base pairs, (b) two opposite strands of DNA are complementary to each other, (c) B-DNA double helix showing grooves (nucleic acid database (NDB) ID: BD0003).

A (adenine) pairs with T (thymine) and G (guanine) pairs with C (cytosine) (Figure 1.3a, b). The double helix of B-DNA possesses two grooves: the major groove (width: 12 Å) and minor groove (width: 6 Å) as shown in Figure 1.3c. The series of events that cells undergo leading up to cell division is described by the cell cycle. This involves four distinct phases: G₁, S (DNA synthesis), G₂ and M (mitotic phase). G₁, S and G₂ phases are together known as interphase (Figure 1.4). In addition to these there is a resting phase G₀, where cells remain viable but do not proliferate. The cell cycle is strictly regulated by numerous proteins and monitored by checkpoints which operate within S-phase, between S and M phase, as well as at the G₁/S and G₂/M phase boundaries.

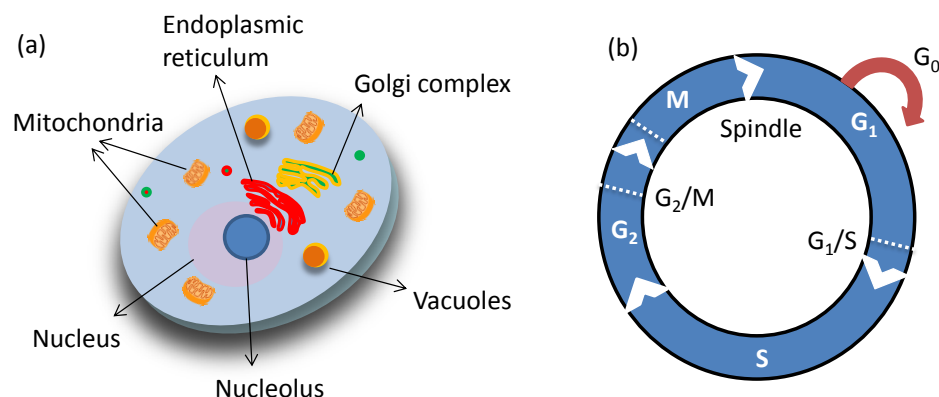


Figure 1.4. (a) Structure of eukaryotic cell, (b) various phases of cell cycle involved during cell division.

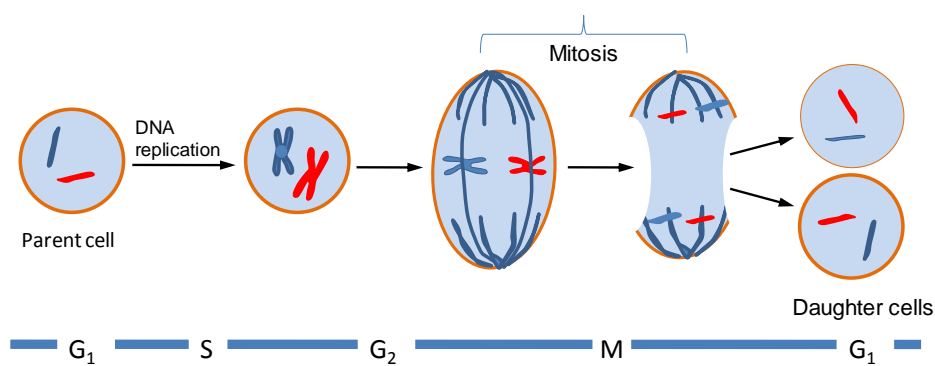


Figure 1.5. Schematic representation of various stages of the cell division.

In addition, a spindle checkpoint ensures that segregation of sister chromatids cannot occur unless all chromosome pairs are attached to the mitotic spindle, thus preventing aneuploidy (an abnormal number of chromosomes).⁵ The ability for cells to divide and multiply is fundamentally important to their growth and maintenance of the organism. During eukaryotic cell division, chromosomes are first duplicated through DNA replication before pairs of chromosomes condense and then separate using a mitotic spindle into two identical sets located in opposite regions of the cell (mitosis). The parent cell then divides to form two daughter cells the process called cytokinesis, each of which contains one of these sets and thus an exact copy of the parental DNA (Figure 1.5).

1.2. Cellular uptake and localization

To interact with DNA in living cells, the molecules should enter the interior of cells and must be able to reach the cell nucleus (or mitochondria). In the case of eukaryotic cells, the first barrier is the cell membrane (Figure 1.6). This is composed of a lipid bilayer, containing phospholipids (composed of a hydrophilic head group attached to hydrophobic hydrocarbon chains) and a variety of proteins and lipids that regulate the cellular uptake of extracellular particles.

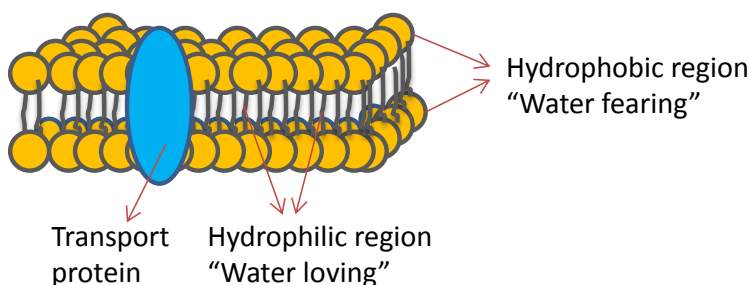


Figure 1.6. Pictorial representation of the cell membrane and its components.

The hydrophobic interior of the bilayer means that membrane diffusion is determined by the polarity as well as the size of a molecule. It has been argued that molecules with high polarity are generally not efficient in penetrating the cell membrane. If a

molecule is less membrane permeable, then it will require a transport mechanism or endocytosis for cellular internalization. Other than passive diffusion, these mechanisms are strongly regulated by specific proteins or receptors. Figure 1.7 demonstrates the broad mechanisms by which cells uptake the small molecules. Vital molecules such as amino acids, sugars and ions pass across the cell membrane through the action of membrane pumps, channels or carrier proteins. This may be energy-independent (passive transport), driven by an electrochemical gradient, or energy-dependent (active transport)-usually driven by the conversion of ATP to ADP. These mechanisms are highly selective and rely upon protein-specific binding to a target molecule or ion.

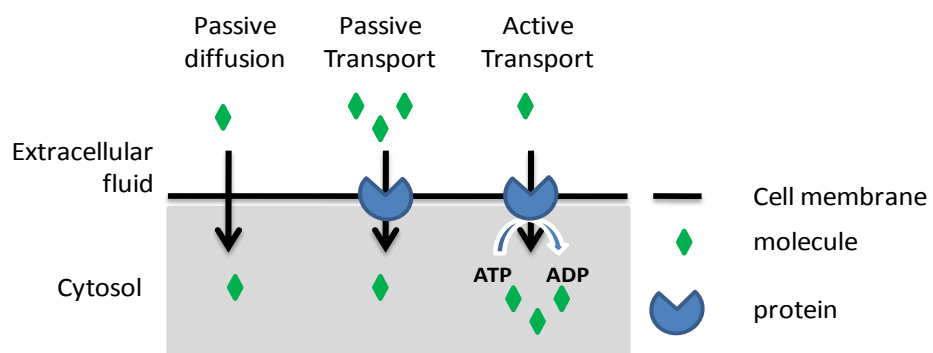


Figure 1.7. Pictorial representation of cellular uptake processes.

There is an alternate methodology to internalize the molecules inside cellular interior, which is famously known as cell fixation. This preserves cell or tissue morphology through the preparation process. Most cell fixation procedures involve adding a chemical fixative that creates chemical bonds between proteins to increase their rigidity. Common fixatives include formaldehyde, ethanol, methanol, and/or picric acid.⁶ It is well documented in the literature that the cell fixation can alter the cellular compartmentalization of the molecules. Formaldehyde or glutaraldehyde compounds, crosslinks proteins to the cytoskeleton and elements of the cytoskeleton to one another. This is generally the preferred method for double labeling of membrane bound and cytoskeletal antigens. This method modifies proteins

chemically and can potentially destroy antigens. Generally, this is not a problem when cells are being fixed using dilute PFA over a shorter duration (typical cell-fixation protocols use 2-4 % paraformaldehyde for 10-20 min); however, fixation of tissues usually takes appreciably long treatments to allow sample penetration and this alters the protein structure. Organic solvents, such as methanol, ethanol and acetone, fail to alter target proteins covalently; essentially, they precipitate proteins out of solution maintaining a protein “shell”, but ‘flattening’ cells as protein solubility is reduced. This process removes lipids and dehydrates the cells, while precipitating the proteins on the cellular architecture. However, the cells are generally non-viable to perform any further experiments after fixation. Treatment of cells with a mild surfactant, commonly termed as “permeabilization” generally dissolves cell membranes and allows larger dye molecules to enter inside the cell.⁷

1.3. Small molecules binding to DNA

The processes such as replication, transcription and translations are introduced, controlled and terminated by molecules and/or proteins which bind to the nucleic acids in site specific ways. Accordingly, the synthetic molecules that are able to bind with nucleic acids can also interfere with these steps (positively or negatively). Hence, the synthetic molecules find variety of uses as therapeutic agents. The structure of DNA allows synthetic molecules to bind in different mechanisms, which will be described in the following section. Scope of our discussion will be restricted to structure and chemical composition of duplex DNA that allows several mechanisms by which molecules can bind to the DNA-while such interactions could be reversible or irreversible. The following section provides an overview of these modes explained by selected examples from the literature.

1.3.1. Irreversible binding to DNA

The synthetic molecules or biomolecules those bind to DNA by forming covalent bonds can interact with the negatively charged phosphate backbone or sugar residues or nucleic acids. The initiation of DNA damage by a drug molecule forms the origin for “classical chemotherapy”. Due to the genetic instability initiated by this binding event, cancer cells are unable to effect the correct cell cycle and initiate checkpoint responses to induced damage and accordingly undergo cell cycle arrest, which eventually leads to apoptosis, or “programmed cell death”.⁸ Promptly dividing cells, such as cancer cells, are specially targeted by such a therapeutic regime.

Cisplatin and its derivatives offer the archetype of this approach: Platinum complexes binds to DNA through the coordination bonds formed between Pt(II) centres and available nitrogen atoms (N7 on adjacent purine base, guanine) on nucleotides subsequent substitution of the labile chloride ion and water molecule as shown below.

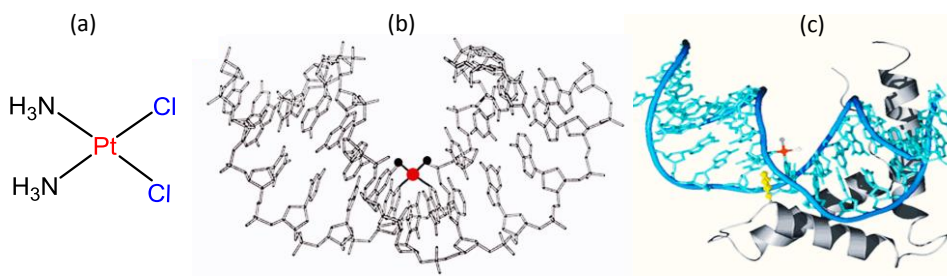
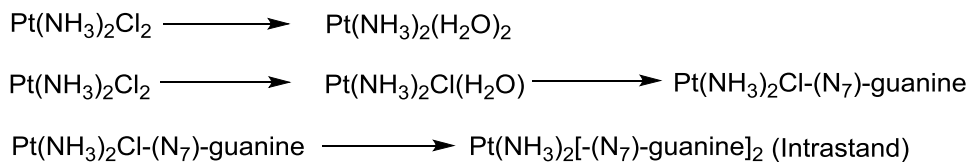


Figure 1.8. The interaction of cisplatin (a) with DNA nucleotide followed by the enfolding of HMG1 protein, (b) crystal structure showing cisplatin (red) binding to and 'kinking' DNA (grey) (adopted from ref.9.), (c) HMG1-domain protein domain shown as gray ribbon inserts a phenyl group (yellow) into the groove created when cisplatin forms a complex with DNA, causing it to bend.

As established by X-ray and NMR structural experimental studies, the formation of intrastrand cross-links causes a large bend in duplex structure and a change in the GG dihedral angle to 59°.⁹ These distortions open up and flatten the minor groove and making it more accessible to an irreversible binding to huge molecular group protein 1(HMG-1), which results in the inhibition of the cell cycle progression (Figure. 1.8).⁸ Based on the success of cisplatin and its derivatives, various metal complexes, including ruthenium(II)-based systems, were designed for achieving analogous activity. Further information on such systems is available in a number of excellent reviews on this fascinating area of research.^{1,10–12}

1.3.2. Reversible binding to DNA

Coordination complexes that bind reversibly to DNA are of increasing interest.^{10,13} In such systems the three-dimensional or spatial arrangement of ligands delivers a means by which binding to DNA can be achieved. Since ligands can be simply interchanged or modified, this provides a mechanism to control hydrophobicity, binding affinity and selectivity, in addition to cellular uptake. The judicious selection of ligands and the metal center also provides the opportunities for tuning of the photophysical properties of metal complex as a whole. Research in this area has been dominated by octahedral d⁶ metal polypyridyl complexes as they are kinetically inert, have well-built substitution chemistry, and retain attractive photophysical properties for this purposes. These systems can exploit numerous reversible-binding motifs.

The negative charge of DNA facilitates the cationic molecules to associate with the biopolymer. Undoubtedly, the naturally occurring polyamines for example spermine and spermidine can bind to DNA through polyvalent electrostatic interactions (Figure 1.9a). As most of the coordination complexes are charged, electrostatic binding properties often contribute to the binding affinity of complexes, which predominantly recognize DNA through binding modes described below. For example, simple metal

complexes, such as $[\text{Ru}(\text{bpy})_3]^{2+}$ ($\text{bpy} = 2,2'\text{-bipyridine}$), interacts with DNA exclusively through electrostatic effects typically possesses very low binding affinities (Figure 1.9).¹⁴

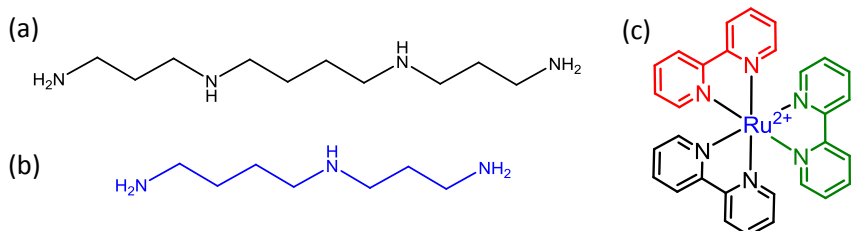


Figure 1.9. (a) Structure of spermine, (b) spermidine and (c) $[\text{Ru}(\text{bpy})_3]^{2+}$.

So far the most widely studied group of metal complexes that reversibly interact with duplex DNA is metallo-intercalators.^{15–20} Intercalation happens when planar aromatic compounds are inserted between adjacent base pairs in the DNA double helix. Intercalation which includes significant π system overlap between DNA bases and the intercalated molecule, as well as van-der Waals, hydrophobic and electrostatic interactions has the effect of unzipping and lengthening the DNA double helix.

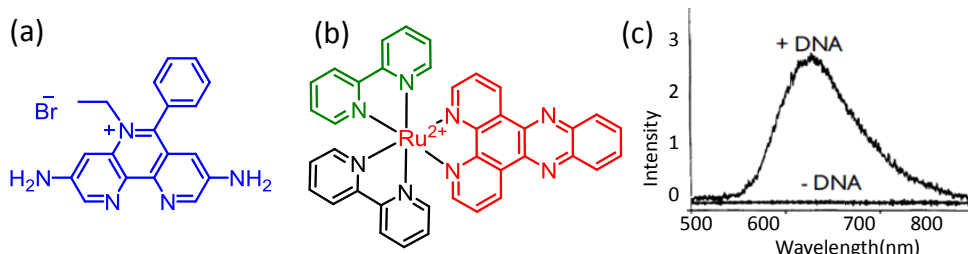


Figure 1.10. (a) Structures of ethidium bromide, (b) structure of $[\text{Ru}(\text{bpy})_2(\text{DPPZ})]^{2+}$, (c) emission spectral responses of $[\text{Ru}(\text{bpy})_2(\text{DPPZ})]^{2+}$ before and after addition of the CT-DNA.

The typical ruthenium metallo-intercalators are greatly studied $[\text{Ru}(\text{bpy})_2(\text{dppz})]^{2+}$ / $[\text{Ru}(\text{phen})_2(\text{dppz})]^{2+}$ cations (Figure 1.10; where phen = 1,10-phenanthroline, and dppz = dipyridophenazine) or analogous derivatives. Barton and Thomas groups demonstrated that these dppz-based complexes bind to DNA with a high affinity ($K_b \sim 10^6 \text{ M}^{-1}$) following an intercalation mode of binding.^{13,19,21–23} It is well documented that

Ru(II)-polypyridyl complexes show strong MLCT (MLCT = Metal-to-Ligand Charge-Transfer) absorption band at around 455 nm and excitation at this wavelength leads to the generation of an excited $^1\text{MLCT}$ state. This will undergo a fast (< 40 fs) and efficient ($\Phi \sim 1$) inter system crossing (IC) with subsequent and quantitative generation of the excited $^3\text{MLCT}$ state. Interestingly, such complexes display an intense $^3\text{MLCT}$ based luminescence band at ~ 620 nm.²⁴ However, $[\text{Ru}(\text{bpy})_2(\text{dppz})]^{2+}/[\text{Ru}(\text{phen})_2(\text{dppz})]^{2+}$ or analogous derivatives generally show a poor emission quantum yield in aqueous medium. This is primarily due to an efficient hydrogen bonding interaction between the solvent water molecules and the lone pair of electrons of the $\text{N}_{\text{Imidazole}}$ functionality, which favors the non-radiative deactivation of the excited $^3\text{MLCT}$ states of these complexes.¹⁹ All such complexes show a significant enhancement of emission quantum yield in aq. buffer medium on the addition of DNA. The phenomenon, is popularly known as “light switch” effect, and is attributed to the intercalation of the dppz moiety of $[\text{Ru}(\text{bpy})_2(\text{dppz})]^{2+}/[\text{Ru}(\text{phen})_2(\text{dppz})]^{2+}$ cations in the A-T rich region of the DNA molecules.¹³ Such intercalation in the hydrophobic pocket interrupts the interaction of the lone pair of electrons of the $\text{N}_{\text{Imidazole}}$ functionality and water molecules and the non-radiative deactivation. Such luminescence on responses are being utilized for monitoring the intercalative mode of binding of $[\text{Ru}(\text{bpy})_2(\text{dppz})]^{2+}/[\text{Ru}(\text{phen})_2(\text{dppz})]^{2+}$ or related complexes to DNA.

Another mode of reversible binding to DNA is by association within the minor or major grooves that run down the double helix.^{25,26} Molecules which bind DNA through grooves could span many base pairs and hence they can display very high levels of DNA sequence-specific recognition. Molecules come within the Van-der Waals distances of the grooves and then occupy the DNA grooves. Recognition and sequence-selective binding is governed by either individual or a combination of interactions, namely, hydrogen bonding, Van der Waals, hydrophobic contacts and

electrostatic interactions.²⁷ Classical groove binders for example DAPI and Hoechst 33528 are usually cationic and composed of aromatic rings linked by bonds with torsional freedom so that they are capable to twist and become isohelical with the DNA groove (Figure 1.11a).²⁸ Such systems have a tendency to reside in the minor groove of B form of DNA and exclusively bind to narrower and more electro-negative A-T rich sequences.

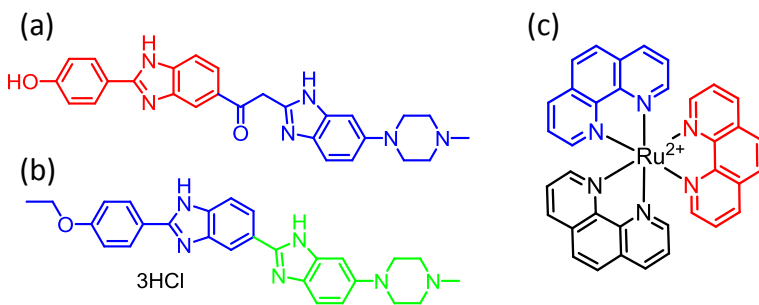


Figure 1.11. (a) Structure of DAPI, (b) Hoechst groove binding agent and (c) structure of $[\text{Ru}(\text{phen})_3]^{2+}$.

The first confirmed groove binding Ru(II) complex was $[\text{Ru}(\text{phen})_3]^{2+}$ (Figure 1.11c).²⁹ It was primarily thought that this complex intercalated into B-DNA, with the Δ -enantiomer displaying the highest affinity.¹⁴ But, more recent reports revealed that the complex was not an intercalator, but a groove binder. Furthermore; the Λ -enantiomer was a major groove binder at all loading ratios with one phenanthroline ligand approximately parallel to the base pair planes (partial insertion). In contrast, the Δ -enantiomer is almost exclusively a minor groove binder; although at high loading some partial insertion into the major groove also occurs.¹⁴

1.4. Characterization of metal complexes binding to DNA

A range of physicochemical techniques could be utilized for revealing the important factors that govern interaction(s) of a molecule with DNA. The optical spectroscopy can monitor molecular reagent-DNA interactions if the complex has distinct spectroscopic properties in its free state and when exists in the DNA-bound state.

The associated changes in the electronic and luminescence spectra help in evaluating the efficiency of the binding interaction(s) between the reagent and the DNA molecules. Quantitative measurement of the equilibrium binding constant (K_b) provides an insight into the strength of the intermolecular interaction.

Since, DNA is polymorphic; it can shield a bound reagent from solvent to various degrees and the level of shielding can be determined from the amount of luminescence changes upon reagent-DNA interactions, which helps in correlating the spatial arrangement of the reagent in the DNA bound condition.

As mentioned earlier, affective intercalator helps in lengthening the DNA double helix structure and this eventually leads to an increase in viscosity. Such change(s) in viscosity is an useful marker for understanding the intercalative binding mode for a reagent.¹²

Finally, the energetics that drives the binding interaction between DNA molecule and the reagent can be investigated using Isothermal titration calorimetry (ITC). ITC is the only technique that allows the direct measurement of the change in enthalpy for the reagent-DNA interaction process. This also enables us to evaluate association constant and stoichiometry for the reagent-DNA binding process and this methodology is used extensively in studying the interaction of DNA with the complexes that are discussed in this thesis. To fully appreciate the importance of ITC, the parameters that are being used for understanding the equilibrium thermodynamics is discussed. When a macromolecule (M) reacts with a ligand (L) reversibly it can be expressed by the following equilibria where K_b is the equilibrium binding constant.^{30,31}



The equilibrium constant K_b can be determined by the equation 2

$$K_b = \frac{[ML]}{[M][L]} \quad \text{Equation 2}$$

The Gibbs free energy for this interaction process can be defined by the standard thermodynamic relationship

$$G^{\circ} = -RT \ln K_b = \Delta H^{\circ} - T\Delta S^{\circ} \quad \text{Equation 3}$$

Where ΔH° and ΔS° are changes in standard enthalpy and entropy. R is the gas constant and T is the absolute temperature. The enthalpy change of bimolecular interactions can be found directly by ITC, and so the Gibbs free energy and entropy can be derived from equation 3, since K_b is also measured with ITC or by spectroscopy.

1.5. Ruthenium complexes as anti-cancer drugs

Despite its chemotherapeutic success, cisplatin is by no means the perfect drug. It is not effective against certain types of cancer. It also suffers from the problem of drug resistance and has a deplorable range of side effects, which can include nerve damage, hair loss and nausea and cytotoxicity towards healthy cells too. This leads to the search for more efficient anti-cancer drugs based on various transition metal ions complexes. In this context various ruthenium based complexes have been explored for this purpose. In spite of this flexibility in oxidation state, ruthenium complexes display relatively slow ligand exchange rates in water.³² In general, kinetics associated with the substitution reaction for ruthenium complexes are on the timescale of cellular reproduction (mitosis), which implies that ruthenium ion (bound to certain component in the cell) is likely to remain bound for the remainder of that cell's lifetime.³² Among various complexes, Ru(II)-polypyridyl complexes adopt a slightly distorted octahedral geometry and inert towards substitution process either in the ground and excited states. Such inertness in general helps such molecules to be benign to human physiology and exhibit only nominal toxicity towards live cells in their ground state. Possibility of using such reagent as photodynamic therapeutic reagent is discussed below.

1.5.1. Hypotheses on the mechanism of action of ruthenium complexes

In the blood, ruthenium mimics iron in binding to certain biomolecules, such as albumin and transferrin.³³ Specific intake of Ru(II) and Ru(III) ions might be mediated by the transferrin-based iron transport system.³⁴ The serum transferrin system specifically recognizes Fe(III) (and not Fe(II)) along with a synergistic anion (usually carbonate).³³ Transferrin binds strongly to its receptor when it is loaded with two Fe(III) ions, after which it is internalized by cells. Release of Fe(III) from transferrin is induced at low pH. The protein is then recirculated into the blood.

There is a distinct possibility for this transport mechanism to be operational in cancer therapy, as high levels of transferrin receptors are expressed by many solid tumor cells, due to their higher iron requirement than normal cells. Moreover, the relatively low pH of tumor cells facilitates readily the release of transferrin-bound metal ions. Selective tumor toxicity may also be reached by what is known as the “activation by reduction” mechanism. It has been suggested that Ru(III) complexes may serve as prodrugs,³⁵ which will get activated by reduction *in-vivo* to coordinate more rapidly to biomolecules, since Ru(II) species are usually less inert than the corresponding Ru(III) complexes.³⁶

The low oxygen content and low pH in tumor cells cause a relatively low electrochemical potential inside tumors. Therefore, the reduction of Ru(III) to Ru(II) is favored in tumors relative to normal tissue. *In-vivo*, reduction of Ru(III) species can occur by glutathione (GSH) and redox proteins available in the cell. Glutathione, which appears to contribute to cisplatin resistance in tumor cells, may also be involved in the metabolism of many types of ruthenium pharmaceuticals. GSH has been shown to bind to ammineruthenium(III) complexes, and depending on its concentration it either facilitates or inhibits ruthenium coordination to DNA.^{36,37}

1.5.2. Existing ruthenium anticancer compounds: State of the art

A number of amine and amine ruthenium complexes, as well as complexes with monodentate and chelating heterocyclic ligands have been synthesized for anticancer purposes.^{38,39} The tetrachlororuthenium(III) complexes of the type (HL)[RuCl₄L₂] (where L is imidazole (im) or indazole (ind)) have emerged as promising compounds as they display activity against number of cancer cell lines, and in particular against colorectal tumors.^{32,39} Human colon cancer is the second highest occurring cancer after bronchial carcinomas.⁴⁰ The complex KP1019, (Hind)[RuCl₄(in)₂] (Figure 1.12a) is highly active against a model of colorectal cancer, which has been used as sometimes only weak activity is observed against colorectal tumors using conventional treatments.^{41,42} The drug KP1019 is completely devoid of side effects and drug induced lethality at active dosages, and it has shown a better therapeutic index than the imidazole derivative.⁴² The complex has been announced to enter phase I clinical trials.⁴³ Results have demonstrated that the transferrin-bound species of both KP1019 and its imidazole analogue, as well as the apotransferrin form of (Him)[RuCl₄(im)₂] exhibit anticancer activity superior to that of the protein-free complexes.³⁵

Therefore, the low toxicity of KP1019 presumably stems from a transferrin-mediated accumulation in tumor cells.⁴² The mechanism of KP1019 was based on the “activation by reduction mechanism” and a different DNA binding mode compared to cisplatin has been proposed to explain the unique cytotoxicity in tumor cells.⁴⁴ The first ruthenium complex, i.e. NAMI-A (trans-(H₂im)[RuCl₄(dmso)(Him)]), (Figure 1.12), has recently accomplished phase I clinical trials.⁴⁵ This complex belongs to the class of ruthenium dimethylsulfoxide complexes. Such complexes are known to be relatively nontoxic towards the tumor cells under *in-vitro* condition, and show a remarkable high efficiency for *in-vivo* studies against lung metastasis,⁴⁶ a common feature of many human tumors. Because of the S-bonded dmso ligand, NAMI-A is

easily reduced to the corresponding Ru(II) species by biological reducing agents under physiological conditions.⁴¹ It has been proven that these reduced species maintain their anticancer activities.⁴⁷

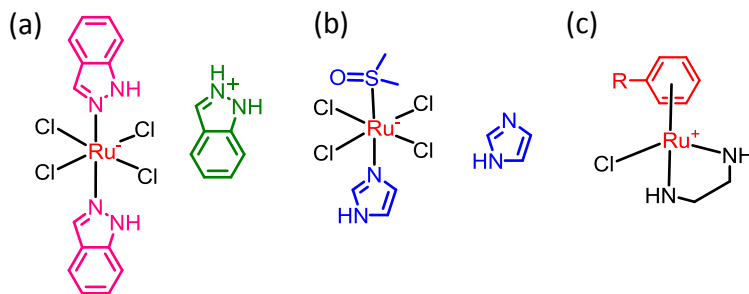


Figure 1.12. (a) Ruthenium(III) pharmaceuticals KP1019, (b) NAMI-A and (c) the ruthenium(II) complex $[(\eta^6\text{-C}_6\text{H}_5\text{C}_6\text{H}_5)\text{RuCl}(\text{en-Et})]\text{PF}_6$; where the R represents a phenyl group.

Interestingly, the anti-metastatic activity appears not to be related to DNA binding, even though the complex interacts with DNA *in-vitro*.⁴¹ Instead, NAMI-A interferes with fibrous collagen of the lung and with basement membrane collagen type IV.⁴⁸ It significantly increases the thickness of connective tissue around the tumor capsule and around tumor blood vessels, thereby probably hindering blood flow to the tumor.⁴⁷ The inhibition of angiogenesis has been attributed to induction of apoptosis, as has recently been shown in ECV304 cells.⁴⁹ Since angiogenesis is crucial for metastasis formation, and in particular for metastases growth, it is likely that the inhibition of this process is relevant for the activity of NAMI-A against metastasis.

Organometallic Ru(II) complexes with arene ligands represent a relatively new group of water-soluble ruthenium compounds with antitumor activity displayed *in-vitro* and *in-vivo*.⁵⁰ No cross-resistance has been observed in cisplatin-resistant cells, but did occur in the multi-drug-resistant cell line 2780AD. The most hydrophobic arene species $[(\eta^6\text{-C}_6\text{H}_5\text{C}_6\text{H}_5)\text{RuCl}(\text{en})](\text{PF}_6)$ (Figure 1.12c) and $[(\eta^6\text{-C}_6\text{H}_5\text{C}_6\text{H}_5)\text{RuCl}(\text{en-Et})]\text{PF}_6$ (en = ethylenediamine, and en-Et = N-ethylethylenediamine), in which a phenyl is substituent at the arene ligand, showed the highest tumor-inhibiting activity.⁵¹ It has been suggested that the presence of the hydrophobic planar arene

ligand facilitates the recognition and transport of these complexes through cell membranes. The relative conformational flexibility of the arene ligand makes simultaneous intercalation and coordination of ruthenium to DNA.

1.5.3. Polynuclear Ruthenium-Platinum complexes

Heteropolynuclear complexes of ruthenium and platinum have been developed to achieve selective reactivity at each metal center. Since ruthenium and platinum anticancer complexes display different mechanisms of action, the combination of the different metals may result in a unique profile of activity. The preparation of only a few ruthenium-platinum polynuclear complexes have been described, but detailed biological activity hitherto not been reported so far. The complex $\left[\{\text{cis-RuCl}_2(\text{dmso})_3\}(\text{H}_2\text{N}(\text{CH}_2)_4\text{NH}_2)\{\text{cis-PtCl}_2(\text{NH}_3)\}\right]$ (Figure 1.13a), in which the two metal centers are linked by a long and flexible α,ω -diaminoalkane linker, was the first heterodinuclear ruthenium-platinum complex reported.⁵² The complex has been found to form DNA crosslinks at which repair-proteins are associated. The DNA lesion that is responsible for efficient DNA-protein crosslinking is the most DNA-DNA interstrand crosslink in which each metal center is coordinated to one strand of the DNA helix. The DNA crosslinks were suggested to act as potential suicide adducts by hijacking away critical proteins from their functions inside the cell. Unfortunately, the complex has been found to be too reactive for use as a probe, due to its light sensitivity and rapid hydrolysis. Heterodinuclear ruthenium-platinum compounds have also been devised to photo react with DNA. Systems, in which a ruthenium light-absorbing unit has been linked to a reactive platinum moiety, have been synthesized using short bridging heterocyclic ligands. The ruthenium unit provides water solubility and electrostatic interaction with DNA by its positive charge. These systems can be photo activated through light absorption of the ruthenium unit, thereby imparting reactivity at the platinum unit. The latter may then coordinate to DNA. The bridging ligand of the complex $[(\text{bpy})_2\text{Ru}(\text{dpb})\text{PtCl}_2]\text{Cl}_2$ (Figure 1.13b), affords an extra

interaction with DNA through an intercalative mode of binding.⁵³ Results have indicated that the complex primarily forms intrastrand crosslinks by coordination of the platinum unit, but a higher percentage of intrastrand cross links than cisplatin has also been found.

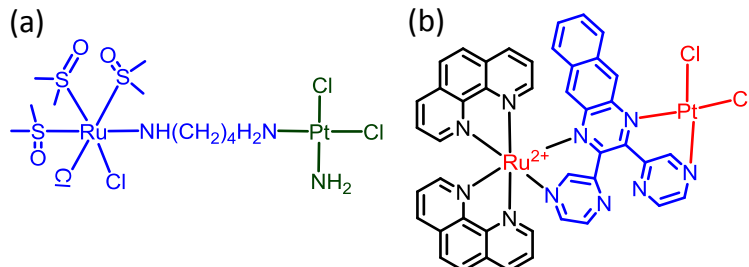


Figure 1.13. (a) The long and the flexible linked heterodinuclear Ru(II)-Pt(II) complex, (b) the short and rigid linked heterodinuclear Ru(II)-Pt(II) complex.

The system has been extended to complexes with 2,2':6',2"-terpyridine as the terminal ligand on ruthenium to eliminate enantiomer forms, and with either chloride or PEt₂Ph as the sixth ligand.⁵³ A variety of bridging ligands with different aromaticity, such as 2,2'-bipyrimidine, 2,3-bis(2-pyridyl)pyrazine and dpq, have been used to tune the spectroscopic and redox properties of the complexes. All have been shown to avidly bind to DNA, but photo reactivity has not been reported for these complexes. Dinuclear dimethyltriazolopyrimidine Ru-Pt complexes have been synthesized using bridging ligands like pyrazine and pyrimidine.⁵³ However, the biological data have not been described.

1.6. Aim of the thesis

The development of dinuclear Ru(II)-Pt(II) and mono nuclear Ru(II)-polypyridyl complexes in search for anticancer agents, which are effective against cisplatin resistant tumors, appears to be a productive field of research. Polynuclear ruthenium complexes on the other hand have not yet extensively been studied for their anticancer activities, and the synthesis of anticancer hetero dinuclear ruthenium-platinum complexes still presents a great challenge. The aim of the research

discussed in this thesis has been the design, syntheses and DNA interactions studies of mononuclear Ru(II)-polypyridyl complexes, as well as of heterodinuclear Ru(II)-Pt(II)-polypyridyl complexes as potential anticancer and cellular imaging reagents. These complexes have been designed to overcome cisplatin resistance. Their development has mainly been based upon the mononuclear complexes $[\text{Ru}(\text{tpy})\text{Cl}_3]$ and $[\text{Pt}(\text{tpy})\text{Cl}]$ ($\text{tpy} = 2,2':6',2''$ terpyridine) (Figure 1.14a, e).

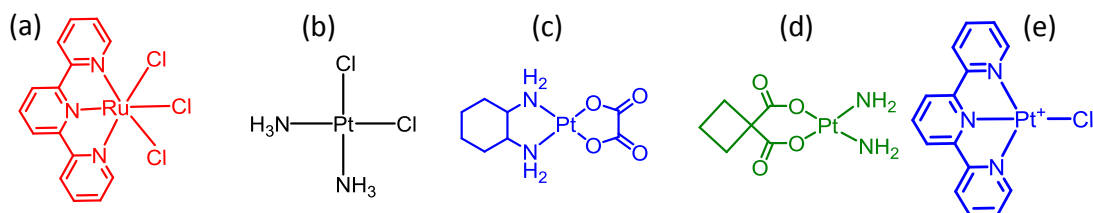


Figure 1.14. Chemical structure of (a) $\text{Ru}(\text{tpy})\text{Cl}_3$, (b) cisplatin, (c) oxaliplatin, (d) carboplatin and (e) $[\text{Pt}(\text{tpy})\text{Cl}]^+$.

The mononuclear Ru(III) complex $[\text{Ru}(\text{tpy})\text{Cl}_3]$ has been shown to display cytotoxicity and antitumor activity, which have been postulated to result from the interstrand binding to two guanines of the DNA in a trans position.⁵⁴ As it was discussed before cisplatin and its modified derivatives like oxaliplatin and carboplatin are well known for their anti-cancer activity and currently being used to treat the cancer patients around the world. On the other hand the mononuclear Pt(II) complex $[\text{Pt}(\text{tpy})\text{Cl}]^+$ has been found to display cytotoxicity against a number of cancer cell lines which has been ascribed to its ability to intercalate into DNA, as well as to coordinate to DNA.⁵⁵ However, the poor water solubility is a major problem for the development of clinically active compounds, and primarily this has attributed to the fact that the mononuclear complex $[\text{Ru}(\text{tpy})\text{Cl}_3]$ has not been developed any further for such application. Therefore, in this thesis more emphasis is given to synthesize heterodinuclear Ru(II)-Pt(II) complexes that have showed cytotoxicity different from the cisplatin. Such complex ideally should be able to generate ${}^1\text{O}_2$ through photo-induced activity of the ruthenium center, while the platinum center, a close analogue to the cisplatin moiety

should exhibit the cellular cytotoxicity on irreversible binding to guanine nucleotide of DNA. In order to show the cytotoxic effect by any drug molecules, first of all it has to penetrate the cell membrane which is composed of phospholipid bilayer. It is believed that the lipophilicity of a molecule plays a crucial role in the process of internalization through the cell membrane. Therefore the efforts have also been contributed towards the improvement of the lipophilicity of the Ru(II)-polyppyridyl complexes by conjugating them with amino acids like tyrosine, tryptophan and the nucleic acids uracil, 5-fluorouracil.

1.7. Ruthenium(II) complexes as cellular imaging agents

As previously discussed, there has been a large amount of research focused on ruthenium metal complexes that reversibly bind to DNA in vitro and attention to their application in biological systems is growing.⁵⁶ In this context, the use of luminescent, kinetically inert metal complexes that possess spectroscopically active metal centres are attractive and potential probes of DNA structure and function.²² Advantages of such systems are their high DNA binding affinities, sequence- and structure-specificity, interesting photophysical properties and flexible chemistry, which allows both ancillary and DNA-binding ligands to be interchanged or functionalized. Specifically for cellular imaging, Ru(II) complexes offer a very attractive set of optical imaging properties which include: photostability, low MLCT excitation energies in the visible region of the spectrum and high Stokes shifts, which helps to eliminate the problem of autofluorescence due to endogenous (organic) fluorophores.⁵⁷ With this in mind, the study of the cellular uptake properties and in cellulo DNA binding of metal complexes is of key importance in their development towards potential applications as cellular imaging agents.

In one of the earlier studies, the intercalator $[\text{Ru}(\text{bpy})_2(\text{taptp})]^{2+}$ (taptp = 4,5,9,18-tetraazaphenanthreno[9,10-b]triphenylene) was observed to act as an indicator of cell viability for both flow cytometry and confocal microscopy.⁵⁸ This non-membrane-

permeable complex was found to exclusively stain the nuclei of dead cells in a manner analogous to the dead cell stain propidium iodide (PI).⁵⁹

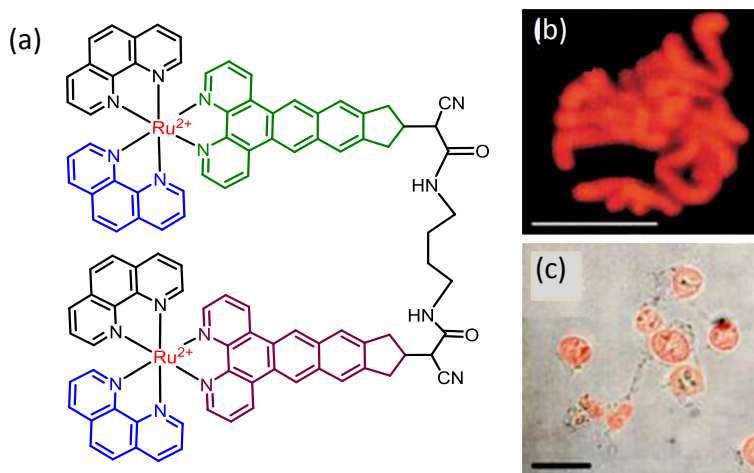


Figure 1.15. (a) Norden and Lincoln's Ru(II) dimer,(b) image of chromosomes in fixed V79 chinese hamster cell and (c) nuclear DNA stained in electroporated V79 cells. Reproduced with permission from ref. 59. Copyright 2002, Oxford University Press.

An important previous study in this area was conducted by Norden, Lincoln et al. where the potential of the liposome permeable, high DNA-affinity bis-intercalating complex $\Delta\text{-}\Delta [\mu\text{-C}_4(\text{cpdppz})_2\text{-}(\text{phen})_4\text{Ru}_2]^{4+}$ ($K_b = 10^8 \text{ M}^{-1}$) ($\text{cpdppz} = 12\text{-cyano-12,13-dihydro-11-hcyclopenta[b]dipyrido[3,2-a:2',3'-c]phenazine-12-carbonyl}$)¹³ to interfere with DNA metabolism was investigated by examining the uptake in V79 Chinese hamster cells (Figure 1.15c). The potential use of the complex as a nuclear DNA stain was clearly illustrated by the complex staining the chromosomes in fixed cells and using electroporation to facilitate membrane-diffusion in live cells (Figure 1.15b). They suggested that a pinocytic mechanism of uptake was occurring due to small areas of low emission in the cytoplasm. Having pioneered research into reversibly-binding Ru(II)-polypyridyl complexes, J.K.Barton group has focused their attention towards examining the cellular uptake properties of their well-characterized dppz DNA-binding systems using the MLCT light switch emission responses for assessing the cellular uptake and localisation.^{7,60} They found that the uptake efficiency was dependent on the nature of the ancillary ligands, with more hydrophobic ancillary

ligands such as DIP (Figure 1.16a) promoting increased cellular uptake, consistent with a mechanism of passive diffusion into the cytosol (Figure 1.16b). A surprising result of this work was the absence of MLCT emission from the nuclei of cells (Figure 1.16c). The fluorescein emission (Figure 1.16d) clearly demonstrated nuclear localization of the complex but again no nuclear MLCT luminescence was observed.

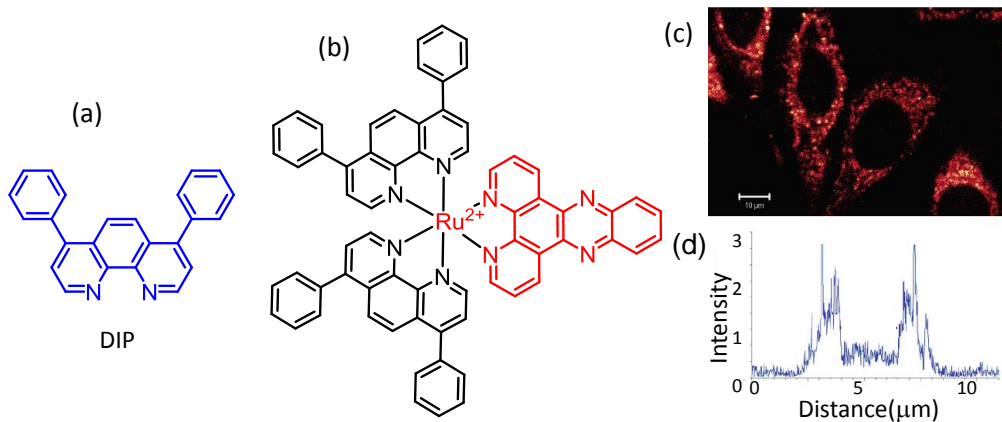


Figure 1.16. (a) Molecular structure of the ligand DIP, (b) $[\text{Ru}(\text{DIP})_2(\text{dppz})]^{2+}$ complex, (c) HeLa cells stained with $[\text{Ru}(\text{DIP})_2(\text{dppz})]^{2+}$, (d) fluorescent intensity profile plot. Reproduced with permission from ref. 60. Copyright 2013 American Chemical Society.

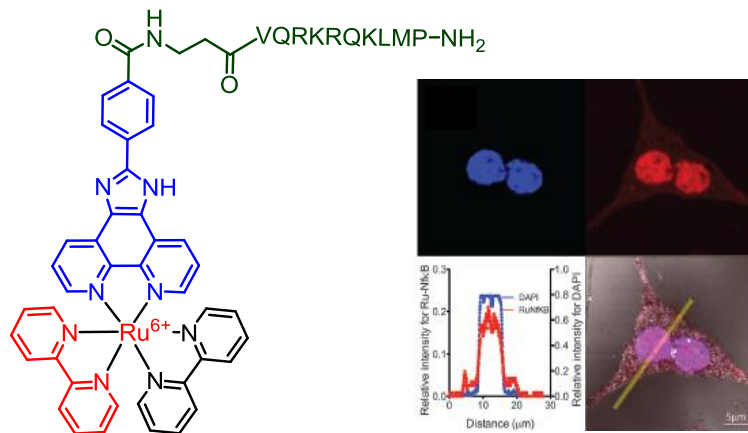


Figure 1.17. Molecular structure of $[\text{Ru}(\text{bpy})_2\text{PIC-bAla-NF-kB}]^{6+}$ and nuclear DNA staining observed in CHO cells. Reproduced with permission from ref. 6. Copyright 2013 The Royal Society of Chemistry.

Tia. E. Keyes et.al. have reported the targeted delivery of luminescent Ru(II)-polypyridyl complexes to the nucleus of live mammalian cells by a nuclear localization signal (NLS) peptide.⁶¹ The poly arginine conjugated ruthenium(II)-

complex; $[\text{Ru}(\text{LL})_2\text{PIC}]\text{ClO}_4$ where PIC is 2-(4-carboxyphenyl)-imidazo-[4,5-f][1,10]-phenanthroline and LL is bpy; 2,2'-bipyridine, (Figure 1.17) were reported which was conjugated to VQRKRQKLMP-NH₂ via a β-alanine bridge bound to the terminal carboxy units of the probes.⁶¹ The dye distribution depended on the hydrophobicity of the metal complex. They concluded that the conjugation of the Ru(II)-polypyridyl unit to the more hydrophilic NLS ligand directed the complex to the nucleus.

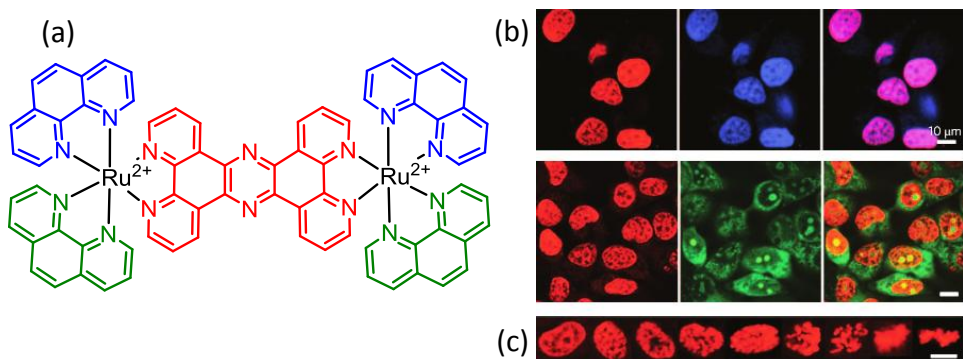


Figure 1.18. (a) Dinuclear Ru(II) tpphz complexes bearing phenanthroline as ancillary ligands, (b) confocal images of live MCF-7 cells incubated with dinuclear ruthenium complex, (c) chromosomes of the MCF-7 cells captured at various phases of the cell division. Reproduced with permission from ref. 22. Copyright 2009 Wiley-VCH.

Despite the fact that coordination complexes that exhibit ³MLCT-based emission has certain advantages described earlier, lower cellular uptake of such complexes has restricted their use as an imaging reagent in live cells. Martin et.al, have previously reported²² a dinuclear Ru(II)-polypyridyl system (Figure 1.18) that works as a multifunctional imaging agent. This reagent could also be used as for staining the DNA of eukaryotic and prokaryotic cells for both luminescence and transmission electron microscopic studies. This dinuclear MLCT ‘light switch’ complex directly images nuclear DNA of living cells without requiring prior membrane permeabilization.²² These compounds were essentially non-emissive in aqueous environments. However, they display bright luminescence when bound to DNA.

1.8. Photo induced cytotoxicity of Ru(II)-polypyridyl complexes

The synergistic action of light, oxygen and a photosensitizer (PS) has found applications for decades in medicine under the name of photodynamic therapy (PDT) for the treatment of skin diseases and, more recently, for the treatment of cancer. However, of the thirteen PSs currently approved for the treatment of cancer over more than 10 countries, only two contain a metal ion. More importantly, about half of the conventional chemotherapies involve the use of cisplatin and other platinum-containing drugs. Since the Ru(II) complexes are also photosensitive they offer better opportunities of using them as PSs in PDT. In addition, recent achievements in the application of Ru(II) complexes in photo activated chemotherapy (PACT) have also been discussed here.

1.8.1 Active components of PDT

PDT requires three elements for an effective treatment: photosensitizer, light, and oxygen. Singlet oxygen is believed to be the main reactive oxygen species (ROS) which destroys tumor cells by necrotic and apoptotic cell death mechanisms.⁵⁶ Following the absorption of light, the photosensitizer is transformed from its ground singlet state (S_0) into an electronically excited triplet state (T_1) via a short-lived excited singlet state (S_1). The excited triplet can undergo two types of reactions as shown in the Jablonski diagram (Figure 1.19). First, it can participate in an electron-transfer process with a biological substrate to form radicals and radical ions, which, after interaction with oxygen, can produce oxygenated products such as superoxide ion, $O_2^{\bullet-}$ (type I reaction). Alternatively, it can undergo a photochemical process known as a type II reaction, which results in the conversion of stable triplet oxygen (3O_2) to the short-lived but highly reactive singlet oxygen (1O_2), the putative cytotoxic agent. Singlet oxygen is produced by inverting the spin of one of the outer most electrons. For ground-state oxygen, the two electrons of highest energy reside

separately in the outermost anti-bonding orbitals with same spin, while in the singlet oxygen; the two highest energy electrons reside together in the same anti-bonding orbital in opposite spin. That is why singlet oxygen is much more reactive than ground state oxygen. In most organic solvents, the lifetime of the ${}^1\text{O}_2$ is 10-100 μs . This restricts its activity to a spherical volume 10 nm in diameter, centered at its point of production.¹⁰ In water, the lifetime of ${}^1\text{O}_2$ is reduced to approximately 1-3 μs because the excited-state energy of singlet oxygen is almost equal to the energy of oxygen–hydrogen (O–H) stretching in water molecule and is easy to dissipate as heat by the stretching and vibrational motions of water molecules.⁶² However, the lifetime of ${}^1\text{O}_2$ is considerably shorter in cellular systems, ranging from 100 ns in the lipid regions of membranes to 250 ns in the cytoplasm. Therefore, the diffusion range of ${}^1\text{O}_2$ is predicted to be limited to approximately 45 nm in cellular media.⁶³

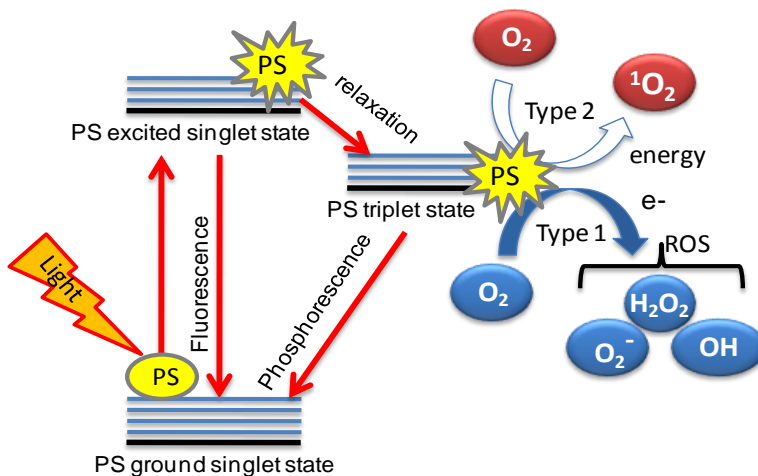


Figure 1.19. The pictorial representation for the formation of reactive oxygen species (ROS).

Since the diameter of human cells ranges from nearly 10 to 100 μm , they cannot diffuse more than a single cell length. Thus, the site of the primary generation of ${}^1\text{O}_2$ determines which sub cellular structures may be accessed and attacked. ${}^1\text{O}_2$ is a powerful indiscriminate oxidant that reacts with variety of biological molecules.

1.8.2. Ruthenium complexes as photosensitizers in PDT

The surgical removal of a part of an organ that is affected by cancer followed by chemo or radiotherapy can only help to decrease the risk of the cancer recurring and cure the tumors.⁶⁴ However, tumor metastasis is a multistep biological process that allows cancer cells to get away from the primary tumor, survive in the circulation, located in distant site and grow.⁶⁵ Therefore, the effective treatment for cancer mainly be governed by the anti-metastatic activity of the chemotherapeutic drug that can inhibit the metastasis process.

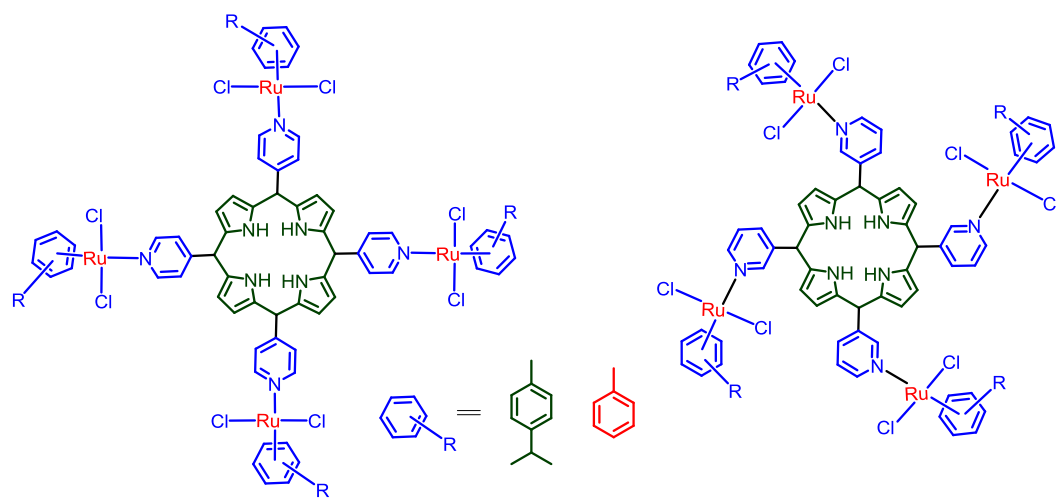


Figure 1.20. Molecular structures of the hematoporphyrins conjugated ruthenium photosensitizers.

Commercially available PS such as hematoporphyrins and its derivatives (HpD) generally suffers from drawbacks such as lower solubility in aqueous solutions, weakest absorption peak intensity at 630 nm that requires high light doses of 100-200 J/cm² to control the tumor also the therapeutic doses of Porfimer sodium result in skin photosensitivity for 4-12 weeks.⁶⁶ An ideal photosensitizer has to achieve certain characteristics properties such as high water solubility, absorption at longer wavelength in the visible region, high singlet oxygen quantum yields, high chemical stability at physiological condition, low photobleaching to prevent degradation of the photosensitizer so it can continue producing singlet oxygen and low dark toxicity. The

existing PS Chlorins which forms “Chlorophyll a” have been regularly used in PDT which suffers from the major flaw of stability issues in physiological conditions, which significantly reduces the fluorescent quantum yield (Φ_f) and drops the photosensitizing efficiency.⁶⁷ Therefore, much attention has been paid in the search of new PS that can overcome the above mentioned characteristic properties. As it was discussed above after successful entry of NAMI-A and KP1019 into human clinical trials, the more research has been devoted on Ru(II)-polypyridyl complexes in search of novel anti-cancer drugs with improved efficiency. With this aim the conjugates of ruthenium-porphyrin systems with improved cytotoxicity at lower light doses have been reported in the literature. However, they required longer exposure times (72 h) and they aggregate in the aqueous solution. Several other research groups have focused on improving solubility and reducing the exposure times. In this regard Ru(II)-polypyridyl complexes alone have attracted the attention as anti-cancer and anti-metastatic drugs.⁴⁵ Ru(II) complexes possess high water solubility, photostability, excitation in the visible light, and their long lived triplet excited state life time (which is essential for the efficient production of singlet oxygen) and these properties make such complexes suitable for use as a photodynamic therapeutic reagent. Over the last few years, several research groups have explored the possibility to move away from tetrapyrrolic systems, studying the potential of metal complexes as PSs themselves. The application of ruthenium complexes as PSs is a reasonable approach due to their tunable photophysics and the aforementioned advantages for biological applications.

1.9. References

1. Z. H. Siddik, *Oncogene*, 2003, **22**, 7265–79.
2. F. Crick, *Nature*, 1970, **227**, 561–563.
3. R. M. Martin, H. Leonhardt and M. C. Cardoso, *Cytom.*, 2005, **67**, 45–52.
4. J. D. Watson and F. H. C. Crick, *Nature*, 1953, **171**, 737–738.
5. B. Alberts, *Molecular Biology of the Cell* in *Cell* 4th Ed. 2002.
6. L. Blackmore, R. Moriarty, C. Dolan, K. Adamson, R. J. Forster, M. Devocelle and T. E. Keyes, *Chem. Commun.*, 2013, **49**, 2658–60.
7. C. A. Puckett, R. J. Ernst and J. K. Barton, *Dalt. Trans.*, 2010, **39**, 1159–1170.
8. Y. Jung and S. J. Lippard, *Chem. Rev.*, 2007, **107**, 1387–1407.
9. P. M. Takahara, C. A. Frederick and S. J. Lippard, *J. Am. Chem. Soc.*, 1996, **7863**, 12309–12321.
10. C. Mari, V. Pierroz, S. Ferrari and G. Gasser, *Chem. Sci.*, 2015, **6**, 2660–2686.
11. V. Ramu, M. R. Gill, P. J. Jarman, D. Turton, J. A. Thomas, A. Das and C. Smythe, *Chem. - A Eur. J.*, 2015, **21**, 9185–9197.
12. M. R. Gill, H. Derrat, C. G. W. Smythe, G. Battaglia and J. A. Thomas, *ChemBioChem*, 2011, **12**, 877–880.
13. M. R. Gill and J. A. Thomas, *Chem. Soc. Rev.*, 2012, **41**, 3179–3192.
14. J. K. Barton, A. T. Danishefsky, and J. M. Goldberg, *J. Am. Chem. Soc.*, 1984, **106**, 2172–2176.
15. F. R. Svensson, M. Matson, M. Li, and P. Lincoln, *Biophys. Chem.*, 2010, **149**, 102–106.
16. O. Mazuryk, K. Magiera, B. Rys, F. Suzenet, C. Kieda and M. Brindell, *J. Biol. Inorg. Chem.*, 2014, **19**, 1305–1316.
17. S. Banerjee, J. A. Kitchen, T. Gunnlaugsson and J. M. Kelly, *Org. Biomol. Chem.*, 2013, **11**, 5642–55.
18. A. Ghosh, A. Mandoli, D. K. Kumar, N. S. Yadav, T. Ghosh, B. Jha, J. A. Thomas and A. Das, *Dalt. Trans.*, 2009, **42**, 9312–9321.
19. R. M. Hartshorn and J. K. Barton, *J. Am. Chem. Soc.*, 1992, **114**, 5919–5925.
20. S. M. Cloonan, R. B. P. Elmes, M. Erby, S. A. Bright, F. E. Poynton, D. E. Nolan, S. J. Quinn, T. Gunnlaugsson and D. C. Williams, *J. Med. Chem.*, 2015, **58**, 4494–4505.
21. C. A. Puckett and J. K. Barton, *Biochemistry*, 2008, **47**, 11711–11716.
22. M. R. Gill, J. Garcia-Lara, S. J. Foster, C. Smythe, G. Battaglia and J. A. Thomas, *Nat. Chem.*, 2009, **1**, 662–667.

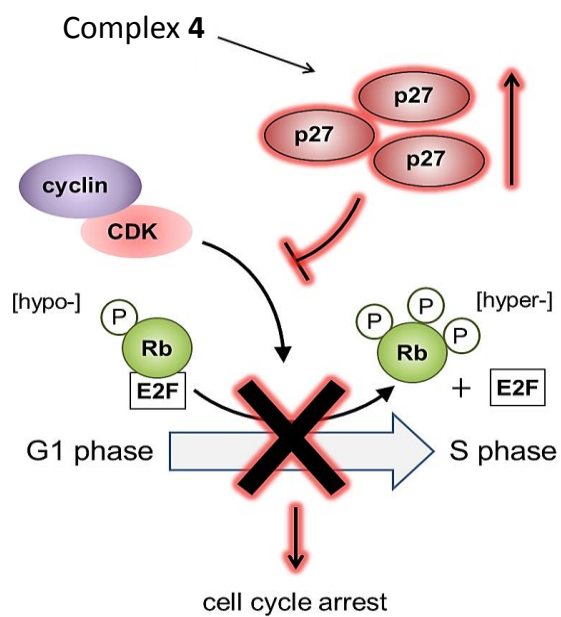
23. J. R. Lakowicz, *Principles of Fluorescence Spectroscopy Principles of Fluorescence Spectroscopy*, Springer, 3rd Ed., 2006.
24. A. Friedman and J. Chambron, *J. Am. Chem. Soc.*, 1990, **112**, 4960–4962.
25. A. Ghosh, P. Das, M. R. Gill, P. Kar, M. G. Walker, J. A. Thomas and A. Das, *Chem. - A Eur. J.*, 2011, **17**, 2089–2098.
26. D. Z. M. Coggan, I. S. Haworth, P. J. Bates, A. Robinson and A. Rodger, *Inorg. Chem.*, 1999, **38**, 4486–4497.
27. D.-L. Ma, H.-Z. He, K.-H. Leung, D. S.-H. Chan and C.-H. Leung, *Angew. Chemie Int. Ed.*, 2013, **52**, 7666–7682.
28. X. Li, A. K. Gorle, T. D. Ainsworth, K. Heimann, C. E. Woodward, J. Grant Collins and F. Richard Keene, *Dalt. Trans.*, 2015, **44**, 3594–3603.
29. C. Turro, S. H. Bossmann, Y. Jenkins, J. K. Barton and N. J. Turro, *J. Am. Chem. Soc.*, 1995, **117**, 9026–9032.
30. C. R. Cardoso, M. V. S. Lima, J. Cheleski, E. J. Peterson, T. Venâncio, N. P. Farrell and R. M. Carlos, *J. Med. Chem.*, 2014, **57**, 4906–4915.
31. B. Z. Ladbury, E. John and Chowdhry, *Chem. Biol.*, 1996, **3**, 791–801.
32. S. Page, *Educ. Chem.*, 2012, 26–29.
33. H. Sun, H. Li and P. J. Sadler, *Chem. Rev.*, 1999, **99**, 2817–2842.
34. A. Bergamo and G. Sava, *Dalt. Trans.*, 2011, **40**, 7817–7823.
35. M. Liu, Z. J. Lim, Y. Y. Gwee, A. Levina and P. A. Lay, *Angew. Chemie - Int. Ed.*, 2010, **49**, 1661–1664.
36. D. R. Frasca and M. J. Clarke, *J. Am. Chem. Soc.*, 1999, 8523–8532.
37. G. Gasser, I. Ott, and N. Metzler-Nolte, *J. Med. Chem.*, 2011, **54**, 3–25.
38. M. J. Clarke, F. Zhu and D. R. Frasca, *Chem. Rev.*, 1999, **99**, 2511–2533.
39. S. H. Van Rijt and P. J. Sadler, *Drug Discov. Today*, 2009, **14**, 1089–1097.
40. L. Kelland, *Nat. Rev. Cancer*, 2007, **7**, 573–584.
41. A. Bergamo, C. Gaiddon, J. H. M. Schellens, J. H. Beijnen and G. Sava, *J. Inorg. Biochem.*, 2012, **106**, 90–99.
42. E. S. Antonarakis and A. Emadi, *Cancer Chemo. Pharmacol.*, 2010, **66**, 1–9.
43. A. P. De Lima, F. De Castro Pereira, C. A. S. T. Vilanova-Costa, A. De Santana Braga Barbosa Ribeiro, L. A. Pavanin, W. B. Dos Santos and E. De Paula Silveira-Lacerda, *J. Biosci.*, 2010, **35**, 371–378.
44. T. Gianferrara, A. Bergamo, I. Bratsos, B. Milani, C. Spagnul, G. Sava and E. Alessio, *J. Med. Chem.*, 2010, **53**, 4678–4690.
45. W. Cao, W. Zheng and T. Chen, *Sci. Rep.*, 2015, **5**, 1– 11.
46. M. Brindell, E. Kulic, S. K. C. Elmroth and K. Urban, *J. Med. Chem.*, 2005,

- 7298–7304.
47. J. M. Rademaker-lakhai, D. Van Den Bongard, D. Pluim, J. H. Beijnen and J. H. M. Schellens, *Clin. Cancer Res.*, 2004, **10**, 3717–3727.
 48. G. Sava, S. Zorzet, C. Turrin, F. Vita, M. Soranzo, G. Zabucchi, M. Cocchietto, A. Bergamo, S. Digiovine, G. Pezzoni and L. Sartor, 2003, **9**, 1898–1905.
 49. A. Vacca, M. Bruno, A. Boccarelli, M. Coluccia, D. Ribatti, A. Bergamo, S. Garbisa, L. Sartor and G. Sava, 2002, **4**, 993–998.
 50. R. Carter, A. Westhorpe, M. J. Romero, A. Habtemariam, C. R. Gallevo, Y. Bark and N. Menezes, *Sci. Rep.*, 2016, **6**, 1–12.
 51. R. E. Morris, R. E. Aird, S. Murdoch, H. Chen, J. Cummings, N. D. Hughes, S. Parsons, A. Parkin, G. Boyd, D. I. Jodrell and P. J. Sadler, *J. Med. Chem.*, 2001, **44**, 3616–3621.
 52. E. S. Information, A. C. S. W. Editions, T. American, C. Society, S. Information, S. Information and A. C. Society, *Biochemistry*, 1993, **32**, 11794–11801.
 53. K. Van Der Schilden, H. Kooijman, A. L. Spek, J. G. Haasnoot and J. Reedijk, *Angew. Chemie - Int. Ed.*, 2004, **43**, 5668–5670.
 54. A. Garza-Ortiz, P. U. Maheswari, M. Lutz, M. A. Siegler and J. Reedijk, *J Biol Inorg Chem*, 2014, **19**, 675–689.
 55. C. Marzano, A. Trevisan, L. Giovagnini and D. Fregona, *Toxicology Vitr.*, 2002, **16**, 413–419.
 56. V. Fernández-Moreira, F. L. Thorp-Greenwood and M. P. Coogan, *Chem. Commun.*, 2010, **46**, 186–202.
 57. M. Monici, *Biotechnol. Annu. Rev.*, 2005, **11**, 227–256.
 58. M. Matson, F. R. Svensson, B. Nordén and P. Lincoln, *J. Phys. Chem. B*, 2011, **115**, 1706–1711.
 59. B. Onfelt, L. Gostring, P. Lincoln, B. Norden and A. Onfelt, *Mutagenesis*, 2002, **17**, 317–320.
 60. C. A. Puckett and J. K. Barton, *J. Am. Chem. Soc.*, 2007, **129**, 46–47.
 61. L. Blackmore, R. Moriarty, C. Dolan, K. Adamson, R. J. Forster, M. Devocelle and T. E. Keyes, *Chem. Commun.*, 2013, **49**, 2658–2660.
 62. C. Mari, V. Pierroz, R. Rubbiani, M. Patra, J. Hess, B. Spingler, L. Oehninger, J. Schur, I. Ott, L. Salassa, S. Ferrari and G. Gasser, *Chemistry*, 2014, **20**, 1–17.
 63. B. Song, C. D. B. Vandevyver, A.-S. Chauvin and J.-C. G. Bünzli, *Org. Biomol. Chem.*, 2008, **6**, 4125–4133.

64. S. Valastyan and R. A. Weinberg, *Cell*, 2011, **147**, 275–292.
65. Q.-X. Zhou, Y. Zheng, T.-J. Wang, Y.-J. Chen, K. Li, Y. Zhang, C. Li, Y.-J. Hou and X. Wang, *Chem. Commun.*, 2015, **51**, 10684–10686.
66. F. Schmitt, P. Govindaswamy, O. Zava, G. Süss-Fink, L. Juillerat-Jeanneret and B. Therrien, *J. Biol. Inorg. Chem.*, 2009, **14**, 101–109.
67. M. Ethirajan, Y. Chen, P. Joshi and R. K. Pandey, *Chem. Soc. Rev.*, 2011, **40**, 340–362.

CHAPTER 2

Synthesis, Characterization and Cytostatic Activity of Ru(II)–Pt(II) bis(terpyridyl) Complex that Blocks Entry into S-phase



Publication

Chem. Eur. J., 2015, **21**, 9185–9197.

2.1. Introduction

The serendipitous discovery of cisplatin is usually considered to be a breakthrough in cancer treatment.¹ Discovery of cisplatin has demonstrated that the combination of transition metal complexes with appropriate coordinating ligand(s) can lead to clinically approved anticancer metallodrugs (carboplatin, oxaliplatin, satraplatin). Some of the others metal complexes like picoplatin, KP1019 and NAMI-A are under clinical trials.² The versatile chemical properties of the central metal atom plays a crucial role in tuning the activity against tumour cells.^{3,4} The electronic and kinetic effects of coordinating ligand(s) also known to influence such activities. In general, four approaches are followed to design new anticancer drugs and are mentioned below.

- (i) Cisplatin analogues or modifications,
- (ii) Use of metals other than platinum,
- (iii) Combination of active organic drugs with metal compounds,
- (iv) Combination of two metal centers for bimodal cytotoxicity.

Platinum coordination compounds have been the main focus for metal-anti-tumour drugs for the last twenty years.⁵ Though cisplatin is the most widely used drug in the treatment of solid tumours (head, neck, ovarian, testicular, bladder, stomach, lung and Oesophageal cancer¹), severe toxic side effects and resistance towards few cancers limits the prolonged applications of cisplatin. The second-generation platinum drugs (carboplatin and Oxaliplatin) are less toxic and are used effectively in combination therapy.⁶ However, achievements till date are much below of our expectation and the search for more efficient, orally administrable drugs with minimum side effects continues. As discussed in the previous chapter, one of the targets of cisplatin is DNA, following substitution of labile Cl⁻/H₂O by the N7 sites of guanine of the nucleobases. This irreversible binding creates both intra- and inter-strand cross-links. Since the cellular

DNA mismatch repair mechanism process or nucleotide excision repair systems do not process these lesions efficiently, an apoptotic cell death response is induced.⁷ Despite the success of cisplatin, intrinsic or acquired drug resistance combined with toxicity represents a significant challenge for the future of platinum chemotherapy.⁸ Mechanisms that contribute to platinum-based resistance include changes in efficiency of drug accumulation, intracellular thiol levels and DNA adduct repair,⁸ with resistance often being multifactorial. Such resistance requires ever-greater doses of platinum therapeutic, eventually precluding safe use of the drug due to the inherent high toxicity of the molecule.

One of the strategies to overcome this problem has involved the design of new transition metal-based compounds with bimodal toxicity. For the last three decades, anticancer chemotherapy was concentrated on cisplatin derivatives in spite of their certain limitations.^{9,10} In the search for drugs with fewer side effects, various other metal complexes have been examined over the past few years. Recent research shows that ruthenium complexes have interesting anticancer properties in vivo condition and such complexes could be a good alternative to platinum-based drugs for anticancer therapy.¹¹

One strategy to overcome this problem has involved the design of new transition metal-based compounds, which aim to utilise the opportunities afforded by co-ordination chemistry to explore novel chemical space in cancer biology. Specifically, by employing a variety of metal centres, the effect of ancillary and active ligand(s) on reactivity, cellular uptake and anti-proliferative potency has been explored in detail.⁵ With some exceptions,⁶ work in this area has often focussed on the development of potent, purely cytotoxic systems. However, clinical application of cytotoxic drugs is often restricted by narrow therapeutic windows and inherent off-target tissue toxicity.⁷ This principle may be illustrated by platinum-based drugs themselves: carboplatin, a less potent cisplatin-

derivative, was introduced in an attempt to reduce the nephrotoxicity and emetic properties of the parent complex,¹ while clinical trials of the highly cytotoxic triplatinum agent BBR 3464 was ceased due to its severe dose-limiting side-effects.⁸

As insights into the cell biology of cancer have developed, targeted therapy has emerged as an alternative approach to conventional cytotoxic chemotherapy.⁹ Utilising a detailed understanding of the molecular aetiology of individual tumours, targeted therapies aim to inhibit the growth and spread of cancer either by selectively down-regulating intra-cellular pathways on which specific cancers have become dependent,¹⁰ and /or by re-activating tumour-suppressor pathways that have been down-regulated in a tumour.¹¹

Most of the current targeted therapy development has focused on use of cytostatic therapeutics¹² to halt cell proliferation by modulating molecular components, currently most often growth factor receptors, involved in cell cycle progression and consequently proliferation. Targeted therapeutics include, but are not restricted to, signal transduction inhibitors that interfere with the transition from G1 to S phase, blocking cellular signalling pathways that regulate this cell cycle progression known as the restriction point. The normal function of the restriction point is to ensure that, in the absence of appropriate extra-cellular proliferative cues, the cyclin-dependent kinase cyclin D/Cdk4 is not activated, preventing cell cycle progression and proliferation.¹³ An example of a clinically relevant targeted therapeutic is the monoclonal antibody trastuzumab (Herceptin), which suppresses growth of relevant (Her2⁺) human breast cancers by interfering with the receptor tyrosine kinase HER2.¹⁴ Further clinical examples include the combinational therapeutic drug Lapatinib (Tyverb, GW572016), a dual inhibitor of the epidermal growth factor (EGF) and HER2 receptor tyrosine kinases¹⁵, as well as the small molecule

Tamoxifen which, in active form, antagonises the activation of estrogen receptors (ER) by estrogen in ER-positive breast cancer cells.^{15,16} Tamoxifen is a very effective primary treatment, in pre- and post-menopausal women, as well as in the metastatic setting for tumours that express the estrogen receptor,¹⁷ despite the fact that in relevant cells it is not especially potent, with a reported half inhibitory concentration (IC_{50}) of 27 μ M.¹⁸ In all cases, these therapeutic approaches have the effect of preventing cyclin D/Cdk4 activation to bring about cytostatic G1 arrest. However, therapeutic efficacy in prevention of cyclin D/Cdk4 activation requires significant levels of the cyclin-dependent kinase inhibitor, p27^{KIP1},¹⁹ a tumour suppressor that binds to and inactivates the kinase. While not mutated in cancer, p27^{KIP1} levels are frequently down-regulated in multiple cancer types.¹³ Clearly then, there is significant unmet need for novel therapeutics that up-regulate p27^{KIP1} function to induce growth arrest in human cancers, not least where the targeted therapeutics above are clinically indicated,^{15,16} but also where signal transduction targets have yet to be identified, as in so-called “triple-negative” breast and ovarian cancers.²⁰ Herein, we report the synthesis, DNA-binding properties, and anticancer activity of a new Ru(II)-Pt(II) binuclear terpyrine-derived complex **4** (Figure 2.1), where the ditopic ligand tpypma (tpypma = 4-([2,2':6',2"-terpyridine]-4'-yl)-N-(pyridin-2-ylmethyl)aniline) allows an octahedral ruthenium(II) terpyridyl centre to be linked to a Pt(II) moiety. We show that complex **4** halts the growth of human ovarian cell lines and, importantly, sensitivity to the compound is retained in cisplatin-resistant cells.

2.2. Experimental Section

2.2.1. Materials and Methods

RuCl₃.3H₂O, 2,2':6',2"-terpyridine, 2-picinaldehyde, NaBH₄, K₂PtCl₄, and dimethyl sulfoxide were purchased from Sigma Aldrich. ¹H NMR spectra were recorded on a Bruker 500 MHz FT-NMR (model: Advance-DPX 500) spectrometer at room temperature

(RT, 25 °C). ESI-MS measurements were carried out on a Waters QToF-Micro instrument. Microanalyses (C, H, N) were performed using a Perkin-Elmer 4100 elemental analyzer. Infrared spectra were recorded as KBr pellets using a Perkin Elmer Spectra GX 2000 spectrometer. UV-Vis spectra were obtained using a Cary 500 Scan UV-Vis-NIR spectrometer. Viscosity measurements were carried out using Cannon50 viscometer at 25° C ± 1° C.

2.2.2. General experimental procedures for interaction studies with CT-DNA

Solutions of **2** (3.7×10^{-5} M) or **4** (1.0×10^{-5} M) (5 mM Tris-HCl, 25 mM NaCl, pH 7.2, 0.5% DMSO) in 1 cm path length optical glass cuvettes were prepared and maintained at 25 °C. The absorption spectra were recorded before 2 µL of a concentrated, known, DNA solution was added, mixed by pipette and allowed to equilibrate for 5 min. Spectra after mixing were recorded. The titration process was repeated until there was no change in the spectrum for at least four titrations indicating binding saturation had been achieved. Absorption data were used to construct nonlinear Scatchard plots (r/C_f versus r) and fitted to the McGhee-von Hippel model,¹⁴ in which neither the site size (s) nor binding constant (k_b) was set. Viscosity measurements were carried out in a Cannon-Manning semi-micro viscometer (size 50) immersed in a thermostat bath maintained at 27 °C. The concentration of DNA was kept constant at 0.5 mM (base pairs), and samples were prepared by adding ligand to the DNA solution to give an increase in the ligand/bp ratios. The flow times were measured after thermal equilibration of at least 20 minutes. Each sample was measured three times and the averaged time was used in calculations. Irreversible binding studies followed the protocol described by Wheate *et al.*¹⁵ Briefly, each complex was pre-dissolved in DMF and added to guanosine in D₂O (final concentrations 200 µM, 1:1 ratio). The solutions were incubated at 25 °C and the

¹H NMR spectrum of each was recorded at 0, 6, 24 and 48 h time points.

2.2.3. Calculation of lipophilicities of metal complexes (Partition coefficients/logP)

The n-octanol-saturated water and water-saturated n-octanol were obtained using Millipore water stirred with n-octanol for 24 h before the two layers were separated by centrifugation (3000 rpm, 5 min). Cisplatin and chloride salts of **2**, **4** and **5** were dissolved in n-octanol-saturated water. This was then mixed with water-saturated n-octanol in the ratio of 1:1 (v/v). Resulting solvent mixtures were vortexed for 30 min at room temperature, and then were subjected to centrifugation (3000 rpm, 5 min) to obtain two distinct separate layers. Samples from each layer were obtained using a fine-gauge needle and the absorbance of respective complex in each phase determined using high performance liquid chromatography (HPLC) coupled to a UV-visible detector. The concentration in each phase was calculated using reference to calibration absorbance/concentration graphs in each phase and the octanol/water partition coefficient (log P) for each respective complex was then calculated using equation 4. The value obtained for cisplatin by this method was in agreement with previously published data.¹⁶

$$\text{LogP}_{\text{Oct/water}} = \log [(\text{complex})_{\text{Oct}} / (\text{complex})_{\text{water}}] \quad \text{Equation 4}$$

2.2.4. Isothermal Titration Calorimetry (ITC) studies with CT-DNA

Isothermal titration calorimetry (ITC) studies ITC experiments were performed using Microcal iTC200. CT-DNA concentration (0.1 mmol) and complexes **2** (5 mmol), **4** (5 mmol) and **5** (5 mmol) concentrations were used for these experiments. All titrations were conducted in Tris-HCl buffer (5 mmol Tris and 25 mmol NaCl), pH = 7.4 at 25° C. In each titration CT-DNA was loaded into the cell and complexes **2** or **4** or **5** were taken into the syringe. Aliquots of 2 µL of complexes were added to the cell containing CT-

DNA. In each experiment, the raw isotherms were corrected for heat of dilution by subtracting the isotherms representing the complexes injected into the Tris-HCl buffer. The resulting isotherms were fitted with one set of site binding model provided with Microcal iTC200.

2.3. Experimental procedures for various cell biology studies

2.3.1. Cell Culture

A2780 and A2780CIS cells were cultured in RPMI1640 supplemented with 10% FBS and penicillin/streptomycin. Cell lines were maintained at 37 °C in an atmosphere of 5% CO₂ and routinely sub-cultured. A2780CIS growth media was supplemented with 2 µM cisplatin every fourth passage to maintain cisplatin-resistance.

2.3.2. Cell proliferation assay

A2780 or A2780CIS cells were seeded in 48-well plates at a seeding density of 2x10⁴ cells/well and allowed to proliferate for 24 h. Cell cultures were treated with 0 – 200 µM solutions of **2**, **4**, **5** (final medium composition = 90% cell media, 9.5% PBS, 0.5% DMSO) or cisplatin (90 % cell media, 10 % PBS) in triplicate for 48 h. After incubation, the solutions were removed and 0.5 mg mL⁻¹ MTT (thiazolyl blue tetrazolium bromide) dissolved in serum-free media added for 30 min.⁸ The formazan product was eluted using acidified isopropanol and the absorbance at 540 nm quantified by plate reader (reference peak 620 nm). An average absorbance for each concentration was obtained and the metabolic activity of the cell population was determined as a percentage of the relative solvent negative control.

2.3.3. Nuclear morphology

Cells were incubated with **4** (40 µM) or cisplatin (30 µM) for 24 or 48 h, washed with PBS and fixed with ethanol. Slides were stained with 5 µg /mL DAPI and visualized with

a Zeiss LSM 510 inverted confocal microscope using a 405 nm diode laser for excitation and emission detected using a 420-480 nm BP filter. At least 200 cells were counted for each experiment.

2.3.4. Cell growth and cell viability (Trypan Blue)

A2780CIS cells were treated with **4** or cisplatin at 0, 40 or 100 µM for 48 h. Cells were detached by scraping and concentrated via centrifugation. Pellets were re-suspended in 1 mL of serum-free medium, a sample of which was stained with Trypan Blue solution (0.4 %) and the number of total cells and Trypan Blue-positive cells counted by haemocytometer. A minimum of 200 cells were counted. For each independent experiment, counts were made in triplicate and an average value used.

2.3.5. Cellular uptake quantification (ICP-MS)

A2780CIS cells were treated with 50 µM solutions of **2**, **4**, **5** or cisplatin or an untreated control in triplicate for 24 h. Cells were washed in PBS and detached with Trypsin. Cell numbers were counted by haemocytometer and each sample then solubilized using 60% nitric acid at 60 °C overnight. Samples were made up to exactly 10 mL using deionized water and the levels of Pt and Ru determined by ICP-MS (see reference^{17,18} for details on machine calibration). For data expressed in ng/mg protein format, the ICP-MS data was plotted against a cell number/protein concentration calibration subsequently determined. Briefly, a range of cell concentrations were lysed (2.5×10^5 – 1×10^6 cells, lysis protocol as described below), the protein content determined using Bradford reagent and a protein content/cell number plot (R^2 value = 0.99) constructed.

2.3.6. Sub-cellular fractionation

A2780 cells were treated with 50 µM **4** or control solvent for 24 h prior to subcellular fractionation using standard procedures.¹⁹ Briefly, cells were harvested as above and

resuspended in 3 volumes of hypotonic buffer (210 mM sucrose, 70 mM mannitol, 10mM Hepes, pH 7.4, 1 mM EDTA) containing protease inhibitor cocktail (see below). After gentle homogenization with a Dounce glass homogenizer, cells were subjected to a freeze thaw cycle, and cell lysates were either retained for total lysate analysis by ICP-MS, or centrifuged at 1,000 X g for 5 min (Eppendorf 5417 centrifuge) to isolate a nuclear fraction. The supernatant was collected and centrifuged at 10,000 X g (Beckman TLS100 Ultracentrifuge, TLS-55 rotor) to pellet the mitochondria-enriched membrane fraction. The supernatant was collected and utilized as a cytosolic fraction. Aliquots of each fraction were retained for protein content analysis by Bradford assay. Total cell lysates or individual subcellular fractions were individually processed by ICP-MS to determine levels of Pt and Ru as described above. Recovery of metals after fractionation compared to unfractionated controls was 102 % (Ru) and 106 % (Pt).

2.3.7. Cell cycle analysis (Flow Cytometry) studies

Cells were treated with solutions of **4** or solvent control for 24 h. Samples were harvested by trypsinization, washed with PBS and fixed with 70 % cold ethanol. Cells were RNAase treated, stained with 30 µg /mL propidium iodide (1 h at room temperature) and the DNA content analyzed using a Biosciences LSRII Flow Cytometer. Data were processed for cell cycle phase apportionment using FloJo software.

2.3.8. Immunoblot Analysis (Western Blotting)

A2780 or A2780CIS cells were treated for indicated times with solutions of each compound at the stated concentration. After treatment, unless otherwise indicated, the cells were collected and lysed in lysis buffer (20 mM Tris, pH 7.5, 0.27 M sucrose, 1 mM EDTA, 1 mM EGTA, 1 % Triton X-100, protease inhibitors (10 µg/mL leupeptin, 2 µg/mL pepstatin, 50 µg/mL antipain, 2 µg/mL aprotinin, 20 µg/mL chymostatin and 2 µg/mL

benzamidine), and phosphatase inhibitors (50 mM NaF, 1 mM Na₃VO₄ and 20 mM Na β-glycerophosphate)). Aliquots of cell lysates were resolved by 8-15 % SDS-PAGE, transferred onto nitrocellulose membrane and probed with the appropriate antibodies. Antibodies against cleaved caspase 3, p-Chk1 (Ser345), p-H2AX (Ser139), p-Chk2 (Ser516), Chk2, p-p53 (Ser20), p27, p-Rb (Ser780) and Rb were obtained from Cell Signaling and used at the recommended dilution. Anti-β-actin and α-tubulin monoclonal antibodies (1/5000 dilution) were obtained from Sigma. Antibodies against p21 (1/1000 dilution) were obtained from Santa Cruz Biotech. Anti-Lamin A/C antibodies were from Abcam. Anti-Tom20 antibodies were a kind gift from Prof. O. Bandmann (University of Sheffield). Anti-Chk1 was generated in-house. HRP-conjugated anti-rabbit or anti-mouse antibodies (Santa Cruz Biotech.) were used at 1/5000 dilution. Blots were visualized using ECL or ECL+ chemiluminescence reagents (GE Healthcare Life Sciences) with X-ray development (Fuji medical film and Optimax 2010 processor).

2.4. Design, synthesis and characterization of Ru(II)-Pt(II) complex

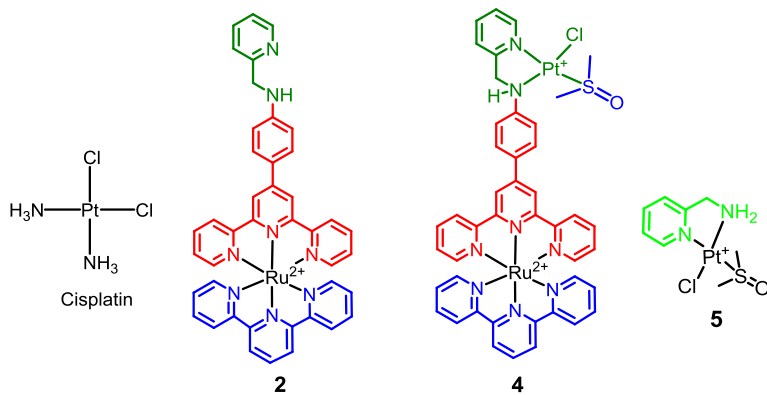
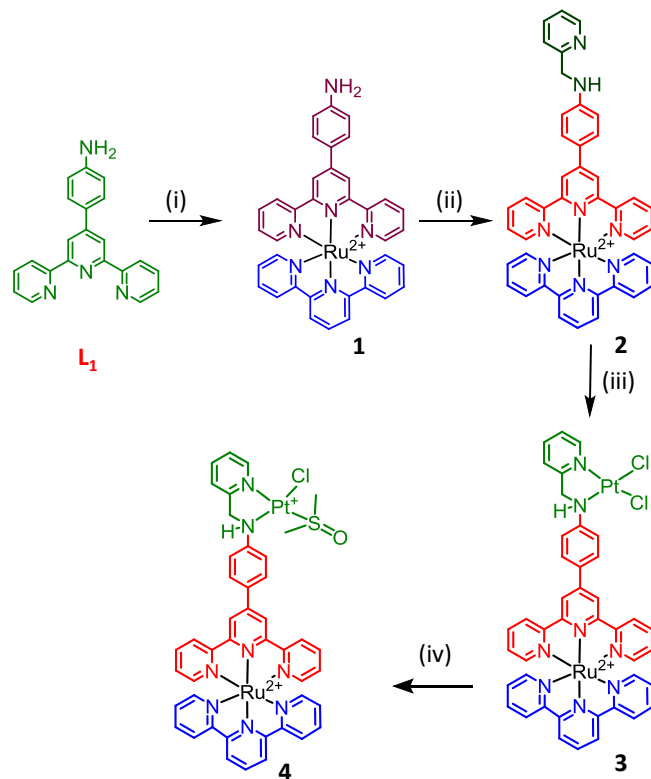


Figure 2.1. The chemical structures of cisplatin, complexes **2**, **4** and **5**.

This chapter 2 describes mainly the synthesis, DNA-binding properties, and anticancer activity of a new Ru(II)-Pt(II) binuclear terpyridine-derived complex, **4** (Figure 2.1), where the ditopic ligand tpypma (tpypma=4-([2,2':6',2"-terpyridine]-4'-yl)-N-(pyridin-2-

ylmethyl)aniline) allows an octahedral Ru(II) terpyridyl centre to be linked to a Pt(II) moiety.

2.4.1. Synthesis and characterization



Scheme 2.1. Synthetic methodology followed for the preparation of **2** and **4**. (i) Ru(tpy)Cl₃ in ethyleneglycol refluxed for 2 h at 140°C; (ii) 2-aminomethylpyridine, NaBH₄, acetonitrile: methanol (1:50, v/v) refluxed for 8 h; (iii) K₂PtCl₄, H₂O in dark at r.t. for 3 h; (iv) DMSO: H₂O (1:9, v/v), stirred at r.t for 3 h.

Complex **4** has been found to halts the growth of human ovarian cell lines and, importantly, sensitivity to the compound is retained in cisplatin-resistant cells. Through comparison with the mononuclear Ru(II) and Pt(II) compounds **2** and **5**, we established that both metal centres of **4** are required for bioactivity. A systematic analysis at the molecular and cellular level show has been carried out, unlike conventional platinum therapeutics, **4** does not coordinate with the nucleobase guanosine, and consequently does not generate a cytotoxic response or pro-apoptotic signals via the activation of the

DNA-damage response network. Instead it was found that **4** acts by up-regulating the Cdk inhibitor p27KIP1, leading to hypo-phosphorylation of retinoblastoma protein (Rb) and thereby blocking cell-cycle progression from G1 to S phase.

2.4.2. Synthesis of L₁: 4-([2,2':6',2"-terpyridin]-4'-yl)aniline:(tpy-a)

Synthesis of 4-([2,2':6',2"-terpyridin]-4'-yl)aniline(tpy-a) was achieved by following the reported literature procedure.²⁰⁻²² 2-Acetylpyridine (4.0 g, 33.0 mmol) was added into a solution of 4-Nitrobenzaldehyde (2.5 g, 16.5 mmol) in ethanol (100 mL). KOH pellets (1.3 g, 85%, 33.0 mmol) and aq.NH₃ (50 mL, 25%, 44 mmol) was then added to the solution. The solution was stirred at room temperature for 24 h. The chocklet brown color solid was formed. The complete evaporation of ethanol using rotary evaporator resulted in black colored solid substance which was redissolved in chloroform and distilled water 200 mL (1:1v/v). The pH of the resultant solution was adjusted to neutral (pH 7.0) by adding diluted HCl (1N). Aqueous layer washed thrice with chloroform (3 X 50 mL) and the organic layers collected using separating funnel was dried using Na₂SO₄. The chloroform was evaporated and the resultant black solid material was subjected to the column chromatography. Petroleum ether (75%) and ethyl acetate (25%) were used as mobile phase and silica gel (100-200 mesh) as stationary phase. ESI-HRMS: calculated 325.1448; found: 325.1446; δ (200 MHz in CDCl₃) 8.74 – 8.73 (m, 1H), 8.71 (dd, J 1.8, 0.9, 1H), 8.68 (s, 2H), 8.64 (s, 1H), 7.91 – 7.82 (m, 3H), 7.80 – 7.76 (m, 2H), 7.37 – 7.30 (m, 2H), 6.82 – 6.77 (m, 2H), 3.87 (s, 2H). Elemental analysis calculated: C 77.76; H 4.97; N 17.27; found C 77.50; H 4.87; N 17.19.

2.4.3. Synthesis of Ru(tpy)Cl₃

A commercial grade RuCl₃.3H₂O (1.20 g, 5.7 mmol), and 2,2':6',2"-terpyridine (1.34 g, 4.2 mmol) were dissolved in 70 mL of ethanol. The reaction mixture was heated at reflux

for 3 h with continuous stirring. After cooling to the room temperature the reaction mixture was kept at 4° C in refrigerator for overnight. The chocklet brown precipitate formed was filter through G-4 glass sintered crucible at pump and washed several times with cold ethanol followed by diethyl ether. Yield: 90.43 % (1.83 g, 4.10 mmol). Note: Since this ruthenium complex [Ru(tpy)(Cl)₃] is a paramagnetic, it is not possible to produce ¹H NMR.

2.4.4. Synthesis of [Ru(tpy)(tpy-a)](PF₆)₂ (1)

In to a 100 mL two neck round bottom flask tpy-a (0.145 g, 0.45 mmol) was dissolved in 30 mL of ethylene glycol. Then Ru(tpy)Cl₃ (0.2 g, 0.45 mmol) was added and refluxed for 2 h under the nitrogen atmosphere with continuous stirring. The color of the solution was changed from yellow to blood red color. After 2 h the reaction mixture was cooled to the room temperature. The addition of saturated KPF₆ solution was resulted in dark red precipitate which was filtered at pump through G-4 glass sintered crucible and washed several times with cold water followed by diethyl ether. The precipitate was dried in the presence of P₂O₅ then subjected to the column chromatography using neutral Al₂O₃ (grade-I) as stationary phase and pure acetonitrile as mobile phase. The second red spot on the TLC from the bottom was collected as pure compound and characterized by standard analytical techniques. Yield: 29 % (0.170 g, 0.17 mmol) HRMS: Calculated = 972.0547; found = 972.0552. [M + 2PF₆ + Na]. ¹H NMR 500 MHz, in DMSO-d₆ (δ , ppm): 8.90 (s, 2H), 8.73 (d, 2H; J = 8.2 Hz), 8.39 (t, 1H; J = 8.2 Hz), 8.60 (d, 2H; J = 8.0 Hz), 8.48 (d, 2H; J = 8.1 Hz), 8.01 (d, 2H; J = 8.6 Hz), 6.95 (d, 2H; J = 8.6 Hz) 7.94 – 7.89 (m, 4H) 7.19 – 7.11 (m, 4H), 7.44 (d, 2H; J = 5.5 Hz), 7.30 (d, 2H; J = 5.6 Hz), 4.78 (s, 2H).

2.4.5. Synthesis of [Ru(tpy)(tpypma)](PF₆)₂ (2)

In to a 100 mL two neck round bottom flask [(tpy)Ru(tpy-a)](PF₆)₂ (0.2 g, 0.211 mmol) of was dissolved in the minimum amount of dry CH₃CN (1mL) and 30 mL of dry methanol. 2-pyridinecarboxaldehyde (0.04 mL, 0.422 mmol) was added and the reaction mixture was refluxed for 9 h with continuous stirring. After cooling to room temperature, the solvent was evaporated under reduced pressure. The reaction mixture was redissolved in 100mL of dry methanol and refluxed for 1 h followed by the addition of excess of NaBH₄ (100 mg). The reaction mixture was allowed to reflux for 3 h with continuous stirring. Then cooled to room temperature and 10 mL of distilled water was added to quench excess NaBH₄. Saturated KPF₆ (2 mL) solution was added to exchange the counter anions and the metal complex was extracted by the solvent extraction method using dichloromethane/water. A minimum amount of acetonitrile (0.5 mL) was added in order to bring the complex in to the organic layer from aqueous layer. This crude compound was purified by column chromatography, using silica gel as stationary phase and CH₃CN as a mobile phase. Yield: 75.82 % (0.120 g, 0.16 mmol). ESI HRMS: m/z (%): 972.0552 [M + 1 + 2PF₆]. ¹H NMR 500 MHz, in DMSO-d₆ (δ , ppm): 9.30 (s,2H), 9.09 (d, 2H; J = 8.2 Hz), 9.04 (d,2H; J = 8.1 Hz), 8.83 (d,2H; J = 8.1 Hz), 8.60 (d,1H;J = 4.1 Hz), 8.52 (t,1H;J = 8.1 Hz), 8.23 (d,2H; J = 8.7 Hz), 8.03 (dd, 4H;J = 13.0, 6.5 Hz), 7.82 (t, 1H;J = 7.7 Hz), 7.53 (d,2H; J = 5.3 Hz), 7.45 (d,1H; J = 7.9 Hz), 7.39 (d,2H; J = 5.2 Hz), 7.32 (dd, 4H; J = 7.3, 5.1 Hz), 7.29 – 7.21 (m), 7.14 (t,1H;J = 6.0 Hz), 6.92 (d,2H; J = 8.7 Hz), 4.57 (d,2H; J = 6.0 Hz). Elemental analysis calculated: C 44.50; H 2.80; N 10.09; found C 44.34; H 2.90; N 10.12.

2.4.6. Synthesis of [Ru(tpy)(tpypma)Pt(Cl)₂]Cl₂ (3)

[Ru(tpy)(tpypma)](PF₆)₂ was converted to its chloride salt by anion metathesis, and dried under vacuum. Potassium tetrachloro platinum (0.032g, 0.077 mmol) was dissolved in 10 mL water, followed by the addition of [(tpy)Ru(tpypma)]Cl₂ (0.08g, 0.077 mmol). The reaction mixture was stirred at room temperature (25° C) for 2 h in the dark. The precipitate formed was collected by centrifugation and washed with water (3 x 2 mL) to remove excess K₂[PtCl₄] before drying under vacuum. Purity and formation of the complex was established using ¹H NMR, High Resolution Mass Spectrometry (HRMS) and observing the spectral change in the emission spectrum before and after adding the platinum (in general bimetallic complexes show less emission than their monometallic complexes due to lowest lying ³MLCT emission state in bimetallic complexes). % Yield: 69.7 % (54.5 mg, 0.0536 mmol). ESI-HRMS: m/z (%) 1015.0823 [Ru(tpy)(tpypma)Pt(Cl)₂]²⁺, 1050.1135. [Ru(tpy)(tpypma)PtCl₂]Cl⁺. ¹H NMR 500 MHz, in DMSO-d₆ (δ , ppm): 9.31 (s, 2H), 9.14 (d, 2H; J = 8.2 Hz), 9.07 (d, 2H; J = 8.1 Hz), 8.88 (d, 2H; J = 8.1 Hz), 8.60 (d, 1H; J = 4.4 Hz), 8.53 (t, 1H; J = 8.1 Hz), 8.25 (d, 2H; J = 8.7 Hz), 8.07 – 8.00 (m, 4H), 7.82 (t, 1H; J = 7.7 Hz), 7.53 (d, 2H; J = 5.4 Hz), 7.46 (d, 2H; J = 8.0 Hz), 7.39 (d, 2H; J = 5.3 Hz), 7.32 (dd, 1H; J = 6.9, 5.3 Hz), 7.30 – 7.23 (m, 4H), 7.15 (t, 1H; J = 6.0 Hz), 6.92 (d, 2H; J = 8.6 Hz), 4.57 (d, 2H; J = 5.9 Hz).

2.4.7. Synthesis of [Ru(tpy)(tpypma)Pt(Cl)(DMSO)](PF₆)₃ (4)

Step 1: Formation of intermediate complex [Ru(tpy)(tpypma)Pt(Cl)₂]Cl₂ (3)

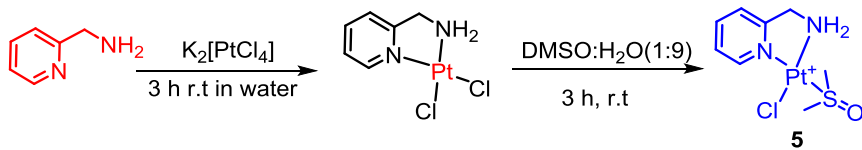
Complex **2** was converted to its chloride salt by anion metathesis and dried under vacuum. Potassium tetrachloro platinate (32 mg, 0.077 mmol) was dissolved in 10 ml water, followed by the addition of complex **2** (80 mg, 0.097 mmol). The reaction mixture was stirred at room temperature (25° C) for 3 h in the dark. The precipitate formed

complex **3** was collected by centrifugation and washed with water (3 X 2 mL) to remove excess $K_2[PtCl_4]$ before drying under vacuum. Yield: 64.8 % (54.5 mg, 0.050 mmol); ESI-MS m/z: [M]²⁺ 507.03.

Step 2: Conversion of complex **3** to complex **4**

Complex **3** (0.05g, 0.046 mmol) was dissolved in DMSO/H₂O (1:9, v/v). The reaction mixture was stirred at room temperature (25° C) for 120 h in the dark. The addition of saturated KPF₆ solution (1 mL) afforded a deep red coloured precipitate (complex **4**), which was collected by using grade-4 crucible followed by washing with water (3 x 2 mL). % Yield: 36.9 % (0.026g, 0.017 mmol). ¹H NMR (500 MHz, DMF-d₇): δ = 9.46 (s, 2H), 9.25–9.22 (m, 4H), 8.99 (d, *J* = 8.1 Hz, 2H), 8.65 (d, *J* = 5.0 Hz, 1H), 8.61 (s, 1H), 8.36 (d, *J* = 8.7 Hz, 2H), 8.12 (dd, *J* = 7.1,4.2 Hz, 5H), 7.89 (s, 2H), 7.70 (d, *J* = 5.4 Hz, 2H), 7.55 (d, *J* = 7.8 Hz, 1H), 7.38 – 7.34 (m, 5H), 7.22 (s, 1H), 7.05 (d, *J* = 8.7 Hz, 2H), 4.67 (d, *J* = 3.6 Hz, 2H), 3.35 ppm (s, 6H); ¹⁹⁵Pt NMR (DMSO-d₆): δ = 2967 ppm (s, 1Pt); elemental analysis (with chloride as counter anion: C₄₄H₃₈Cl₄N₈OPtRuS): calculated: C 45.37, H 3.29, N 9.62; found: C 45.21, H 3.30, N 9.47; ESI-MS (m/z): [M]³⁺ calculated: 352.7084; found: 352.7087.

2.4.8. Synthesis of [Pt(amp)(Cl)(DMSO)]⁺ (**5**)



Scheme 2.2. The synthetic procedure followed for the preparation of complex **5**.

[Pt(Cl)₂(amp)] (0.1 g, 0.26 mmol) was dissolved in DMSO/H₂O (1:9, v/v). The reaction mixture was stirred at room temperature for 2 h in the dark. The addition of saturated KPF₆ solution (1 mL) afforded a pale yellow-coloured precipitate, which was collected by

using G-3 crucible followed by washing with water (3×2 mL) and diethyl ether (2×5 mL). Yield: 50.7% (0.076g, 0.135 mmol). ^1H NMR (500 MHz, DMF-d₇): δ = 9.06 (dd, $J = 5.9, 0.8$ Hz, 1H), 8.39 (dd, $J = 7.8, 6.3$ Hz, 1H), 7.99 (dd, $J = 7.9, 0.4$ Hz, 1H), 7.84 – 7.81 (m, 1H), 6.86 (s, 2H), 4.74 (t, $J = 5.9$ Hz, 2H), 3.69 ppm (s, 6H); ^{195}Pt NMR (DMSO): δ = -3142 ppm (s, 1Pt); elemental analysis (Chloride as counter anion; C₈H₁₄CIN₂OPtS): calculated: C 21.25, H 3.12, N 6.19; found: C 21.18, H 3.1, N 6.17; ESIMS (m/z): [M]⁺ calculated: 416.016; found: 416.015.

2.5. Results and discussion

2.5.1. Photophysical Properties

Optical spectra for complexes **2**, **4** and **5** were recorded in acetonitrile, which clearly revealed that the electronic spectra in the visible region for both **2** and **4** complexes was dominated by broad metal-to-ligand charge-transfer (MLCT; Ru(dπ)→bpy/L₁(π*) and/or bpy/L₂(π*) based transitions at ~485 nm,

Table 2.1. The photophysical characterization of the synthesized complexes were carried out in aqueous solvent medium.

Complex	λ_{abs} (nm)	$10^{-3} (\epsilon/\text{M}^{-1} \text{ cm}^{-1})$	Assignment	λ_{em}	$\lambda_{\text{abs/exc}}$
2	272	31.2	$\pi \rightarrow \pi^*$		289
	308	43.9	$\pi \rightarrow \pi^*$	660	325
	485	15.3	MLCT		482
4	272	10.5	$\pi \rightarrow \pi^*$		287
	308	19.2	$\pi \rightarrow \pi^*$	643	327
	488	7.37	MLCT		487
5	274	8.51	$\pi \rightarrow \pi^*$		

while emission band for respective complex was attributed to a $^3\text{MLCT}$ transition (~660 nm for $\lambda_{\text{Ext}} = 485$ nm) as the Φ_{ISC} for the ISC process for Ru(II)-polypyridyl complexes is reported to be ~1 and occur within 40 fs.²⁴ Spectroscopic data for complex **2**: $\lambda_{\text{Max}}^{\text{Abs}} = 272$ nm, $\epsilon = 28780 \text{ M}^{-1}\text{cm}^{-1}$; $\lambda_{\text{Max}}^{\text{Abs}} = 485$ nm, $\epsilon = 19170 \text{ M}^{-1}\text{cm}^{-1}$; $\lambda_{\text{Max}}^{\text{Ems}} = 660$ nm for λ_{Ext} of 485 nm; Spectroscopic data for complex **4**: $\lambda_{\text{Max}}^{\text{Abs}} = 272$ nm ($\epsilon = 29850 \text{ M}^{-1}\text{cm}^{-1}$); $\lambda_{\text{Max}}^{\text{Abs}} = 488$ nm, $\epsilon = 15750 \text{ M}^{-1}\text{cm}^{-1}$; $\lambda_{\text{Max}}^{\text{Ems}} = 643$ nm. Spectroscopic data for **5**: $\lambda_{\text{Max}}^{\text{Abs}} = 274$ nm ($\epsilon = 5100 \text{ M}^{-1}\text{cm}^{-1}$). As is common for $[\text{Ru}(\text{tpy})_2]^{2+}$ derivatives,^{22,23} **2** and **4** demonstrated negligible luminescence upon MLCT excitation and are virtually non-emissive.

2.5.2. DNA-binding studies: UV-Visible titration with CT-DNA

Metal complexes have been widely studied for their ability to interact with DNA by either reversible or irreversible mechanisms.²⁴ Indeed, several conjugate Ru(II)-Pt(II) Cl_n complexes have been designed for this specific purpose.^{25,26} With these in mind, we characterized the interactions of **2** and **4** with DNA. The absorption spectra of **2** and **4** have display distinctive changes in the presence of increasing concentrations of DNA, with both the $\pi \rightarrow \pi^*$ and MLCT absorption bands showing appreciable hypochromicity (Figures 2.2a, b). The changes in the MLCT band yield a typical saturation ligand-DNA binding curve (Figures 2.2c, d) and higher binding ratios produced no additional changes in absorption spectra.

$$\frac{r}{C_f} = K_b (1 - nr) \left[\frac{(1 - nr)}{\{1 - (n - 1)r\}} \right]^{(n-1)} \quad \text{Equation 5}$$

Where, K_b represents the intrinsic binding constant of the complex with DNA and n is the size of a binding site in base pairs.

Fitting of these data in to the McGhee von-Hippel binding model²⁷ revealed that both complexes have a similar affinity for DNA, with equilibrium binding constants, K_b , of $3 \times 10^5 \text{ M}^{-1}$ and $1.3 \times 10^5 \text{ M}^{-1}$ for **2** and **4** respectively. The concentration of the free complex, C_f , is equal to $C - C_b$. A plot of r/C_f vs. r where r is $C_b / [\text{DNA}]$ was constructed according to the McGhee von-Hippel equation 5.

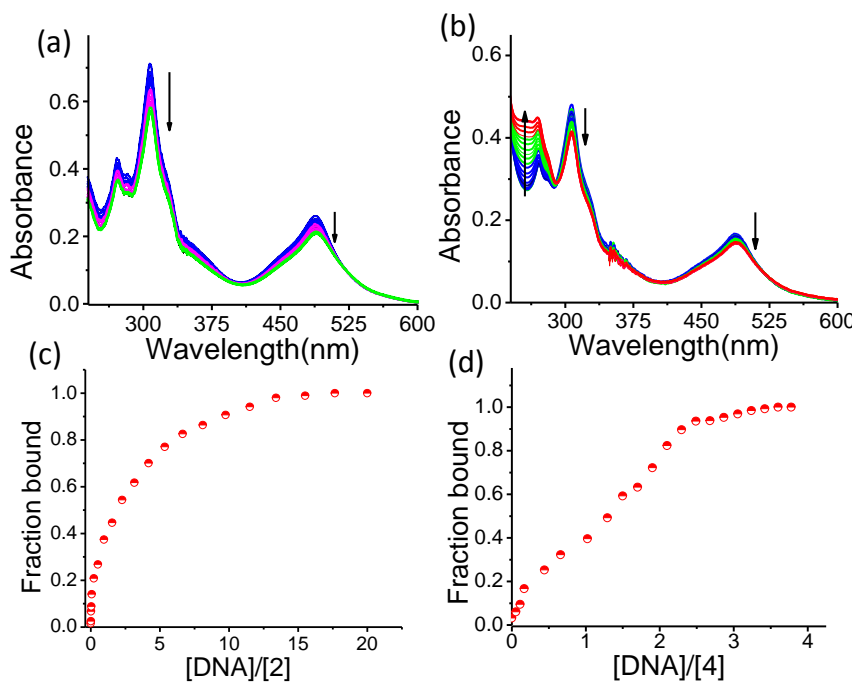


Figure 2.2. UV-Visible titration spectra and binding saturation curves for the **2** (a, c) and **4** (b, d) with CT-DNA in Tris-HCl buffer (pH 7.4).

2.5.3. Viscosity Measurements

To determine DNA binding mode, relative viscosity of DNA was measured in the presence of increasing concentrations of **2** and **4**. The intercalator ethidiumbromide and groove-binder $[\text{Ru}(\text{tpy})_2]^{2+}$ were used as controls for their respective modes of binding. In contrast to ethidiumbromide, neither complex **2** nor **4** increased the relative viscosity of DNA solutions (Figure 2.3), indicating that these complexes are not metallo-intercalators. This behavior is consistent with previous reports on other extended Ru(II)-terpyridyl

complexes.²⁸ since, **5** is known groove binder, viscosity measurement studies for this complex with DNA was not included.

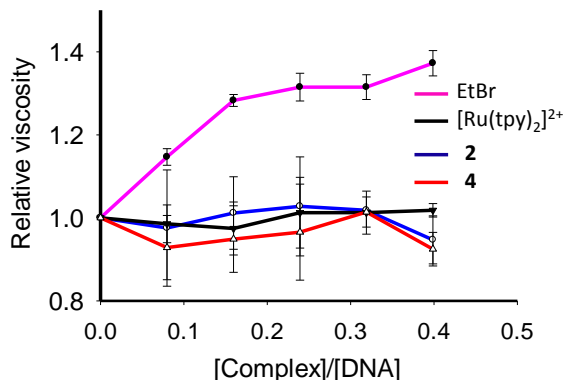


Figure 2.3. Change in the viscosity of the CT-DNA upon addition of **2**, **4** and $[\text{Ru}(\text{tpy})_2]^{2+}$, ethidiumbromide used as control.

2.5.4. ^1H NMR titration studies with guanosine

Cisplatin has previously been shown to possess a high affinity for guanine, where specifically the platinum(II) centre coordinates to the N7 position after chloride ligand(s) substitution. Reactions with guanine derivatives such as guanosine are therefore commonly employed to assess whether platinum-containing drug candidates can bind DNA irreversibly.^{29,30} A structural comparisons between **4** and cisplatin suggest that the Ru(II)-Pt(II) complex could similarly react with DNA by way of direct coordination of the Pt(II) metal centre to nucleobases. To explore this possibility, the extent of reaction of **4** or cisplatin with solutions of guanosine in D_2O was followed by ^1H NMR spectroscopy. In order to assess the contribution, if any, of the Ru(II) metal centre to Pt(II) co-ordination, the reaction of the monometallic DMSO-substituted Pt(II) complex **5** with guanosine was included for comparison. As can be seen in Figure 2.4a, the addition of cisplatin to guanosine results in a decrease in the intensity of the H_8 guanosine resonance at 8.10 ppm, accompanied by the appearance of two new resonance peaks at 8.51 and 8.63 ppm (Figure 2.4b), which increase in magnitude with exposure time. Likewise, a

decrease in the H₂ guanosine resonance at 5.95 ppm and corresponding appearance of the downfield-shifted peak at 6.10 ppm is observed (Figure 2.4a).

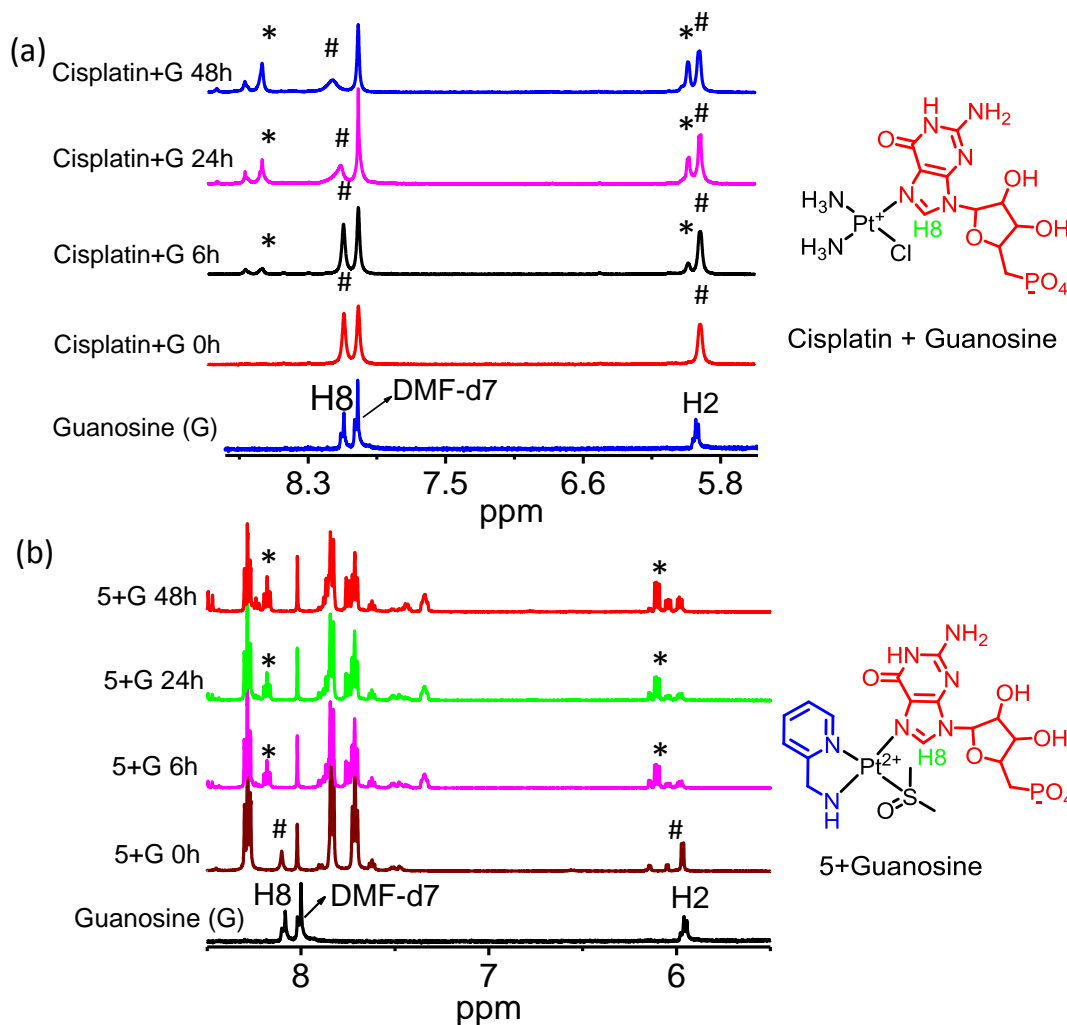


Figure 2.4. ¹H NMR spectra showing the reaction of guanosine (G) with cisplatin (a) and **5** (b) in DMF-d₇ over 48 h. Region including H8 and H2 guanosine protons shown. Peaks labelled * are Pt bound guanosine and peaks labelled # are free guanosine. The residual DMF-d₇ solvent peak used for complex dissolution before addition to guanosine is indicated.

This expected behaviour confirms that cisplatin binds guanosine via direct coordination (platination) of the Pt(II) metal centre to the N7 position of guanosine.²⁹ Similarly, addition of **5** to guanosine resulted in rapid loss of H8 guanosine resonance and the appearance

of two new resonance peaks at ~9.0 ppm, which is also consistent with the notion that **5** interacts with this nucleobase via N7 platination (Figure 2.4b).

In contrast to the behaviour demonstrated by cisplatin and **5**, no evidence of any effect on the NMR spectra of guanosine was observed following addition of **4** (Figure 2.5b), indicating the Ru(II)-Pt(II) complex does not react with the nucleoside, behaviour comparable to the mononuclear Ru(II) complex **2** (Figure 2.5a). Taken together, this indicates that complex **4** is highly unlikely to interact with DNA by irreversible binding following ligand substitution.

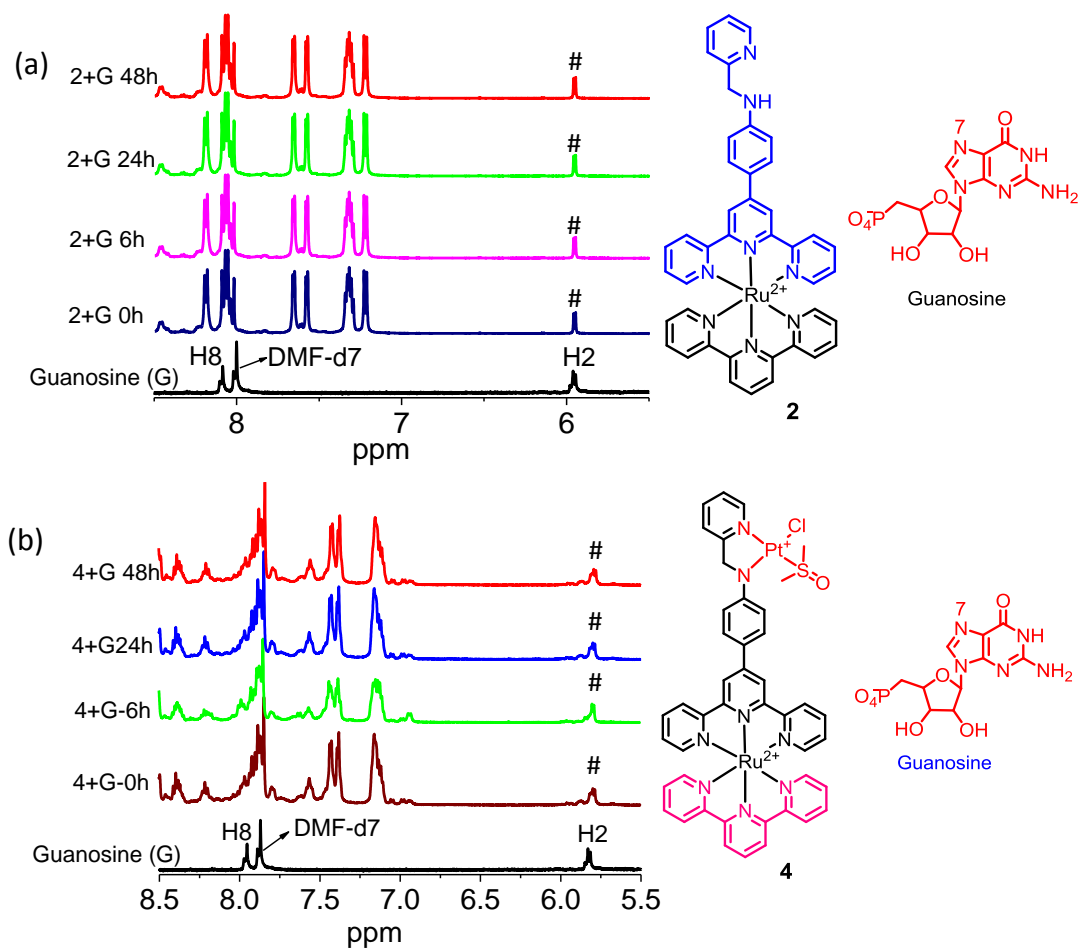


Figure 2.5. ^1H NMR spectra for the reaction of guanosine (G) with **2** (a), **4** (b) in DMF-d_7 over 48 h. Region including H8 and H2 guanosine protons shown. Peaks labelled # is free guanosine. The residual DMF-d_7 solvent peak used for complex dissolution before addition to guanosine is indicated.

2.5.5. Isothermal titration calorimetry studies with CT-DNA

Relative binding affinity of complexes **2**, **4**, and **5** towards calf-thymus DNA (CT-DNA) were evaluated using isothermal titration calorimetry (ITC) (Figure 2.6). Association constants and thermodynamic parameters (Table 2.2) clearly reveal that the binding affinities for complexes **2**, **5** are lower than that of **4** towards CT-DNA.

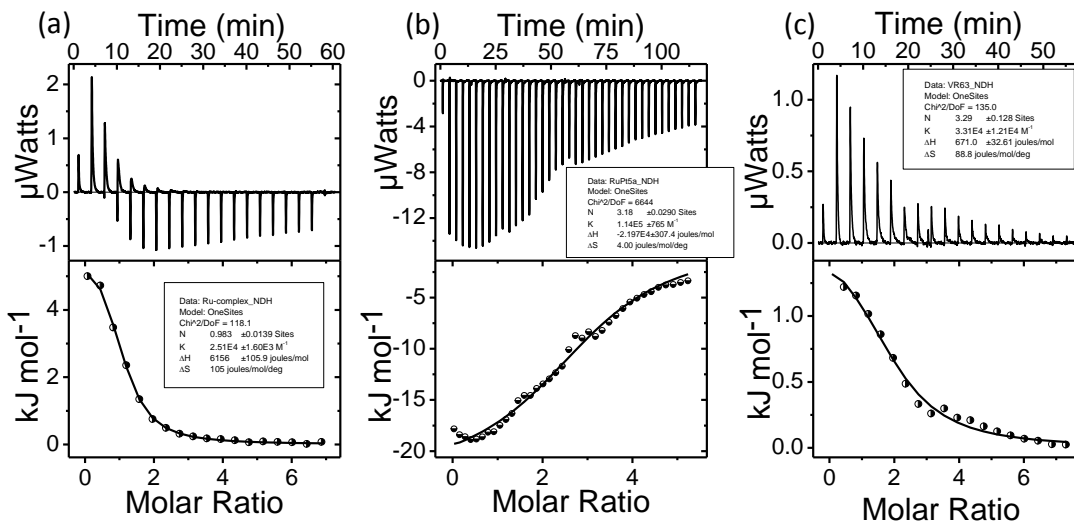


Figure 2.6. The ITC binding profiles for the **2** (a), **4** (b) and **5** (c) with CT-DNA.

Table 2.2. ITC derived binding parameters for **2**, **4** and **5** with CT-DNA.

Complex	2	4	5
K_b [M ⁻¹]	$(2.51 \pm 0)10^4$	$(1.14 \pm 0)10^5$	$(3.3 \pm 0)10^4$
ΔH [KcalM ⁻¹]	6.15±0.1	-21.9	0.67
$-\Delta S$ [KcalM ⁻¹]	31.2	11.9	26.2
ΔG [KcalM ⁻¹]	-25.1	-33.8	-25.5
N [bp]	0.9	3.1	3.2

Since the platinum containing complexes can form electrostatic interactions with guanine nucleobases the interaction of complex **4** and **5** were higher compared with complex **2**. From the table 2.2 the site size as well as the binding constant is following the order **5** >

4 >2. The interactions of complexes **2** and **5** with CT-DNA were driven by higher positive entropy and with a small positive enthalpy. But in the case of complex **4** the interactions was driven by higher negative enthalpy and with smaller positive entropy.

2.5.6. Partition coefficient measurement

The partition coefficients were calculated using shake-flask method. n-octanol-saturated water and water-saturated n-octanol solutions were prepared using millipore water stirred with n-octanol for overnight. Before the two layers were separated by centrifugation (3000 rpm, 5 min). Concentration of each complex was calculated by recording the absorption in each phase.

Table 2.3. Partition coefficient values for the **4**, **2**, **5** and cisplatin.

Complex	Mass/Da	log P
4	1128	-1.90 ± 0.10
2	966	-3.85 ± 0.19
5	450	-2.24 ± 0.11
cisplatin	300	-2.3 ± 0.09

The Cisplatin and chloride salts of **2**, **4** and **5** were dissolved in n-octanol-saturated water. The complex **4** and **5** were predissolved in to small aliquots of dimethyl sulfoxide solvent before solubilizing in aqueous layer. The concentration in each phase was calculated by reference to calibration absorbance graphs in each phase and the octanol/water partition coefficient (logP) for each respective complex was then calculated.¹

2.5.7. The impact of complex **4** on cancer cell proliferation

As discussed, both drug-resistance, in addition to the absence of identified specific targets in particular cancers, represents a significant on-going challenge for

chemotherapy. Therefore, the effect of **4** on the proliferation of cisplatin-resistant, A2780CIS ovarian cancer cells was investigated. Quantitative analysis of cell numbers over time in the presence of **4** indicated a dose-dependent decrease in proliferation with a half inhibitory concentration (IC_{50} , defined as the concentration resulting in 50% reduction in the fold extent of proliferation) of approximately 40 mM after 48 h exposure (Figure 2.7a). Interestingly, negligible signs of cell stress or death were observed, even at higher concentrations of **4** (Figure 2.7b). Importantly, although cell proliferation was significantly affected by **4**, the viability of cells (proportion of cells that exclude Trypanblue) exposed to active doses (40–100 mM) remained unchanged (Figure 2.7b); cell numbers reached a plateau after approximately 48 h, behaviour which implies cytostatic activity. In contrast, cell numbers in samples treated with cisplatin progressively decreased until cells numbers were negligible, as expected for cytotoxic activity (Figure 2.7a, see cisplatin data).

Table 2.4. IC_{50} values for **2**, **4**, **5** and Cisplatin.

Complex	A2780	A2780CIS
2	>200 μ M	>200 μ M
4	$29 \pm 6 \mu$ M	$38 \pm 1 \mu$ M
5	$114 \pm 4 \mu$ M	>200 μ M
Cisplatin	$3 \pm 1 \mu$ M	$30 \pm 1 \mu$ M

To provide an indication of the anti-proliferative capability of **4** towards a cisplatin-sensitive cell line compared to resistant cells, a direct comparison between parental (cisplatin-sensitive) A2780 and derivative (cisplatin-resistant) A2780CIS cells was undertaken using a complementary approach. Cells were exposed to a range of concentrations of **4** or cisplatin for 48 h and the resultant metabolic activity of each cell population was assessed using MTT (3-(4,5-dimethylthiazol-2-yl)-2,5-

diphenyltetrazolium bromide) assays (Figure 2.7c and d).³¹ The mononuclear Ru(II) parent complex **2** and mononuclear Pt(II) complex **5** were included in parallel to provide information on the structural properties required for the potency of **4** (Figure 2.7e, f). As shown in Figure 2.7c and Table 2.4, these experiments confirm the impact of **4** on cell proliferation, and are consistent with the IC₅₀ value for **4** determined by analysis of cell numbers in A2780CIS cells after 48 h exposure as determined above.

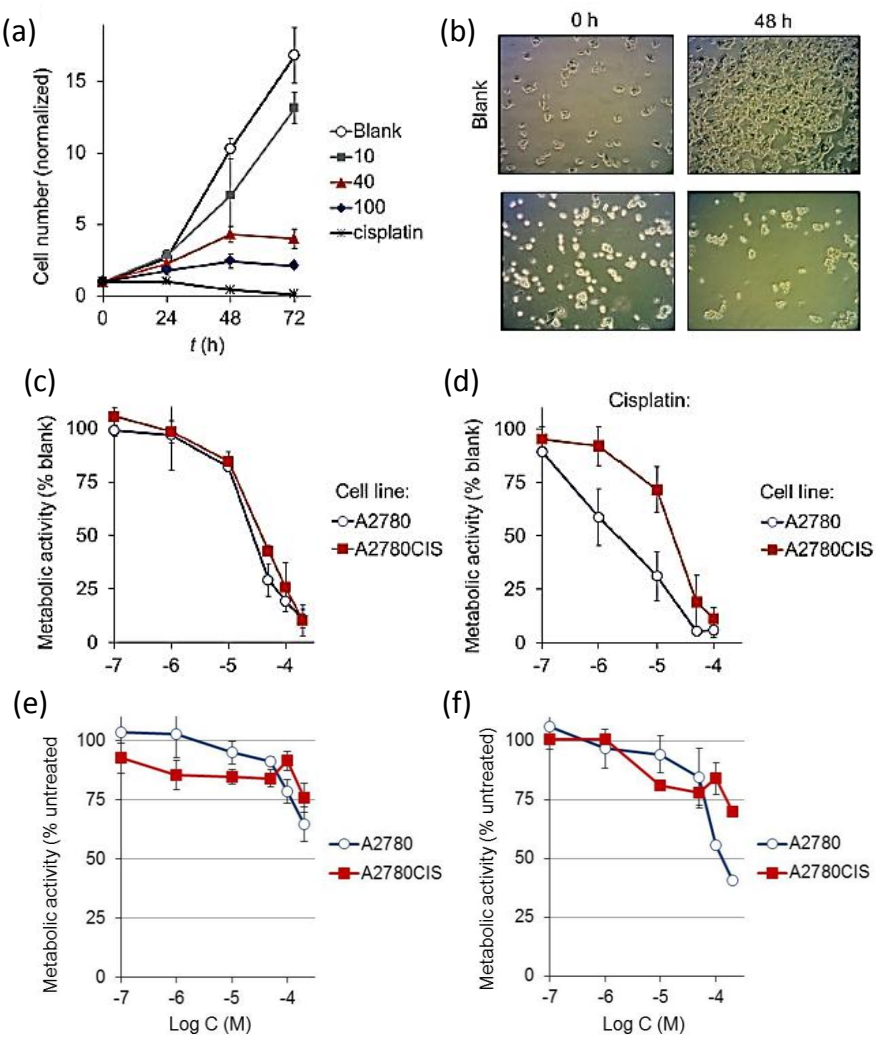


Figure 2.7. (a) Cell number as a result of exposure of A2780CIS cells to **4** (viable cells counted by Trypan-blue exclusion), (b) Images of A2780CIS cells treated with 100 μM **4**, (c, d, e & f) Effect of **4** or cisplatin **2** and **5** on total metabolic activity of A2780 and A2780CIS cell populations after 48 h exposure.

As expected,³² a tenfold decrease in potency was observed in A2780CIS cells treated with cisplatin compared with the A2780 cells (Figure 2.7d and Table 2.4). Significantly, and in direct contrast to results obtained with cisplatin, no cross-resistance to **4** was observed (Figure 2.7c), with potency of **4** almost identical in both cisplatin-sensitive and cisplatin-resistant ovarian cancer cell lines (IC_{50} of 29 and 38 μM for A2780 and A2780CIS cells, respectively). The mononuclear Ru(II) analogue **2** had negligible effects on either cell line, while the mononuclear Pt(II) complex **5** exhibited a fourfold lower potency towards A2780 cells ($IC_{50} = 114 \mu\text{M}$) and had no impact on A2780CIS cell numbers/viability in the concentration range tested (Table 3 and Figure 2.7e, f). These results indicate that both the Ru(II) structural moiety and Pt(II) metal centre are required for the anti-proliferative behaviour demonstrated by **4**.

2.5.8. Cellular uptake properties of **2**, **4**, **5** and cisplatin

It is well established that the internalization characteristics of metal anticancer complexes may contribute to their efficacy.^{33,34} Given that **4** has a significantly greater impact on cell proliferation compared to either mononuclear complexes **2** or **5**, we investigated whether the extent of cellular uptake could explain the difference in A2780CIS cells was determined using inductively coupled plasma mass spectrometry (ICPMS). For cells incubated with solutions of **2**, **4**, **5** or cisplatin prior to analysis, the levels of Ru and/or Pt were measured in untreated control therefore correspond to the cellular accumulation of the relevant complex. As **4** is a Ru(II)-Pt(II) bimetallic system, this approach has the additional advantage as the Ru and Pt concentrations can be obtained separately and directly compared. Results are expressed as the concentration of metal per cell (fmoles per cell). Treatment of A2780CIS cells with **4** or cisplatin for 24 h resulted in a comparable intracellular Pt content (1.46 ± 0.90) and (1.28 ± 0.13) fmoles Pt per cell for **4** and cisplatin, respectively), indicating **4** is internalized to similar levels as

the established anticancer drug (Figure 2.8). The Pt content obtained for cells treated with cisplatin is in agreement with literature values. Assuming an average A2780CIS cell volume of approximately ~2 μ L, the Ru and Pt contents (2.06 ± 0.10) and 1.46 ± 0.90 fmol per cell, respectively) obtained by this method therefore correspond to an approximate intracellular concentration of 1013 ± 51 and 730 ± 45 nm for Ru and Pt ions, respectively, in cells treated with **4** (after blank subtraction). Encouragingly, these values are consistent with each other and indicate that the intracellular concentration of **4** (~1 nm) is approximately 20-fold higher than the external exposure concentration (50 nm). The slight decrease in the absolute levels of Pt content compared to Ru for cells treated with **4** may reflect the relative sensitivity of the technique towards each metal ion at these relatively low concentrations, however, ICP-MS characterization of isolated **4** solutions show the expected 1:1 molar ratio of each metal present (Figure 2.8b). Therefore, we cannot exclude the possibility of complex fragmentation upon cellular internalization, and that **4** might function as a pro-drug. These results also clearly indicate a greater cellular accumulation of the binuclear conjugate complex **4** than either mononuclear complexes **2** or **5**, where data indicate fivefold lower levels of Ru metal ion content for cells incubated with **2** (**2** = 0.37 ± 0.03 fmoles Ru per cell) and a 2.5-fold lower Pt content for **5** (0.58 ± 0.10 fmoles Pt per cell) compared to the results for **4** (Figure 2.8a).

Subsequently, normalizing these ICP-MS data for cellular protein content (Figure 2.8b, c). It is clear that **4**, and even the poorly active **2**, both demonstrate a greater degree of internalization than certain cytotoxic Ru(II)-polypyridyl DNA intercalators. The relationship between an increase in hydrophobicity and extent of cellular uptake of metal complexes has been demonstrated for a range of metal compounds.³⁵ In agreement with this concept, the relative cellular uptake levels of **4**, **2** and **5**, and their anticancer

potency, correlate with the hydrophobicity of each complex, as quantified by octanol/water partition coefficient, logP (Figure 2.8a). Despite this clear trend, it is apparent that **5**, which has a comparable logP to cisplatin, has a lower level of cellular uptake and corresponding decrease in potency than would be predicted if hydrophobicity were the sole factor in governing internalization.

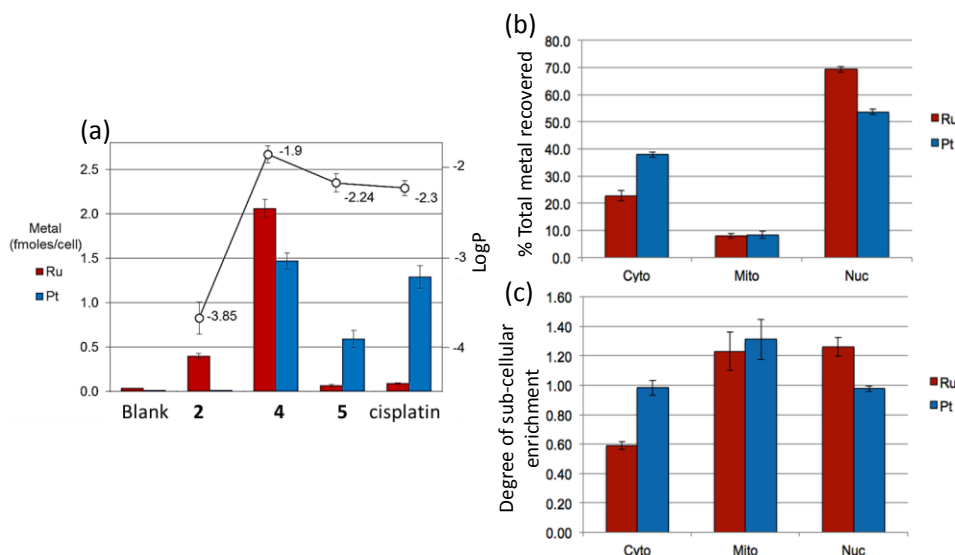


Figure 2.8. (a) Left hand y-axis: cellular uptake levels of **2**, **4**, **5** and cisplatin in A2780CIS cells (50 mm, 24 h), as quantified by ICP-MS analysis of Ru and Pt content ($n = 3, \pm SD$). DMSO (0.1%) blank sample included for reference. Right hand y-axis: log P octanol/water partition coefficients as determined by HPLC, (b) The Ru and Pt content in nuclear-, mitochondrial- and cytosolic-enriched fractions, (c) Degree of sub-cellular enrichment.

To examine the subcellular localization of **4**, A2780 cells were incubated with the complex and cell fractions from the resultant lysates were prepared. The Ru and Pt content in all fractions (nuclear, mitochondrial and cytosolic-enriched fractions were then analysed by ICP-MS (Figure 2.8b, c). These data show a high proportion of both Pt and Ru content in the nuclear fraction. However, upon normalization to protein content of each fraction, it is clear that accumulation of both metals is relatively consistent across these intracellular compartments with a small degree of enrichment(amount of

metal/protein per subcellular fraction divided by amount of metal/protein in total cell lysate; in the mitochondrial and (for Ru) nuclear fractions (Figure 2.8c). The differences in the proportions of Ru and Pt in each subcellular fraction again indicate that we cannot exclude the possibility of intracellular fragmentation, and some degree of differential accumulation within distinct cell compartments.

2.5.9. Complex 4 does not induce apoptosis or necrosis

The intra-strand and inter-strand crosslinks arising from exposure to cisplatin and derivatives activate several DNA damage signalling pathways that ultimately culminate in apoptosis. Therefore, as a starting point to elucidate the cellular mechanism of action of **4**, relative levels of apoptosis after exposure to active doses of the Ru(II)–Pt(II) complex were characterised. Firstly, cells were incubated with either **4** or cisplatin at their respective IC₅₀ concentrations for up to 48 h and the extent of pyknosis and/or karyorrhexis, typical indicators of late-stage apoptosis, were determined. In addition, lysates derived from treated cells were immunoblotted for the active (cleaved) form of the apoptotic marker, caspase-3. Figure 2.9a shows that, as expected with cisplatin treatment, the fraction of cells with observable nuclear fragmentation increased with time and accounted for over 35 % of cells remaining after 48 h. In contrast, cells incubated with **4** showed minimal (<1 %) evidence of chromatin abnormality. Consistent with this, cells treated with the IC₅₀ concentration of cisplatin contained significant levels of activated caspase-3 after 24 h, which continued to increase with time of exposure; clearly indicating an apoptotic response (Figure 2.9b). In contrast to cisplatin treatment, no activation of caspase-3 was observed in cells treated with an equipotent dose of **4** (Figure 2.9b). These results indicate that exposure to anti-proliferative doses of **4** does not result in significant levels of apoptosis in A2780CIS cells. In the absence of an apoptotic response to **4**, we next characterised the levels of total cell death, independent

of pathway. To achieve this, A2780CIS cells were treated with anti-proliferative doses of **4** and the number of Trypanblue-positive (membrane-compromised) cells was quantified. While not able to discriminate between cell-death pathways, this assay will quantify levels of secondary necrosis, that is, cells which have lost plasma membrane integrity. Once more, cisplatin was used in parallel as a cytotoxic control.

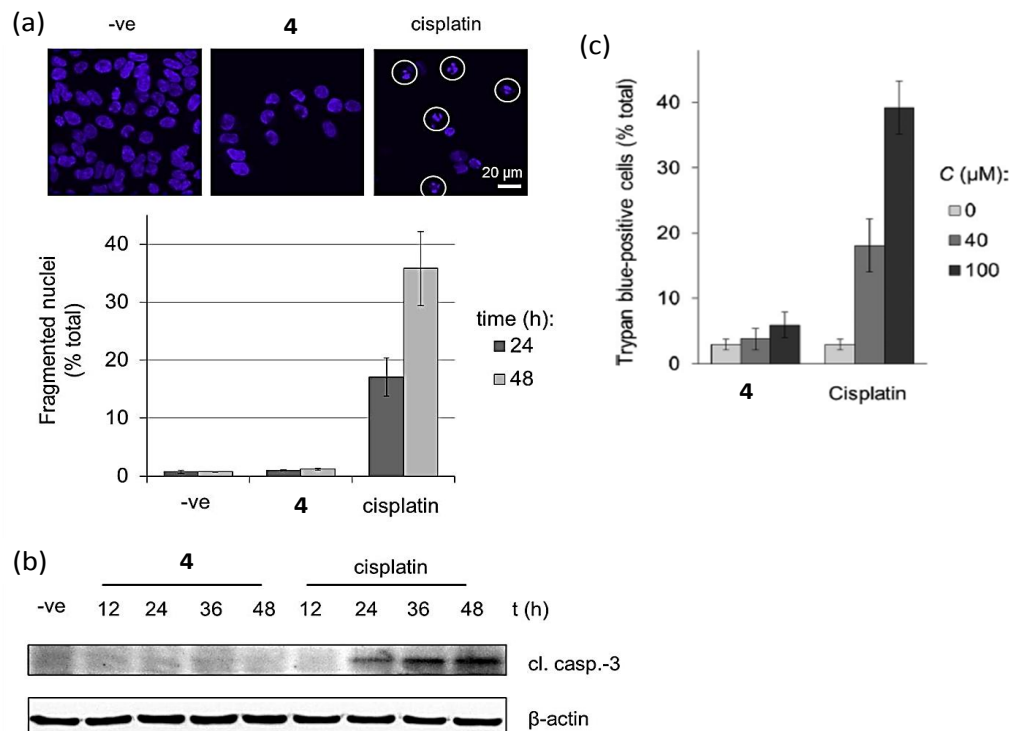


Figure 2.9. (a) Morphological analysis for apoptosis (fragmented nuclei: top, circled) within A2780CIS cell populations incubated with **4** or cisplatin ($n=2, \pm SD$), (b) Immunoblotting analysis of lysates derived from A2780CIS cells treated either with **4** or cisplatin for the presence of cleaved caspase-3 (17 kDa fragments), (c) The % of secondary necrosis in A2780CIS cells treated at 40 and 100 μM concentrations.

Trypanblue staining revealed exposure of A2780CIS cells to **4** did not result in the generation of significant levels of membrane compromised necrotic cells above an untreated control: treatment with the IC₅₀ concentration (determined as described in Table 2.4) of 40 μM **4** resulted in 4% necrosis and even at doses of 100 μM **4** less than 6 % of the cell population has undergone secondary necrosis (Figure 2.8c). Each of

these values is comparable to background levels of 3% Trypan-blue positive cells obtained for untreated control cells. In contrast, exposure to cisplatin generates a large proportion of membrane-compromised cells, where 18% secondary necrosis is observed for cells treated with the IC₅₀ concentration and the levels of nonviable cells approach 40% for cells treated with 100 μM cisplatin, clearly indicating high levels of cell death due to treatment with the cytotoxic compound. These data provide compelling evidence that **4** inhibit the proliferation of cancer cells without inducing significant levels of cell death. Thus, we conclude **4** is predominantly acting in a cytostatic (Cytostasis is defined as the inhibition of cell growth and multiplication), rather than cytotoxic.³⁶

2.5.10. Complex **4** induces G1 cell cycle arrest

As **4** exerts an anti-proliferative effect by inducing cytostasis, we hypothesized that cell-cycle arrest could explain the inhibition of cell growth by the complex. To explore the effect of **4** on the cell cycle, cells were either untreated or exposed to **4** for 24 h before fixation and flow cytometric analyses. The percentage of cells within each phase of the cell cycle was determined by propidium iodide (PI) staining and DNA content quantification.

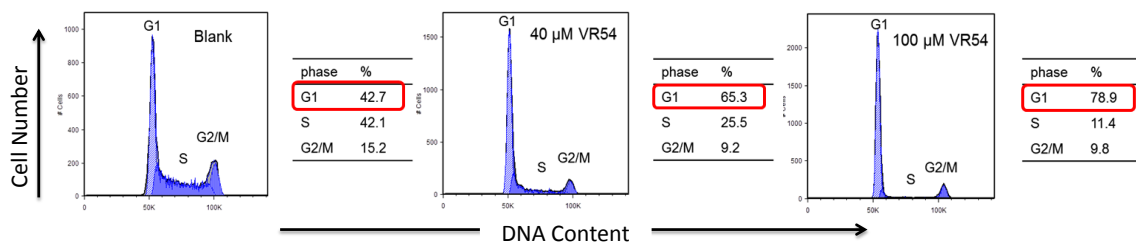


Figure 2.10. Cell cycle distributions for A2780CIS cells incubated with 0 (blank), 40 μM or 100 μM **4** for 24 h, and subsequently analysed by flow cytometry. DNA content was quantified using propidium iodide (PI).

Figure 2.10 shows that treatment of cycling A2780CIS cells with 40 μM **4** results in a significant concentration dependent increase in cells in G1 phase compared to the

control (65.3% of the total population in G1 versus 42.7 %, respectively), a dramatic apparent reduction in the proportion of S-phase cells (25.5% versus 42.1 %), and concomitant decrease in the proportion of cells in G2/M phase (9.2 % versus 15.2 %). The higher dose of **4** (100 nm) results in an approximately twofold increase in G1 phase cells (78.9 %) compared to the untreated control (Figure 2.10). Consistent with the low levels of apoptotic markers described in Figure 2.9 above, there was no sub-G1 (apoptotic) population in cells treated with **4**. The large increase in G1 phase cells upon **4** treatment indicates **4** inhibits cell proliferation through impeding cell cycle progress, either by inducing cell-cycle arrest during G1 phase or by inhibiting the transition from G1 to S phase. **4** does not activate the DNA-damage response network.

2.5.11. Complex **4** does not activate the DNA damage response network

We next set out to elucidate the molecular mechanism responsible for **4** induced cell cycle arrest. Since cell cycle checkpoints modulate DNA damage/genome integrity responses by controlling the timing of cell cycle progression, and univariate cytometric analyses cannot easily distinguish between cells arrested in G1 or in early S phase, we examined whether **4** induced cell cycle arrest occurs via activation of DNA damage signalling pathways. Therefore, the status of both ATR/Chk1 and ATM/Chk2 checkpoint signalling pathways, which are activated primarily in response to replication stress and double-strand breaks respectively,³⁷ was examined. Pathway activation was assessed by determining the extent of phosphorylation of both Chk1 and Chk2 using phospho-specific and total protein antibodies that recognize activated, and all forms of each protein, respectively. Furthermore, the levels of the phosphorylated form of the checkpoint regulator, p53, and a proxy marker of DNA double-strand breaks, phospho-histone H2AX (γ -H2AX), were also determined. As Figure 2.11 shows, there was no increase in phospho-Chk1 (Ser345) levels in cells treated with **4** compared to an

untreated (-ve) control. In stark contrast, cells incubated with cisplatin exhibited a progressive, time-dependent increase in Chk1 activation, presumably due to replication stress caused by the presence of cisplatin-induced lesions. Similarly, cisplatin, but not **4**, induced significant time-dependent activation of Chk2 (phospho-Chk2, Ser516), as well as an increase in phospho-H2AX (Ser139) and phospho-p53 (Ser10).

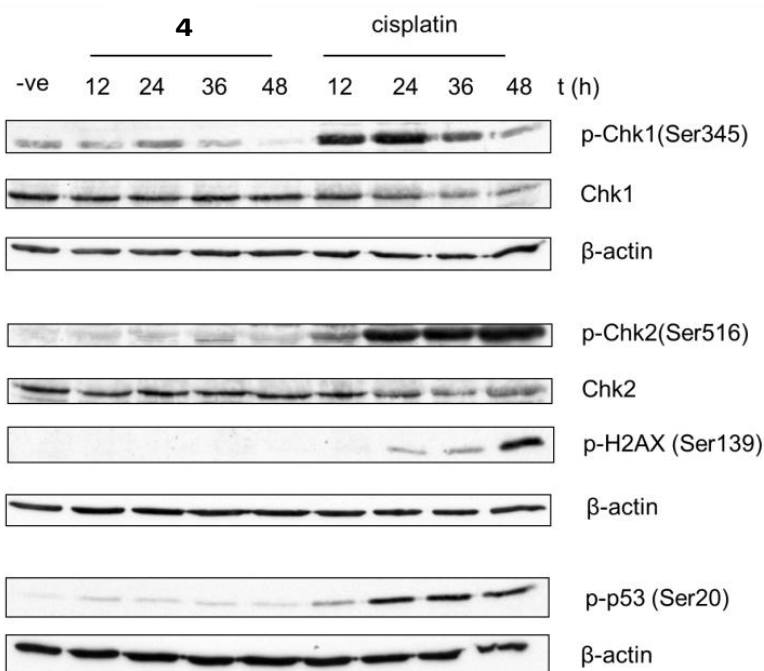


Figure 2.11. Complex **4** does not activate DNA damage checkpoints. A2780CIS cells were treated with either 40 μ M **4** or 30 μ M cisplatin for the indicated times prior to lysate preparation and immunoblotting for anti-phospho Chk1 (Ser345), anti-total Chk1, anti-phospho Chk2 (Ser516), anti-total Chk2, anti-phospho H2AX (Ser139) and anti-phospho p53 (Ser20). β -actin levels were monitored as loading controls.

Again this observation is consistent with the expected generation of cisplatin mediated inter-strand crosslinking, resulting in double-strand breaks and a consequent cellular DNA damage response. These data indicate that treatment of A2780CIS cells with **4** does not activate the DNA damage response signalling network, providing confirmation that the cytostatic **4** operates via a cellular mechanism of action distinct from cisplatin.

2.5.12. Complex 4 up-regulates p27 and inhibits Rb phosphorylation

The transition from G1 to S phase is mediated by activation of cyclin D-Cdk4/6 and cyclin E-Cdk2 protein kinases. Cdk's may be inhibited by specific cyclin-dependent kinase inhibitors (CKIs) such as p21^{CIP1} and p27^{KIP1}, and increased levels of either can result in failure to progress from G1 into S-phase. The former is frequently up-regulated in a p53-dependent manner as part of the DNA damage response.³⁸ External signals predominantly modulate p27^{KIP1} levels, with serum deprivation and contact inhibition resulting in its up-regulation, and serum addition or growth factors inducing its down-regulation.

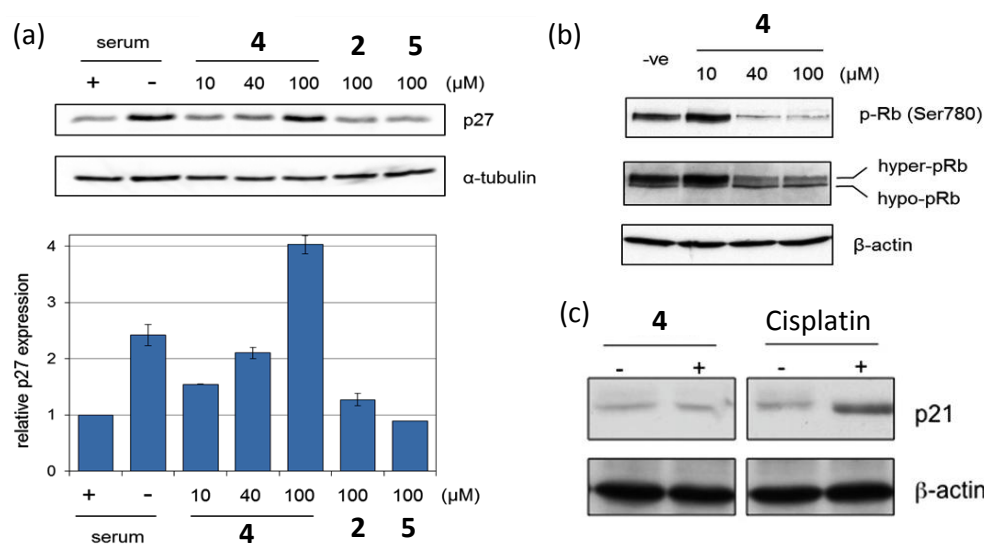


Figure 2.12. (a) A2780CIS cells growing in serum-containing medium were treated with 0.1% DMSO (control), **4**, **2** or **5** at the stated concentrations for 24 h. Serum-starved cells (24 h) were employed as a positive control. α-tubulin levels were monitored as a loading control, (b) A2780CIS cells were incubated with **4** or a negative control (0.1% DMSO) for 24 h prior to lysate preparation and immunoblotting with anti-phospho-Rb (Ser780) and anti-total Rb antibodies, independent of phosphorylation state, β-actin levels were used as a loading control. All results are representative of two independent experiments. (c) Unlike cisplatin complex **4** has not up regulated the p²¹.

As indicated above, exposure to **4** results in significant G1/S cell cycle arrest. In the absence of evidence of p53 activation (Figure 2.12, lower panels), we investigated whether **4** acts through the up-regulation of the G1 Cdk inhibitor, p27KIP1 by determining levels of p27KIP1 expression as a result of treatment with **4**. Serum starvation was used as a positive control for up-regulation of p27KIP1. Western blot analysis of A2780CIS cells treated with **4** for 24 h showed a significant dose-dependent increase in the levels of p27KIP1 compared to an untreated control (Figure 2.12a, upper and lower panels).

Quantifying this increase, treatment of cells with 40 μM **4** resulted in a ~ 2-fold increase in p27KIP1 levels, while cells exposed to 100 μM **4** resulted in levels of p27KIP1 significantly greater than observed in serum-starved (i.e. quiescent) cells, a four-fold increase compared to the (serum-containing) untreated control (Figure 2.12a, lower panels). p27 levels in cells treated with 100 μM **2** or **5** showed comparable p27KIP1 levels to the untreated control, consistent with the absence of an effect of either mononuclear complex on cell proliferation at these concentrations. The increased p27KIP1 levels arising from exposure to **4** directly correlate with the inhibition of cell growth and cell cycle accumulation in G1 phase. In order to confirm that **4** exerts its cell cycle inhibitory effect via up-regulation of p27KIP1 and consequent inhibition of cyclin-Cdk complexes, we examined the effect of **4** on the activation status of the tumour suppressor retinoblastoma protein (Rb), which plays a key role in the exit from G1 phase. During the progression from G1 into S phase, active hypo-phosphorylated Rb is deactivated via phosphorylation by the cyclin D-Cdk4/6 and cyclin E-Cdk2 kinases to facilitate cell cycle progression. Using antibodies that recognize either phosphorylated Rb (at Ser780) or total Rb levels, we examined the phosphorylation status of Rb in **4** treated cells by western blot analysis to determine the activation status of this pathway.

Figure 2.12b (upper panel) shows cells exposed to **4** exhibit a progressive, concentration-dependent decrease in levels of p-Rb phosphorylated at Ser780, indicating the strong inhibition of Rb phosphorylation at this site. Consistent with this observation, the ratio of hyper-phorylated Rb to hypo-phosphorylated Rb decreased with exposure to **4** (Figure 2.12b, middle panel). These results indicate the phosphorylation of Rb is dramatically inhibited by **4** and are in agreement with the concept that **4** up-regulates p27KIP1. In order to investigate any contribution of p21 to the hypophosphorylation of Rb, we undertook western blot analysis of p21 levels following exposure to **4**; however, no increase in p21 was observed after 24 h exposure (Figure 2.12c).

2.6. Conclusion

In conclusions, we have successfully synthesised Ru(II)-Pt(II)-terpyridine based heterodinuclear complex and its components for comparative purpose and studied their DNA binding behaviour.

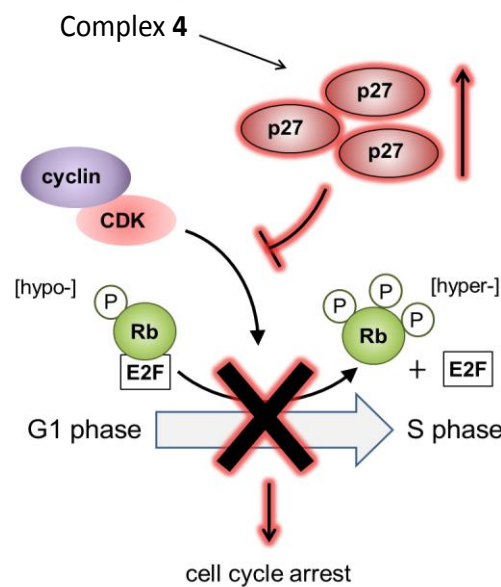


Figure 2.13. Diagram illustrating the proposed mechanism of action of **4**.

UV-Visible and viscosity studies clearly show that these metal complexes are interacting with CT-DNA via groove binding. ¹H NMR studies with nucleotide guanosine indicated except **5** neither **2** nor **4** binds to the N7 position. ITC studies described the spontaneous reaction between the DNA and the synthesised metal complexes. **4** was found to be anti-proliferative in nature and stops the cell cycle at S1. We therefore conclude that the mechanism of action of **4** is through the up-regulation of p27KIP1 and resultant inhibition of Rb phosphorylation. The inhibition of Rb phosphorylation acts to block cell cycle entry into S phase at the G1 restriction point, culminating in G1 cell cycle arrest and the inhibition of cell growth (Figure 2.13).

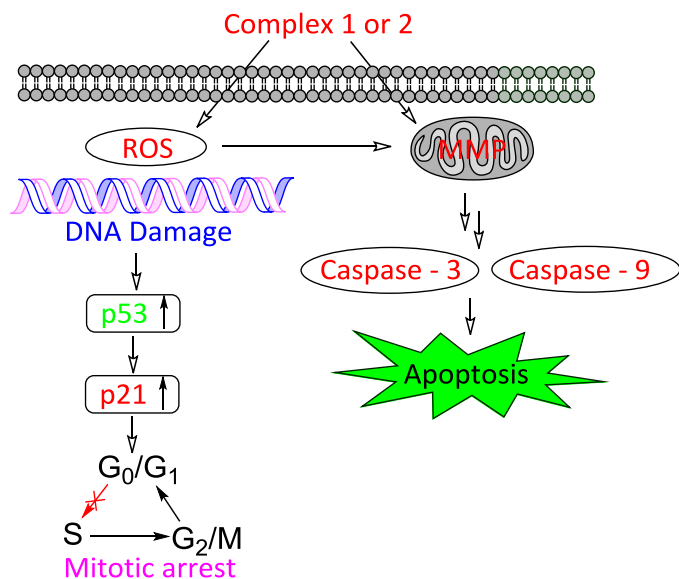
2.7. References

1. E. R. Jamieson and S. J. Lippard, *Chem. Rev.*, 1999, **99**, 2467–2498.
2. A.-M. Florea and D. Büselberg, *Cancers*, 2011, **3**, 1351–1371.
3. J. Reedijk, *Proc. Natl. Acad. Sci. U. S. A.*, 2003, **100**, 3611–3616.
4. X. Qu, *J. Inorg. Biochem.*, 2006, **100**, 1955–1964.
5. J. J. Wilson and S. J. Lippard, *Chem. Rev.*, 2014, **114**, 4470–4495.
6. L. Kelland, *Nat. Rev. Cancer*, 2007, **7**, 573–584.
7. Y. Jung and S. J. Lippard, *Chem. Rev.*, 2007, **107**, 1387–1407.
8. Z. H. Siddik, *Oncogene*, 2003, **22**, 7265–79.
9. A. Bergamo, C. Gaiddon, J. H. M. Schellens, J. H. Beijnen, and G. Sava, *J. Inorg. Biochem.*, 2012, **106**, 90–99.
10. D. Garcia, M. R. Warr, C. P. Martins, L. B. Swigart, and G. I. Evan, *Genes Dev.*, 2011, **53**, 1746–1757.
11. E. S. Antonarakis and A. Emadi, *Cancer Chemother. Pharmacol.*, 2010, **66**, 1–9.
12. S. Pervin, R. Singh, and G. Chaudhuri, *Proc. Natl. Acad. Sci.*, 2000, **98**, 3583–3588.
13. M. Malumbres and M. Barbacid, *Nat. Rev. Cancer*, 2001, **1**, 222–231.
14. M. R. Gill, H. Derrat, C. G. W. Smythe, G. Battaglia, and J. A. Thomas, *ChemBioChem*, 2011, **12**, 877–880.
15. Y. Jung and S. J. Lippard, *Chem. Rev.*, 2007, **107**, 1387–1407.
16. L. Kelland, *Nat. Rev. Cancer*, 2007, **7**, 573–584.
17. G. Gasser, I. Ott, and N. Metzler-Nolte, *J. Med. Chem.*, 2011, **54**, 3–25.
18. S. H. Van Rijt and P. J. Sadler, *Drug Discov. Today*, 2009, **14**, 1089–1097.
19. C. Scolaro, A. Bergamo, L. Brescacin, R. Delfino, and M. Cocchietto, *J. Med. Chem.*, 2005, **48**, 4161–4171.
20. J. Husson and M. Knorr, *Beilstein J. Org. Chem.*, 2012, **8**, 379–389.
21. J. Wang and G. S. Hanan, *Synlett*, 2005, 1251–1254.
22. A. Graczyk, F. A. Murphy, D. Nolan, V. Fernández-Moreira, N. J. Lundin, C. M. Fitchett, and S. M. Draper, *Dalt. Trans.*, 2012, **41**, 7746–7754.
23. E. A. Medlycott and G. S. Hanan, *Coord. Chem. Rev.*, 2006, **250**, 1763–1782.
24. M. R. Gill and J. A. Thomas, *Chem. Soc. Rev.*, 2012, **41**, 3179–3188.
25. K. Sakai, H. Ozawa, H. Yamada, T. Tsubomura, M. Hara, A. Higuchi, and M.-A. Haga, *Dalton Trans.*, 2006, **2**, 3300–3305.

26. K. Van Der Schilden, H. Kooijman, A. L. Spek, J. G. Haasnoot and J. Reedijk, *Angew. Chemie - Int. Ed.*, 2004, **43**, 5668–5670.
27. A. Ghosh, A. Mandoli, D. K. Kumar, N. S. Yadav, T. Ghosh, B. Jha, J. A. Thomas and A. Das, *Dalt. Trans.*, 2009, **42**, 9312–9321.
28. C. Metcalfe, C. Rajput and J. A. Thomas, *J. Inorg. Biochem.*, 2006, **100**, 1314–1319.
29. N. J. Wheate, B. J. Evison, A. J. Herlt, D. R. Phillips, and J. G. Collins, *Dalt. Trans.*, 2003, 3486–3492.
30. E. Pantoja, A. Gallipoli, S. Van Zutphen, S. Komeda, D. Reddy, D. Jaganyi, M. Lutz, D. M. Tooke, A. L. Spek, C. Navarro-Ranninger, and J. Reedijk, *J. Inorg. Biochem.*, 2006, **100**, 1955–1964.
31. C. R. Cardoso, M. V. S. Lima, J. Cheleski, E. J. Peterson, T. Venâncio, N. P. Farrell, and R. M. Carlos, *J. Med. Chem.*, 2014, **57**, 4906–4915.
32. Y. Najajreh, J. M. Perez, C. Navarro-ranninger, and D. Gibson, *J. Med. Chem.*, 2002, **45**, 5189–5195.
33. B. Peña, A. David, C. Pavani, M. S. Baptista, J. P. Pellois, C. Turro, and K. R. Dunbar, *Organometallics*, 2014, **33**, 1100–1103.
34. R. Cao, J. Jia, X. Ma, M. Zhou and H. Fei, *J. Med. Chem.*, 2013, **56**, 3636–3644.
35. C. A. Puckett, R. J. Ernst and J. K. Barton, *Dalt. Trans.*, 2010, **39**, 1159–1170.
36. S. Pervin, R. Singh and G. Chaudhuri, *Proc Natl Acad Sci*, 2001, **98**, 3583–3588.
37. C. A. Hall-Jackson, D. A. Cross, N. Morrice and C. Smythe, *Oncogene*, 1999, **18**, 6707–6713.
38. C. J. Sherr and J. M. Roberts, *Genes Dev.*, 1999, **13**, 1501–1512.

CHAPTER 3

Photo-Induced Cytotoxicity and Anti-Metastatic Activity of Ru(II)-Polypyridyl Complexes



[Publication](#)

Manuscript to be communicated.

3.1. Introduction

According to the world health organization cancer is the leading cause of death all around the world.¹ One of the defining features of cancer is the rapid creation of abnormal cells that grow beyond their usual boundaries, which can invade adjoining parts of the body and spread to other organs, the latter process is known as metastasizing. Photodynamic therapy (PDT) is a non-invasive and one of most extensively used technique for the treatment of dermatological diseases and various types of cancers, which could be controlled and used selectively to treat tumors.²⁻⁴ The main advantage over traditional therapies such as surgery, radiation and chemotherapy is that PDT produces lesser side effects. PDT is a treatment that uses a drug called a photosensitizer or photosensitizing (PS) moiety that shows activity against tumor in presence of light.¹ Ideally, PDT reagent should not show any such activity in dark. Activity of such PDT reagent mainly depends on the efficiency of the PS or fragment in generating long lived excited state that eventually led to the generation of reactive oxygen species (ROS) like superoxide anion ($O_2^{\bullet-}$), hydroxyl radical ($HO^{\bullet-}$), hydrogen peroxide and singlet oxygen (1O_2) following energy or electron transfer process on excitation of PS moiety at an appropriate wavelength (Figure 3.1). Such ROS species, specifically 1O_2 is known to be cytotoxic to living cells and can be judiciously utilized for targeted singlet oxygen chemotherapy.

Surgical intervention for the removal of a part of an organ that is affected by cancer is generally followed by chemo- or radio-therapy, which helps in decreasing the risk of the cancer re-occurrence.⁵ However, tumor metastasis is a multistep biological process that allows cancer cells to get away from the primary tumor, survive in the circulation, located in distant site and grow.⁶ Thus, more recently it has been argued that the effective treatment for cancer largely depends on the anti-metastatic activity and cell cycle arrest of affected live cells. Accordingly, there are considerable ongoing efforts for developing

appropriate chemotherapeutic drugs which can prohibit the metastasis process. Commercially available PS such as hematoporphyrins and its derivatives (HpD) generally suffers from drawbacks such as lower solubility in aqueous solutions and weak absorption band at 630 nm. This necessitates the use of high light doses of 100-200 J/cm² for achieving the desired control on tumor growth. Also, severe side effect is observed for a common PDT drug like Porfimer sodium, as it is retained in the body for about 4 months and results in skin photosensitivity.⁷

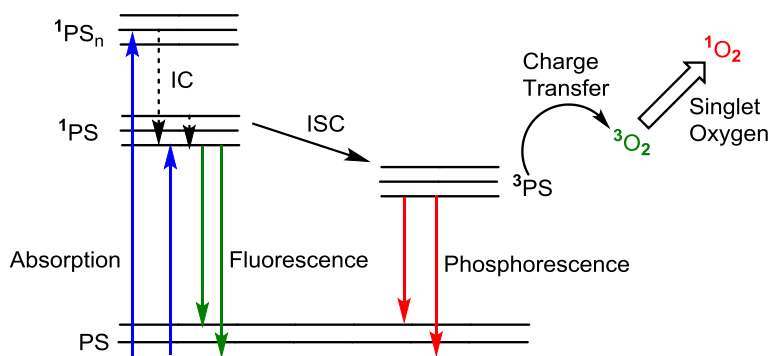


Figure 3.1. Schematic of Jablonski diagram that shows the mechanism for the $^1\text{O}_2$ generation.

More recently, European Union has approved the use of meso-tetra hydroxyphenyl chlorine (mTHPC) as a PS for PDT application.^{2,3,8} Relatively much lower light doses (10-20 J/cm²) at a longer wavelength (652 nm) for tumor control is the primary reason for the edge of this reagent over HpD derivatives. Chlorins is basically "Chlorophyll a" and this is being regularly used as a PDT reagent.¹ However, this also suffers from the major problem of desired stability in physiological conditions as well as from the problem of photobleaching on irradiation.^{1,9} These somehow limit the use of this reagent as PDT reagent. Thus, there is a definite scope for developing an appropriate reagent that can overcome the aforesaid drawbacks. After successful entry of ruthenium based drugs (NAMI-A and KP1019) into human clinical trials, there is a definite surge of interest for developing Ru(II)-based novel anticancer drugs with improved efficiency.^{9,10} Recently,

certain ruthenium-porphyrin conjugates with improved cytotoxicity at lower light doses have been reported in the literature.^{11–13} However, these reagents require longer exposure times (72 h) and they tend to form molecular aggregates in the aqueous solution.¹² There were definite attempts for improving solubility of the PDT reagents for reducing the effective exposure times.^{14,15} Possibility of achieving higher solubility for Ru(II)-polypyridyl complexes by choosing appropriate counter anions as well as through appropriate functionalization of the coordinated bpy functionality has actually contributed in designing new Ru(II)-polypyridyl complexes for their use as anti-cancer and anti-metastatic drugs.^{6,16} Apart from these, visible light excitation, reasonably long lived triplet excited states, higher stability towards photobleaching have made this class of complexes an attractive choice for use as photodynamic therapeutic reagent.¹⁷

Recent reports suggest that the conjugation of biologically relevant molecules to the Ru(II)-polypyridyl complexes could improve the cellular internalization. Ru(II)-polypyridyl complexes having appropriately functionalized bpy derivative could also help in enhancing the lipophilicity of the complex and recent reports also suggest that higher lipophilicity of a reagent is linked to a more efficient internalization.^{18–21} Herein, we have discussed the possibility of using two novel Ru(II)-polypyridyl based reagents having pendant tyrosine or tryptophan moiety as efficient PDT reagents. Photo-induced cytotoxicity, anti-metastatic property, cellular uptake and ROS mediated DNA cleaving pathways for the complexes **1** and **2** (Scheme 3.1) have been discussed with special emphasis for using lower dose of light (10 J/cm²) for PDT purposes.

Synthesis of **1** and **2** were achieved by following previously reported literature procedures.^{22,23} Both complexes were characterized using various spectroscopic (¹H NMR, ¹³C NMR, ESI-Ms, FTIR) and analytical techniques. All the spectroscopic results as well as the results of the elemental analysis confirmed the desired purity for both complexes, which were utilized for our studies. Photophysical properties of these two

complexes are well established and this is the primary reason for choosing these two complexes for our studies. Tyrosine is a non-essential amino acid that plays a crucial role in the protein synthesis and act as a receiver of phosphate groups in biological systems that are transferred by way of protein kinases (so-called receptor tyrosine kinases).²⁴ Also, it is involved in the mechanism of photosynthetic oxidation of water into molecular oxygen in photosystem II (PSII).²⁵ Tryptophan is utilized for designing the complex **2** for our studies is an essential amino acid that is required and cannot be synthesized by the organisms. Certain tyrosine and tryptophan derivatives are known to readily cross the blood–brain barrier and facilitate the cellular internalization.²⁶ On the other hand, the Ru(II)-polypyridyl complexes are known to generate radical species (e.g. $^1\text{O}_2$ or OH^\bullet) on irradiation at their MLCT band in the visible region of spectrum and such ROS species are generally known to damage DNA and to be cytotoxic to the living cells. Thus, these two complexes, functionalized with amino acid moieties that help in cellular internalization and with well-defined photophysical/physicochemical properties, were utilized for checking the photo-induced damage of DNA molecules as well as the cytotoxicity imparted on living cancer cells. These eventually lead to a ROS mediated cell death.

3.2. Experimental section

3.2.1. N,N-Dimethyl-4-nitrosoaniline/histidine assay

The singlet oxygen production was measured by the N,N-dimethyl-4-nitroso-aniline/histidine assay based on the oxidation of histidine by singlet oxygen and the subsequent reaction of the oxidised histidine with N,N-dimethyl-4-nitrosoaniline as previously described.²⁷ The absorbance of the compound was adjusted to approximately 0.2 at the irradiation wavelength. In practice, 20 mM DMSO stock solution of compound was diluted in 4 mL PBS solution (pH 7.4) containing N,N-dimethyl-4-nitrosoaniline (25

μM) and histidine (0.01 M) and irradiated in fluorescence quartz cuvettes (width 1 cm). Bleaching of N,N-dimethyl-4-nitrosoaniline was followed by monitoring of the absorption at 440 nm. Negative control experiments were run by repeating the measurements in the absence of histidine. The same conditions were also used for singlet oxygen detection in acetonitrile, except that imidazole was used instead of histidine due to the low solubility of histidine in this solvent. In addition, the absorbance peak of N,N-dimethyl-4-nitrosoaniline shifts to 415 nm in acetonitrile. The absorbance at 440/415 nm was then plotted as a function of irradiation time and the quantum yields of singlet oxygen formation (Φ_{sample}) were calculated using phenalenone as the standard ($\Phi_{\text{reference}}$) with the equation 6.

$$\Phi_{\text{Sample}} = \Phi_{\text{reference}} \frac{S_{\text{sample}}}{S_{\text{reference}}} \frac{I_{\text{reference}}}{I_{\text{sample}}} \quad \text{Equation 6}$$

3.2.2. Cytotoxicity and confocal studies

Cell cultures were treated with 0 - 300 μM solutions of **1** and **2** in triplicate for 24 h. After incubation, 5 μL of MTT reagent was added and incubated for 4 h. MTT = (3-(4,5-dimethyl thiazol-2-yl)-2,5-diphenyltetrazolium bromide) dissolved in serum-free media. The media was removed and the formazan dissolved using isopropanol and the absorbance at 570 nm quantified by plate reader (reference 620 nm). IC₅₀ values for the two complexes were found to be >300 μM . A549 and Hct116 cells were cultured in DMEM media. Cell lines were maintained at 37° C in an atmosphere of 5 % CO₂ and routinely sub-cultured. For CLSM, cell cultures were grown on 6 well plate with coverslips and after 24 h of incubation, these cells were treated with solutions of **1** and **2** (30 μM) in serum containing media and further incubated for 4 h. After incubation, media was removed and cells were washed with 1XPBS buffer. Endoplasmic reticulum staining studies were performed using lysotracker green form life technologies. Cells were

fluorescently imaged on a Fluoview confocal laser scanning microscope by using 60X oil-immersion lenses. Complexes **1** and **2** were excited with laser at 442 nm and emission monitored at 620 nm (red) wavelengths. Lysotracker was excited at 504 nm.

3.2.3. Wound healing (scratch motility) assay

MDA-MB-231 cells were cultured in Leibovitz's L15 medium with 10 % FBS. 1×10^5 / mL cells were seeded in 6 well plate and incubated for 24 h in a 5 % CO₂ incubator at 37° C to form a monolayer. After 24 h gaps were created using pipette tip on the confluent monolayer and washed with media to remove cellular debris. The fresh medium supplemented with 10 % FBS was added into well and incubated with **1** and **2** (30 μM) for 4 h to allow the uptake by cells. Following with same conditions one cell culture plate was photo-irradiated for 4 h and the other place kept in the dark conditions. The cell migration observed and imaged at regular intervals (0-10 h) using Nikon live cell imaging microscope for 10 h. The rate of migration of the cells was calculated using image pro 6.0 software provided along with Nikon microscope.

3.2.4. Comet assay

Live A549 cells were incubated with **1** and **2** for 4 h and then these cells were suspended in PBS buffer. This suspension of the cells was embedded into the low melting agarose (0.5 %) gel. 100 μL of this mixture is poured on top of the agarose pre-coated comet slides. Coverslip was placed on top of the comet slides and removed after solidification of agarose. A549 cells were lysed with alkaline solution over night at 4°C. Then slides were removed and rinsed twice with rinsing solution to remove the residual amounts of excess salt and detergents. The comet slide incubated for 2 h in electrophoresis unit in 1XPBS buffer solution. Voltage (0.6 V/cm for 25 min with current of 40 mA) applied to accumulate the damaged DNA at the end of the cathode. Then slide was removed from electrophoresis chamber and rinsed with 400 mL of distilled water. The comet slide was placed in staining solution (syber green solution) for 20 min.

Again the comet slide was rinsed with 400 mL of deionised water to remove the excess stain. The DNA damage was visualized using microscope under ultra-violet light.

3.2.5. Cellular uptake & quantification of 1, 2, by MP-AES

In order to quantify the amount of Ru(II)-complexes taken up by the A549 cells, the complexes **1** and **2** (30 μ M) were incubated with A549 cell for the 4 h at 37°C. Cells were washed twice with PBS buffer to remove the ruthenium in culture media. Cells digested with 1N nitric acid followed by the diluting with 10 mL of distilled water. The accumulation of **1** and **2** were then quantified by conducting the microwave plasma atomic emission spectroscopy (MP-AES).

3.2.6. Cell cycle analysis

A549 cells seeded in 60 mm petri dishes and cultured in DMEM medium. Post 24 h cells were treated with complex **1** and **2** for 4 h. Later, these cells were photo-irradiated continuously for 2 h from a distance of 2 cm. Using trypsin EDTA cells dislodged and collected in 15 mL falcon tubes. Cells thoroughly washed with PBS to remove media/serum and trypsin EDTA. Then cells were suspended in 500 μ L PBS and 4.5 mL 70 % chilled ethanol added drop wise to fix the cells overnight at -20° C. Ethanol removed by PBS wash for three times at 4° C. To the cell pellet 50 μ L RNase A (50 μ g/mL) added and incubated for 30 min at 37° C. Cells were added with 400 μ L propidiumiodide (100 μ g/mL) and incubated for 15 min at room-temperature maintaining dark conditions. This was subjected to flow cytometry and different phases of the cell cycle determined.

3.2.7. Invasion assay

2.5×10^4 MDA-MB231 highly metastatic breast cancer cells seeded onto each well of 24 well matrigel plate chamber. Below the matrigel chamber 750 μ L of fetal bovine serum was placed as chemo-attractant for the MDA-MB231 cells to invade. Cells were treated with complex **1** and **2** for 4 h and then either exposed to dark or blue wavelength light

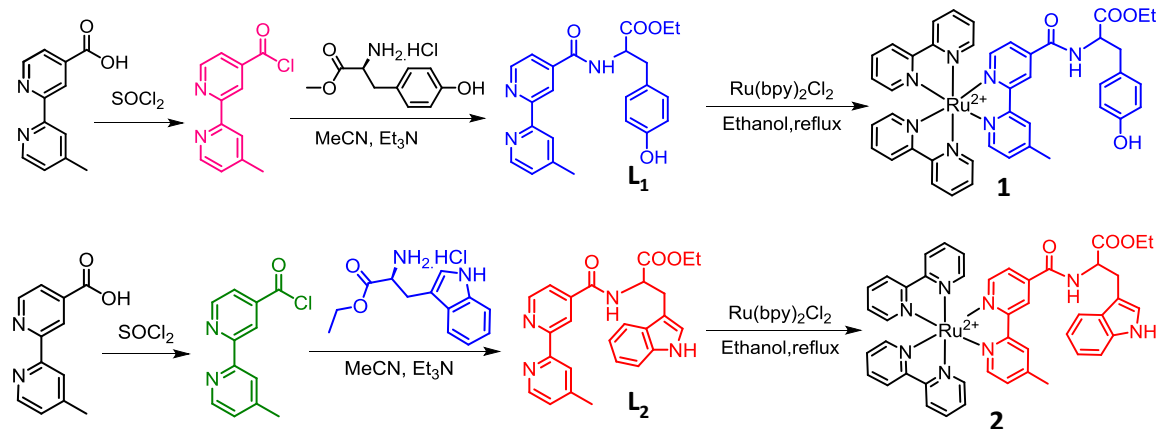
conditions for 2 h. The cells were then allowed to invade the matrigel over-night at 37° C in a humidified 95 % incubator. Next day, the non-invading cells were removed using moistened cotton swabs. Cells were fixed with 100 % chilled methanol for 15 min and then washed with phosphate buffered (1XPBS) three times. 0.4 % crystal violet was prepared and then 500 µL was applied into the chamber containing matrigel and invaded cells. After 15 min of crystal violet staining three PBS washes given and then air dried. The chamber was then placed under inverted microscope to count the number of invaded cells. The % of cell invasion calculated using equation 7.

$$\% \text{ Invasion} = \left(\frac{\text{mean number of cells invading through matrigel matrix coated permeable support membrane}}{\text{number of cells migrating through uncoated permeable support membrane}} \right) \times 100 \quad \text{Equation 7}$$

3.2.8. Western blotting

Cells were lysed in TNN buffer (50 mM tris, pH 7.5, 5 mM EDTA, 0.5 % NP40 150 mM NaCl and 1 mM DTT), supplemented with protease inhibitor cocktail. The concentration of total protein in the cell lysate was determined by Bradford reagent (Thermo Scientific). Each protein of 40 µg was loaded onto 10 % SDS-PAGE, and protein was transferred onto PVDF membrane (Millipore) using western blot technique. After the completion of protein transfer, the membrane was blocked for 2 h at room temperature in 5% BSA (MP Biomedicals). The blot was then washed with 1X TBST (tris buffer saline, 0.1% Tween 20) 3 times, each for 5 min. The blot was probed with primary antibodies against caspase-3, caspase-9, β-actin and GAPDH (Santa Cruz) for 2 h in 1:1000 dilutions for caspase 3 and caspase 9 and 1:4000 dilutions for β-actin and GAPDH. After washing the blot in 1XTBST, secondary antibody which was conjugated with Horseradish peroxidase was then added in 1:4000 dilutions in 1XTBST buffer. The blot was then developed using autoradiography in X-ray film.

3.3. Synthesis and characterization



Scheme 3.1. Synthetic route adopted for the preparation of **L₁**, **L₂**, **1** and **2**.

3.3.1. Synthesis of **L₁**: Ethyl (4'-methyl-[2,2'-bipyridine]-4-carbonyl)tyrosinate

4'-methyl-[2,2'-bipyridine]-4-carboxylic acid (500 mg, 2.336 mmol) was taken in a two necked round bottom flask. To this thionyl chloride (25 mL) was added under inert atmosphere. Then the solution was heated to reflux for 6 h with constant stirring. Excess thionyl chloride was removed by distillation under reduced pressure. Dry triethylamine (1 mL) was added to a solution of L-tyrosine ethyl ester hydrochloride (636.7 mg, 2.562 mmol) in dry distilled acetonitrile (30 mL) and the resulting solution was stirred thoroughly. To this, acid chloride solution in dry acetonitrile was added in a drop wise manner over one hour. The solution was stirred for half an hour at room temperature and then it was set to reflux for 12 h under inert atmosphere. The solution was then cooled and filtered. The filtrate was evaporated to dryness, and the residue was dissolved in dichloromethane (\approx 30 mL) and washed three times with water to remove excess triethylamine. The organic phase was dried with anhydrous sodium sulfate and the solvents evaporated to dryness. The crude product was purified by chromatography using silica as the stationary phase and ethyl acetate/hexane as the eluent; yield 476.35 mg, 50 %. ESI-MS (m/z): calculated 405.45; found 406.38 [M + H⁺]. ¹H NMR (200 MHz,

CDCl_3): δ ppm = 8.71(d, J = 5 Hz, 1H), 8.55 (s, 1H), 8.48 (d, J = 4.8 Hz, 1H), 8.12 (s, 1H), 7.64 (d, J = 4.8 Hz, 1H), 7.25 (d, J = 4.2 Hz, 1H), 7.1 (d, J = 8.4 Hz, 2 H), 6.72 (d, J = 8.2 Hz, 2H), 4.86 - 4.78 (m, 1H), 4.18 (q, J = 7.2 Hz, 2H) 3.26 - 2.98 (m, 2 H), 2.43 (s, 3 H), 1.23 (t, J = 7.2 Hz, 3 H).

3.3.2. Synthesis of L_2 : Ethyl (4'-methyl-[2,2'-bipyridine]-4-carbonyl)tryptophanate

4'-methyl-[2,2'-bipyridine]-4-carboxylic acid (500 mg, 2.336 mmol) was taken in a two necked round bottom flask. To this thionyl chloride (25 mL) was added and the solution was heated to reflux for 6 h. Excess thionyl chloride was removed by distillation under reduced pressure. To a solution of L-tryptophan ethyl ester hydrochloride (650 mg, 2.41 mmol) in dry distilled acetonitrile (30 mL), dry triethylamine (1 mL) was added and stirred. To This solution, acid chloride (dissolved in dry acetonitrile) was added in a drop wise manner over one hour. The solution was stirred for half an hour at room temperature and then refluxed for 12 h under inert atmosphere. The solution was then cooled and filtered. The filtrate was evaporated to dryness, and the residue was dissolved in 30 mL of dichloromethane and washed three times with water to remove excess triethylamine. The organic phase was dried with anhydrous sodium sulfate and the solvents evaporated to dryness. The crude product was purified by chromatography using silica as the stationary phase and ethyl acetate/hexane as the eluent; yield 475 mg, 49.5 %. ESI-MS (m/z): calculated 428.49; found 428.38 [M + H⁺]. ¹HNMR (200 MHz, δ ppm): 8.75 (d, J = 5.0 Hz), 8.58 (s), 8.54 (d, J = 5.0 Hz), 8.21 (s), 8.14 - 8.04 (m), 7.60 (dd, J = 9.7, 2.7 Hz), 7.36 (d, J = 7.8 Hz), 7.20 - 7.10 (m), 7.07 (d, J = 6.2 Hz), 6.98 - 6.88 (m), 5.22 - 5.07 (m), 4.18 (dt, J = 7.0, 3.8 Hz), 3.48 (d, J = 5.4 Hz), 2.45 (s), 1.25 (t, J = 7.1 Hz).

3.3.3. Synthesis of complex 1

Complex 1 was synthesized according to the reported literature procedure.²³ About 0.19 g (0.36 mmol) of Ru(bpy)₂Cl₂·2H₂O was dissolved in 30 mL of dry ethanol and ligand L_1

(0.15 mg, 0.36 mmol) was added to this solution. The reaction mixture was allowed to reflux for 8 h under N₂ atmosphere with continuous stirring. Then the reaction mixture was cooled to room temperature and the solvent was removed under vacuum. The desired Ru(II)-complex was collected by the solvent extraction method using the dichloromethane and water system. Few drops (~0.5 mL) of CH₃CN were used while performing solvent extraction process (0.5 mL) for efficient extraction of the complex into the organic layer. Dichloromethane solution (having little CH₃CN) was dried under reduced pressure and the crude red solid was subjected to the column chromatography. For this, silica gel was used as the stationary phase and CH₃CN-saturated aq. KPF₆ solution was used as mobile phase. Second major fraction was collected for isolating the desired compound in pure form. Characterization of complex **1** was carried out by using standard analytical and spectroscopic techniques. Yield: 58.3 % (196 mg, 0.17 mmol). ESI-HRMS (m/z) for formula: C₄₃H₃₉F₆N₇O₄PRu; calculated 964.1740; found: 964.1743. ¹H NMR 500 MHz, in CH₃CN (δ , ppm): δ ppm 8.73 (s), 8.53 (d, *J* = 8.4 Hz), 8.09 (t, *J* = 7.9 Hz), 7.88 (dd, *J* = 5.8, 2.6 Hz), 7.78-7.70 (m), 7.64 (d, *J* = 7.9 Hz), 7.62-7.59 (m), 7.58 (d, *J* = 5.8 Hz), 7.43 (t, *J* = 6.7 Hz), 7.31 (d, *J* = 5.5 Hz), 7.13 (dd, *J* = 8.5, 3.5 Hz), 6.75 (dd, *J* = 8.5, 4.5 Hz), 4.86-4.80 (m), 4.18 (q, *J* = 8.5 Hz), 3.22 (dd, *J* = 14.0, 5.8 Hz), 3.09 (dd, *J* = 14.1, 8.6 Hz), 2.59 (s), 1.24 (t, *J* = 7.1 Hz).

3.3.4. Synthesis of complex 2

Complex **2** was also synthesized according to the reported literature procedures²³. About 0.19 g (0.36 mmol) of Ru(bpy)₂Cl₂.2H₂O was dissolved in 30 mL of dry ethanol followed by the addition of ligand **L**₂ (0.15 mg, 0.35 mmol). The reaction mixture was allowed to reflux for 8 h under N₂ atmosphere with continuous stirring. Then the reaction mixture was cooled to room temperature and the solvent was removed by rotary evaporation. The Ru(II)-complex was collected by the solvent extraction method using the

dichloromethane (in presence of little CH₃CN) and water system. Minimum amount of acetonitrile (0.5 mL) was added for efficient extraction of the desired complex in the organic layer. This crude compound was subjected to the column chromatography. Silica gel was used as stationary phase and CH₃CN-aqueous saturated KPF₆ solution was used as the mobile phase. Characterization of complex **2** was carried out by using standard analytical and spectroscopic techniques. Yield: 50 % (180 mg, 0.159 mmol). ESI-HRMS m/z (%) for formula C₄₅H₄₀N₈O₃Ru, calculated 841.2183; found: 841.2184. ¹HNMR (200 MHz) δ ppm 9.19 (d, *J* = 1.2 Hz), 8.60 (s), 8.49 (d, *J* = 8.1 Hz), 8.38 (s), 8.06 (dd, *J* = 11.1, 4.6 Hz), 7.81 (d, *J* = 5.7 Hz), 7.70 (d, *J* = 5.0 Hz), 7.57 (d, *J* = 5.9 Hz), 7.52 (s), 7.39 (t, *J* = 6.5 Hz), 7.25 (s), 7.21 (d, *J* = 4.3 Hz), 7.17 (s), 7.03 - 6.89 (m), 5.03 - 4.88 (m), 4.15 (q, *J* = 7.1 Hz), 3.46 - 3.34 (m), 2.55 (s), 1.21 (t, *J* = 7.1 Hz).

3.4. Results and discussion

3.4.1. UV-Visible and fluorescence titration studies with CT-DNA

Ruthenium(II)-polypyridyl complexes have been widely studied for their ability to bind with DNA through reversible or irreversible binding interaction. Water soluble complexes **1** and **2** were obtained via their anion metathesis of their respective PF₆⁻ salts using [n-Bu₄N]Cl in acetone. Interaction of the respective complex **1** (Figure 3.2a, b) and **2** (Figure 3.2c, d) with CT-DNA was investigated using UV-Visible and fluorescence spectroscopy. Systematic titration studies (Figure 3.2a, c) revealed that addition of small aliquots of CT-DNA to the buffer solution containing **1** or **2** induce an appreciable hypochromic shift in π→π* (290 nm) and MLCT bands (450 nm) of the respective complexes. The changes in the MLCT band yield a typical saturation ligand-DNA binding curve (inset in Figures 3.2) and higher binding ratios produced no additional changes in absorption spectra.

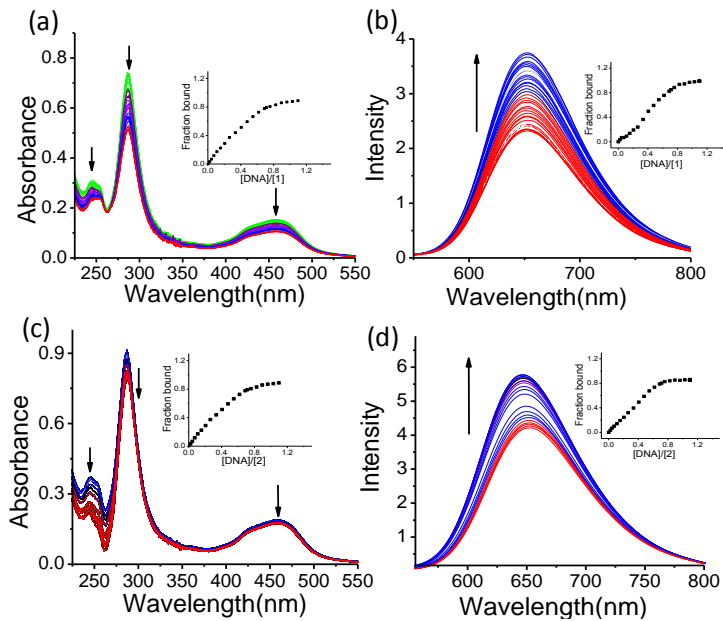


Figure 3.2. UV-Visible and fluorescence spectral changes for **1** (a, b) and **2** (c, d) by the addition of CT-DNA in Tris-HCl buffer pH = 7.4 at 25° C.

By fitting the changes in absorption at 450 nm in to the McGhee von-Hippel binding model²⁸ revealed that both complexes have a similar affinity for DNA, with equilibrium binding constants, K_b , of $3.2 \times 10^5 \text{ M}^{-1}$ and $3.3 \times 10^5 \text{ M}^{-1}$ for **2** and **4** respectively.

Table 3.1. Binding parameters obtained from UV-Visible and fluorescence titrations for **1** and **2** with CT-DNA in Tris-HCl buffer (pH = 7.4).

Titration	1		2	
	$K_b[\text{Mol}^{-1}]$	S[bp]	$K_b[\text{Mol}^{-1}]$	S[bp]
Absorbance	3.2×10^5	0.8	3.3×10^5	1.20
Fluorescence	1.6×10^5	0.6	2.1×10^5	0.75

The addition of small aliquots of CT-DNA until there was no enhancement in the emission intensity of **1** and **2** at 620 nm was observed. The fluorescence emission intensity at 620 nm was used to calculate the binding constants by fitting the data in to the same binding model used above and the values were mentioned below in Table 3.1. From fluorescence titration studies the addition of CT-DNA to the buffer solutions of **1**

and **2** leads to the enhancement in the fluorescence intensity of the respective complexes. The binding affinity K_b , and site size S , were calculated by fitting the obtained data from UV-Visible and fluorescence spectroscopic titrations in to McGhee Von-Hippel model (Table 3.1). The binding affinities obtained by absorption titrations were found to be in good agreement with those obtained by fluorescence titrations. The changes in MLCT band yield a saturation ligand–DNA binding curve (Insets in Figure 3.2 a, b, c, d) and higher binding ratios produced no additional changes in absorption and emission spectra of **1** and **2**.

3.4.2. Isothermal titration calorimetry studies with CT-DNA

To corroborate the binding parameters obtained from the UV-Vis and fluorescence titrations we have also conducted the isothermal titration calorimetry (ITC) measurements. ITC experiments were used to measure the thermodynamical parameters associated with the interaction of complexes **1**, **2** with CT-DNA (Figure 3.3). The thermographs displayed in Figure 3.3a and 3.3b indicates the interaction of **1** and **2** with CT-DNA respectively.

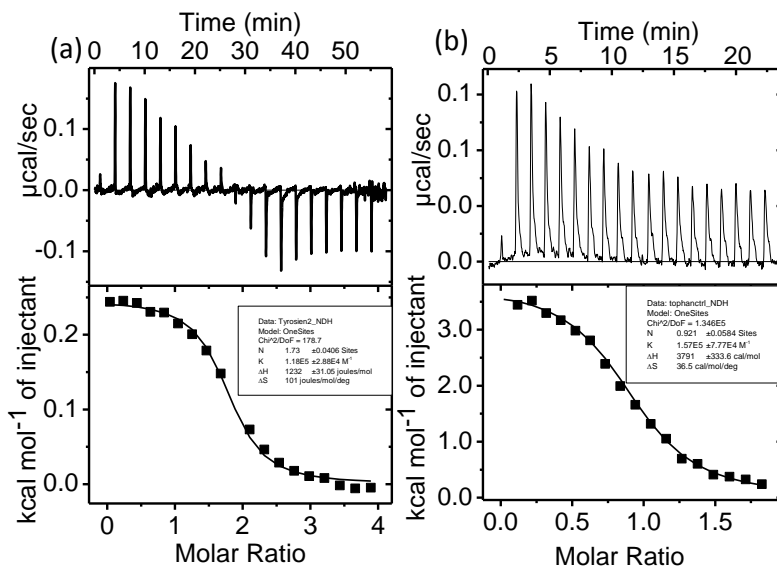


Figure 3.3. Results of the ITC studies depicting the binding profiles for the interaction of complexes **1** (a) and **2** (b) with CT-DNA in Tris-HCl buffer pH = 7.4 at 25° C.

Table 3.2. ITC derived thermodynamic parameters for the interaction of **1** and **2** with CT-DNA.

Complex	1	2
$K_b[\text{Mol}^{-1}]$	$(1.18 \pm 0.2)10^5$	$(1.57 \pm 0.7)10^5$
$\Delta H [\text{KcalMol}^{-1}]$	1.23 ± 0	3.79 ± 0.3
$T\Delta S [\text{KcalMol}^{-1}]$	2.52	10.87
$\Delta G [\text{KcalMol}^{-1}]$	-1.29	-7.087
S [bp]	1.73 ± 0	0.92 ± 0

The binding affinities for **1** ($K_b^1 = 1.18 \times 10^5$) and **2** ($K_b^2 = 1.57 \times 10^5$) towards CT-DNA were in good agreement with those obtained from VU-Visible and fluorescence titrations. Interactions of **1** and **2** were found to be enthalpically driven with small favourable entropy (Table 3.2). The best fit for the integrated heat data was obtained using a single set of identical sites model. Since, ITC and spectroscopic techniques used two different binding models to calculate the binding constant (K_b) and site size (S), one can find the slight differences in the values of K_b and S (bp).

3.4.3. Viscosity studies

To understand the mode of DNA binding of complexes **1** and **2** we have further conducted viscosity measurements in Tris-HCl buffer (pH = 7.4) at $(27 \pm 1)^\circ \text{C}$ using canon viscometer

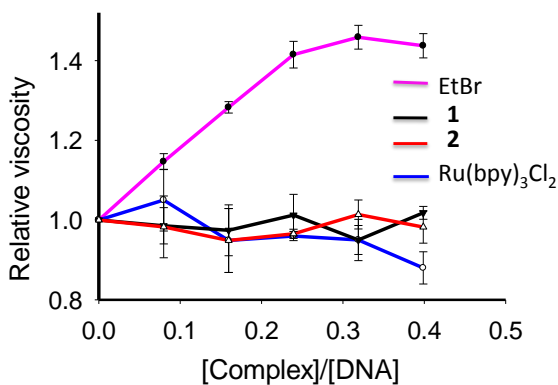


Figure 3.4. The relative viscosity changes of CT-DNA upon interaction with complex **1**, **2** ethidiumbromide and $[\text{Ru}(\text{bpy})_3\text{Cl}_2]^{2+}$ used for control purpose.

Viscosity results (Figure 3.4) confirmed that neither **1** nor **2** can alter the relative viscosities of aqueous DNA solutions indicating that these two complexes are not intercalating between the DNA base pairs. For the control purpose $[\text{Ru}(\text{bpy})_3]^{2+}$ and ethidiumbromide were used, which are known to bind CT-DNA through groove and intercalation modes respectively.^{29,30} All these observations suggested that **1** and **2** could interact with CT-DNA predominantly through groove binding. However, certain effect of the electrostatic interactions between these cationic complexes with the negatively charged phosphate backbone of the DNA cannot be completely ruled out.

3.4.4. Light induced cytotoxicity: MTT assay

Ru(II)-polypyridyl complexes are known for the generation of reactive oxygen species (ROS) upon irradiation with light source at the respective MLCT band maximum for the respective complex.

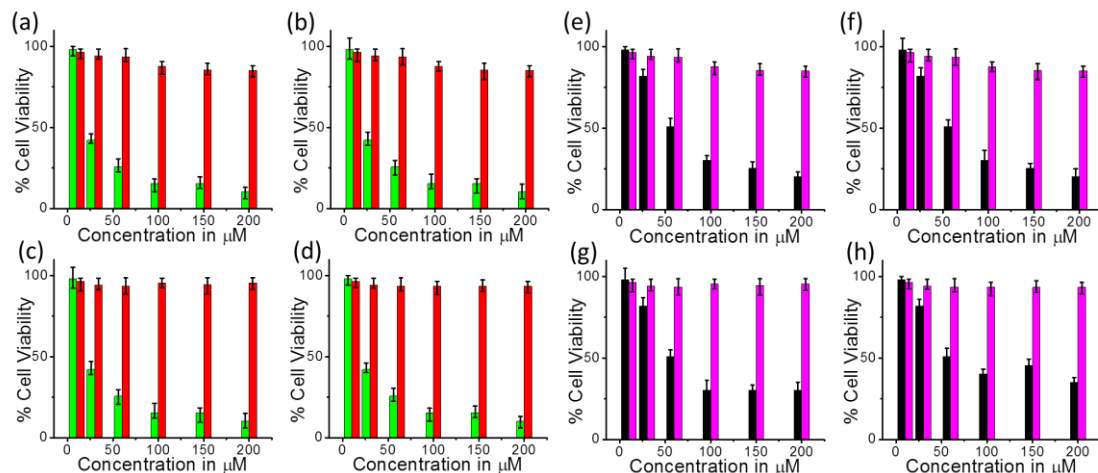


Figure 3.5. Photo-induced cytotoxicity of **1** and **2** in 2D tumors spheroids of A549, Hct116 cells (a-d) after photo-irradiation for 4 h (green bars), and in dark for 4 h (red bars). Photo-induced cytotoxicity of **1** and **2** in 3D tumors spheroids of A549, Hct116 cells (e-h) after photo-irradiation for 4 h (black bars), and in dark for 4 h (pink bars).

Accordingly, we have examined light induced cytotoxicity of complexes **1** and **2** towards the two different cancer cell lines. Live human lung cancer cells (A549) and colon cancer

cells (Hct116) were incubated with **1** and **2** for 4 h in the dark conditions for control experiments. These cells were also incubated on photo irradiation at the MLCT bands of **1** and **2** with blue LED light source ($\lambda_{\text{Range}} \sim 450 - 500$ nm having flux of 10 J/cm^2) under otherwise identical condition. The MTT assay studies revealed (Figure 3.5) that these two complexes are non-toxic in the dark conditions ($\text{IC}_{50} > 300 \mu\text{M}$). More than 85 % of the cells survived at $300 \mu\text{M}$ concentration when incubated in dark. However, upon photo irradiation for 4 h, the calculated IC_{50} values (Table. 3.3) were 25 and $28 \mu\text{M}$, respectively, for complexes **1** and **2**.

Table 3.3. IC_{50} values for the complexes **1** and **2** incubated with A549 and Hct116 2D, 3D tumor cells in the dark and upon photo-irradiation.

$\text{IC}_{50}(\mu\text{M})$	Complex 1				Complex 2			
	Dark		Light		Dark		Light	
Cell type	2D	3D	2D	3D	2D	3D	2D	3D
A549	>300	>300	28 ± 0.6	58 ± 0.2	>300	>300	25 ± 0.5	62 ± 0.4
Hct116	>300	>300	30 ± 0.4	65 ± 0.1	>300	>300	30 ± 0.2	59 ± 0.3

The >10-fold difference in light and dark IC_{50} values adds to the significance of these complexes for possible application as PDT agent. It is worth mentioning that literature reports suggest most initial drug screening is performed with two dimensional cell culture.^{10,31} A solid cancer, such as those of the breast, colon, stomach, lung and liver, is a tumour mass that is hypoxic at the centre and denser than the surrounding tissue. With recent development of tumor engineering allowed us to adopt 3D cell culture model. This 3D cell culture model performs better than the commonly used 2D models in capturing complexity of *in-vivo* processes within the tumor microenvironment and this provides a more realistic platform and physiological environment than traditional monolayer cultures

or flat biology.^{32,33} These spheroids mimic the pathophysiology of tumors, including hypoxic/necrotic regions as well as mimics the changes in cell shape, high proportions of quiescent cells, alterations in gene expression profiles, and diminished permeability to drugs.³⁴ Spheroids exhibit the phenomena of multicellular resistance (MCR), which is manifested in the diminished efficacy of chemotherapeutics similar to *in-vivo* activities.³⁵ Thus, to examine the cytotoxicity of these two photoresponsive Ru(II)-polypyridyl complexes towards such 3D tumors under more biologically relevant conditions, efficacy was examined with 3D tumor model by generating tumor spheroids with A549 and Hct116 cells. Spheroids of ca. 600 µm in diameter were dosed with compounds **1** and **2** (10 – 300 µM) and then these tumors were either kept in the dark for control experiments or were kept under photo-irradiation for 4 h with blue LED light having $\lambda_{\text{Range}} \sim 450 - 500$ nm having flux of 10 J/cm² (Figure 3.5e-h). Significant photo-induced cytotoxicity was observed for both complexes (**1** and **2**) with an IC₅₀ values two different cell lines are provided in the Table 3.3. For control experiments, where cells were kept in the dark conditions, more than 95 % of the cell survival was observed for [**1**] or [**2**] of ~ 300 µM. These data clearly revealed that both complexes are non-toxic to live A549 and Hct116 cells when incubated in dark and showed significant light induced cytotoxicity towards these cells. Further, our studies revealed that for 3D tumor models, a 2-fold increase in IC₅₀ values as compared to the two dimensional cell models.

3.4.5. DNA photo-cleavage: Gel electrophoresis studies

We had further investigated the possible mechanism of cell death caused by complexes **1** and **2**. To assess the DNA damaging ability of **1** and **2** upon photo-irradiation, we had conducted the gel electrophoresis experiment with pUC19 plasmid DNA after incubation with **1** or **2** for 4 h either in the dark conditions for control experiments or after exposing it to the irradiation to light λ source having λ_{Range} of 450-500 nm having flux of 10 J/cm². To

understand the possible role of reactive oxygen species (ROS) for causing cell deaths, extent of DNA damage caused by complexes **1** and **2** on irradiation was studied in detail. pUC19 plasmid DNA (40 µg/mL) was incubated with complexes **1** or **2** (25 or 50 µM) and irradiated for 4 h with light (blue LED light having $\lambda \geq 450$ nm with flux of 10 J/cm²).

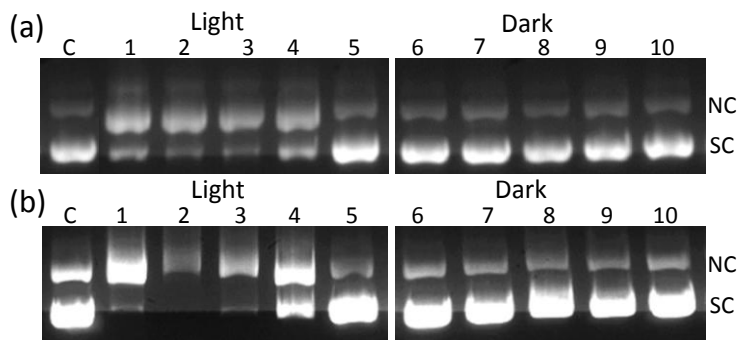


Figure 3.6. Electrophoresis in agarose gel of pUC19 plasmid DNA with **1**(a) and **2** (b) following photo-irradiation for 4 h (lanes 1-5) and incubation in the dark conditions for 4 h (lanes 6-10) in presence of different inhibitors. Lane C: Control plasmid DNA, lane 1: DNA with **1** or **2** (50 µM), lane 2: DNA with **1** or **2** (100 µM), lane 3: DNA with **1** or **2** (100 µM) in presence of D₂O, lane 4: DNA with **1** or **2** (100 µM) in presence of DMSO, Lane 5: DNA with **1** or **2** (100 µM) in presence of NaN₃. In all cases [DNA] = 40 µg/mL, [NaN₃] = 100 mM, [D₂O] = 100 mM, [DMSO] = 200 mM; Lanes 6-10 represents the samples incubated in dark with same experimental conditions followed for lanes 1-3.

Images of the electrophoresis studies in agarose gel of pUC19 plasmid DNA (Figure 3.6) clearly revealed that the DNA cleavage had occurred when plasmid DNA samples were photo-irradiated. Results of the control experiments performed in the dark conditions revealed that no such DNA cleavage had actually occurred. It is well documented in the literature that Ru(II)-polypyridyl complexes are capable of converting water or molecular oxygen in to the respective ROS species (OH[·] or ¹O₂) following an energy transfer process involving their ³MLCT state.^{36,37,38} To understand which one of these two ROS is responsible for the observed pUC19 plasmid DNA cleavage for the present study, control experiments were performed after incubating the plasmid DNA with 50 µM of **1**

(Figure 3.6a) or **2** (Figure 3.6b) along with DMSO (scavenge OH[•] radical) or D₂O (enhances the ¹O₂ lifetime) or NaN₃ (¹O₂ quencher) under photo-irradiation condition for 4 h. These reaction mixtures were subjected to agarose gel electrophoresis (Lanes 1-5, Figure 3.6a for complex **1**; Figure 3.6b for complex **2**). Simultaneous control experiments were performed after incubation in dark for 4 h under otherwise identical experimental conditions (Lanes 6-10, Figure 3.6b for complex **1**, Figure 3.6b for complex **2**). It is evident from Figure 3.6 that pUC19 plasmid DNA on incubation with complex **1** or **2** under irradiation is converted from supercoiled (SC) to nicked circular (NC) DNA. But no such NC form of DNA is observed when samples are incubated with complex **1** or **2** in dark. For experiments that were performed in presence of D₂O, a distinct increase in the SC to NC (lane 3) forms was observed. For experiments that were performed after incubation with DMSO, the pattern of the damage to the plasmid remained unchanged (lane 4). All these tend to confirm that ¹O₂ and not OH[•] is generated in-situ as the ROS on irradiation of Ru(II)-polypyridyl complex **1** or **2** under the experimental conditions that were used for our studies. In order to further confirm this, the samples were co-incubated with NaN₃, which was known to be an efficient scavenger for ¹O₂ (lane 5). It is evident from Figure 3.6 that the presence of NaN₃ results in the inhibition of conversion of SC into NC. Thus, gel electrophoresis results clearly reveal that both **1** and **2** are highly efficient in damaging the plasmid DNA in presence of light through in-situ generation of ¹O₂ as ROS. Results of the control experiments also confirm that these two complexes fail to generate any ROS in the dark condition and are thus inactive for DNA damage. These results are encouraging for developing highly efficient photodynamic therapeutic agents.

3.4.6. Single-Cell Gelelectrophoresis (SCGE) or Comet assay

Over the past two decades, the single-cell gel electrophoresis (SCGE), or comet assay has become the standard and widely used method for measuring DNA damage at cellular level, with applications in genotoxicity testing, human biomonitoring and molecular epidemiology, ecogenotoxicology, as well as fundamental research in DNA damage and repair.³⁹

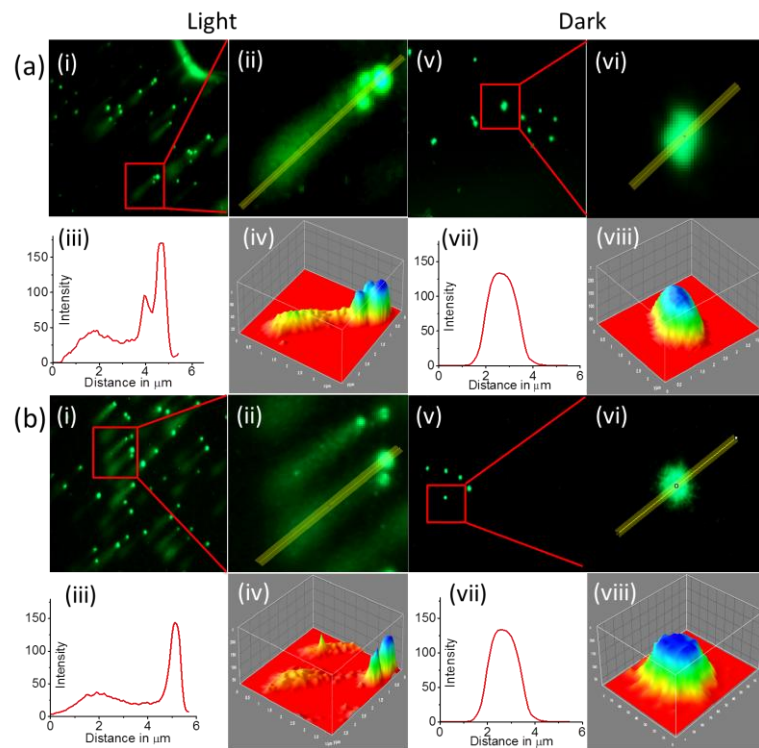


Figure 3.7. Comet images of A549 cells treated with **1** (a) and **2** (b) under photo-irradiation (left) in the dark (right) conditions.

The comet assay works based on the lysis of cells with non-ionic detergent like triton-X and high-molarity sodium chloride. This treatment removes cell membranes, cytoplasm, and nucleoplasm, and disrupts nucleosomes, most of the histones being solubilized by the alkali solution.⁴⁰ In this report, we have treated A549 cells with **1** (30 μ M) and **2** (30 μ M) following photo-irradiation (Figure 3.7a i-iv, 37b i-iv) and kept in the dark conditions (Figure 3.7a, 37b). Then the cells were embedded in low melting agarose (0.5%) on a

microscope comet slide pre-coated with 1% normal melting agarose. The cell lyses with detergent and treatment with alkali solution produced unwind and denatured single stranded DNA containing supercoiled loops linked to the nuclear matrix. The electrophoresis of the comet slid containing cells treated with **1** in presence of light resulted in the cleavage of the DNA (Figure 3.7a, i-iv); But no cleavage was observed in the case of cells treated with **1** in absence of light (Figure 3.7a, v-viii). Similar kind of results were anticipated and also observed in the case of complex **2** (Figure 3.7b i-iv, photo-irradiated cells and Figure 3.7b v-viii, cells in the dark). The results in structures resembling comets, observed by fluorescence microscopy; the intensity of the comet tail relative to the head reflects the number of DNA breaks. The likely basis for this is that loops containing a break lose their supercoiling and become free to extend toward the anode. SYBR green was used to visualize the DNA by exposing to UV light. The increasing the longer and darker the comet tail is direct evidence for the amount of DNA damage. From Figure 3.7a (iii, viii), the fluorescence intensity profile plots for **1** and Figure 3.7b iii, viii for **2** indicating that the DNA damage on the tail was more compared with heads of the comets.

3.4.7. Evaluation of $^1\text{O}_2$ production ability of **1** and **2**

To measure the quantum yields of $^1\text{O}_2$ generation by complexes **1** and **2** we utilized the *N,N*-Dimethyl-4-nitrosoaniline/imidazole (RNO) assay. The production of $^1\text{O}_2$ by **1** and **2** was monitored and quantified by indirect method in both acetonitrile and water (Figure 3.8). *N,N*-Dimethyl-4-nitrosoaniline/imidazole assay that works based on the reaction of singlet oxygen with imidazole to form tetrannular species that eventually quenches the absorbance of the RNO at 440 nm. Due to the limited solubility of histidine in acetonitrile, imidazole was used for quenching the absorbance of the RNO. The singlet oxygen quantum yields for **1** and **2** were calculated by monitoring the emission intensity of

phenalenone at 440 nm. Phenalenone used as standard in both the solvents acetonitrile and water (Table 3.4).

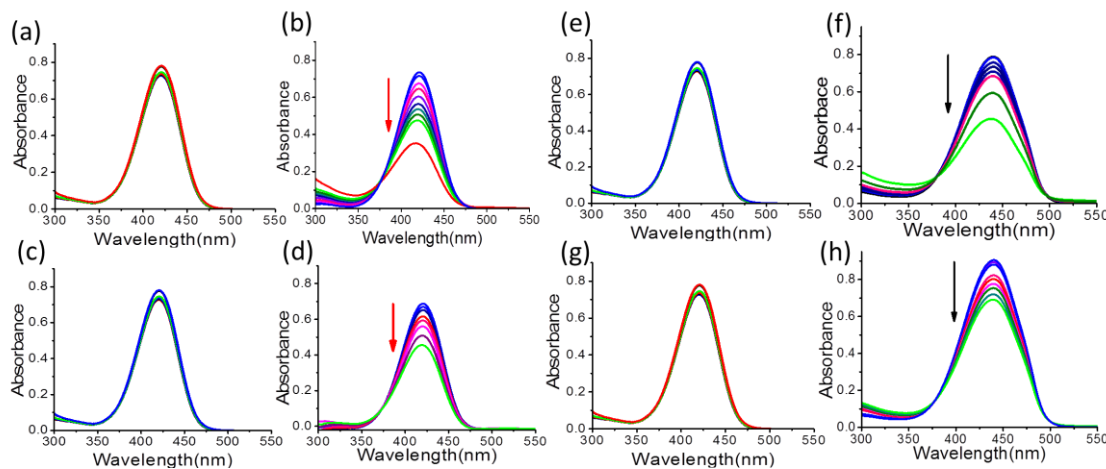


Figure 3.8. Detection of ${}^1\text{O}_2$ generated in acetonitrile by **1** (a, b, e, f) and **2** (c, d, g, h) by RNO assay.

Table 3.4. Singlet oxygen quantum yield for complex **1**, **2** and $[\text{Ru}(\text{bpy})_2(\text{dmbpy})]^{2+}$.

Complex	Water	Acetonitrile
1	0.20	0.80
2	0.25	0.72
$[\text{Ru}(\text{bpy})_2(\text{dmbpy})]^{2+}$	0.32	0.57

The nature of the solvent has greatly affected the ${}^1\text{O}_2$ quantum yields produced by **1**, **2** and $[\text{Ru}(\text{bpy})_2(\text{dmbpy})]^{2+}$. The ${}^1\text{O}_2$ quantum yields were calculated using the following equation 6. Phenalenone a universal reference compound for the determination of singlet oxygen quantum yield was used as a standard.²⁷

$$\phi_{\text{Sample}} = \phi_{\text{reference}} \frac{S_{\text{sample}}}{S_{\text{reference}}} \frac{I_{\text{reference}}}{I_{\text{sample}}} \quad \text{Equation 6}$$

where, S is the slope of the absorption vs. time and I is the rate of absorption which was calculated using the formula $I = 1 - 10^{(-OD)}$ (OD is the absorbance at 440 nm).⁴¹

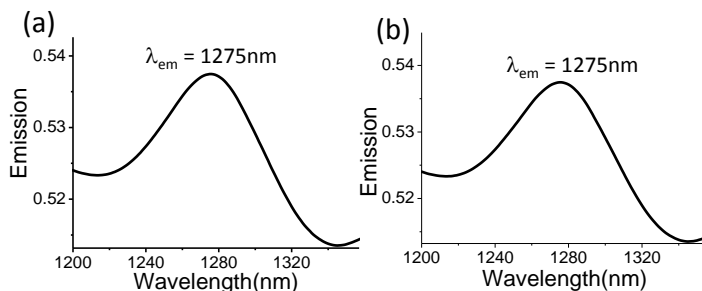


Figure 3.9. Phosphorescence emission spectra of $^1\text{O}_2$ produced by the complex **1** (a) and **2** (b).

Literature reports reveal that the phosphorescence band for $^1\text{O}_2$ appears in the NIR region at 1275 nm.⁴² Steady state luminescence studies with photo-irradiated ($\lambda_{\text{Range}} \sim 450\text{-}500\text{ nm}$ having flux of 10 J/cm^2) aq. buffer sample of **1** or **2** showed a distinct phosphorescence band at 1275 nm, which further confirmed the generation of $^1\text{O}_2$.

3.4.8. Cellular uptake and confocal imaging studies

Since **1** and **2** displayed significant photo-cytotoxicity towards A549 and Hct116 cancer cell lines, we have further conducted the confocal laser scanning microscopy (CLSM) studies to identify the cellular accumulation of these photo-cytotoxic complexes. The live cell imaging studies were conducted by incubating the **1** and **2** with A549 (Figure 3.10a, b) cells for 4 h at 37° C. The co-localization studies were performed using the commercially available lysotracker green. The close comparison of the CLSM images as well as the images of the co-staining experiments with lysotracker staining agent clearly revealed that intracellular emission for **1** and **2** was found that they are not superimposed with lysotracker green. The distinct emission of **1** and **2** was observed from the cell nucleus as well as in the cell membrane (Figure 3.10c) indicating that these two lipophilic complexes have been distributed throughout the cell. The literature reports also reveal that more lipophilic cationic reagents are generally accumulated preferentially in the regions like cell membrane while analogous reagents having

comparable overall charge and relatively low lipophilicity would have preference for nuclei.^{43,44} The dimethyl substituted $[\text{Ru}(\text{bpy})_2(\text{dmbpy})]^{2+}$ complex showed a dot-like structure on the cell membrane (which was previously reported by our group)³⁰ with red fluorescence in bright-field microscopy, a pattern that was observed earlier for localization of lipophilic reagents at the cell membrane.^{45,30}

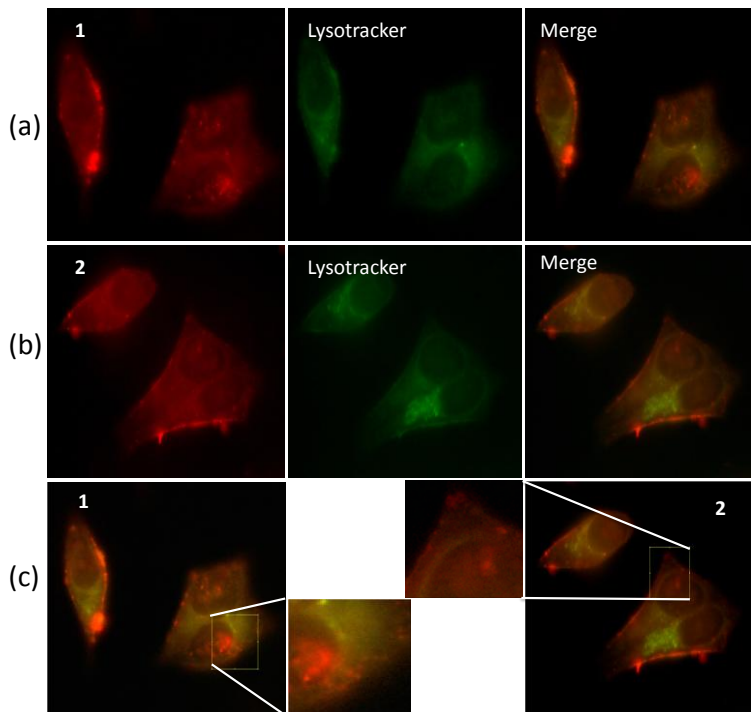


Figure 3.10. CLSM images of A549 cells incubated with **1** (a) and **2** (b) for 4 h at 37° C. The co-localization studies performed with lysotracker green. The enlarged CLSM images of A549 cells incubated with reagents **1** and **2** (c).

From Figure 3.10c the enlarged confocal microscopy images revealed that unlike the parent control dimethyl substituted complex $[\text{Ru}(\text{bpy})_2(\text{dmbpy})]^{2+}$ the reagents **1** and **2** were evenly localized in the cell nucleus, membrane as well as some part of the cytoplasm. This may be attributed due to the conjugation of highly lipophilic tyrosine and tryptophan ligands. Such dot like structures scattered in the cytoplasm presumably suggested that the reagents were also distributed in cytoplasmic vacuoles, which are known to play a subordinate role in endocytosis.^{46,47}

3.4.9. Partition coefficient logP measurement

The partition coefficient (logP) values were calculated using shake-flask method to determine the lipophilicity of **1** and **2**. From Table 3.5 data clearly revealed that the lipophilicity of complex **1** (logP = -1.31) is higher than **2** (logP = -1.72). This experiment also proves that the conjugation of amino acids i.e., tyrosine and the tryptophan to basic structural unit dimethyl substituted $[\text{Ru}(\text{bpy})_2(\text{dmbpy})]^{2+}$ (logP = -1.01) have certainly effected the logP values of the final complexes **1** and **2**.

Table 3.5 Lipophilicity (logP) values obtained for **1**, **2** and $[\text{Ru}(\text{bpy})_2(\text{dmbpy})]^{2+}$ using shake-flask method.³⁰

Complex	LogP	Ru accumulation in ppm/1 $\times 10^6$ cells by MP-AES	
		Light	Dark
1	-1.31 \pm 0.2	0.81 ppm	0.18 ppm
2	-1.72 \pm 0.5	0.54 ppm	0.11 ppm
$[\text{Ru}(\text{bpy})_2(\text{dmbpy})]^{2+}$	-1.01 \pm 0.1	0.98 ppm	0.19 ppm

From the literature reports it has been debated by many research groups that the lipophilicity of a reagent is the most important property than overall charge that influence the cellular internalization process. In our present study the lipophilicity of all three complexes were followed the order $[\text{Ru}(\text{bpy})_2(\text{dmbpy})]^{2+} > \mathbf{1} > \mathbf{2}$. Thus, cellular internalization would presumably follow the order $[\text{Ru}(\text{bpy})_2(\text{dmbpy})]^{2+} \mathbf{1} > \mathbf{2}$. This was further confirmed by the results obtained from MP-AES (Microwave Plasma Atomic Emission Spectroscopy) studies (Table 3.5). As it was assumed that the order of cellular uptake of complexes was followed $[\text{Ru}(\text{bpy})_2(\text{dmbpy})]^{2+} > \mathbf{1} > \mathbf{2}$. These results are in good agreement with the lipophilicity of all three complexes.

3.4.10. Anti-metastatic activity test

The results obtained from the MTT assay and gel electrophoresis, it is evident that these two complexes have high potential for killing the cancer cells. We have further conducted an anti-metastatic experiment in MDA-MB231 cells in which the cell metastatic rate is high to test their anti-metastatic activity. Complexes **1** and **2** were incubated with MDA-MB231 cells in the dark conditions as well as photo-irradiated with blue light ($\lambda = > 450$ nm). A wound was pre-created using wound creating stick before the addition of Ru(II) complexes.

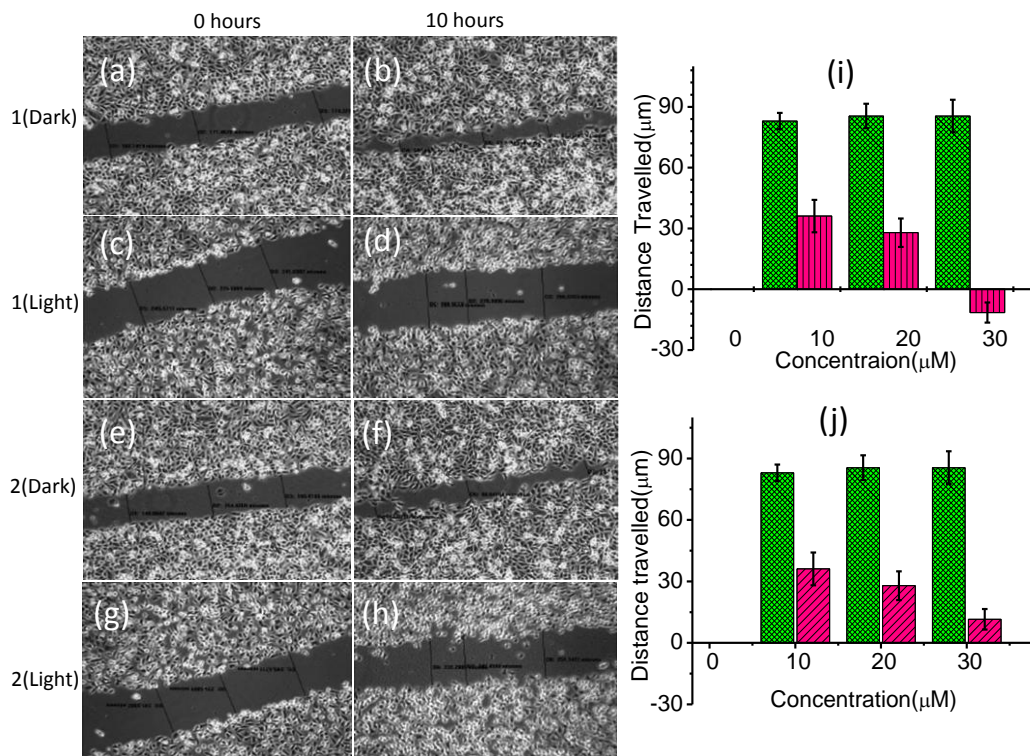


Figure 3.11. Anti-metastatic activity of complex **1** (a-d), and **2** (e-h) tested on MDA-MB231 cells. The distance travelled by MDA-MB231 cells was measured in micrometers upon incubation with various concentrations (7.5, 15, 28 μ M) of **1** (i) and **2** (j) in the dark (green bars) and photo-irradiation conditions (pink bars).

The cells were allowed to metastasize for 10 h. The bright-field images were captured at different time intervals. From the Figure 3.11 the photo-induced anti-metastatic activity of the **1** (Figure 3.11a-d) and **2** (Figure 3.11e-h) can be observed after photo-irradiation for

4 h. The wound was completely healed after 10 h in the dark conditions (Figure 3.11b); however, when the cell cultures were photo-irradiated with blue LED ($\lambda = > 450$ nm) for 4 h, the cells stopped migrating and started dying (Figure 3.11d, and 311h for **1** and **2** respectively). Distance travelled by cells were calculated and plotted a graph (Figure 3.11i for **1** and 3.11j for **2**) which indicated that with respect to the increasing concentration of complexes, the migration of cells were decreased and ultimately leads to cell death. This results concluded that these two Ru(II) complexes induces the greater photo-cytotoxicity by inhibiting cell migration.

3.4.11. Invasion assay

One of the hallmarks of cancers is cell invasions and metastasis into nearby and distal organs initiated by various protein de-regulations. Highly metastatic cells lose cell to cell adherence and break off. This invades basement membrane and endothelial walls to enter the blood stream or lymph nodes.

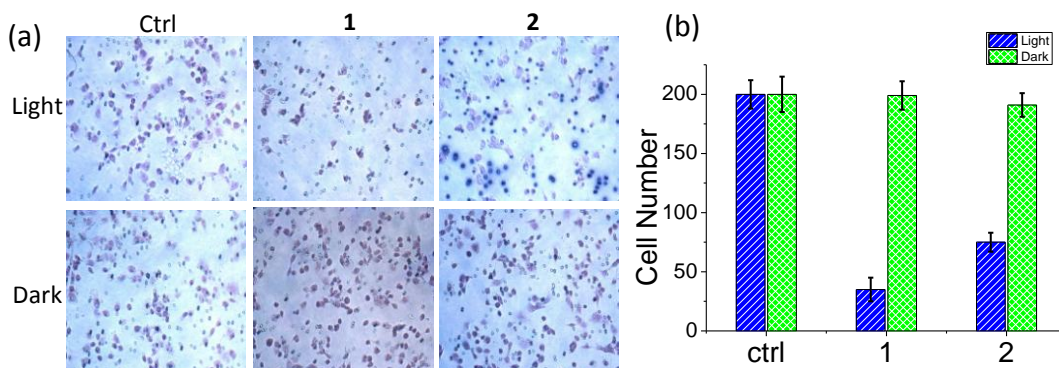


Figure 3.12. (a) Effect of **1** and **2** on MDA-MB231 cell invasion, (b) The percentage of cells invaded was reduced to 17.5 % with **1** and 37.5 % with **2** in the presence of light (blue bars). However there was no change in the dark controls (green bars).

The cells are then carried away to distal organs and gets deposited forming primary metastasis. The tumor forming cells still possess the characteristics to invade and settle into other organs to form tumors giving rise to secondary metastasis. Therefore, invasion

and metastasis needs to be controlled to prevent cancers from spreading throughout the human body. To assess the potential of **1** and **2** in controlling the cell invasion we further incubated them with highly metastatic live MDA-MB231 cells on top of matrigel (Figure 3.12a) and allowed the cell to invade in the presence and absence of visible light. Figure 3.12b clearly reveals that considering the 100 % cells invaded in case of control experiment the percentage of cells invaded through matrigel was drastically reduced by complexes **1** (17.5 %) and **2** (37.5 %). This experiment also revealed that the complex **1** can prevent the cells from invasion more efficiently than complex **2**.

3.4.12. Cell cycle analysis studies

In order to investigate the possible effect of **1** and **2** on cell cycle progression, the A549 cells were treated with **1** and **2** for 4 h in dark and in presence of light (> 450 nm). Cell cycle analysis studies were conducted using flow cytometry. The cell cycle distribution after treating with **1** and **2** at 30 μ M for 4 h in the dark (Figure 3.13) does not have any effect on cell cycle progression.

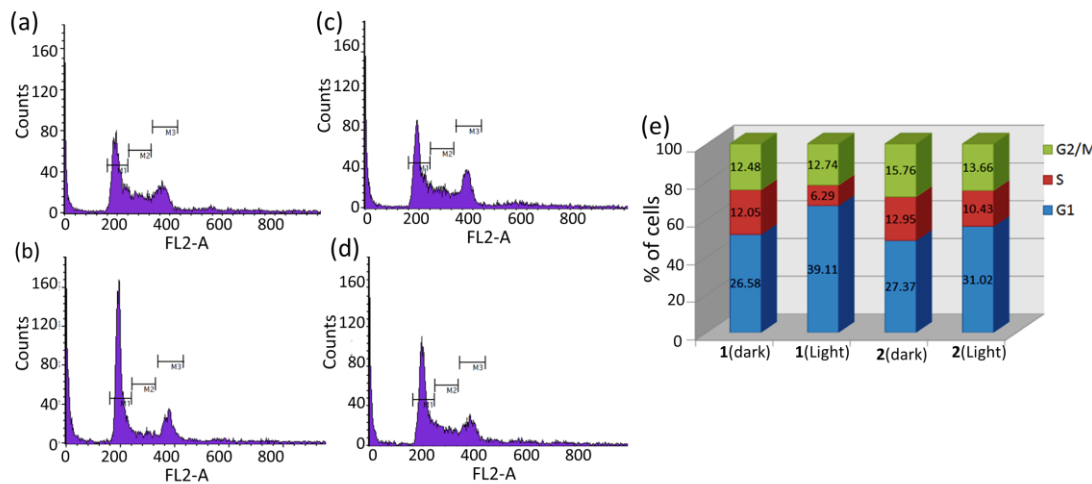


Figure 3.13. The cell cycle analysis of A549 cells treated with **1** and **2** in the dark conditions (a, c) and after photo-irradiation (b, d). The graphical representation, (e) of the cell cycle distribution in A549 cells up on treatment at the IC₅₀ values of **1** and **2**.

However, when exposed to light the percentage of cells at G0/G1 phase showed an

evident increase of 12.53 % and 3.65 % for complex **1** and **2** at their IC₅₀ concentrations (~30 µM) which was accompanied by a corresponding reduction in the percentage of cells in S and G2/M phases. Obviously, **1** caused more pronounced changes in cell cycle than **2** in G0/G1 phases under identical conditions. Hence we conclude that the anti-proliferative mechanism induced by complexes **1** and **2** on A549 cells was G0/G1 phase arrest.

3.4.13. Complex **1** and **2** induces apoptosis by caspase-3 and caspase-9 activation

We next set out to elucidate the molecular mechanism responsible for light induced cell death by complexes **1** or **2**. Cell cycle checkpoints modulate DNA damage and/or genome integrity responses by controlling the timing of cell cycle progression, and it is not easy in univariate cytometric analyses to clearly distinguish between cells arrested in G1 or in early S phase. This led us to examine whether light induced cell cycle arrest occurs through the activation of DNA damage signalling pathways. For this, A549 cells were treated with complex **1** or **2** in dark or under light irradiation.

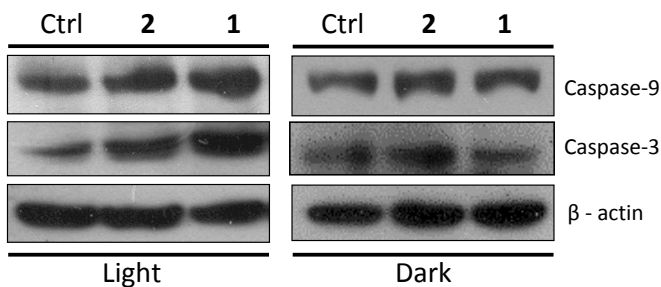


Figure 3.14. A549 cells growing in serum-containing medium were treated with **1** and **2** for 24 h prior to lysate preparation and immunoblotting with antibodies. The blot was probed with primary antibodies against caspase-3, caspase-9. β-actin levels were used as a loading control. All results are representative of two independent experiments.

It was found that there was a significant increase in the expression level of apoptosis markers caspase-9 and caspase-3 in photo-irradiated cells (Figure 3.14). Whereas in the dark treated samples there was no difference in the expression level of caspase-3

and caspase-9. This indicated that compound **1** and **2** with photo-irradiation resulted apoptosis of the A549 cells. As discussed earlier, exposure to visible light for cells incubated with **1** or **2** resulted in the generation of ROS (${}^1\text{O}_2$). The ${}^1\text{O}_2$ is known to damage the DNA and are also responsible for altering the mitochondrial trans membrane potential. Literature reports reveal that the pro-apoptotic proteins, released from mitochondria, are responsible for activation of caspase-3 and caspase-9 and the cell finally leads to apoptosis. Thus, these photoactive compounds could be used for treatment of solid tumors by specifically illuminating in the visible light which would not cause any ROS production in the dark condition.

3.5. Conclusions

Two Ru(II)-polypyridyl complexes conjugated with amino acids tyrosine (**1**) and tryptophan (**2**) was investigated for their potential application as photodynamic therapeutic (PDT) agents. Complexes **1** and **2** showed preferential binding toward CT-DNA with moderately strong binding affinity $K_b = 1.5 \times 10^5 \text{ mol}^{-1}$. Isothermal titration calorimetry (ITC) studies indicate that the reactions of both **1** and **2** with CT-DNA were driven by the endothermic process. Viscosity study proved that **1** and **2** binds CT-DNA through groove binding mode. Most importantly, complexes **1** and **2** exhibits light induced cytotoxicity in the presence of visible light ($\lambda = 450 \text{ nm}, 10 \text{ J/cm}^2$) with less exposure times and found to be non-toxic in the dark conditions (the key feature required by the PDT agents). Gel electrophoresis and comet assay results indicated the DNA damaging capability of these photo active molecules. The invasion assay and wound healing experiments proved that these compounds can inhibit the cells travelling through the tissues. These visible light excitable Ru(II) complexes are showed anti-metastatic activity, and produced ${}^1\text{O}_2$, which damages the DNA upon photo-irradiation.

3.6. References

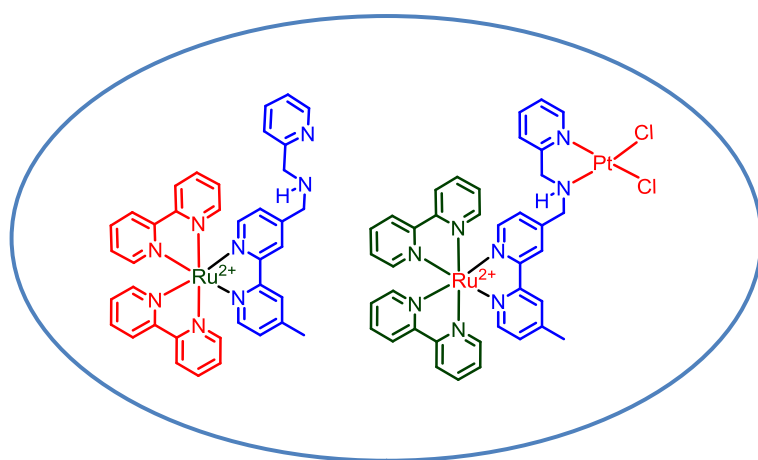
1. M. Ethirajan, Y. Chen, P. Joshi and R. K. Pandey, *Chem. Soc. Rev.*, 2011, **40**, 340–362.
2. Y. Y. Zhao, Baozhong, *Expert Rev Anticancer Ther.*, 2010, **10**, 1797–1809.
3. Z. Huang, *Technol. Cancer Res. Treat.*, 2005, **4**, 283–293.
4. H. K. Hiedki Yamamoto, Testuya Okunaka, Kinya Furukawa, Toshimitsu Hiyoshi and C. Konaka, *Curr. Sci.*, 1999, **77**, 894–903.
5. S. Valastyan and R. A. Weinberg, *Cell*, 2011, **147**, 275–292.
6. W. Cao, W. Zheng and T. Chen, *Sci. Rep.*, 2015, **5**, 9157–9167.
7. C. Mari, V. Pierroz, S. Ferrari and G. Gasser, *Chem. Sci.*, 2015, **6**, 2660–2686.
8. P. Q. Dougherty T., Gomer C., Henderson B., Jori G., Kessel D., Korbelik M., Moan J., *J Natl Cancer Inst*, 1998, **12**, 889–905.
9. N. Narayanaswamy, M. Kumar, S. Das, R. Sharma, P. K. Samanta, S. K. Pati, S. K. Dhar, T. K. Kundu and T. Govindaraju, *Sci. Rep.*, 2014, **4**, 6476–6482.
10. J. Liu, Y. Chen, G. Li, P. Zhang, C. Jin, L. Zeng, L. Ji and H. Chao, *Biomaterials*, 2015, **56**, 140–153.
11. F. Schmitt, P. Govindaswamy, G. Süss-Fink, H. A. Wee, P. J. Dyson, L. Juillerat-Jeanneret and B. Therrien, *J. Med. Chem.*, 2008, **51**, 1811–1816.
12. T. Gianferrara, A. Bergamo, I. Bratsos, B. Milani, C. Spagnul, G. Sava and E. Alessio, *J. Med. Chem.*, 2010, **53**, 4678–4690.
13. F. Schmitt, P. Govindaswamy, O. Zava, G. Süss-Fink, L. Juillerat-Jeanneret and B. Therrien, *J. Biol. Inorg. Chem.*, 2009, **14**, 101–109.
14. C. Mari, V. Pierroz, R. Rubbiani, M. Patra, J. Hess, B. Spingler, L. Oehninger, J. Schur, I. Ott, L. Salassa, S. Ferrari and G. Gasser, *Chemistry*, 2014, **20**, 1–17.
15. M. Dickerson, Y. Sun, B. Howerton and E. C. Glazer, *Inorg. Chem.*, 2014, **53**, 10370–10377.
16. M. Liu, Z. J. Lim, Y. Y. Gwee, A. Levina and P. A. Lay, *Angew. Chemie - Int. Ed.*, 2010, **49**, 1661–1664.
17. A. D. Ostrowski and P. C. Ford, *Dalt. Trans.*, 2009, 10660–10669.
18. S. W. Botchway, M. Charnley, J. W. Haycock, A. W. Parker, D. L. Rochester, J. A. Weinstein and J. A. G. Williams, *Proc. Natl. Acad. Sci.*, 2008, **105**, 16071–16076.
19. V. Fernández-Moreira, F. L. Thorp-Greenwood and M. P. Coogan, *Chem. Commun.*, 2010, **46**, 186–202.
20. R. G. Balasingham, M. P. Coogan and F. L. Thorp-Greenwood, *Dalton Trans.*,

- 2011, **40**, 11663–11674.
21. L. Blackmore, R. Moriarty, C. Dolan, K. Adamson, R. J. Forster, M. Devocelle and T. E. Keyes, *Chem. Commun.*, 2013, **49**, 2658–2660.
 22. M. Sjödin, S. Styring, B. Åkermark, L. Sun and L. Hammarström, *J. Am. Chem. Soc.*, 2000, **122**, 3932–3936.
 23. M. Sjödin, S. Styring, H. Wolpher, Y. Xu, L. Sun and L. Hammarström, *J. Am. Chem. Soc.*, 2005, **127**, 3855–3863.
 24. D. R. Robinson, Y.-M. Wu and S.-F. Lin, *Oncogene*, 2000, **19**, 5548–5557.
 25. R. Ghanem, Y. Xu, J. Pan, T. Hoffmann, J. Andersson, T. Polívka, T. Pascher, S. Styring, L. Sun and V. Sundström, *Inorg. Chem.*, 2002, **41**, 6258–6266.
 26. N. R. Smalheiser, W. Zhou and V. I. Torvik, *J. Biomed. Discov. Collab.*, 2008, **3**, 1–10.
 27. R. Schmidt, C. Tanielian, R. Dunsbach and C. Wolff, *J. Photochem. Photobiol. A Chem.*, 1994, **79**, 11–17.
 28. A. Ghosh, A. Mandoli, D. K. Kumar, N. S. Yadav, T. Ghosh, B. Jha, J. A. Thomas and A. Das, *Dalt. Trans.*, 2009, **42**, 9312–9321.
 29. V. Ramu, M. R. Gill, P. J. Jarman, D. Turton, J. A. Thomas, A. Das and C. Smythe, *Chem. - A Eur. J.*, 2015, **21**, 9185–9197.
 30. V. Ramu, F. Ali, N. Taye, B. Garai, A. Alam, S. Chattopadhyay and A. Das, *J. Mater. Chem. B.*, 2015, **3**, 7177–7185.
 31. H. L. Ma, Q. Jiang, S. Han, Y. Wu, J. C. Tomshine, D. Wang, Y. Gan, G. Zou and X. J. Liang, *Mol. Imaging*, 2012, **11**, 487–498.
 32. S. M. Ehsan, K. M. Welch-reardon, M. L. Waterman, C. W. Christopher, S. C. George and M. Genetics, *Integr. Biol.*, 2015, **6**, 603–610.
 33. K. M. Yamada and E. Cukierman, *Cell*, 2007, **130**, 601–610.
 34. A. Abbott, *Nature*, 2003, **424**, 870–872.
 35. B. S. Howerton, D. K. Heidary and E. C. Glazer, *J. Am. Chem. Soc.*, 2012, **134**, 8324–8327.
 36. J. D. Knoll, B. A. Albani and C. Turro, *Acc. Chem. Res.*, 2015, **48**, 2280–2287.
 37. M. Stephenson, C. Reichardt, M. Pinto, M. Wa, T. Sainuddin, G. Shi, H. Yin, S. Monro, E. Sampson, B. Dietzek and S. A. Mcfarland, *J. Phys. Chem. A*, 2014, **118**, 10507–10521.
 38. M. C. DeRosa and R. J. Crutchley, *Coord. Chem. Rev.*, 2002, **233-234**, 351–371.
 39. A. R. Collins, *Mol. Biotechnol.*, 2004, **26**, 249–261.

40. A. P. De Lima, F. De Castro Pereira, C. A. S. T. Vilanova-Costa, A. De Santana Braga Barbosa Ribeiro, L. A. Pavanin, W. B. Dos Santos and E. De Paula Silveira-Lacerda, *J. Biosci.*, 2010, **35**, 371–378.
41. P. Majumdar, X. Yuan, S. Li, B. Le Guennic, J. Ma, C. Zhang, D. Jacquemin and J. Zhao, *J. Mater. Chem. B*, 2014, **2**, 2838–2850.
42. A. Leonidova, V. Pierroz, R. Rubbiani, J. Heier, S. Ferrari and G. Gasser, *Dalt. Trans.*, 2014, **43**, 4287–4294.
43. E. Baggaley, M. R. Gill, N. H. Green, D. Turton, I. V. Sazanovich, S. W. Botchway, C. Smythe, J. W. Haycock, J. A. Weinstein and J. A. Thomas, *Angew. Chemie Int. Ed.*, 2014, **53**, 3367–3371.
44. M. R. Gill, J. Garcia-Lara, S. J. Foster, C. Smythe, G. Battaglia and J. A. Thomas, *Nat. Chem.*, 2009, **1**, 662–667.
45. N. Zhang, Y. Yin, S. J. Xu and W. S. Chen, *Molecules*, 2008, **13**, 1551–1569.
46. O. Zava, S. M. Zakeeruddin, C. Danelon, H. Vogel, M. Gratzel and P. J. Dyson, *ChemBioChem*, 2009, **10**, 1796–1800.
47. F. R. Svensson, M. Matson, M. Li and P. Lincoln, *Biophys. Chem.*, 2010, **149**, 102–106.

CHAPTER 4

Synthesis, Characterization and DNA Interaction Studies of Heterodinuclear Ru(II)–Pt(II)-bipyridyl Complex



[Publication](#)
Manuscript to be communicated

4.1. Introduction

The major limitation of the Ru(II)-terpyridine complexes, discussed in chapter 2, was the short lived excited state of the Ru(II)-terpyridine center. This accounted for a faster deactivation and lower efficiency for generation of the active $^1\text{O}_2$.¹ Terpyridine based Ru(II) complexes generally have small energy gap between the emissive $^3\text{MLCT}$ state and the ^3MC state (Figure 4.1),² which consequently accounts for a faster deactivation through ^3MC state. To get around this problem, we have synthesized the 2,2'-bipyridine analogue of the earlier reported version of the terpyridine derivative. Synthesis, physicochemical as well as its DNA binding properties and cytotoxicity activity are reported in this chapter 4. From the Figure 4.1 it can be seen that in the absence of an external quencher, the decay from the $^3\text{MLCT}$ state mainly occurs via non-radiative decay to the ground state or via thermal activation to higher lying excited states, i.e. metal-centered triplet states (^3MC) or higher MLCT states.^{3–5} This higher MLCT state is believed to be more singlet in character and is therefore, more short-lived than the lowest $^3\text{MLCT}$ state. It was reported to be between 400 and 1000 cm^{-1} higher in energy than the lowest excited state. Depending on the energy difference between and ordering of the $^3\text{MLCT}$ and ^3MC states, the thermal activation can either result in the establishment of equilibrium between the lowest $^3\text{MLCT}$ state and a higher state, or irreversible thermal activation leading to decay through the ^3MC state. Once in the ^3MC state the non-radiative decay is typically very fast due to large structural distortion with respect to the ground state. This is a prominent deactivation pathway for many excited Ru(II)-polypyridyl complexes. If the energy gap between the emissive $^3\text{MLCT}$ state and the ^3MC state is small, this will consequently decrease the observed excited state lifetime significantly.² The excited state lifetime of Ru(II) complexes mainly dependent on the radiative and non-radiative rate constants as given by equation 8.

$$\tau = 1 / [K^o + K^{o'} \exp(-E_a/RT)]$$

Equation 8

Where $K^o = K_r + K_{nr}$ (sum of radiative (k_r) and non-radiative (k_{nr}) process). Since $[\text{Ru(tpy)}_2]^{2+}$ complexes are weakly emitting, the non-radiative decay constant is more important than radiative rate constant. The two major pathways for non-radiative decay are as follows.

- (i) Direct contribution from ${}^3\text{MLCT}$ to ground state,
- (ii) Through thermally accessible ${}^3\text{MC}$ to ground state.

To reduce K_{nr} , we need to increase the gap between ${}^3\text{MLCT}$ and ${}^3\text{MC}$. The best possible way to reduce the gap between them is either the stabilization of ${}^3\text{MLCT}$ or destabilization of ${}^3\text{MC}$ or both.

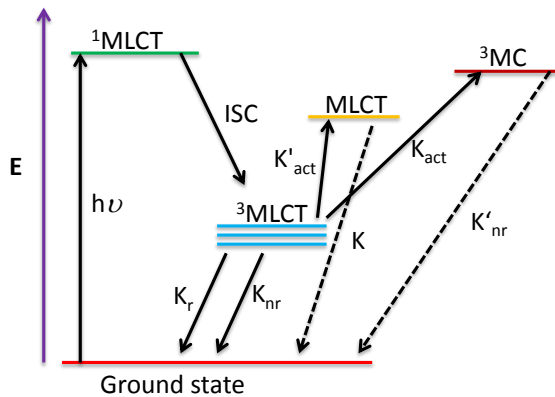


Figure 4.1. Schematic description of the excited states of Ru(II)-polypyridyl complexes. The rate constants are denoted 'k' together with a suffix indicating the type of transition.

Consequently, the relative energy ordering as well as the energy difference between the different excited states is very important for the photophysical behavior of Ru(II)-polypyridine complexes. $[\text{Ru(tpy)}_3]^{2+}$ and related bis-tridentate complexes typically have a smaller ${}^3\text{MLCT}$ - ${}^3\text{MC}$ energy gap than $[\text{Ru(bpy)}_3]^{2+}$, and thus significantly shorter excited state lifetimes at room temperature which consequently leads to the production of insignificant levels of ${}^1\text{O}_2$. Accordingly, synthesis, characterization, photophysical properties and DNA binding studies were conducted for mono nuclear Ru(II) and

binuclear Ru(II)-Pt(II) complexes in this chapter 4. From the cellular uptake studies in MCF-7 cancer cell lines we found that these two complexes accumulated in the cytoplasm and exhibited low cytotoxicity even after 24 h incubation period in the dark as well as in the photo-irradiation conditions. UV-Visible, fluorescence titrations and isothermal titration calorimetry studies with calf-thymus DNA suggest that these two complexes show moderately strong binding interaction for CT-DNA (calf-thymus DNA). The viscosity studies proved that they interact with DNA through groove binding mode.

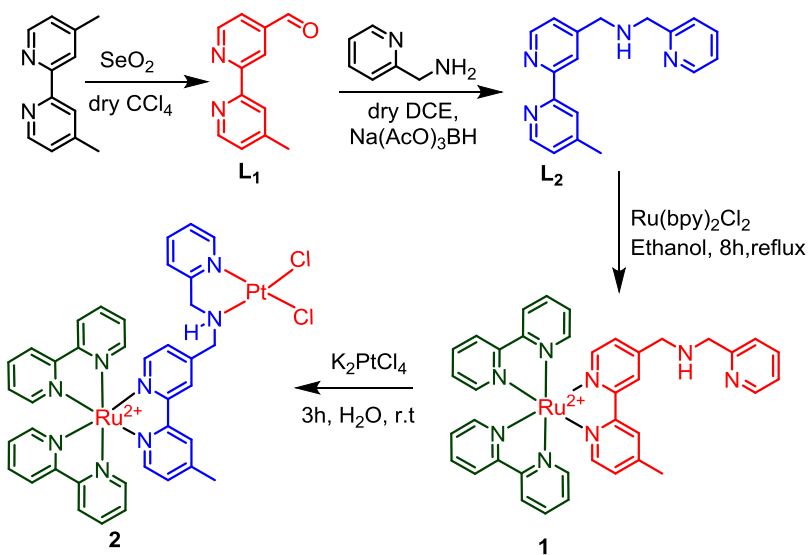
4.2. Experimental section

4.2.1. Confocal microscopy and MTT assay

Cell cultures were treated with 0 - 300 μ M solutions of **1** and **2** in triplicate for 24 h. After incubation, 0.5 mg/ml appropriate reagent for MTT (3-(4, 5-dimethylthiazol-2-yl)-2,5-diphenyltetrazolium bromide) assay was added and further incubated for 4 h. The media was removed and the formazan was dissolved using isopropanol and the absorbance at 570 nm was quantified by plate reader (reference 620nm). IC₅₀ values for the three complexes were found to be >300 μ M. MCF-7 cells were cultured in DMEM media. Cell lines were maintained at 37° C in an atmosphere of 5 % CO₂ and routinely sub-cultured. For live CLSM studies, cell cultures were grown on 6 well plate with coverslips, after 24 h of incubation the cells were treated with solutions of **1** and **2** (50 μ M) in serum containing media and incubated for 4 h. After incubation, media was removed and cells were washed with 1XPBS buffer. After fixation with 4 % paraformaldehyde, the coverslip mounted onto glass slide using mounting medium. Endoplasmic reticulum staining studies were performed using ER tracker green (E34251) from life technologies. For fixed cells, studies with complexes **1** and **2** were performed after fixing the cells with 4 % paraformaldehyde and treatment with 0.2 % TritonX-100. Cells were fluorescently imaged on a Fluoview confocal laser scanning microscope by using 60X oil-immersion

lenses. Complexes **1** and **2** were excited with laser at 442 nm and emission monitored at 620 nm (red) wavelengths. ER tracker was excited at 504 nm, emission recorded at 540 nm. All the captured images were modified using the ImageJ software for better results.

4.3. Synthesis and characterization



Scheme 4.1. The synthetic methodology adopted for the preparation of **1** and **2**.

4.3.1. Synthesis of **L₁**: 1-(4'-methyl-[2,2'-bipyridin]-4-yl)ethan-1-one

The compound 4,4'-dimethyl-2,2'-bipyridine (dmb) (1.8 g, 9.68 mmol) and SeO_2 (1.1 g, 9.9 mmol) were added into 1,4-dioxane (50 mL) and the mixture was heated to reflux for 24 h. the solution was filtered off while hot to remove Selenium, the filtrate was cooled to room temperature and allowed to stand for 1 h, and filtrate was removed. The pale yellow colored precipitate of carboxylic acid derivative, the filtrate was evaporated to dryness and the residue was redissolved in ethylacetate (200 mL) this solution was treated with Na_2CO_3 (0.1 M, 20 mL) to remove residual carboxylic acid and solvent extraction was done using 0.2 M aqueous solution of sodium bisulphite (NaHSO_3 , 3 X 30 mL). The combined aqueous solutions were adjusted to pH 9.0 using NaCO_3 and this final aqueous solution were extracted with dichloromethane following solvent extraction

procedure. Organic layers were combined and evaporated to dryness under reduced pressure. No further purification was required for this compound. Sample was characterized by standard analytical methods. Yield: 25 % (0.48 g, 2.4 mmol). ESI-MS = 198.2 (M^+); 1H NMR (200 MHz, $CDCl_3$) δ ppm: 10.1 (s, 1H), 8.81 (d, J = 4.9 Hz, 1H), 8.75 (d, J = 0.6 Hz, 1H), 8.50 (d, J = 4.9 Hz, 1H), 8.20 (s, 1H), 7.64 (dd, J = 4.9, 1.5 Hz, 1H), 7.12 (d, J = 4.9 Hz, 1H), 3.63 (d, J = 1.2 Hz, 1H), 2.38 (s, 3H), 1.97 (s, 2H). Elemental analysis: Calculated: C, 72.71; H, 5.09; N, 14.13; Found C, 72.52; H, 5.08; N, 14.1.

4.3.2. Synthesis of L_2 : 1-(4'-methyl-[2,2'-bipyridin]-4-yl)-N-(pyridin-2-ylmethyl)methanamine

The ligand L_2 was synthesized following the previous literature reports.^{6,7} One equivalent of 2-aminomethyl pyridine (102 μ L, 1 mmol) and one equivalent of 1-(4'-methyl-[2,2'-bipyridin]-4-yl)ethan-1-one (0.2 g, 1 mmol) were dissolved in dry 1,2-dichloroethane and then treated with solid sodiumtriacetoxyborohydride [$Na(AcO)_3BH$, 1.5 equivalent]. The reaction mixture was stirred at room temperature, and completion of the reaction was monitored by TLC using dichloromethane/methanol (9:1, v/v) solvent system. The reaction mixture was then quenched with saturated $NaHCO_3$ solution and the desired product was extracted thrice with dichloromethane. The combine organic layers were dried over sodium sulfate and solvent was removed under reduced pressure on a rotary evaporator. Desired compound was isolated as a brownish colored oily substance and this was further purified by column chromatography using the dichloromethane/methanol (95:5, v/v) as the mobile phase and the silica gel as stationary phase. Yield: 47 % (0.15 g, 0.51 mmol), ESI-HRMS = 291.1604 (M^+); 1H NMR (200 MHz, $CDCl_3$) δ ppm: 8.63 (d, J = 5.0 Hz, 1H), 8.55 (dd, J = 7.8, 5.0 Hz, 2H), 8.36 (s, 1H), 8.23 (s, 1H), 7.65 (dd, J = 10.6, 4.7 Hz, 1H), 7.39 (d, J = 5.0 Hz, 2H), 7.21 (d, J = 4.9 Hz, 1H), 7.15 (d, J = 4.8 Hz,

1H), 3.97 (s, 2H), 2.78 (s, 2H), 2.44 (s, 3H). Elemental analysis calculated: C, 74.46; H, 6.25; N, 19.30; found C, 74.50; H, 6.40; N, 19.10.

4.3.3. Synthesis of $[\text{Ru}(\text{bpy})_2(\text{bpy-amp})]^{2+}$ (1)

$\text{Ru}(\text{bpy})_2\text{Cl}_2$ (0.96 g, 0.18 mmol) and ligand L(1-(4'-methyl-[2,2'-bipyridin]-4-yl)-N-(pyridin-2-ylmethyl)methanamine) (0.5 g, 0.18 mmol) were taken in to a two neck round bottom flask and were dissolved in 40 mL of ethanol. The reaction mixture was allowed to reflux for 8 h under nitrogen atmosphere. Then it was cooled to the room temperature and ethanol was evaporated to dryness under reduced pressure. The orange red solid obtained was redissolved in minimum amount of water (10 mL). To this about 2 mL of saturated KPF_6 solution was added and stirred at room temperature. An orange red color precipitate was obtained, which was further kept at 8° C for 4 h. This was then filtered and the crude product was collected. This was subjected to the column chromatography using acetonitrile as a solvent phase. Second major fraction was isolated as the desired product and this pure complex was characterized by standard analytical and spectroscopic techniques. Yield: 55 % (0.10 g, 0.1 mmol); ESI-HRMS: 703.1878; ^1H NMR (200 MHz, CD_3CN) δ ppm: 8.49 (dd, $J = 7.9, 5.4$ Hz, 1H), 8.37 (d, $J = 5.8$ Hz, 3H), 8.27 (d, $J = 7.7$ Hz, 1H), 8.20 – 8.14 (m, 1H), 8.00 – 7.86 (m, 4H), 7.81 – 7.74 (m, 1H), 7.69 – 7.57 (m, 5H), 7.52 (d, $J = 5.9$ Hz, 1H), 7.49 – 7.39 (m, 2H), 7.33 – 7.26 (m, 2H), 7.23 (d, $J = 4.9$ Hz, 1H), 7.17 (dd, $J = 4.6, 0.9$ Hz, 1H), 7.14 – 7.09 (m, 1H), 7.06 (dd, $J = 3.4, 1.9$ Hz, 1H), 7.04 – 7.01 (m, 2H), 6.98 (dd, $J = 4.1, 3.6$ Hz, 2H), 2.41 (t, $J = 5.9$ Hz, 2H), 2.25 (s, 3H), 2.12 (s, 2H). Elemental analysis calculated C, 45.93; H, 3.45; N, 11.28. Found: C, 45.85; H, 3.5; N, 11.70.

4.3.4. Synthesis of $[\text{Ru}(\text{bpy})_2(\text{bpy-amp})\text{PtCl}_2]^{2+}$ (**2**)

Into a 100 mL two neck round bottom flask, $[\text{Ru}(\text{bpy})_2(\text{bpy-amp})](\text{PF}_6)_2$ (0.15 g, 0.15 mmol) and K_2PtCl_4 (0.08 g, 0.15 mmol) were dissolved in 5 mL of millipore water and allowed to react for 3 h in the dark conditions. The deep orange color precipitate was formed and this was filtered. The precipitate was washed thrice with millipore water to remove the excess K_2PtCl_4 and followed by washing with diethyl ether and dried in the desiccator. The crude product was not subjected to the column chromatography due to the labile nature of the chloride ligand the compound may decompose in the silica column. Further characterization was done using standard analytical methods. Yield: 96 % (0.15 g, 0.19 mmol); ESI-HRMS: 242.2840; ^1H NMR (200 MHz, CD_3CN) δ ppm: 8.49 (dd, $J = 7.9, 5.4$ Hz, 1H), 8.37 (d, $J = 5.8$ Hz, 3H), 8.27 (d, $J = 7.7$ Hz, 1H), 8.20 – 8.14 (m, 1H), 8.00 – 7.86 (m, 4H), 7.81 – 7.74 (m, 1H), 7.69 – 7.57 (m, 5H), 7.52 (d, $J = 5.9$ Hz, 1H), 7.49 – 7.39 (m, 2H), 7.33 – 7.26 (m, 2H), 7.23 (d, $J = 4.9$ Hz, 1H), 7.17 (dd, $J = 4.6, 0.9$ Hz, 1H), 7.14 – 7.09 (m, 1H), 7.06 (dd, $J = 3.4, 1.9$ Hz, 1H), 7.04 – 7.01 (m, 2H), 6.98 (dd, $J = 4.1, 3.6$ Hz, 2H), 2.41 (t, $J = 5.9$ Hz, 2H), 2.25 (s, 3H), 2.12 (s, 2H). ^{195}Pt NMR ($\text{Pt}(\text{N})_2\text{Cl}_2$) = 2100 ppm. Elemental analysis: Calculated C, 43.86; H, 3.29; N, 10.77 and Found: C, 43.85; H, 3.32; N, 10.70.

4.4. Results and Discussion

4.4.1. Photophysical characterization

The water soluble chlorides salts of **1** and **2** were synthesized by the anion metathesis method. The UV-Visible spectra for both the complexes were recorded in acetonitrile solvent media. $[\text{Ru}(\text{bpy})_3]^{2+}$ was used as reference for evaluating the relative quantum yields.

Table 4.1. Photophysical properties of **1** and **2** recorded in acetonitrile.

Complex	$\lambda_{\text{abs}} / \text{nm} (\varepsilon / 10^3 \text{ M}^{-1} \text{ cm}^{-1})$	$\lambda_{\text{ex max}} / \text{nm} (\lambda_{\text{Ems}})$	$\lambda_{\text{Ems max}} / \text{nm}$	Φ_f	$\tau(\text{ns})$
1	244 (18.59)	249	620	0.048	336
	287 (54.74)	305			
	463 (9.41)	463 (617)			
2	244 (28.08)	232	619	0.045	340
	287 (79.35)	293			
	464 (13.85)	464 (617)			

The absorption spectra clearly revealed that the visible region for both **1** and **2** complexes was dominated by broad Ru(dπ)→bpy/L(π*) and/or bpy/L(π*) based MLCT transitions at ~463 nm, while emission band for respective complex was attributed to a ³MLCT-based transition (~ 623 nm for λ_{Ext} = 463 nm). Spectroscopic data for complex **1**:

$\lambda_{\text{Max}}^{\text{Abs}} = 287 \text{ nm}$, $\varepsilon = 22100 \text{ M}^{-1} \text{ cm}^{-1}$; $\lambda_{\text{Max}}^{\text{Abs}} = 463 \text{ nm}$, $\varepsilon = 12920 \text{ M}^{-1} \text{ cm}^{-1}$; $\lambda_{\text{Max}}^{\text{Ems}} = 623 \text{ nm}$ for λ_{Ext} of 463 nm; Spectroscopic data for **2** complex: $\lambda_{\text{Max}}^{\text{Abs}} = 287 \text{ nm}$ ($\varepsilon = 22850 \text{ M}^{-1} \text{ cm}^{-1}$); $\lambda_{\text{Max}}^{\text{Abs}} = 465 \text{ nm}$, $\varepsilon = 12920 \text{ M}^{-1} \text{ cm}^{-1}$; $\lambda_{\text{Max}}^{\text{Ems}} = 623 \text{ nm}$. The excited state life time and quantum yield for these two molecules were calculated in acetonitrile solvent and reported in the Table 4.1

4.5. DNA-binding studies

4.5.1. UV-Visible and fluorescence titration with CT-DNA

The water soluble complex **1** and **2** were obtained via their anion metathesis of their respective PF₆⁻ salts using [n-Bu₄N]Cl in acetone. Chloride salt of the respective complex, thus obtained, was isolated as precipitate in the acetone solution and was isolated by filtration with necessary washing with cold acetone. The chloride salts of complex **1** and **2** were utilized for investigation of the interaction with CT-DNA was using UV-Visible (Figure 4.2) and fluorescence spectroscopy (Figure 4.3). From the Figure 4.2

addition of small aliquots of CT-DNA to the buffer solution containing **1** or **2** (Figure 4.3a, b) did not show any bathochromic shift either in $\pi \rightarrow \pi^*$ (290 nm) or in MLCT (450 nm) bands but leads to the considerable amount of hypochromic shift in $\pi \rightarrow \pi^*$ (290 nm) and MLCT bands (450 nm). Typical enhancement in emission intensities for complexes **1** and **2** were observed when emission spectra for respective complex were recorded in presence of increasing amount of CT-DNA (in an aq. buffer solution) (Figures 4.3a & 4.3b).

Table 4.2. CT-DNA binding constants were derived following McGhee Von-Hippel method.

Titration	1		2	
	$K_b[\text{Mol}^{-1}]$	S[bp]	$K_b[\text{Mol}^{-1}]$	S[bp]
Absorbance	3.2×10^4	0.9	5.3×10^4	1.0
Fluorescence	1.6×10^4	0.8	2.1×10^4	0.9

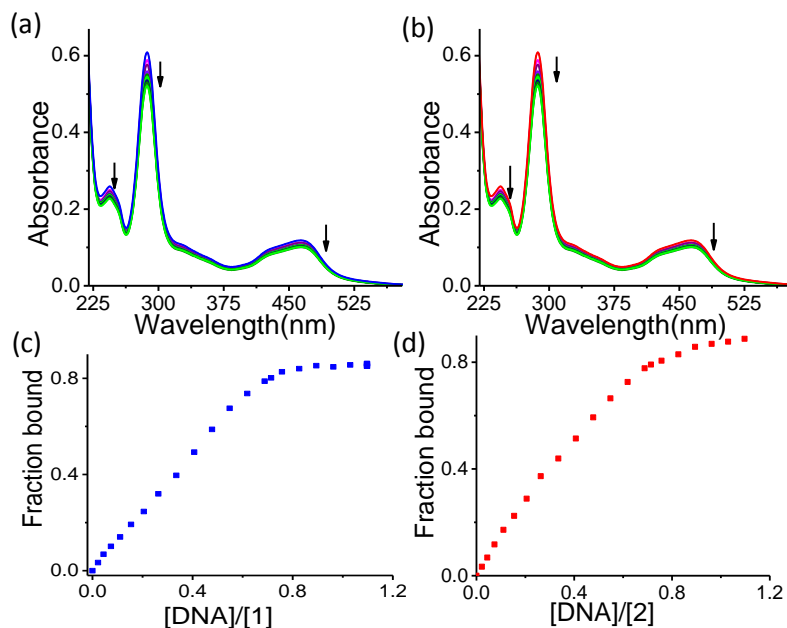


Figure 4.2. Change in the absorption spectra of **1** (a, c) and **2** (b, d) on interaction with CT-DNA. The spectra were recorded in Tris-HCl buffer, pH 7.4.

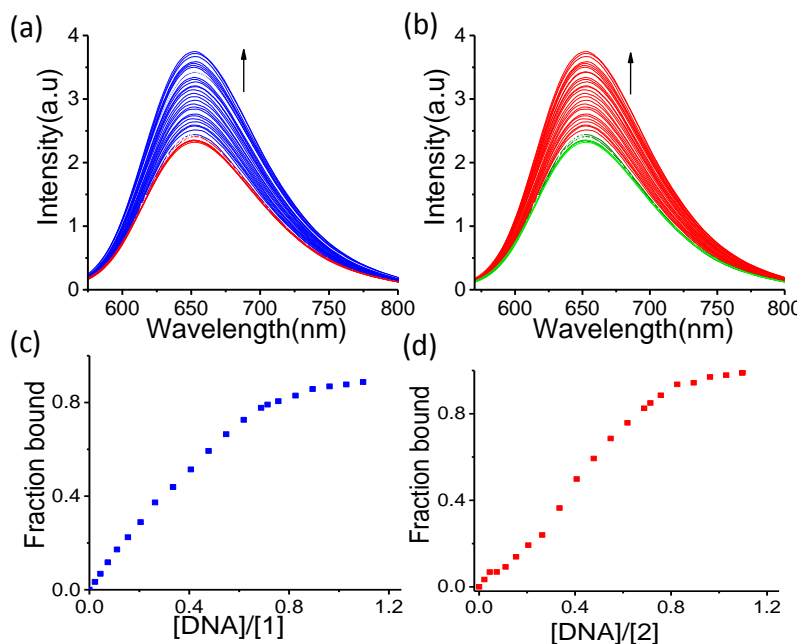


Figure 4.3. Change in the absorption spectra of **1** (a, c) and **2** (b, d) interacting with CT-DNA. The spectra were recorded in Tris-HCl buffer, pH 7.4.

The changes in MLCT band yield a saturation complex–DNA binding curve (Figures 4.3c & 4.3d) and higher binding ratios produced no additional changes in absorption and emission spectra of **1** and **2**. The binding affinity K_b , and the number of binding sites S , were calculated by fitting the data obtained from UV-Visible and fluorescence titrations to McGhee von-Hippel model (Table 4.2). The binding affinities obtained from the absorption titrations were found to be in good agreement with those obtained from the fluorescence titrations.

4.5.2. Isothermal titration calorimetry studies

Relative binding affinity of complexes **1** and **2** towards calf-thymus DNA (CT-DNA) were evaluated using isothermal titration calorimetry (Figure 4.4). Binding constants and thermodynamic parameters reported in the Table 4.3 clearly revealed that the binding affinities for both the complexes moderately strong, however, much weaker than those which binds DNA through intercalation.^{8,9,10} The data shown in Table 4.3 indicates that

these two complexes are spontaneously bound to DNA are lower than those of analogous Ru(II)-terpyridine derivatives having the same platinum functionality group that was discussed in the chapter 2.¹¹

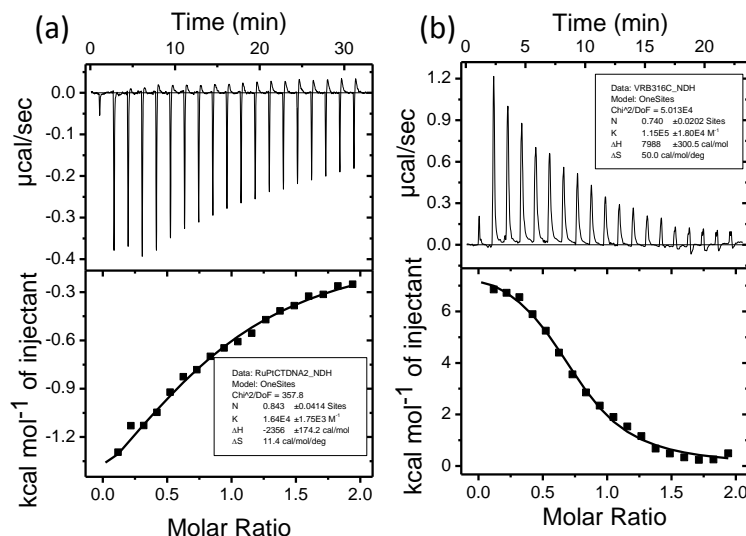


Figure 4.4. ITC binding profiles for the interaction of CT-DNA with complexes **1** (a) and **2** (b).

Table 4.3. The ITC derived DNA binding constants and thermodynamic parameters.

Complex	1	2
$K_b[M^{-1}]$	$(1.5 \pm 0.18)10^4$	$(1.6 \pm 0.17)10^5$
$\Delta H [KcalM^{-1}]$	7.9 ± 0.3	-2.3 ± 0.17
$-\Delta S [KcalM^{-1}]$	-14.9	-28.87
$\Delta G [KcalM^{-1}]$	-6.9 ± 0.02	-5.7 ± 0.41
S [bp]	0.7 ± 0.0	0.8 ± 0.0

Complex **2** with platinum center was expected to be more hydrophilic than the analogous complex **1** and anticipated to favor the interaction with DNA. Binding affinity of **2** towards CT-DNA was higher than the complex **1** by a factor of ~10 times. A positive enthalpy ($\Delta H_{ITC} = 7.9 \pm 0.3 \text{ KcalM}^{-1}$) and a high negative entropy (-14.9 KcalM^{-1}) changes was observed for interaction of **1** with CT-DNA. These observations tend to suggest that the interaction of **1** with CT-DNA was entropically driven.

The interaction of **2** with CT-DNA showed a small negative enthalpy ($\Delta H_{ITC} = (-2.3 \pm 0.1)$ KcalM⁻¹) and a large negative entropy change (-28.87 KcalM⁻¹). Therefore, the interaction of **2** with CT-DNA is driven by high negative entropy change and this means that the randomness of the system is drastically decreased by the formation of adduct of complex with CT-DNA. The High negative entropy change was anticipated, as platinum containing compounds generally interacts with the N7 atom of the guanosine in the duplex DNA. The binding affinity of these two complexes is **2** > **1**. All these observations suggested both of these compounds interact with CT-DNA predominantly through groove binding. However, as it was mentioned before, certain trivial influence of the electrostatic interactions between these cationic complexes with the negatively charged phosphate backbone cannot be completely ruled out.

4.5.3. Viscosity studies

Viscosity defines a fluid's internal resistance to flow; an increase in the viscosity indicates more resistance to flow. Hence, viscosity has become one of the indispensable methods to monitor the interaction of ligand with DNA. There are several effects on DNA viscosity that can describe the binding modes of a DNA-ligand. As discussed in previous chapter, intercalators such as ethidium bromide and $[Ru(phen)_2(dppz)]^{2+}$ cause an increase in the relative viscosity of the DNA.^{12,13} However, a partial and/or non-classical intercalation process may results in bending/kinking of the DNA helix, with typically less dramatic (positive or negative) or negligible changes in the relative DNA viscosity.¹⁴ On the other hand, a groove binder which binds in the DNA grooves fails to lengthen the DNA helix and to enhance the viscosity.¹⁴ In addition, cationic complexes such as $[Ru(bpy)_3]^{2+}$, which interacts with DNA through an electrostatic binding mode, have no influence on DNA viscosity.¹⁵

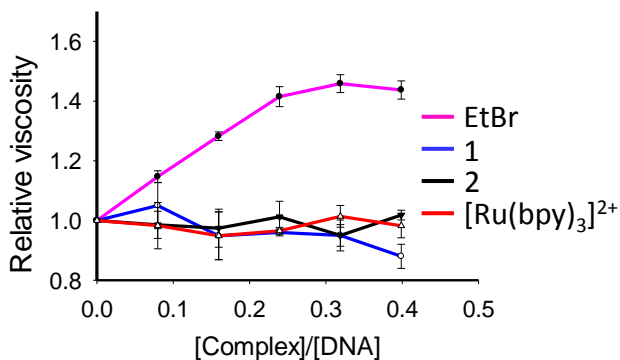


Figure 4.5. Change in the relative viscosity of CT-DNA with increasing amount of ethidiumbromide, **1**, **2** and $[\text{Ru}(\text{bpy})_3]^{2+}$.

The effects of ethidiumbromide, $[\text{Ru}(\text{bpy})_3]^{2+}$, **1** and **2** complexes on the viscosity of CT-DNA are showed in Figure 4.5. On increasing the amounts of ethidiumbromide the relative viscosity of DNA was found to increase, which confirmed that ethidiumbromide interacted with CT-DNA via intercalation. However, the $[\text{Ru}(\text{bpy})_3]^{2+}$, **1** and **2** complexes tested for their effect on relative DNA viscosity which indeed showed groove binding mode.

4.5.4. Gelectrophoresis studies

As it was discussed in chapter 3 the Ru(II)-polypyridyl complexes can cause damage to DNA by generating the reactive oxygen species (ROS).¹⁶⁻¹⁹ To investigate the ability of **1** and **2** to damage DNA upon photo-irradiation, we have conducted the gel electrophoresis experiment of pUC19 plasmid DNA by incubating with both **1** and **2** for 2 h in the dark conditions and photo-irradiated at $\lambda = 450 \text{ nm}$.²⁰ The pUC19 plasmid DNA (40 $\mu\text{g}/\text{mL}$) was incubated with **1** and **2** (25 or 50 μM) and irradiated for 2 h with light ($\lambda = 450 \text{ nm}$, 10 J/cm^2). After this the samples were loaded on to the 0.8 % agarose gel. The gel was allowed to run at 100 mA for 45 min. Ethidiumbromide was used as DNA intercalating agent to visualize under the UV-light illumination.

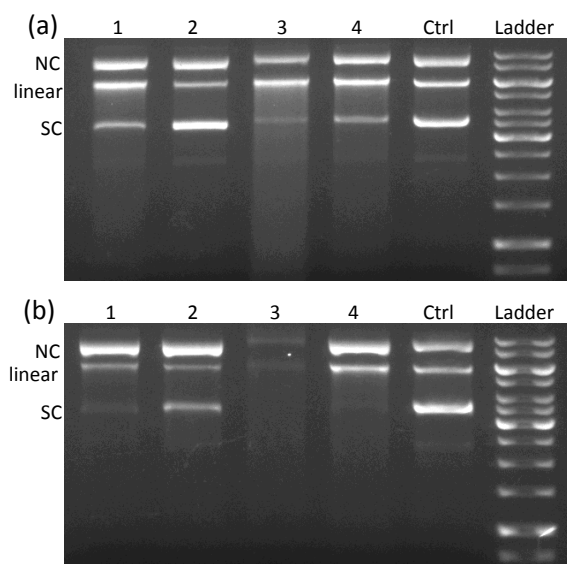


Figure 4.6. Gelelectrophoresis of pUC19 plasmid DNA with **1** (a) and **2** (b) following photo-irradiation for 4 h (lanes 3, 4) and incubation in the dark conditions for 4 h (lanes 1, 2) Lane Ctrl: Control plasmid DNA. 1 kb ladder was loaded for comparison purpose.

Gel images shown in Figure 4.6 clearly indicate that the DNA cleavage occurred when the samples were photo-irradiated (lane 3, 4 in both). While in the dark conditions, no DNA cleavage was observed (lanes 1, 2). It is well known that the Ru(II)-polypyridyl complexes can convert the water or molecular oxygen in to their ROS ($^1\text{O}_2$ or OH^\bullet) through energy transfer process from their ${}^3\text{MLCT}$ state.^{21,22,23} Complex **1** or **2** converted the supercoiled (SC) DNA into the nicked circular DNA (NC) when the samples were photo-irradiated (Figure 4.6a/b, lanes 3, 4). But the partial DNA conversion was found when the samples treated in the dark (Figure 4.6a/b, lanes 1, 2). For comparison purpose we have loaded the 1kb ladder along with the reaction mixtures. This was clearly revealed that complexes **1** and **2** are causing damage to the DNA in the presence of light.

4.5.5 Cytotoxicity studies: MTT assay

In order to assess the potential application of these two reagents as PDT agent we have further conducted the cytotoxicity studies these complexes **1** and **2**. We have incubated the MCF-7 cells at various concentrations starting from 0 - 300 μM for 24 h. Cytotoxicity tests were performed using MTT assay in triplicate. After 24 h incubation, cells were treated with 5 μL of MTT reagent for 4 h. After this the MTT = (3-(4, 5-dimethylthiazol-2-yl)-2,5-diphenyltetrazolium bromide) dissolved in serum-containing media.

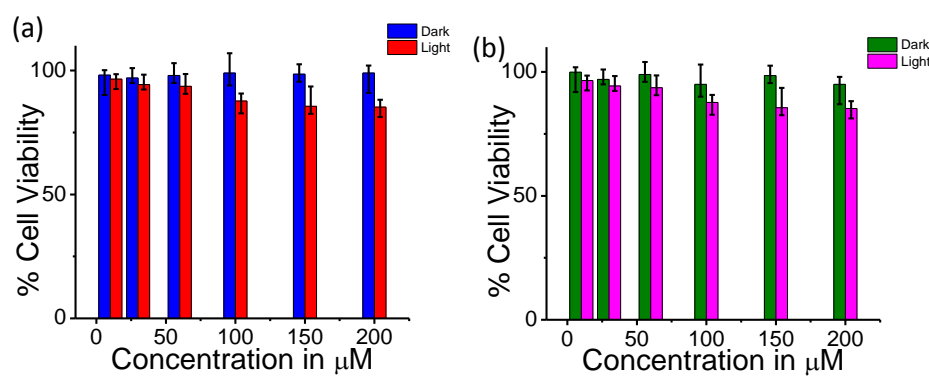


Figure 4.7. Cytotoxicity results of MCF-7 cells for **1** (a), **2** (b) in the absence and presence of light.

The media was removed and the formazan crystals was dissolved using isopropanol and the absorbance at 570 nm quantified by plate reader (reference 620 nm). The evaluated IC₅₀ values for the two complexes were found to be > 200 μM (Figure 4.7a for **1** and Figure 4.7b for **2**). Even though both complexes are causing the DNA damage, the low toxicity of these two compounds were not clearly been understood. However, the cellular DNA repair mechanism that exists in the cells presumably the reason behind the cell survival even after 24 h treatment. Figure 4.7 shows the MTT assay results for both the complexes. Even at the higher concentration (> 200 μM) of the complexes 90 % of the cell survival was observed. Since, these complexes does not show any dark toxicity we have further incubated MCF-7 cells with **1** and **2** and followed by photo-irradiation with visible light ($\lambda > 450$ nm). Even in the presence of visible light excitation these

compounds failed to induce any toxicity. However, one cannot avoid the possibility that these complexes producing insignificant amount of reactive oxygen species (ROS).

4.5.6. Cellular uptake and confocal microscopy studies

The results obtained from the MTT assay suggested that these two complexes were not toxic toward MCF-7 cells. To investigate, whether these compounds were taken up by the live MCF-7 cells or not, we have further incubated the **1**, **2** complexes with live MCF-7 cells at 37° C for 4 h and conducted the confocal laser scanning microscopy (CLSM) studies.

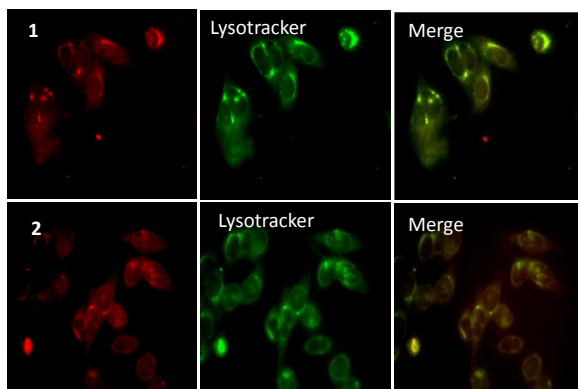


Figure 4.8. CLSM images of MCF-7 cells incubated with **1**, **2** for 4 h. Co-staining experiments were conducted using lysotracker green.

The co-localization studies were achieved using the commercially available lysotracker green. From the Figure 4.8 the comparison of the CLSM images of the cells incubated alone with **1** or **2** and the images of the co-staining experiments with lysotracker staining agent clearly revealed that these two complexes are mainly accumulated in the cytoplasm. The intracellular emission signals detected for the **1** and **2** was found that they were not exactly superimposed with lysotracker green. The literature reports also reveal that lipophilic cationic reagents generally accumulated in the regions such as cell membrane while analogous reagents having positive charge and relatively low

lipophilicity would have preference for nuclei.^{24,25} The dimethyl substituted $[\text{Ru}(\text{bpy})_2(\text{dmbpy})]^{2+}$ complex showed a dot-like structures on the cell membrane.¹⁵ With red fluorescence in bright-field microscopy, a pattern that was observed earlier for localization of lipophilic reagents at the cell membrane.^{26,15} Such dot like structures scattered in the cytoplasm presumably suggested that the reagents were also distributed in vacuoles, which are known to play a role in endocytosis.^{27,28}

4.6. Conclusions

In conclusion, we have successfully synthesized, characterized mono nuclear Ru(II)- polypyridyl and heterodinuclear Ru(II)-Pt(II) complexes. UV-Visible and fluorescence titration of both the complexes with CT-DNA indicated that the binding efficiency towards DNA is rather weak. These results were corroborated with ITC titration experiments where we found similar binding constants. ITC studies also showed the interaction between the metal complexes and CT-DNA was highly spontaneous and entropically driven. Viscosity measurements proved that **1** and **2** interacting with to the DNA through grooves binding mode. From the MTT assay results we conclude that these two metal complexes were low-cytotoxic or non-toxic ($\text{IC}_{50} > 200 \mu\text{M}$) to the MCF-7 cells in both absence and presence of visible light exposure. The lower cytotoxicity of was accounted for their inability to produce the significant amount of ${}^1\text{O}_2$ in the aqueous environment. Form the confocal microscopy studies it was very clear that these two complexes were taken up by the live MCF-7 cells and accumulated in the cytoplasm.

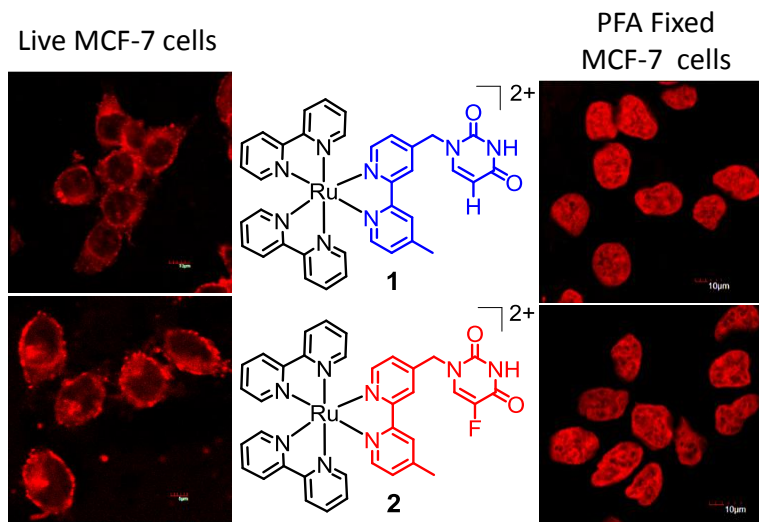
4.7. References

1. J. Sauvage, J. Collin, J. Chambron and S. Guillerez, *Chem. Rev.*, 1994, **94**, 993–1019.
2. A Ph.D thesis by M. Abrahamsson entitled "*Tuning of the Excited State Properties of Ruthenium (II) - Polypyridyl Complexes*", 2006, 28-35.
3. G. H. Allen, R. P. White, D. P. Rillema and T. J. Meyer, *J. Am. Chem. Soc.*, 1984, **106**, 2613–2620.
4. A Ph.D thesis by O. Johansson entitled "*Ruthenium (II) Polypyridyl Complexes Applications in Artificial Photosynthesis*", 2004, 1-60.
5. F. Barigelli, A. Juris, V. Balzani, P. Belser and A. von Zelewsky, *Inorg. Chem.*, 1983, **22**, 3335–3339.
6. S. Mundinger, U. Jakob, P. Bichovski and W. Bannwarth, *J. Org. Chem.*, 2012, **77**, 8968–8979.
7. M. C. Liu, T. S. Lin and A. C. Sartorelli, *J. Med. Chem.*, 1992, **35**, 3672–3677.
8. J. K. Barton, *Curr. Opin. Chem. Biol.*, 2000, **4**, 199–206.
9. C. A. Puckett, R. J. Ernst and J. K. Barton, *Dalt. Trans.*, 2010, **39**, 1159–1170.
10. C. A. Puckett and J. K. Barton, *J. Am. Chem. Soc.*, 2007, **129**, 46–47.
11. V. Ramu, M. R. Gill, P. J. Jarman, D. Turton, J. A. Thomas, A. Das and C. Smythe, *Chem. - A Eur. J.*, 2015, **21**, 9185–9197.
12. E. That and E. Structural, 1990, **23**, 8–10.
13. J. K. Barton, L. A. Basile, A. Danishefsky and A. Alexandrescu, *Proc. Natl. Acad. Sci.*, 1984, **81**, 1961–1965.
14. C. Hiort, B. Nordn and A. Rodgerf, *J. Am. Chem. Soc.*, 1990, **112**, 1971–1982.
15. V. Ramu, F. Ali, N. Taye, B. Garai, A. Alam, S. Chattopadhyay and A. Das, *J. Mater. Chem. B*, 2015, **3**, 7177–7185.
16. Z.-Z. Li, Y.-L. Niu, H.-Y. Zhou, H.-Y. Chao and B.-H. Ye, *Inorg. Chem.*, 2013, **52**, 10087–10095.
17. T. Gunnlaugsson, S. M. Cloonan, R. Elmes, M. Erby, S. A. Bright, F. E. Poynton, D. E. Nolan, S. J. Quinn and D. C. Williams, *J. Med. Chem.*, 2015, **58**, 4494-4505.
18. C. Tan, S. Lai, S. Wu, S. Hu, L. Zhou, Y. Chen, M. Wang, Y. Zhu, W. Lian, W. Peng, L. Ji and A. Xu, *J. Med. Chem.*, 2010, **53**, 7613–7624.
19. O. Oter and A.-C. Ribou, *J. Fluoresc.*, 2009, **19**, 389–397.
20. A. Leonidova, V. Pierroz, R. Rubbiani, J. Heier, S. Ferrari and G. Gasser, *Dalton*.

- Trans.*, 2014, **43**, 4287–4294.
- 21. J. D. Knoll, B. A. Albani and C. Turro, *Acc. Chem. Res.*, 2015, **48**, 2280–2287.
 - 22. M. Stephenson, C. Reichardt, M. Pinto, M. Wa, T. Sainuddin, G. Shi, H. Yin, S. Monro, E. Sampson, B. Dietzek and S. A. Mcfarland, *J. Phys. Chem. A*, 2014, **118**, 10507–10521.
 - 23. M. C. DeRosa and R. J. Crutchley, *Coord. Chem. Rev.*, 2002, **233-234**, 351–371.
 - 24. E. Baggaley, M. R. Gill, N. H. Green, D. Turton, I. V. Sazanovich, S. W. Botchway, C. Smythe, J. W. Haycock, J. A. Weinstein and J. A. Thomas, *Angew. Chemie Int. Ed.*, 2014, **53**, 3367–3371.
 - 25. M. R. Gill, J. Garcia-Lara, S. J. Foster, C. Smythe, G. Battaglia and J. A. Thomas, *Nat. Chem.*, 2009, **1**, 662–667.
 - 26. N. Zhang, Y. Yin, S. J. Xu and W. S. Chen, *Molecules*, 2008, **13**, 1551–1569.
 - 27. O. Zava, S. M. Zakeeruddin, C. Danelon, H. Vogel, M. Gratzel and P. J. Dyson, *ChemBioChem*, 2009, **10**, 1796–1800.
 - 28. F. R. Svensson, M. Matson, M. Li and P. Lincoln, *Biophys. Chem.*, 2010, **149**, 102–106.

CHAPTER 5

Ru(II)-polypyridyl based Imaging Reagents for Lipid dense Regions in Live Cells and the Nucleus in Fixed MCF-7 Cells



[Publication](#)

J. Mater. Chem. B, 2015, **3**, 7177–7185.

5.1. Introduction

Non-invasive imaging methodology is usually preferred for observing individual events in cells associated to those traditional biochemical methods that give average results for cells exposed to certain experimental treatment for studying cell functioning, differentiation, reproduction and also the gene expression in living organisms.¹ Such processes are expected to affect the natural intracellular processes while the imaging studies are accomplished in physiologically authentic environments. They have relevance for cell/molecular biology, studying biochemical processes, medicine, pharmacology and diagnostics.² Hence, visualization of cellular structure by fluorescence microscopy is a powerful technique in modern days. There are significant steps involved in designing suitable imaging reagents for visualization of specific organelles with organelle-selective dyes in the membrane-enclosed intracellular structures, because this helps in acquisition of insight for monitoring important biological processes.^{3,4} Stability towards photo-bleaching, cell membrane permeability, nominal cytotoxicity and luminescence in the longer wavelength following excitation with non-harmful visible light are some of the essential criteria for any such efficient imaging reagent.^{5,6,7,8}

For imaging application, target like ER, a specific organelle in the cells of eukaryotic organisms, is of great significance.^{9,10} Proteins for the secretory pathway are inserted into the membrane of the ER, where they are processed/folded into their native conformation. Misfolded proteins are retained in the ER and transported to the cytosol for ER-associated protein degradation, which has a serious implication in physiology.¹⁰ ER can be stained with a variety of commercially available lipophilic probes and typical highly ER specific dyes

include the lipophilic carbocyanine (DiOC₆ or DiOC₅ with Stokes shift ($\Delta\lambda_{SS}$) of ~14 nm) or boron-dipyrromethane (BODIPY) dyes (E34251 or E34250 with $\Delta\lambda_{SS}$ of ~28 and 7 nm, respectively).¹¹ Such dyes suffer from the limitations of narrow $\Delta\lambda_{SS}$, photo-bleaching and partial toxicity.¹² There are only two reports, which reveal that the above referred limitations could be addressed for either ER or mitochondria-specific dyes by using dinuclear Ru(II)-polypyridyl based complexes.¹³ Martin et al. also showed that the DNA groove-binding dinuclear complex [{Ru(phen)₂}₂-{ μ -tpphz}]⁴⁺ (where tpphz = tetrapyridophenazine) could be used to image nuclear DNA in eukaryotic cells,¹⁴ while the 4,7-diphenyl-1,10-phenanthroline (DIP) analogue [{Ru(DIP)₂}₂-{ μ -tpphz}]⁴⁺ was localised in ER.⁹ To the best of our knowledge, barring these two publications, there is no such report for ER-specific Ru(II)-polypyridyl based imaging reagent for live mammalian cells. It has been argued that lipophilicity of the dye molecule is crucial for ER-specific dyes.¹⁵ A recent report also reveals that Ru(II)-polypyridyl-peptide conjugated with lower lipophilicity is preferentially localized in nucleus.^{16,17} All the above referred Ru(II)- and some Ir(III)-based ER-specific dyes are known to induce the toxicity by ER stress and the IC₅₀ values for these reagents are typically $\leq 150 \mu\text{M}$ which defies the suitability of using such reagent for application as an imaging reagent.^{18,19,15,20}

This chapter describes the synthesis characterization and biological applications of two new and easily accessible uracil (**1**) or 5-fluorouracil (**2**) functionalized Ru(II)-polypyridyl derivatives having $\Delta\lambda_{SS}$ of ~160 nm for specific imaging of endoplasmic reticulum, cell membrane and cytoplasmic vacuoles, lipid dense regions in live MCF-7 cells (Figure 5.1). Both complexes showed insignificant cytotoxicity and a lipophilicity dependent cellular internalization process.

Importantly, in fixed MCF-7 cells, localization of dyes **1** and **2** were observed only in nucleus and such observation is hitherto unknown. It is noteworthy that the model complex **3** $[\text{Ru}(\text{bpy})_2(\text{L}_3)]^{2+}$; bpy = 2,2'-bipyridine & L_3 = 4,4'-dimethyl-2,2'-bipyridine, (Figure 5.1) did not show any such specificity either in live or in fixed MCF-7 cells.

5.2. Experimental section

5.2.1. Crystallographic study of complex **1**

As-synthesized crystal of complex **1** was obtained by slowly diffusion of diethyl ether in to a CH_3NO_2 solution of complex **1**. The data collection was done at 298K. The crystal was mounted on a Super Nova Dual source X-ray diffractometer system (Agilent Technologies) equipped with a CCD area detector and operated at 250 W power (50 kV, 0.8 mA) to generate Mo $\text{K}\alpha$ radiation ($\lambda = 0.71073 \text{ \AA}$) and Cu $\text{K}\alpha$ radiation ($\lambda = 1.54178 \text{ \AA}$) at 298K. Data were integrated using CrysAlisPro software with a narrow frame algorithm. Data were subsequently corrected for absorption by the program SCALE3 ABSPACK1 scaling algorithm. Additional crystallographic data is available in supporting information.

5.2.2. MTT assay and confocal studies

Cell cultures were treated with 0-300 μM solutions of **1**, **2** and **3** in triplicate for 24 h. After incubation 0.5 mg/ml of MTT reagent was added and incubated for 4 h. MTT = (3-(4, 5-dimethylthiazol-2-yl)-2,5-diphenyltetrazolium bromide) was dissolved in water at 5 mg/ml. The media was removed and the formazan was dissolved using isopropanol and the absorbance at 570 nm quantified by plate reader (reference 620 nm). IC_{50} values for the entire three complexes were found to be $> 300 \mu\text{M}$. MCF-7 cells were cultured in DMEM media. Cell lines were maintained at 37° C in an atmosphere of 5 % CO_2 and

routinely sub-cultured. For live confocal imaging studies, cell cultures were grown on 6 well plate with coverslips, after 24 h of incubation the cells were treated with solutions of **1**, **2**, and **3** (50 µM,) in serum containing media and incubated for 4 h. After incubation, media was removed and cells were washed with 1XPBS buffer. After fixation with 4 % paraformaldehyde, the coverslip mounted onto glass slide using mounting medium. Nuclear staining was performed by using DAPI. Endoplasmic reticulum staining studies were performed using ER tracker green (E34251) form life technologies. For fixed cells, studies with complexes **1**, **2**, and **3** were performed after fixing the cells with 4 % paraformaldehyde and treatment with 0.2 % TritonX-100. To study different stages of mitosis, MCF-7 cells were seeded in coverslips and treated with 150 nM nocodazole for 14 h for mitosis arrest. Later nocodazole was removed and was supplemented in fresh complete DMEM medium. At 90th minutes after release from mitosis metaphase stage, cells were fixed with formaldehyde and stained for CLSM studies. At 160th minutes telophase stage of these cells was collected and stained for CLSM. Cells were fluorescently imaged on a Fluoview confocal laser scanning microscope by using 60X oil-immersion lenses. Complexes **1**, **2**, and **3** were excited with laser at 442 nm and emission monitored at 620 nm (red) wavelengths. DAPI was excited by using a 359 nm diode laser and emission detected with a 420-480 nm long-pass band-filter. ER tracker was excited at 504 nm.

5.2.3. Cellular uptake & Quantification of **1, **2**, and **3** by (MP-AES)**

Cellular accumulation studies for complexes **1**, **2**, and **3** were conducted on the MCF-7 cell line. Briefly, $2.5 \times 10^5 - 1.0 \times 10^6$ cells were seeded on a petridish; the metal complexes were then added to give final concentrations of 50 µM and allowed a further 24h of drug exposure at 37° C. After this time, cells were treated with trypsin, counted using haemocytometer and cells collected were digested

overnight in concentrated nitric acid (73 %) at 60° C; Samples were made up to exactly 10 mL using deionized water and the amount of ruthenium taken up by the cells was estimated by MP-AES (Microwave Plasma Atomic Emission Spectroscopy), using an Agilent Technologies instrument (Model No: 4100 MP-AES). The solvent used for all MP-AES experiments was double deionized water (DDW). The concentrations used for the calibration curve were in all cases 0, 5, 7.5, 10 ppm. The isotope detected was ^{101}Ru ; readings were made in duplicate (N_2 gas mode).

5.3. Synthesis and characterization

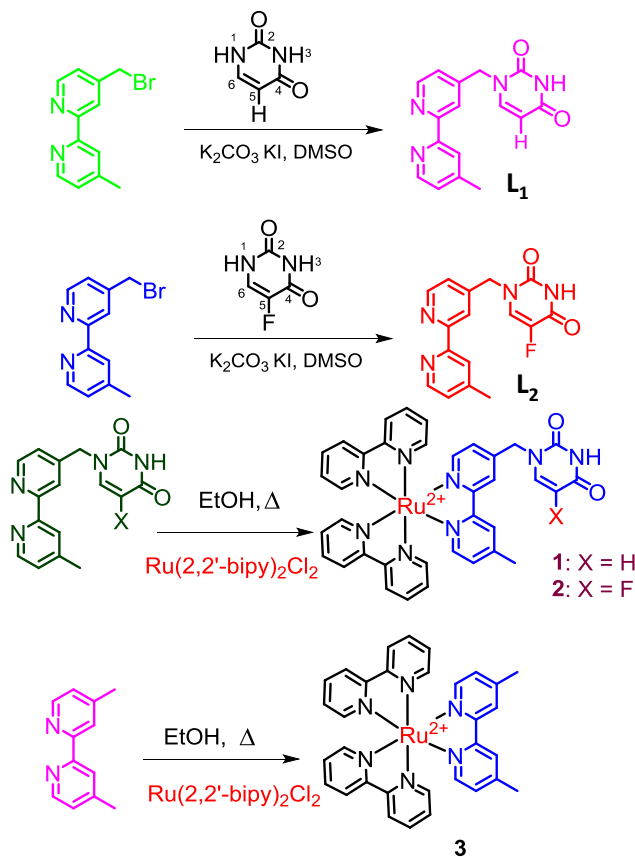


Figure 5.1. Synthetic methodology adopted for the synthesis of \mathbf{L}_1 , \mathbf{L}_2 , $\mathbf{1}$, $\mathbf{2}$ and $\mathbf{3}$.

5-Flourouracil (5-FU) and Uracil (U) are well known for their rapid cellular uptake.²¹ With an aim to exploit this property two new uracil derivatives

[Ru(bpy)₂(L₁)]²⁺ (**1**); and [Ru(bpy)₂(L₂)]²⁺ (**2**) were synthesized. The model complex [Ru(bpy)₂(L₃)]²⁺ (**3**) was also prepared for the comparison purpose. Selection of Cl⁻ as counter anions for **1**, **2**, and **3** enabled us to achieve the desired solubility in aq. buffer (Tris-HCl buffer, pH = 7.4) media. Synthetic methodology as well as various analytical and spectroscopic data (¹H/¹⁹F NMR and HRMS spectra) of complexes **1** (Cl)₂, **2** (Cl)₂, and **3** (Cl)₂ are agreed well for the desired purity of these complexes. It can be assumed that the U and 5-FU permeate cell membrane using the facilitated transport mechanism and 5-FU remains the main reagent for the treatment of colorectal cancer.^{15,21} 5-FU is known to be converted to fluorodeoxyuridine monophosphate, which forms a stable complex with thymidylate synthase. This further inhibits deoxythymidine monophosphate production and interrupts the DNA synthesis.²² However, the presence of N¹H₅-FU is crucial for such action (scheme 4.1). Our synthetic design involved the removal of this N¹H with an aim to block its cytotoxicity as well as to avail the advantage of the cell membrane permeability.²³ Accordingly, complexes **1** and **2** were synthesized. Complex **3** was prepared as a model compound to investigate the role of U/5-FU in cell membrane permeability.

5.3.1. Synthesis of L₁ and L₂: The ligands L₁ and L₂ were prepared by alkylation of 4-(bromomethyl)-4'-methyl-2,2'-bipyridine in DMSO directly with uracil to give 1-((4'-methyl-[2,2'-bipyridin]-4-yl)methyl)pyrimidine-2,4(1H,3H)-dione(L₁) and with 5-fluorouracil at N¹ position to give 5-fluoro-1-((4'-methyl-[2,2'-bipyridin]-4-yl)methyl)pyrimidine-2,4(1H,3H)-dione(L₂). Reaction of L₁ and L₂ with [Ru(bpy)₂Cl₂].xH₂O in ethanol for 8 h under reflux conditions afford a deep orange colored complexes **1** and **2** which were then purified by column chromatography (silica 100-200 mesh and 100 % acetonitrile as eluent) and characterized using

standard analytical techniques. Note: Ligand L₃ (4,4'-dimethyl-2,2'-bipyridine) was obtained from Sigma-Aldrich and used without further purification for the synthesis of complex 3.

5.3.2. Synthesis of L₁: 1-((4'-methyl-[2,2'-bipyridin]-4-yl)methyl)pyrimidine-2,4(1H,3H)-dione

A mixture of uracil (0.112 g, 1 mmol), K₂CO₃ (0.276 g, 2 mmol) and KI catalytic ca. 25 mg, a catalytic amount) in 10 mL of DMSO was stirred under N₂ for 10 min. 4-(bromomethyl)-4'-methyl-2,2'-bipyridine (0.644 g, 2.45mmol) predissolved in DMSO was then slowly added via a syringe and the resultant chocolate brown mixture was stirred under N₂ at room temperature for 3h. Water (100 mL) was then added and the suspension was extracted with dichloromethane. The collected organic layers were dried over anhydrous sodium sulphate and solvent was removed in vacuum to give a half-white solid. The crude was subjected to the silica column chromatography using dichloromethane and acetone as eluent 99:1 (v/v). The second spot on the TLC plate was collected as L₁: Yield (0.145 g, 49.26 %). ESI-MS: *m/z* = 316.91 [L₁+Na⁺]; ¹H NMR (200MHz, methanol-d₄) 8.65 (d, 1H, *J* = 5.7 Hz), 8.52 (d, 1H, *J* = 4.8 Hz), 8.24 – 8.18 (2H, m), 7.73 (d, 1H, *J* = 7.9 Hz), 7.38 (d, 1H, *J* = 3.4 Hz), 7.32 (d, 1H, *J* = 6.6 Hz), 5.77 (d, 1H, *J* = 7.9 Hz), 5.10 (2H, s), 2.49 (3H, s). Elemental analysis calculated: C, 65.30; H, 4.79; N, 19.04; Found: C, 64.9; H, 4.73; N, 18.98.

5.3.3. Synthesis of L₂: 5-Fluoro-1-((4'-methyl-[2,2'-bipyridin]-4-yl)methyl)pyrimidine-2,4(1H,3H)-dione

A mixture of 5-fluorouracil (0.130 g, 1 mmol), K₂CO₃ (0.276 g, 2.0 mmol) and KI (ca. 25 mg) in 10 mL of DMSO was stirred under N₂ for 10 min. 4-(bromomethyl)-

4'-methyl-2,2'-bipyridine (0.644 g, 2.45 mmol) pre-dissolved in DMSO (5 mL) was then slowly added via a syringe and the resultant chocolate brown mixture was stirred under N₂ at room temperature for 3 h. Water (100 mL) was then added and the suspension was extracted with dichloromethane. The collected organic layers were dried over anhydrous sodium sulphate and the solvent removed in vacuum to give a half-white solid. The crude was subjected to the silica column chromatography using dichloromethane and acetone as solvent mixture 99:1 (v/v). The second spot from the bottom on the TLC plate was collected as L₂: Yield (0.150 g, 48 %) ESI-MS: *m/z* = 334.93 [L₂+Na⁺]. ¹H NMR (200 MHz, CDCl₃) 8.89 (1H, s), 8.68 (d, 1H, *J* = 4.8 Hz), 8.54 (d, 1H, *J* = 4.8 Hz), 8.33 (1H, s), 8.25 (1H, s), 7.19 (d, 2H, *J* = 10.3 Hz), 5.77 (d, 1H, *J* = 7.7 Hz), 5.00 (2H, s), 2.45 (3H, s). ¹⁹F NMR (400 MHz, CDCl₃) -74.85 (1F, s). Elemental analysis calculated: C, 61.53; H, 4.20; N, 17.94; Found: C, 61.1; H, 4.14; N, 17.86.

5.3.4. Synthesis of [Ru(bpy)₂(L₁)](PF₆)₂ (**1**), [Ru(bpy)₂(L₂)](PF₆)₂ (**2**) and [Ru(bpy)₂(L₃)](PF₆)₂ (**3**)

Two new uracil/5-fluorouracil derivatives [Ru(bpy)₂(L₁)]²⁺ (**1**); and [Ru(bpy)₂(L₂)]²⁺ (**2**) were synthesized. Model complex that was used for studies was [Ru(bpy)₂(L₃)]²⁺ (**3**) (where L₃ = 4,4'-dimethyl-2,2'-bipyridine). For complexes **1** and **2**, L₁ is 1-((4'-methyl-[2,2'-bipyridin]-4-yl)methyl)pyrimidine-2,4(1H,3H)-dione) and L₂ = 5-fluoro-1-((4'-methyl-[2,2'-bipyridin]-4-yl)methyl) pyrimidine-2,4(1H,3H)-dione). Complexes **1**, **2** and **3** were prepared using the reaction of [Ru(bpy)₂Cl₂]²⁺ (0.145 g, 0.3 mmol) with the appropriate ligand L₁ (0.105 g, 0.3 mmol) or L₂ (0.112 g, 0.3 mmol) or L₃ (0.05 g, 0.3 mmol) in ethanol under reflux condition for 8 h. After cooling, addition of saturated aqueous potassium hexafluorophosphate (KPF₆) solution precipitated out the complexes as orange red solids. Which were

filtered off using G4 glass centered crucible. The precipitate washed with Millipore water (5 X 3 mL) followed by diethyl ether and dried over P_2O_5 in desiccator. Both the complexes were purified by silica gel (100-200 mesh) column chromatography using acetonitrile and saturated KPF_6 solution 98:2 (v/v) as eluent.

Characterization of 1: yield (0.159 g, 53 %), ESI-MS: m/z for $M^{2+} = 707.1448$ found, 707.1451 calculated, $[M-2PF_6]^+$. 1H NMR (400 MHz, CD_3CN) 9.26 (1H, s), 8.52 (4H, d, $J = 8.0$), 8.43 (1H, s), 8.34 (1H, s), 8.10-8.04 (4H, m), 7.75 (4H, d, $J = 4.5$), 7.69 (1H, d, $J = 5.8$), 7.57 (1H, d, $J = 5.7$), 7.49-7.39 (5H, m), 7.31-7.25 (2H, m), 5.70 (1H, d, $J = 7.8$), 5.05 (2H, s), 2.56 (3H, s). Elemental analysis (as chloride salt) calculated: C, 55.53; H, 3.88; N, 14.39; Found: C, 55.41; H, 3.9; N, 14.4.

Characterization of 2: yield (0.165 g, 55 %) ESI-MS: m/z for $M^{2+} = 725.1362$ found; 725.1357 calculated $[M-2PF_6]^+$. 1H NMR (500 MHz, CD_3CN) 9.52 (1H, s), 8.51 (4H, d, $J = 7.4$), 8.44 (1H, s), 8.31 (1H, s), 8.07 (4H, t, $J = 7.8$), 7.73 (4H, t, $J = 6.6$), 7.69 (1H, d, $J = 5.8$), 7.64 (1H, d, $J = 6.2$), 7.57 (1H, d, $J = 5.8$), 7.46-7.38 (4H, m), 7.32 (1H, d, $J = 5.4$), 7.27 (1H, d, $J = 5.6$), 5.01 (2H, s), 2.57 (3H, s). ^{19}F NMR (400MHz, CD_3CN) -168.99 ppm. Elemental analysis as chloride salt calculated: C, 54.28; H, 3.67; N, 14.07; Found: C, 54.2; H, 3.65; N, 13.96.

Characterization of 3: yield (0.151g, 57 %) ESI-MS: m/z for $M^{2+} = 299.07$. 1H MR (200 MHz, CD_3CN) 8.58 (2H, s), 8.54 (2H, s), 8.43 (2H, s), 8.14-8.04 (4H, m), 7.80 (4H, d, $J = 5.6$), 7.60 (2H, d, $J = 5.8$), 7.50-7.40 (4H, m), 7.31-7.26 (2H, m), 2.57 (6H, s). Elemental analysis as chloride salt calculated: C, 57.49; H, 4.22; N, 12.57; Found: C, 57.4; H, 4.2; N, 12.48.

5.3.5. Single crystal X-Ray diffraction studies and crystal structures of complex 1

As-synthesized crystal of complex **1** was coated with paratone-N and placed on top of a nylon cryoloop (Hampton research) and then mounted in the diffractometer. The data collection was done at 298 K. The crystal was mounted on a Super Nova Dual source X-ray diffractometer system (Agilent Technologies) equipped with a CCD area detector and operated at 250 W power (50 kV, 0.8 mA) to generate Mo K α radiation ($\lambda = 0.71073 \text{ \AA}$) and Cu K α radiation ($\lambda = 1.54178 \text{ \AA}$) at 298 K. Initial scans of each specimen were performed to obtain preliminary unit cell parameters and to assess the mosaicity (breadth of spots between frames) of the crystal to select the required frame width for data collection. CrysAlis^{Pro} program software was used suite to carry out overlapping φ and ω scans at detector (2θ) settings ($2\theta = 28^\circ$). Following data collection, reflections were sampled from all regions of the Ewald sphere to redetermine unit cell parameters for data integration. In no data collection was evidence for crystal decay encountered. Following exhaustive review of collected frames the resolution of the dataset was judged. Data were integrated using CrysAlis^{Pro} software with a narrow frame algorithm. Data were subsequently corrected for absorption by the program SCALE3 ABSPACK¹ scaling algorithm.

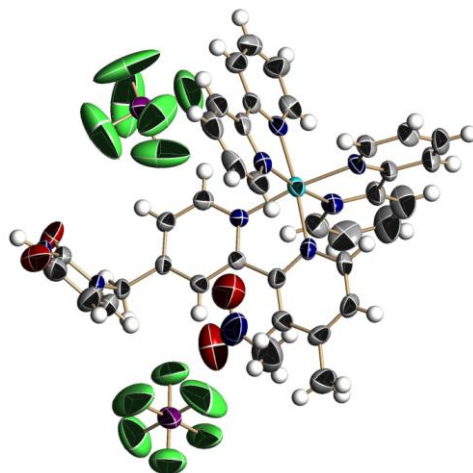


Figure 5.2. The ellipsoids in ORTEP diagrams are displayed at the 50 % probability level.

These structures were solved by direct method and refined using the SHELXTL 97 software suite. Atoms were located from iterative examination of difference F-maps following least squares refinements of the earlier models. Final model was refined anisotropically (if the number of data permitted) until full convergence was achieved. Hydrogen atoms were placed in calculated positions (C-H = 0.93 Å) and included as riding atoms with isotropic displacement parameters 1.2-1.5 times Ueq of the attached C atoms. In some cases modeling of electron density within the voids of the frameworks did not lead to identification of recognizable solvent molecules in these structures, probably due to the highly disordered contents of the large pores in the frameworks. Highly porous crystals that contain solvent-filled pores often yield raw data where observed strong (high intensity) scattering becomes limited to ~1.0 Å at best, with higher resolution data present at low intensity. A common strategy for improving X-ray data, increasing the exposure time of the crystal to X-rays, did not improve the quality of the high angle data in this case, as the intensity from low angle data saturated the detector and minimal improvement in the high angle data was achieved.

Additionally, diffused scattering from the highly disordered solvent within the void spaces of the framework and from the capillary to mount the crystal contributes to the background and the ‘washing out’ of the weaker data. Electron density within void spaces has not been assigned to any guest entity but has been modeled as isolated oxygen and/or carbon atoms. The foremost errors in all the models are thought to lie in the assignment of guest electron density. The structure was examined using the ADSYM subroutine of PLATON to assure that no additional symmetry could be applied to the models. The ellipsoids in ORTEP diagrams are displayed at the 50 % probability level.

Table 5.1. Crystal structure refinement details of complex 1.

Empirical formula	C ₃₇ H ₃₃ F ₁₂ N ₉ O ₄ P ₂ Ru
Formula weight	1058.73
Temperature	298 K
Wavelength	0.71073 Å
Crystal system	Monoclinic
Space group	C 2/c
Unit cell dimensions	$a = 39.898(4)$ Å $\alpha = 90^\circ$ $b = 10.0280(8)$ Å $\beta = 107^\circ$ $c = 22.1207(14)$ Å $\gamma = 90^\circ$
Unit cell volume	8462.4(13)
Z	8
Density (calculated)	1.662 mg mm ⁻³
Absorption coefficient	0.551
F(000)	4256
Crystal size	0.3 × 0.2 × 0.2 mm ³
Theta range for data collection	2.95 to 29.14
Index ranges	-51 ≤ h ≤ 53, -13 ≤ k ≤ 13, -27 ≤ l ≤ 29
Reflections collected	23879
Independent reflections	22963
Absorption correction	Semi-empirical from equivalents
Refinement method	Full-matrix least-squares on F ²
Data / restraints / parameters	9749/0/587
Goodness-of-fit on F ²	1.606
Final R indices [I>=2sigma(I)]	R ₁ = 0.0812, wR ₂ = 0.1504
R indices (all data)	R ₁ = 0.1609, wR ₂ = 0.1662
Largest diff. peak and hole	0.841 and -0.626 e.Å ⁻³
CCDC No	1035338

5.4. Results and discussion

5.4.1 Photophysical characterization of complexes 1 and 2

Optical spectra for complexes **1** and **2** are shown in Figure 5.3, which clearly revealed that the electronic spectra in the visible region for both complexes was

dominated by broad metal-to-ligand charge-transfer (MLCT; Ru(d π) \rightarrow bpy/L₁(π^*) and/or bpy/L₂(π^*) based transitions at ~455 nm.

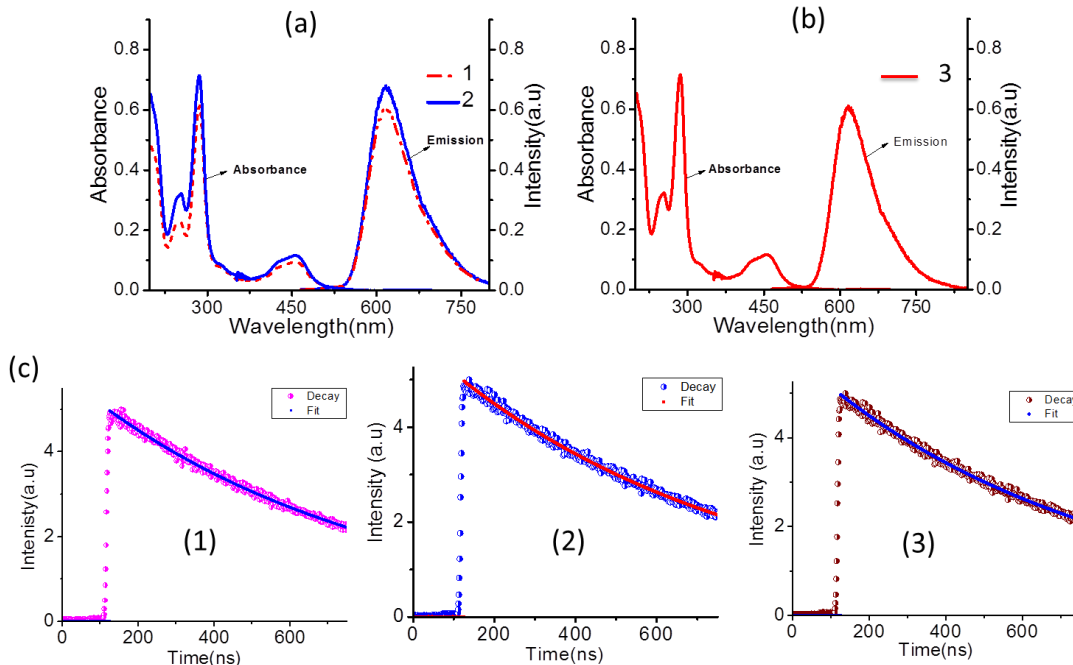


Figure 5.3. (a) Absorption, (b) emission, and (c) lifetime spectra for **1**, **2**, and **3** recorded in acetonitrile.

while emission band for respective complex was attributed to a ³MLCT transition (~620 nm for $\lambda_{\text{Ext}} = 455$ nm) as the Φ_{ISC} for the ISC process for Ru(II)-polypyridyl complexes is reported to be ~1 and occur within 40 fs.²⁴ Spectroscopic data for complex **1**: $\lambda_{\text{Max}}^{\text{Abs}} = 290$ nm, $\varepsilon = 22130 \text{ M}^{-1}\text{cm}^{-1}$; $\lambda_{\text{Max}}^{\text{Abs}} = 457$ nm, $\varepsilon = 12920 \text{ M}^{-1}\text{cm}^{-1}$; $\lambda_{\text{Max}}^{\text{Ems}} = 620$ nm ($\Phi_{\text{Ems}} = 0.048$) for λ_{Ext} of 455 nm and $\tau_{1/2} = 323$ ns ($\chi^2 = 1.14$) using 442 nm laser source; Spectroscopic data for complex **2**: $\lambda_{\text{Max}}^{\text{Abs}} = 290$ nm ($\varepsilon = 23060 \text{ M}^{-1}\text{cm}^{-1}$); $\lambda_{\text{Max}}^{\text{Abs}} = 456$ nm, $\varepsilon = 13850 \text{ M}^{-1}\text{cm}^{-1}$; $\lambda_{\text{Max}}^{\text{Ems}} = 617$ nm ($\Phi_{\text{Ems}} = 0.050$) for λ_{Ext} of 455nm and $\tau_{1/2} = 336$ ns ($\chi^2 = 1.02$); **3**: $\lambda_{\text{Max}}^{\text{Abs}} = 290$ nm ($\varepsilon = 23460 \text{ M}^{-1}\text{cm}^{-1}$); $\lambda_{\text{Max}}^{\text{Abs}} = 453$ nm, $\varepsilon = 14051 \text{ M}^{-1}\text{cm}^{-1}$; $\lambda_{\text{Max}}^{\text{Ems}} = 616$ nm ($\Phi_{\text{Ems}} = 0.055$) for $\lambda_{\text{Ext}} = 455$ nm and $\tau_{1/2} = 321$ ns ($\chi^2 = 1.12$) using 442 nm laser source.

Table 5.2. Photophysical properties of the complexes **1**, **2**, and **3** recorded in pure aqueous medium.

Complex	$\lambda_{\text{abs}}/\text{nm}$ ($\epsilon /10^3 \text{ M}^{-1} \text{ cm}^{-1}$)	λ_{ex} max/nm (λ_{em})	λ_{em} max/nm (λ_{ex})	Φ_f	$\tau(\text{ns})$
1	246 (18.59)	249			
	287 (54.74)	305			
	455 (9.41)	461 (617)	617	0.048	336
2	247 (28.08)	232			
	287 (79.35)	293			
	455 (13.85)	461 (619)	619	0.050	323
3	247 (28.08)	232			
	287 (79.35)	293			
	455 (13.85)	461 (620)	620	0.049	326

5.4.2. Isothermal titration calorimetry studies

Relative binding affinity of complexes **1**, **2**, and **3** towards calf-thymus DNA (CT-DNA) were evaluated using isothermal titration calorimetry (Figure 5.4). Association constants and thermodynamic parameters (Table 5.3) clearly reveal that the binding affinities for complexes **1** and **2** are much higher than that of **3** towards CT-DNA.

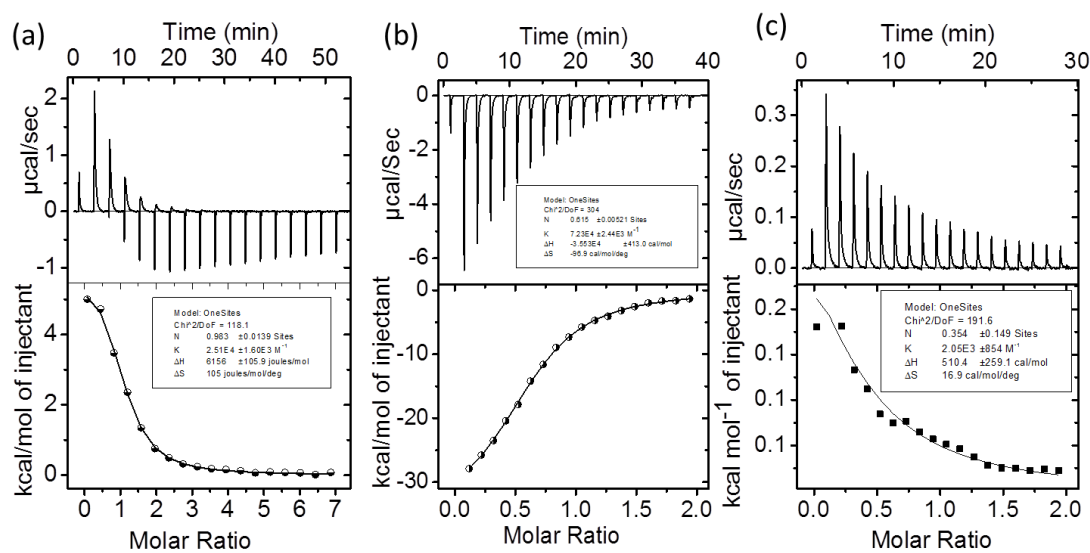


Figure 5.4. ITC binding profiles for the interaction of **1** (a) and **2** (b) and **3** (c) with CT-DNA at 25° C in Tris-HCl buffer pH=7.4.

Table 5.3. ITC derived CT-DNA binding parameters for **1**, **2**, and **3**.

Complex	1	2	3
$K_a [M^{-1}]$	$(2.51 \pm 0.16)10^4$	$(7.23 \pm 0.24)10^4$	$(2.05 \pm 0.85)10^3$
$\Delta H [KcalM^{-1}]$	1.47 ± 0.02	-35.5 ± 0.41	0.51 ± 0.25
$-\Delta S [KcalM^{-1}J]$	7.47	-28.87	5.03
$\Delta G [KcalM^{-1}]$	-6.0 ± 0.02	-6.68 ± 0.41	-4.52 ± 0.25
N [bp]	0.98 ± 0.01	0.61 ± 0.00	0.354 ± 0.14

The data shown in table 5.3 clearly indicate that the affinities of these three complexes are much lower than those of analogous Ru(II)-polypyridyl derivatives having functionality which favour an efficient DNA intercalation process.²² Complex **2** with 5-FU derivative was expected to be more lipophilic than the analogous complex **1** and anticipated to favour the interaction with DNA. Binding affinity of **2** towards CT-DNA was higher than the complex **1** by a factor of 2.9. A small positive enthalpy ($\Delta H_{ITC} = 1.47 \pm 0.02 \text{ KcalM}^{-1}$) and a high positive entropy (7.47 KcalM^{-1}) changes was observed for interaction of **1** with CT-DNA. These observations tend to suggest that the interaction of **1** with CT-DNA was entropically driven. The interaction of **2** with CT-DNA showed negative enthalpy ($\Delta H_{ITC} = -35.5 \text{ KcalM}^{-1}$) and entropy changes (-28.87 KcalM^{-1}). High negative enthalpy change was anticipated, as fluorine containing compounds generally have higher solvation enthalpy. This also indicated that the interaction was enthalpically driven as well. A slight positive enthalpy ($\Delta H_{ITC} = 0.51 \pm 0.25 \text{ Kcalmol}^{-1}$) and a positive entropy (5.03 KcalM^{-1}) changes was observed for interaction of **3** with CT-DNA which is an entropically driven interaction. The binding affinity of all three complexes for the CT-DNA is **2>1>3**. Further studies also confirmed that none of these three complexes could alter the relative viscosities of aqueous DNA solutions. All these observations suggested that **1**, **2**,

and **3** could interact with CT-DNA predominantly through groove binding. However, certain trivial influence of the electrostatic interactions between these cationic complexes (**1**, **2**, and **3**) with the negatively charged phosphate backbone cannot be completely ruled out.

5.4.3. Viscosity measurements

To determine DNA binding mode, relative viscosity of CT-DNA was measured in the presence of increasing concentrations of **1**, **2** and **3**. The intercalator ethidiumbromide and groove-binder $[\text{Ru}(\text{tpy})_2]^{2+}$ were used as controls for their respective modes of binding. In contrast to ethidiumbromide, neither complex **1** nor **2** increased the relative viscosity of DNA solutions, indicating that these complexes are not metallo-intercalators (Figure 5.5).

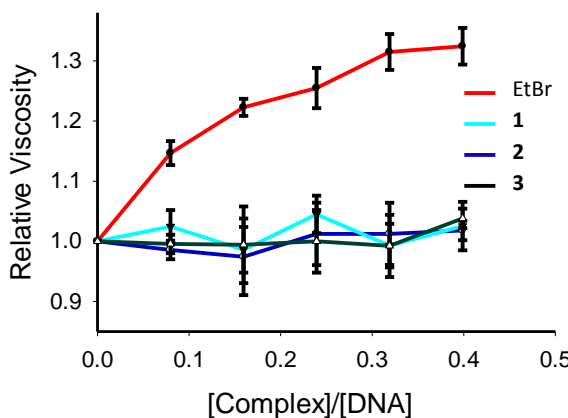


Figure 5.5. Change in relative viscosity of CT-DNA with increasing the concentrations of complex **1**, **2**, and **3**.

Both complexes were bound DNA through groove binding mode. Besides the non-substituted complex **3** was previously reported for its groove binding behavior.²⁴ This behavior is consistent with previous reports on other extended Ru(II)-terpyridyl complexes.²⁵

5.4.4. pBR322 plasmid DNA cleavage studies

Ru(II)-polypyridyl complexes are known for their DNA cleavage property by generating the reactive oxygen species such as $^1\text{O}_2$. We have further conducted the agarose electrophoresis studies by incubating pBR322 plasmid DNA with complexes **1** or **2**.

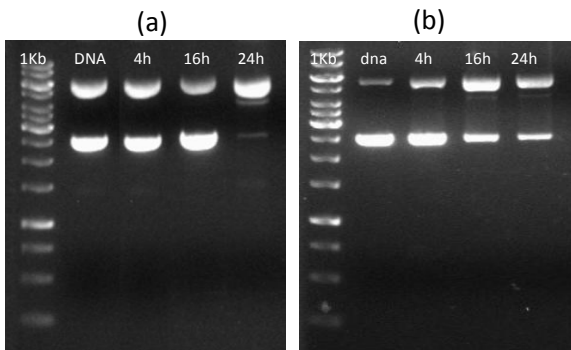


Figure 5.6. The gelectrophoresis image of pBR322 plasmid DNA incubated with **1** (a) and **2** (b) at different (4, 16 and 24 h) time intervals.

Since 5-FU is a well-known anticancer drug which is being used currently for the treatment of colorectal cancer patients it was anticipated that these novel complexes may be cytotoxic and can cleave the plasmid DNA into smaller fragments. Figure 5.6 shows that the complex **1** and **2** can almost completely converted the supercoiled plasmid DNA into nicked circular form in 24 h time. The reaction mixture of the complex **1** or **2** with plasmid pBR322 DNA was incubated at room temperature and allowed to react. At various time intervals the samples were kept at -20° C to monitor the time dependent cleavage. The low concentrations of **1** (40 μM) or **2** (40 μM) were used to check the DNA damage activity of these lipophilic cationic molecules which can convert the supercoiled DNA into nicked circular form. At longer incubation time (16-24 h), the complete conversion of supercoiled form into linear form has been taken place (Figure 5.6a, b).

5.4.5. Cytotoxicity studies

With the positive results obtained DNA cleavage studies it was anticipated that these two complexes will be toxic towards the cancer cell line.

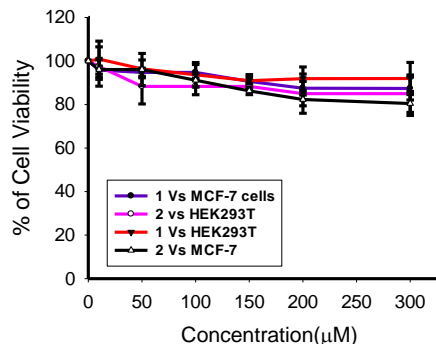


Figure 5.7. MTT assay results for the complexes **1** and **2** in HEK293 and MCF-7 cells after 24 h incubation.

To estimate the IC_{50} values we have conducted the cytotoxicity studies of complexes **1**, **2**, and **3** on HEK293 and MCF-7 cells using MTT (MTT = (3-(4,5-dimethylthiazol-2-yl)-2,5-diphenyltetrazoliumbromide) assay methodology. The cell viability was found to be $\geq 85\%$ after incubation with high concentrations (300 μM) of **1**, **2**, and **3** for 24 h. Thus, MTT assay confirmed that the insignificant toxicity of all three complexes towards HEK293 and MCF-7 cell lines. Evaluated IC_{50} values were found to be $> 300 \mu\text{M}$ (Figure 5.7). These results are against to those obtained from gel electrophoresis studies and accounted for the intra cellular DNA repair mechanism exist in the live cells.

5.4.6. Live cellular imaging studies

Negligible toxicity towards MCF-7 cells encouraged us to explore their application potential as imaging agents and accordingly live MCF-7 cells were incubated separately with 50 μM of **1**, **2**, and **3** at 37° C. Close comparison of the confocal laser scanning microscopic (CLSM) images as well as the images of the co-

staining experiments with well-known ER staining agent clearly revealed that intracellular emission for **1** and **2** were found to be exactly superimposed with those for ER-Tracker™ green (Figure 5.8a, b).

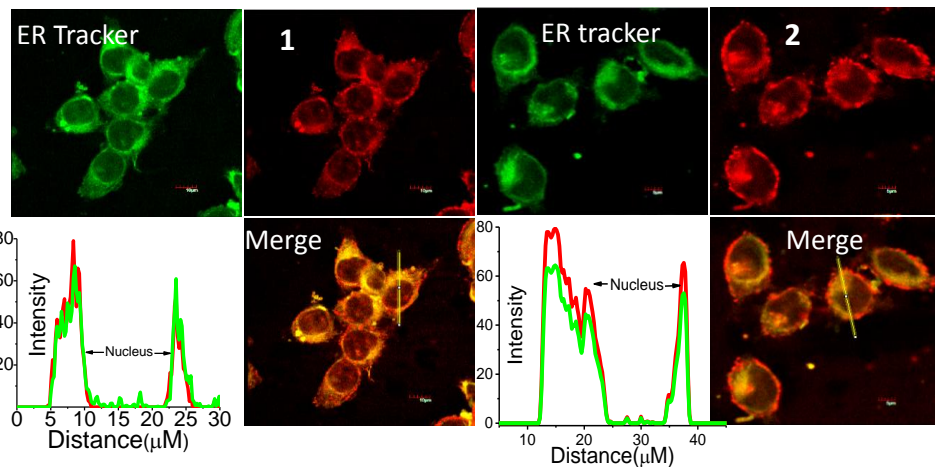


Figure 5.8. CLSM images show the live cell uptake of **1** and **2**. Co-localization studies performed with ER-Tracker™ green.

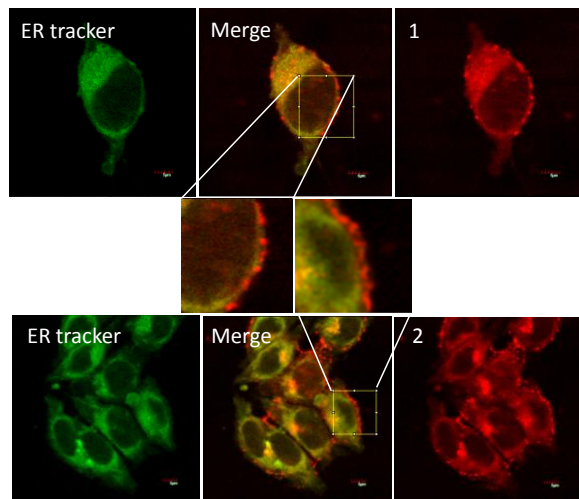


Figure 5.9. Confocal images of live MCF-7 cells incubated with complex **1** and **2**.

Also, distinct emission of **1** and **2** was also observed from the cell membrane, indicating that the cell membrane was also a target for the reagents **1** and **2** (Figure 5.9a). Identical studies with **3** did not show any such specificity towards lipid dense regions like ER or cell membrane. Moreover, complex **3** was

distributed throughout the cell (Figure 5.10a). The enlarged confocal images for reagents **1** and **2** (Figure 5.9) revealed dot-like structures with red fluorescence in bright-field microscopy, a pattern that is observed earlier for localization of lipophilic reagents at the cell membrane.²³ Such dot like structures scattered in the cytoplasm presumably suggested that the reagents were also sequestered in cytoplasmic vacuoles, which are known to play a subordinate role in endocytosis.^{26,24}

5.4.7. Correlation between the lipophilicity and cellular uptake.

Partition coefficients ($\log P$) for these three complexes were evaluated by shake-flask method and these were correlated to the lipophilicity of respective complexes. Lipophilicity of the complexes **1** ($\log P = -0.85$), **2** ($\log P = -0.50$), and **3** ($\log P = -1.1$) were evaluated. (<http://www.molinspiration.com/cgi-bin/properties>). This data clearly reveal that $\log P$ is the highest for complex **2** followed by **1** and **3**. There were some contrasting views in correlating the distinct role of lipophilicity and overall charge of the Ru(II)-polypyridyl derivatives to the cellular internalization.

However, it has been argued by many research groups that lipophilicity of the reagent is more important than the overall charge of the cationic Ru(II)-complexes in influencing the cellular uptake process.^{27,15,24,28,29} For our present study, all three complexes had the same overall charge (2+), while their lipophilicity followed the order **2>1>3**. Thus, one would presume that the cellular internalization would follow the order **2>1>3** and the experimental data are in accordance with the presumption (Table 5.3). This was further confirmed by the results of the MP-AES studies.

Table 5.3. LogP values obtained using shake-flask method. Molinspiration software was used for calculation of logP values for uracil and 5-FU.

Complex	logP	Ru accumulation ppm / 10^6 cells
1	-0.85	1.5
2	-0.50	2.3
3	-1.1	0.8

Fluorine substitution in complex **2** was used to improve the lipophilicity as compared to complex **1**. Thus, evaluated results were in good agreement with the trend described in the previous literature reports.²⁴ The literature reports also reveal that more lipophilic cationic reagent are generally accumulated preferentially in the regions like ER, while analogous reagents having comparable overall charge and relatively lower lipophilicity would have preference for nuclei.^{13,4,30}

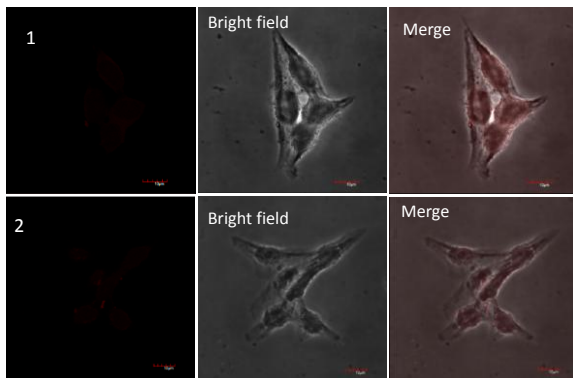


Figure 5.10. Live MCF-7 cells incubated with **1**, **2** at 4° C.

Earlier reports reveal that internalization of Ru(II)-polypyridyl derivatives could occur through energy-dependent and/or energy-independent processes.^{26,31,32} The cellular uptake of complexes **1** and **2** were found to be significantly reduced at temperature 4°C (Figure 5.10). Figure 5.10 clearly reveal that complex **1** and **2** were taken up by the cells with energy-dependent transport mechanism.³³ This

further suggested that the cellular uptake of complexes **1** and **2** presumably happened following an energy dependent endocytosis pathway.^{24,34,35} However, one could not completely rule out the possibilities of an adverse influence of the reagent diffusion through the cell membrane due to reduced reagent solubility and decrease in cell membrane fluidity with lowering of temperature.

5.4.8. Fixed cell imaging studies

Literature reports reveal that the lipid bodies of cytoplasm in living cells are dynamic and their identification has methodological limitations, as lipid bodies dissipate upon drying or dissolve upon cell fixation.³⁶ This clearly reveals that the fixation of cells using paraformaldehyde (PFA) is expected to alter the subcellular distribution of internalized reagents. For example, some peptide-fluorophore conjugates have been shown to move from the cytoplasm to the nucleus following the fixation with formaldehyde.³⁷ To check such a possibility, we examined confocal laser scanning microscopic (CLSM) images of the PFA fixed MCF-7 cells after incubation with 50 µM of reagents **1** and **2** (Figure 5.11).

Co-staining experiments were also performed with DAPI, a commonly used commercial nuclear staining agent. For cells treated with **1** and **2**, CLSM images were recorded following excitation with 442 nm laser and intra cellular emission of respective complexes were observed at 620 nm. Superimposed fluorescence intensity profile plots (blue and red color emission spectra) of the intracellular emission signals of DAPI with those of **1** or **2**, confirmed that both reagents were as efficient as DAPI in staining the nucleus of the MCF-7 cells.

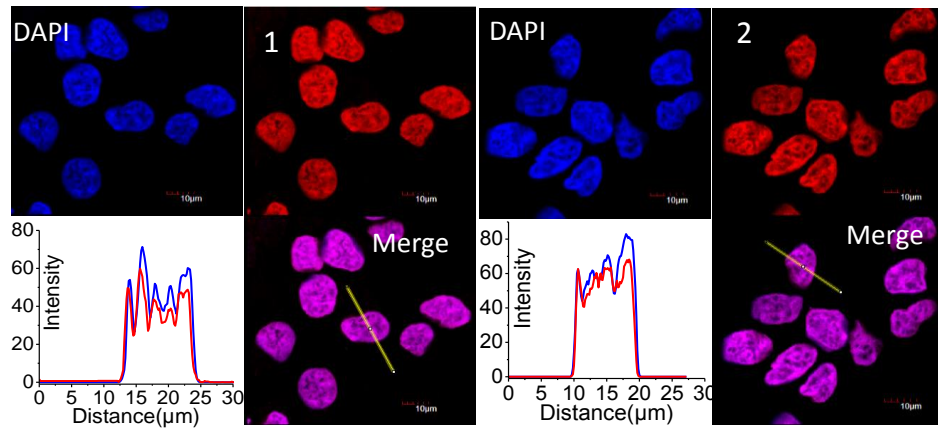


Figure 5.11. Confocal microscopy images of PFA fixed MCF-7 cell stained with **1** and **2**. Co-localization studies performed using DAPI.

To examine the cellular uptake and staining properties of the analogous model complex **3**, we incubated the live MCF-7 cells with complex **3** for 4 h, and then imaged using confocal microscopy. The CLSM images revealed that unlike **1** and **2**, the non-specific internalization of **3** in cytoplasm and nucleus of live MCF-7 cells (Figure 5.10a) was observed.

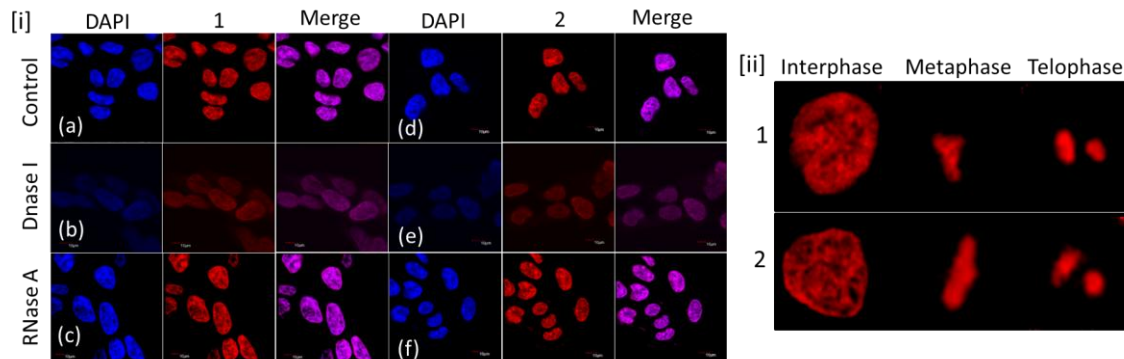


Figure 5.12. Confocal images of MCF-7 cells stained with **1** (a-c) and **2** (d-f), (ii) confocal images of MCF-7 cells during different stages of cell division using **1** and **2** as the cellular imaging agents.

Besides, the treatment of PFA fixed MCF-7 cells with **3** also resulted in non-specific staining of cellular compartments (Figure 5.10b). Presumably, this could be attributed to the lack of the functional moieties (U/5-FU) and lower lipophilicity

(logP = -1.1) of complex **3**. In order to check the preferential binding of these two reagents to nuclear DNA, deoxyribonuclease (DNase I) and ribonuclease (RNase A) digest experiments were carried out. DNase I is an enzyme that catalyzes the hydrolytic cleavage of phosphodiester linkages in the DNA and RNase A is a type of nuclease that catalyzes the degradation of RNA into smaller components.³⁸

DAPI was used for control experiments. Comparison of the CLSM images of the cells pretreated with DNase I (Figure 5.12(i) b & e) and RNase A (Figure 5.12(i) c & f) clearly revealed that the intracellular fluorescence intensities of reagents **1** and **2** from the nucleus of MCF-7 cells were significantly reduced for cells that were pre-treated with DNase I and not for those pre-treated with RNase A. This confirmed that **1** and **2** are mainly targeting nuclear DNA in the fixed cell nucleus. To emphasize more on the specificity of complexes **1** and **2** binding to DNA, we synchronized the cells by treating with colchicine and released at different time points to obtain the cell cycle stages of prophase, metaphase, and telophase (Figure 5.12(ii)). Clear staining of the DNA at various stages could be seen using complexes **1** and **2**.

5.4.9. Photostability test

We have also examined the photostability of these two dyes and compared with that for DAPI by using confocal microscopy (Figure 5.13(a)) and fluorescence spectroscopy methods (Figure 5.13(b)). The fluorescence intensity of DAPI upon continuous irradiation in fixed MCF-7 cells (at 359 nm for 300 sec) was drastically reduced.

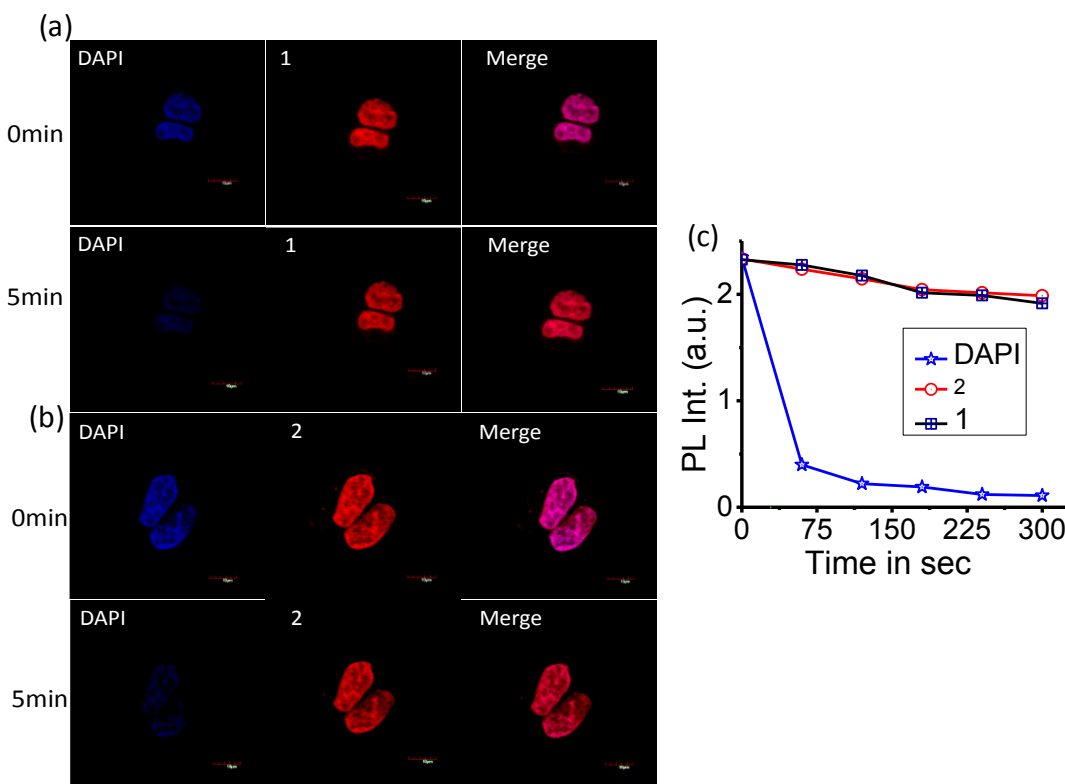


Figure 5.13. Photostability test for **1**, **2**, and DAPI in MCF-7 cells tested by confocal microscopy (a), (b) and by fluorescence spectroscopy (c).

In contrast, fluorescence intensity of **1** and **2** were only reduced by ~ 20% upon exposure at 442 nm for 300 sec, reflecting the photostability of these two fluorescent staining reagents. Despite remarkable stability and high emission quantum yield, the use of quantum dot material as imaging reagent is restricted owing to the high toxicity.^{39,40,41} Considering these features; the scope of visible light excitable reagents **1** and **2** with a $\Delta\lambda_{Ss}$ of ~ 160 nm is significant.

5.5. Conclusion

In conclusion, we have successfully developed two new U/5FU conjugated Ru(II)-complexes (**1** and **2**) as imaging reagents. Unlike model reagent **3**, both reagents were preferentially localized in lipid dense regions like ER, cell membrane, and

cytoplasmic vacuoles of live MCF-7 cells. This illustrated the role of U/5FU functionality in achieving specificity for the lipid dense regions in live cells. Relatively higher lipophilicity of **2** helped in achieving better cellular internalization. For fixed cell, the lipid layer disruption helped in explicit localization in cell nucleus through specific interaction with cellular DNA. Insignificant toxicity, photo-stability, visible light excitation, and large $\Delta\lambda_{SS}$ of ~160 nm are other key features for these two reagents and have significant characteristics for application as an imaging reagent.

5.6. References

1. C. P. Montgomery, B. S. Murray, E. J. New, R. Pal and D. Parker, *Acc. Chem. Res.*, 2009, **42**, 925–937.
2. M. Terasaki, J. Song, J. R. Wong, M. J. Weiss and L. B. Chen, *Cell*, 1984, **38**, 101–108.
3. A. S. Boutorine, D. S. Novopashina, O. A. Krasheninina, K. Nozeret and A. G. Venyaminova, *Molecules*, 2013, **18**, 15357–15397.
4. M. R. Gill, J. Garcia-Lara, S. J. Foster, C. Smythe, G. Battaglia and J. A. Thomas, *Nat. Chem.*, 2009, **1**, 662–667.
5. M. P. Coogan, V. Fernandez-Moreira, J. B. Hess, S. J. A. Pope and C. Williams, *New J. Chem.*, 2009, **33**, 1094–1099.
6. A. J. Amoroso, M. P. Coogan, J. E. Dunne, V. Fernández-Moreira, J. B. Hess, A. J. Hayes, D. Lloyd, C. Millet, S. J. A. Pope and C. Williams, *Chem. Commun.*, 2007, 3066–3068.
7. V. Fernández-Moreira, F. L. Thorp-Greenwood and M. P. Coogan, *Chem. Commun.*, 2010, **46**, 186–202.
8. M. P. Coogan, P. J. Dyson and M. Bochmann, *Organometallics*, 2012, **31**, 5671–5672.
9. M. R. Gill, D. Cecchin, M. G. Walker, R. S. Mulla, G. Battaglia, C. Smythe and J. A. Thomas, *Chem. Sci.*, 2013, **4**, 4512–4523.
10. J. P. Lu, Y. Wang, D. S. Sliter, M. M. P. Pearce and R. J. H. Wojcikiewicz, *J. Biol. Chem.*, 2011, **286**, 24426–24433.
11. S. Zhang, T. Wu, J. Fan, Z. Li, N. Jiang, J. Wang, B. Dou, S. Sun, F. Song and X. Peng, *Org. Biomol. Chem.*, 2013, **11**, 555–558.
12. J. R. Lakowicz, *Principles of Fluorescence Spectroscopy Principles of Fluorescence Spectroscopy*, Springer, 3rd Ed., 2006.
13. E. Baggaley, M. R. Gill, N. H. Green, D. Turton, I. V. Sazanovich, S. W. Botchway, C. Smythe, J. W. Haycock, J. A. Weinstein and J. A. Thomas, *Angew. Chemie Int. Ed.*, 2014, **53**, 3367–3371.
14. M. R. Gill, J. Garcia-Lara, S. J. Foster, C. Smythe, G. Battaglia and J. A. Thomas, *Nat. Chem.*, 2009, **1**, 662–667.
15. F. R. Svensson, M. Abrahamsson, N. Strömberg, A. G. Ewing and P. Lincoln, *J. Phys. Chem. Lett.*, 2011, **2**, 397–401.

16. L. Blackmore, R. Moriarty, C. Dolan, K. Adamson, R. J. Forster, M. Devocelle and T. E. Keyes, *Chem. Commun.*, 2013, **49**, 2658–2660.
17. C. A. Puckett and J. K. Barton, *J. Am. Chem. Soc.*, 2009, **131**, 8738–8739.
18. X. Li, A. K. Gorle, T. D. Ainsworth, K. Heimann, C. E. Woodward, J. Grant Collins and F. Richard Keene, *Dalt. Trans.*, 2015, **44**, 3594–3603.
19. R. Cao, J. Jia, X. Ma, M. Zhou and H. Fei, *J. Med. Chem.*, 2013, **56**, 3636–3644.
20. X. Meng, M. L. Leyva, M. Jenny, I. Gross, S. Benosman, B. Fricker, S. Harlepp, P. Hebraud, A. Boos, P. Wlosik, P. Bischoff, C. Sirlin, M. Pfeffer, J.-P. Loeffler and C. Gaiddon, *Cancer Res.*, 2009, **69**, 5458–5466.
21. D. B. Longley, D. P. Harkin and P. G. Johnston, *Nat. Rev. Cancer*, 2003, **3**, 330–338.
22. S. Farquharson, A. Gift, C. Shende, F. Inscore, B. Ordway, C. Farquharson and J. Murren, *Molecules*, 2008, **13**, 2608–2627.
23. N. Zhang, Y. Yin, S. J. Xu and W. S. Chen, *Molecules*, 2008, **13**, 1551–1569.
24. O. Zava, S. M. Zakeeruddin, C. Danelon, H. Vogel, M. Gratzel and P. J. Dyson, *ChemBioChem*, 2009, **10**, 1796–1800.
25. C. Metcalfe, C. Rajput and J. A. Thomas, *J. Inorg. Biochem.*, 2006, **100**, 1314–1319.
26. M. R. Gill and J. A. Thomas, *Chem. Soc. Rev.*, 2012, **41**, 3179–3188.
27. R. Cao, J. Jia, X. Ma, M. Zhou and H. Fei, *J. Med. Chem.*, 2013, **56**, 3636–3644.
28. V. Fernández-Moreira, F. L. Thorp-Greenwood, A. J. Amoroso, J. Cable, J. B. Court, V. Gray, A. J. Hayes, R. L. Jenkins, B. M. Kariuki, D. Lloyd, C. O. Millet, C. F. Williams and M. P. Coogan, *Org. Biomol. Chem.*, 2010, **8**, 3888–3901.
29. X. Liang, J. Mack, L.-M. Zheng, Z. Shen, and N. Kobayashi, *Inorg. Chem.*, 2014, **53**, 2797–2802.
30. W. Xu, J. Zuo, L. Wang, L. Ji and H. Chao, *Chem. Commun.*, 2014, **50**, 2123–2125.
31. W. Cao, W. Zheng and T. Chen, *Sci. Rep.*, 2015, **5**, 9157–9168.
32. S. M. Cloonan, R. B. P. Elmes, M. Erby, S. A. Bright, F. E. Poynton, D. E. Nolan, S. J. Quinn, T. Gunnlaugsson and D. C. Williams, *J. Med. Chem.*, 2015, **58**, 4494–4505.
33. G. Drin, S. Cottin, E. Blanc, A. R. Rees and J. Temsamani, *J. Biol. Chem.*, 2003, **278**, 31192–31201.
34. M. P. Coogan and V. Fernández-Moreira, *Chem. Commun.*, 2014, **50**, 384–399.

35. C. A. Puckett and J. K. Barton, *J. Am. Chem. Soc.*, 2007, **129**, 46–47.
36. C. A. Puckett, R. J. Ernst and J. K. Barton, *Dalt. Trans.*, 2010, **39**, 1159–1170.
37. J. P. Richard, *J. Biol. Chem.*, 2002, **278**, 585–590.
38. S. Feng, Y. K. Kim, S. Yang and Y.-T. Chang, *Chem. Commun.*, 2010, **46**, 436–438.
39. W. Liu, M. Howarth, A. B. Greytak, Y. Zheng, D. G. Nocera, A. Y. Ting and M. G. Bawendi, *J. Am. Chem. Soc.*, 2008, **130**, 1274–1284.
40. C.-L. Huang, C.-C. Huang, F.-D. Mai, C.-L. Yen, S.-H. Tzing, H.-T. Hsieh, Y.-C. Ling and J.-Y. Chang, *J. Mater. Chem. B*, 2015, **3**, 651–664.
41. R. Gui, H. Jin, Z. Wang and L. Tan, *Coord. Chem. Rev.*, 2015, **296**, 91–124.

Conclusion of the Thesis

The thesis entitled “Design, synthesis and DNA interaction studies with novel photosensitizer molecules as efficient photodynamic therapeutic agents” describes the synthesis of novel Ru(II) and Ru(II)-Pt(II)-polypyridyl complexes. In this thesis the DNA binding properties of several new Ru(II) complexes have been investigated in search of novel anti-cancer agents. The first chapter is basically the introductory chapter, which describes “Introduction to the eukaryotic cell and its components like DNA, endoplasmic reticulum, cell membrane, cellular uptake and cell division processes etc. This chapter 1 also described the applications of ruthenium base complexes as anti-cancer drugs and cellular imaging reagents.

In chapter 2 we have discussed; how the dinuclear Ru(II)-Pt(II) complexes can interact with DNA and the importance of the combination of both the ruthenium and platinum metal centres in achieving the required cytostatic activity. This chapter also gave the insight to the design, synthesis and cytostatic Ru(II)-Pt(II) bis(terpyridyl) anticancer complex that blocks entry of cell cycle into S-phase. The promising metal complexes other than cisplatin is the Ru(II) or Ru(III) complexes which exhibit relatively low ligand exchange rates, which are comparable to those of platinum(II) complexes. The main aim of the thesis work is to achieve bimodal toxicity by synthesizing the cisplatin analogue which is combined with Ru(II) unit that can generate the ${}^1\text{O}_2$. Accordingly, we have successfully synthesized a new binuclear metal complex and performed detailed biological studies to understand the mechanism of the cytostatic activity of these new anti-proliferative reagent molecules.

The synergistic effect of light, molecular oxygen and a photosensitizer (PS) has been utilized in achieving photodynamic therapeutic (PDT) property for the treatment of

Conclusions

cancer. In search of novel PS the chapter 3 described the photo-induced cytotoxicity, anti-metastatic behaviour of Ru(II)-polypyridyl complexes through the generation of ${}^1\text{O}_2$. These photo-active Ru(II) complexes which were conjugated to the amino acids Tyrosine and Tryptophan have shown the anticipated photo-induced cytotoxicity in both the 2D and 3D tumor cell lines. Due to the conjugation of the lipophilic amino acids these complexes have easily been taken up by the A549 cancer cells. These complexes were also capable of inhibiting the cellular migration and invasion by G1 cell cycle arrest. They also induce the cell apoptosis by up-regulation of the apoptosis markers caspase 3/9.

The foremost limitation of the Ru(II)-terpyridine complexes, discussed in chapter 2, was the short lived excited state of the Ru(II)-terpyridine centre. This accounted for a faster deactivation and lower efficiency for generation of the active ${}^1\text{O}_2$. In this chapter 4 we have synthesized the analogous Ru(II)-Pt(II)-polypyridyl complexes those discussed in chapter 2. These complexes were found to be failed to induce the cytotoxicity in A549 cancer cells under the photo-irradiation conditions or in the dark conditions. However, they could cleave the plasmid DNA into nicked circular form which is a sign for the DNA damaging ability of these two molecules. The reason for the lower cytotoxicity of these complexes was presumably the cellular DNA repair mechanisms exist inside the cell.

There are significant activities in designing appropriate imaging reagents for visualization of specific organelles as this helps in gaining insight for monitoring important biological processes. Chapter 5 discussed about the design and synthesis of new Ru(II)-polypyridyl complexes which were conjugated with uracil or 5-fluorouracil moiety. These reagents were found to stain the nuclear DNA in the PFA fixed MCF-7 cells. In this chapter 5 we have studied the cellular imaging applications of the synthesized Ru(II) complexes. We also have demonstrated the stability towards photo-bleaching, cell

membrane permeability; these complexes have showed the nominal cytotoxicity and luminescence in the longer wavelength following excitation with visible light. Our studies revealed that these lipophilic reagents could get localized specifically in the ER region of the live MCF-7 cells following an endocytosis pathway. Detailed studies with RNase A and DNase I reveal that for fixed cells localization happened in nucleus through interaction with DNA and unlike DAPI, these reagents are stable towards photobleaching. The specific selectivity in the DNA-binding of these molecules means that such complexes may find future potential applications as probes of DNA structure and function in roles ranging from molecular biology to medicine.

Future scope of the research

The studies conducted in this thesis may provide a basis for the future design and optimization of Ru(II)-polypyridyl complexes in searching of novel anti-cancer drugs and cellular imaging reagents. The judicious selection of the lipophilic moiety could improve the cellular internalisation of Ru(II) metal complexes, which consequently leads the higher cytotoxicity of the reagents. Therefore, the flexible substituent chemistry of these Ru(II) complexes allows the design and synthesis of many novel Ru(II)-polypyridyl complexes conjugated with the biologically relevant molecules.

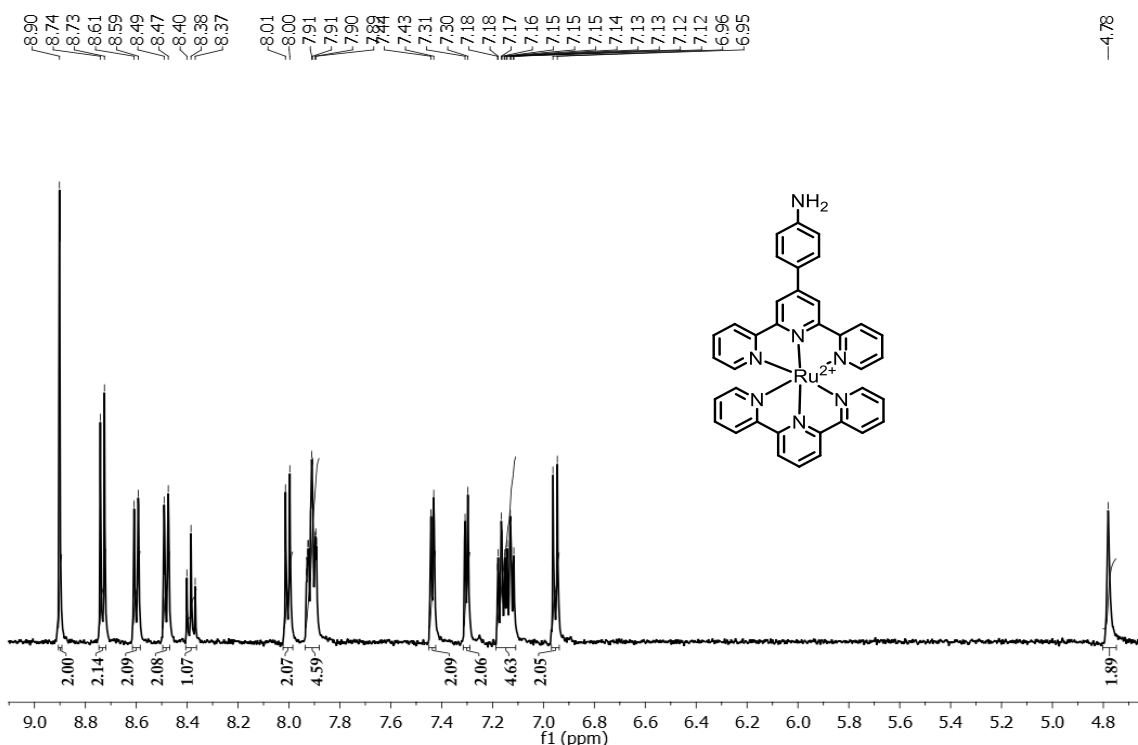


Figure 1. ^1H NMR spectra recorded in DMSO-d_6 .

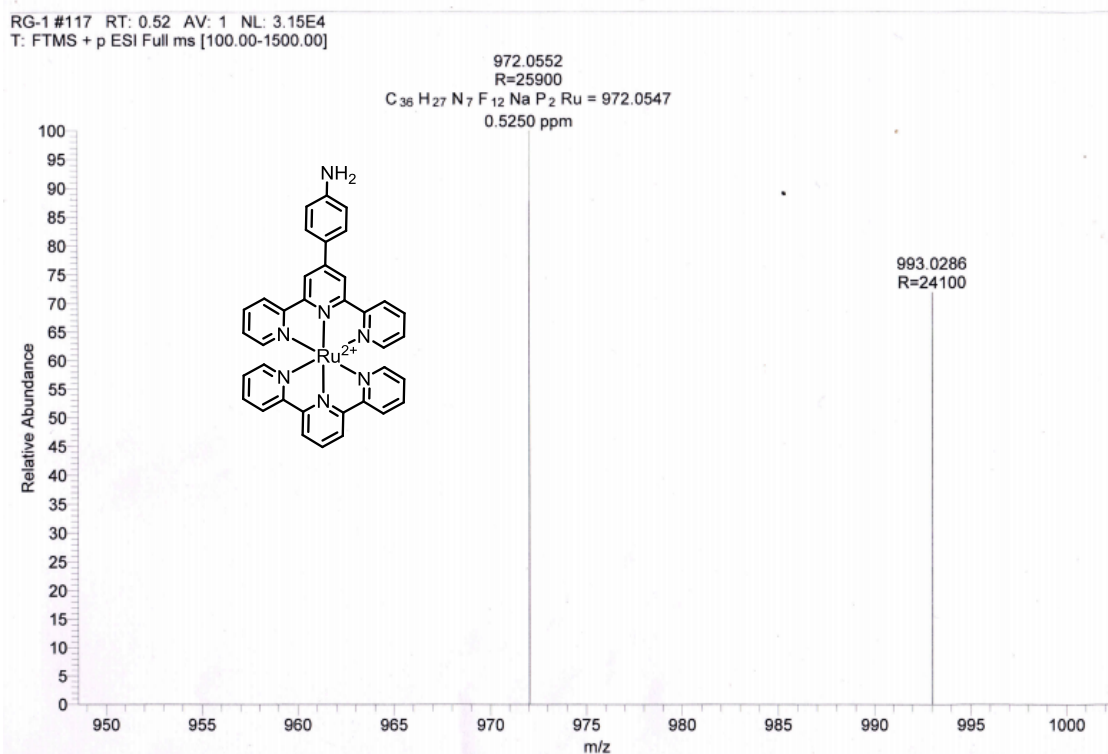


Figure 2. ESI Mass spectra recorded in acetonitrile.

Appendix

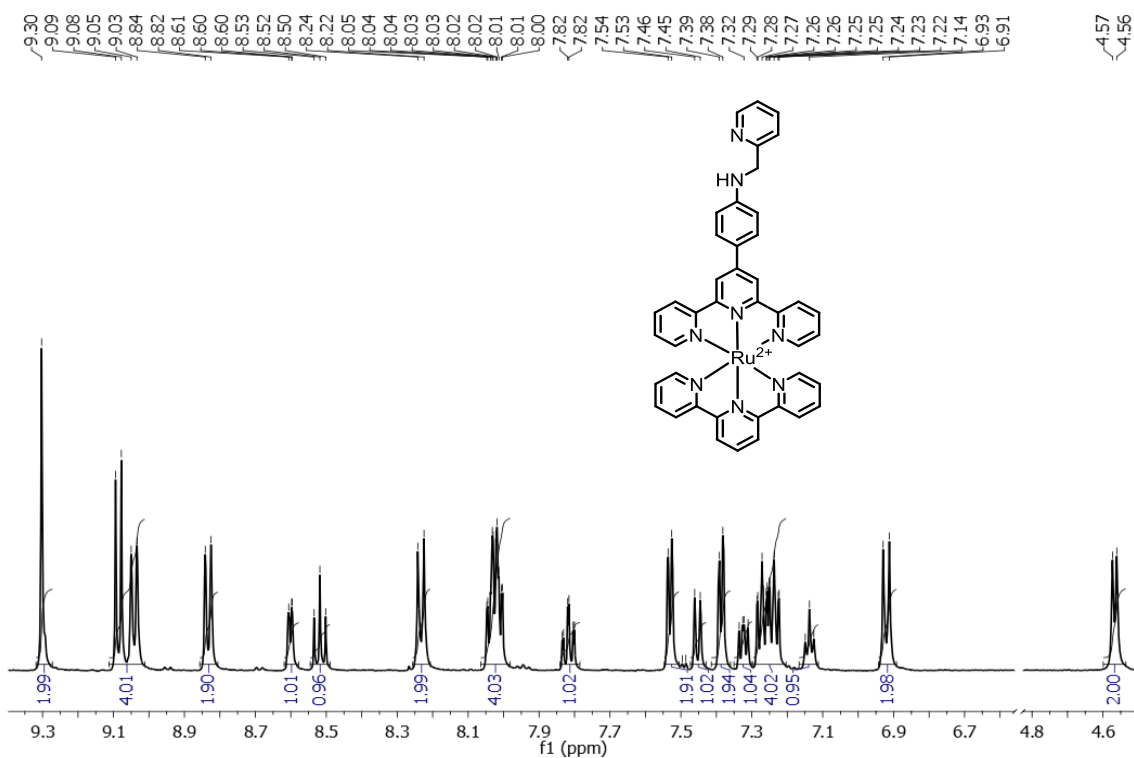


Figure 3. ^1H NMR spectra recorded in DMSO-d_6 .

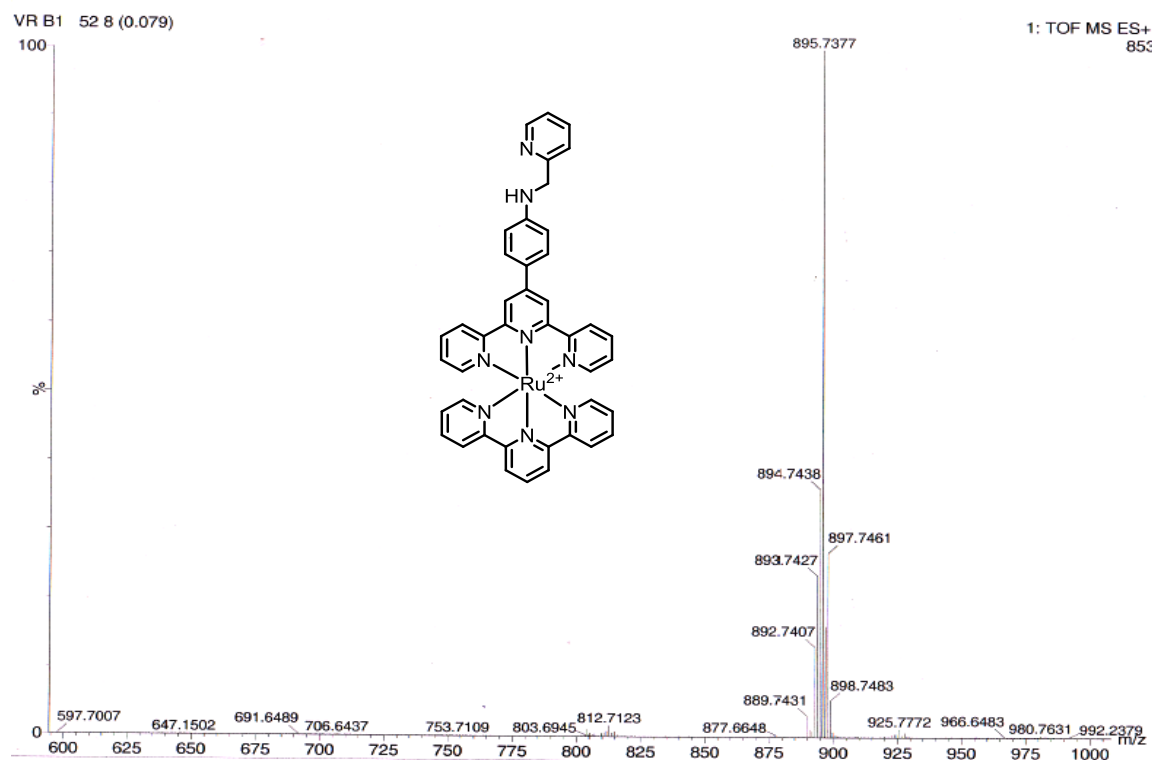


Figure 4. ESI Mass spectra recorded in methanol.

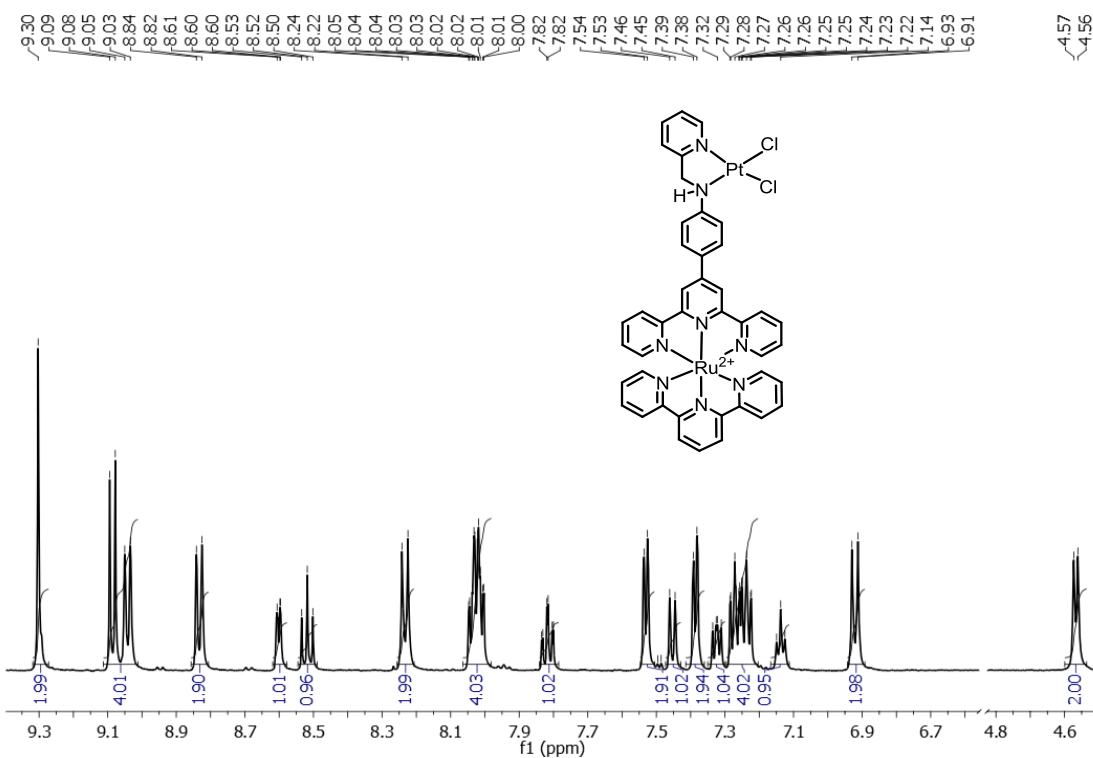


Figure 5. ¹H NMR spectra recorded in DMSO-d₆.

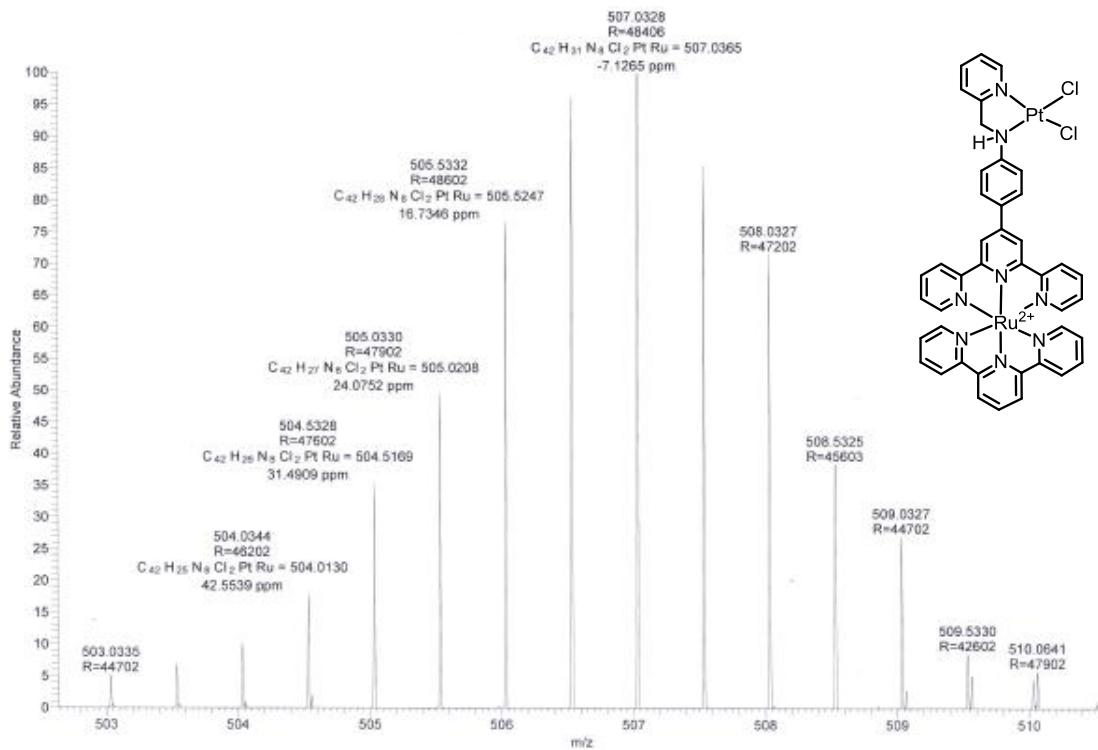


Figure 6. ESI Mass spectra recorded in acetonitrile.

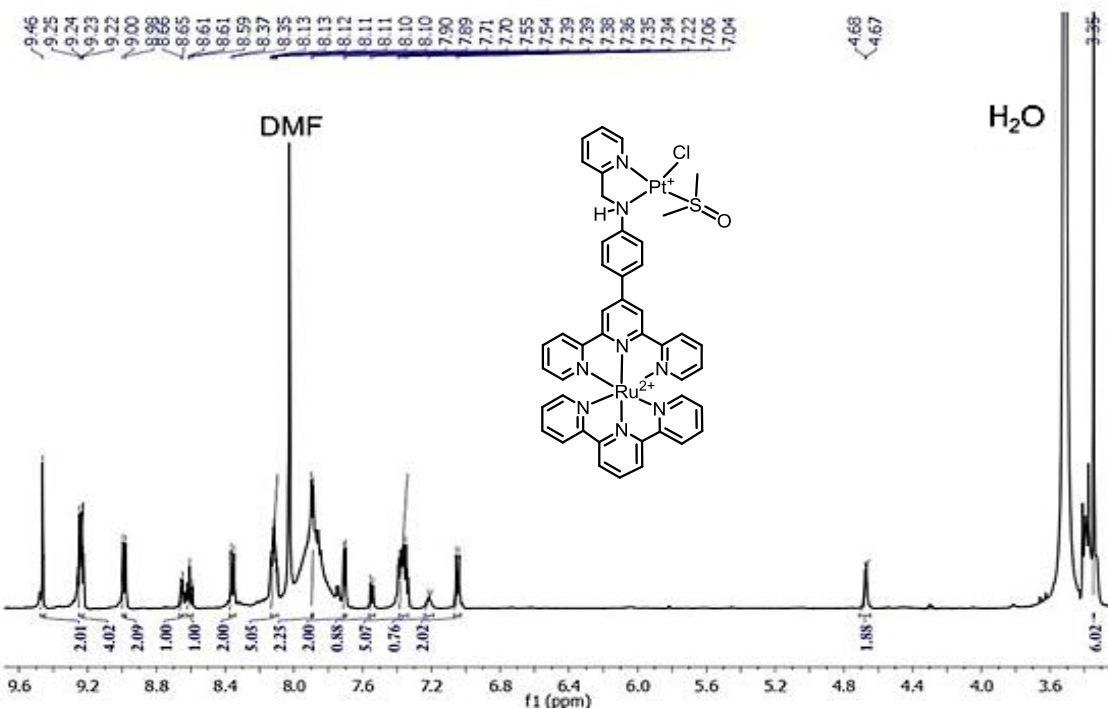


Figure 7. ^1H NMR spectra recorded in DMF-d_7 . Solvent peaks are indicated.

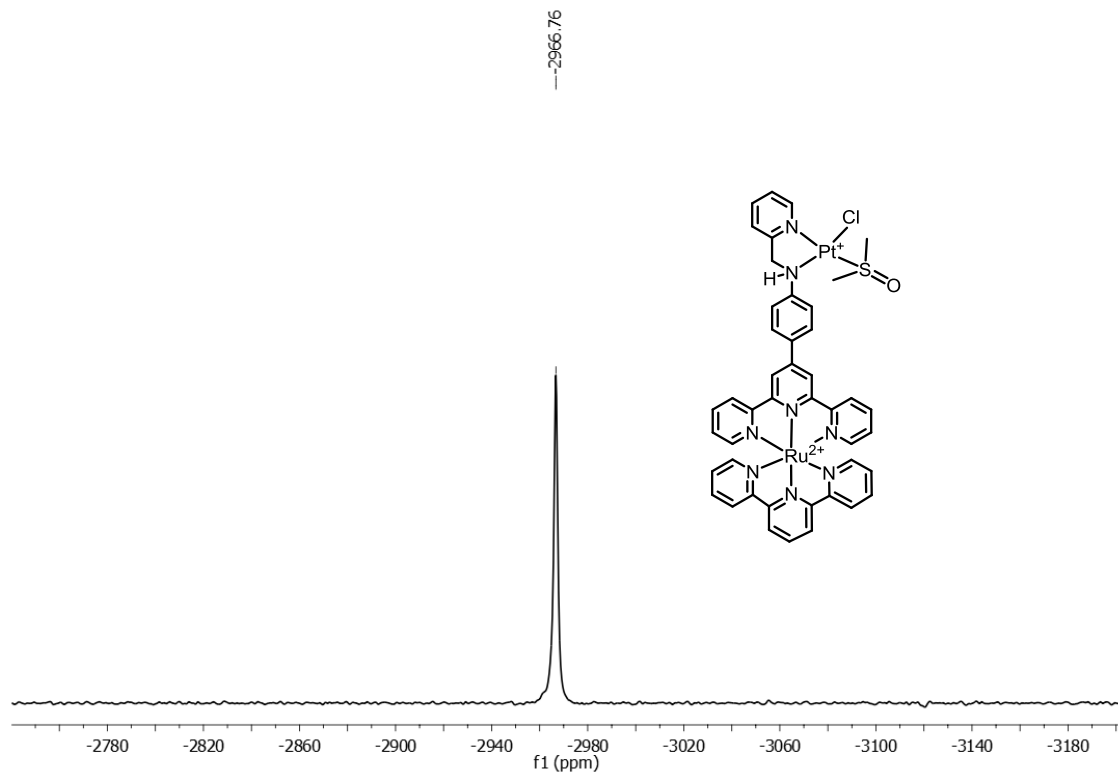


Figure 8. ^{195}Pt NMR spectra recorded in DMF-d_7

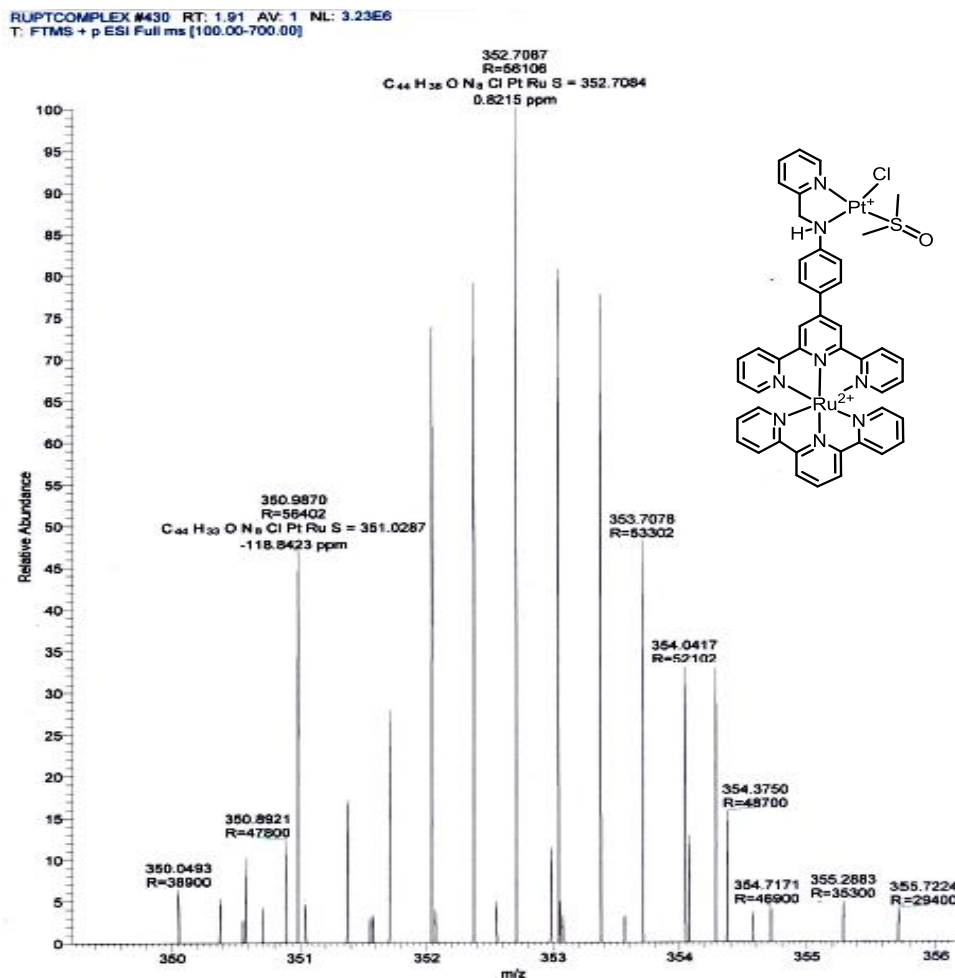


Figure 9. ESI Mass spectra recorded in acetonitrile.

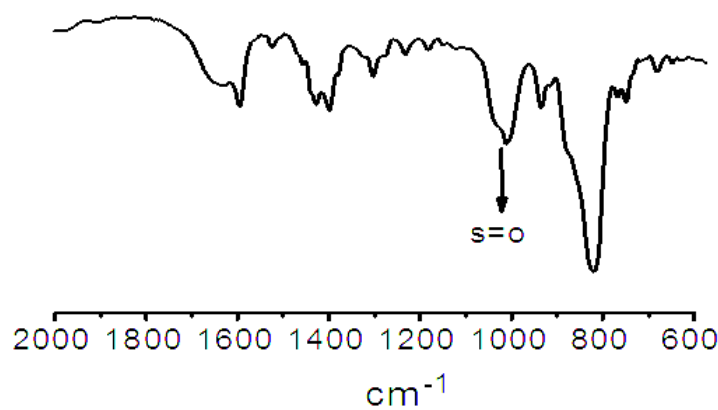


Figure 10. IR spectrum where the ν (SO) stretching frequency is highlighted.

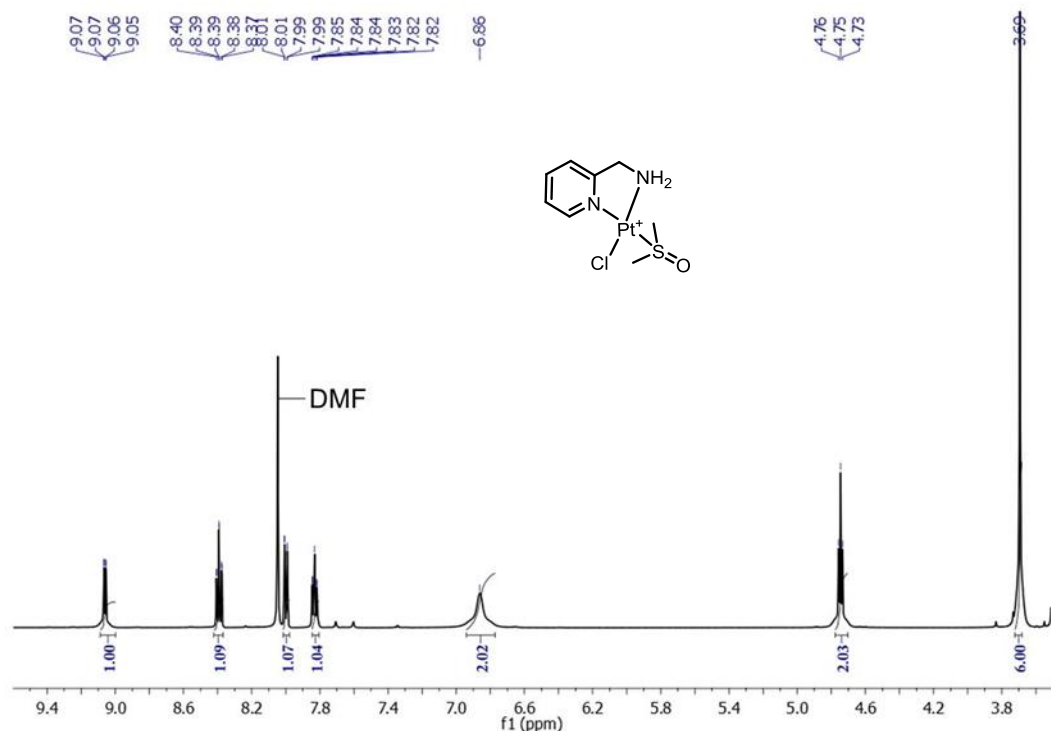


Figure 11. ^1H NMR spectra recorded in DMF-d_7 .

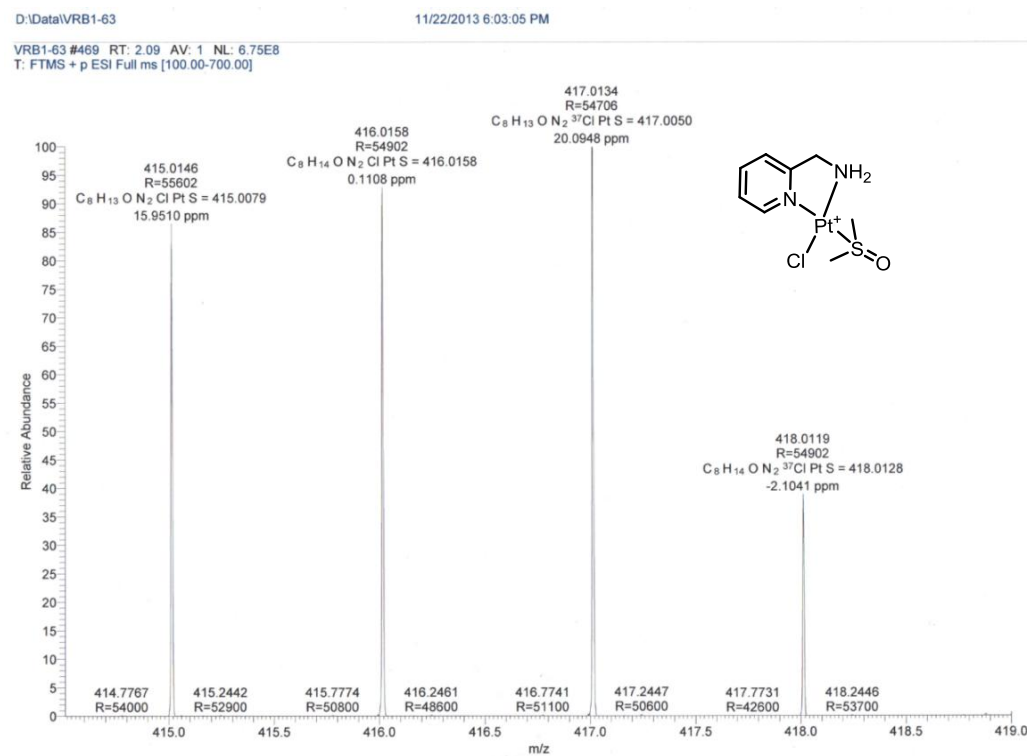


Figure 12. ESI Mass spectra recorded in acetonitrile.

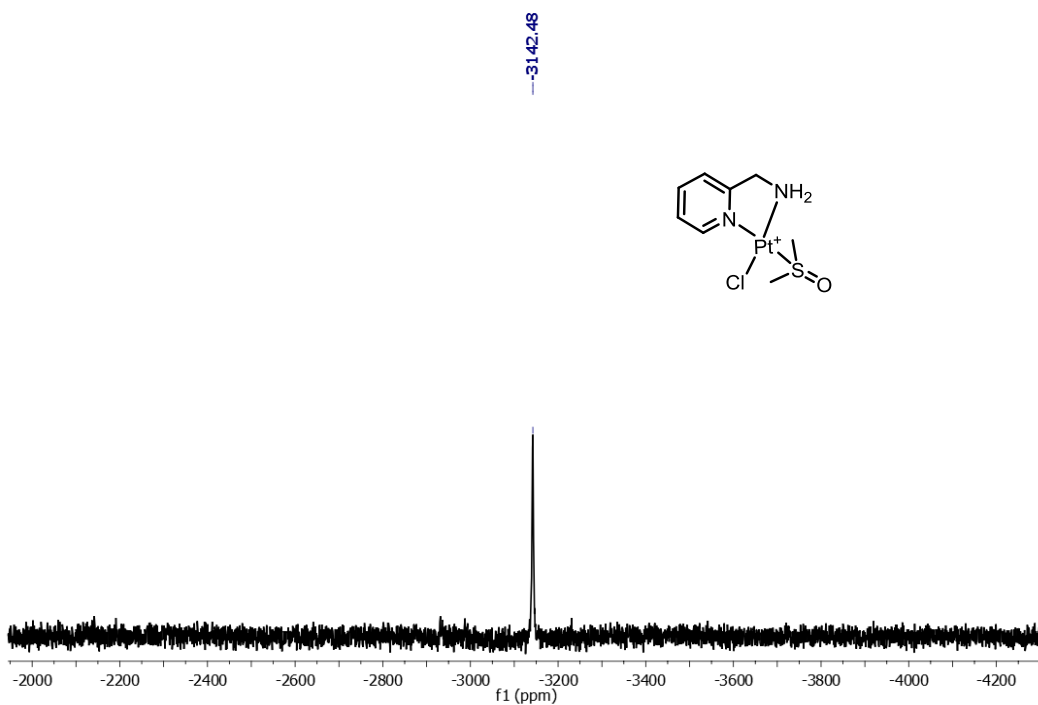


Figure 13. ^{195}Pt NMR spectra recorded in DMF-d_7

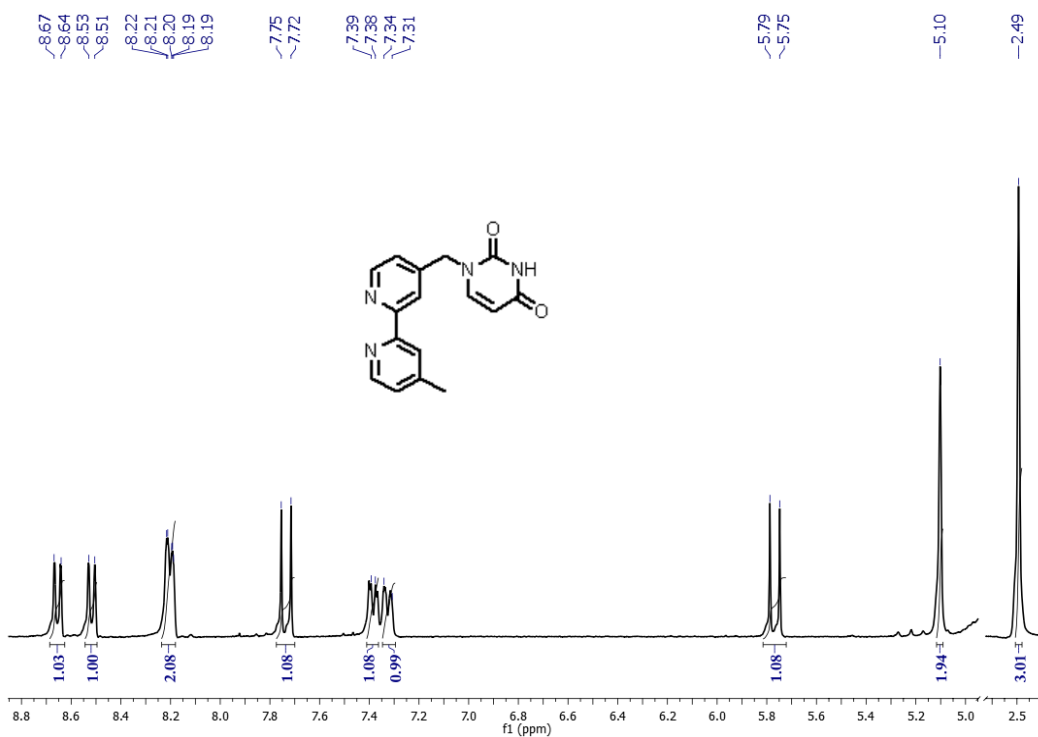


Figure 14. ^1H NMR spectra in methanol- d_4 .

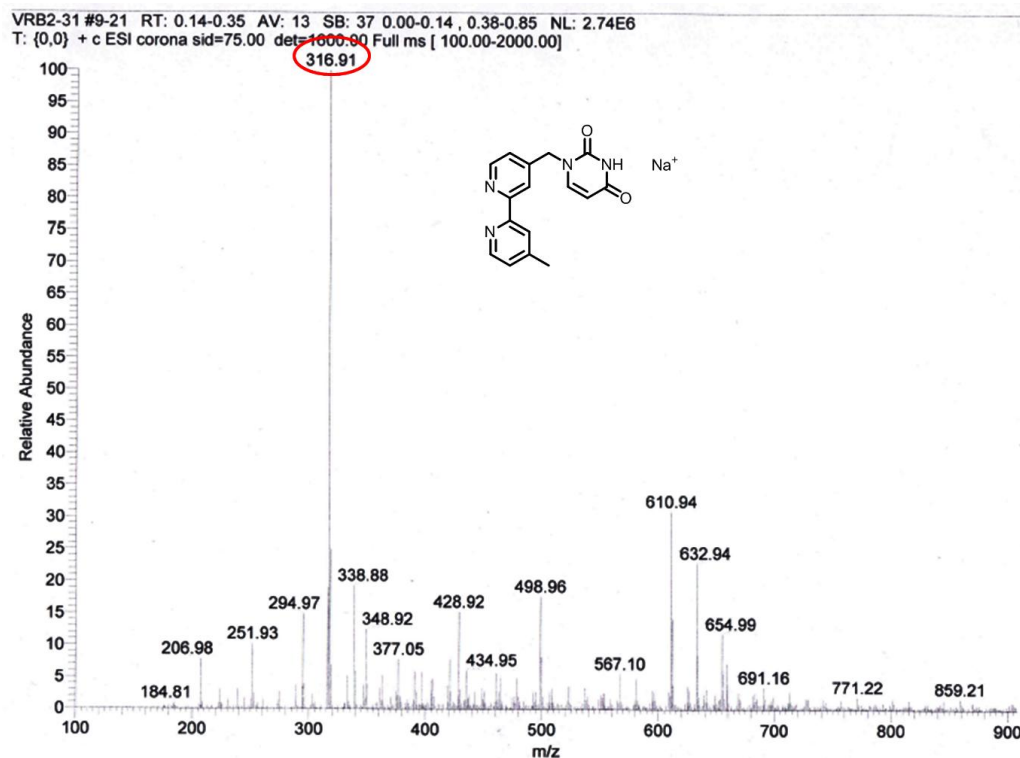


Figure 15. ESI Mass spectra recorded in methanol.

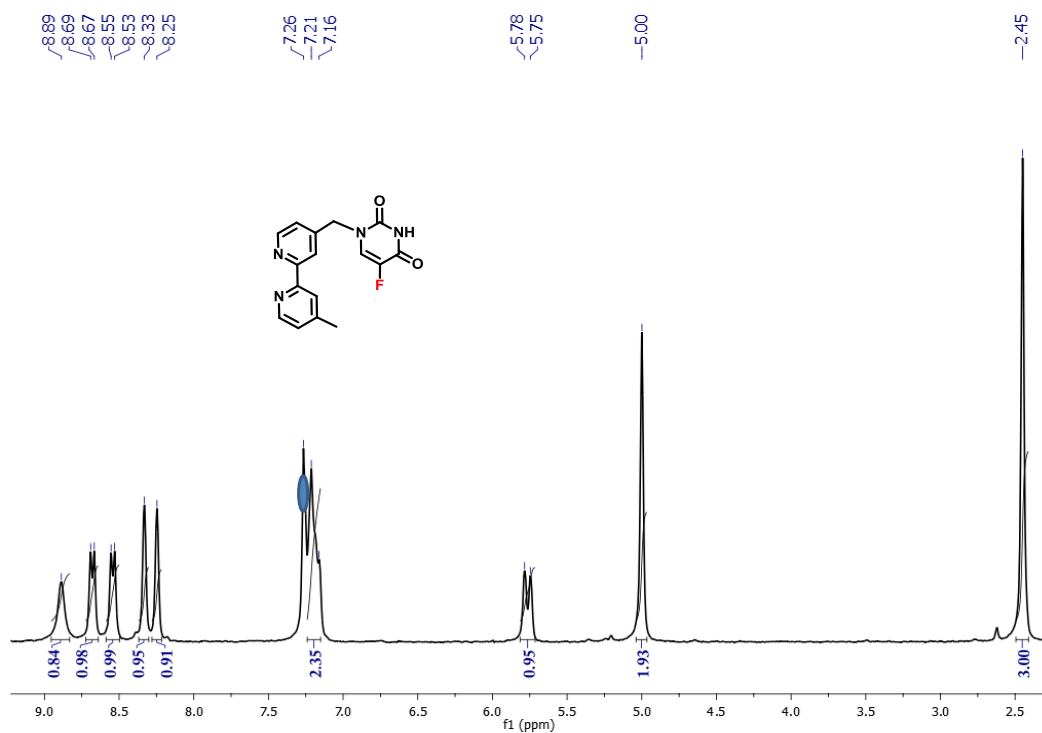


Figure 16. ¹HNMR spectra recorded in chloroform-d.

19F-bpy-5FU

—74.85

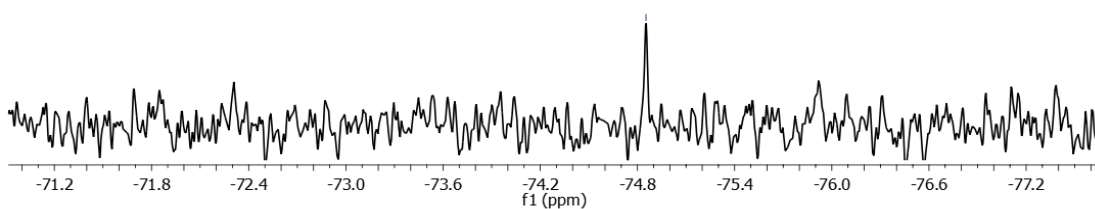
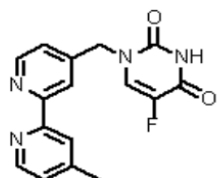


Figure 17. ^{19}F NMR spectra recorded in chloroform-d.

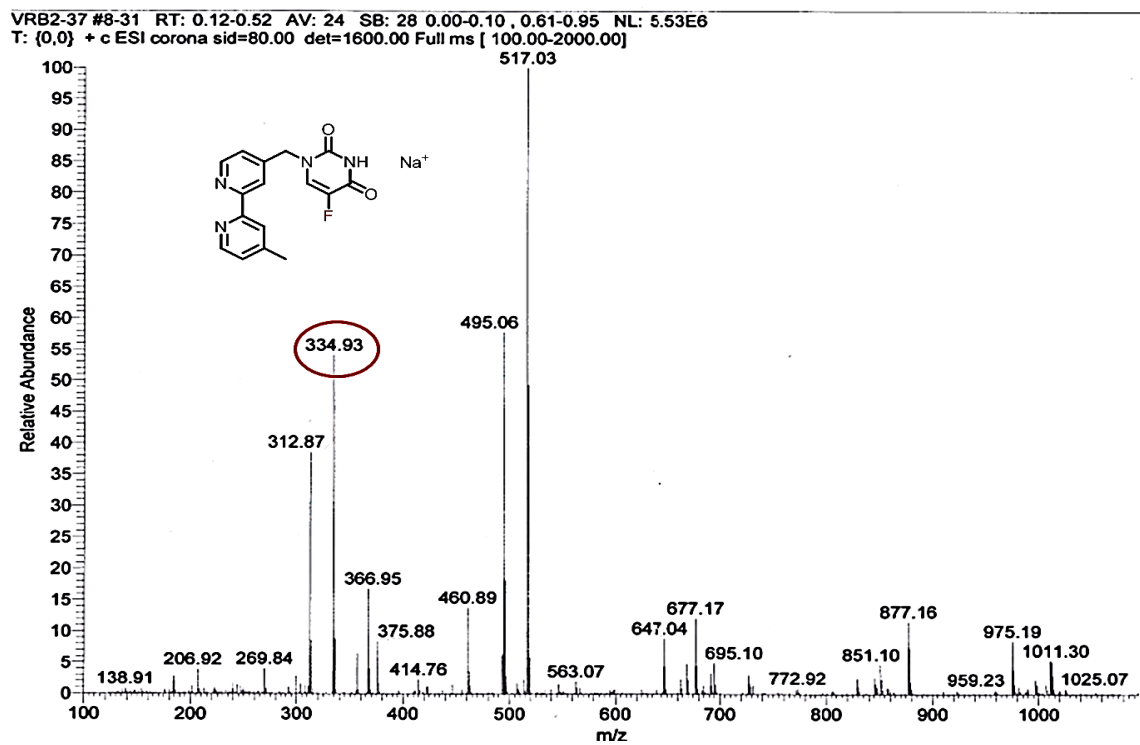


Figure 18. ESI Mass spectra recorded in methanol.

Appendix

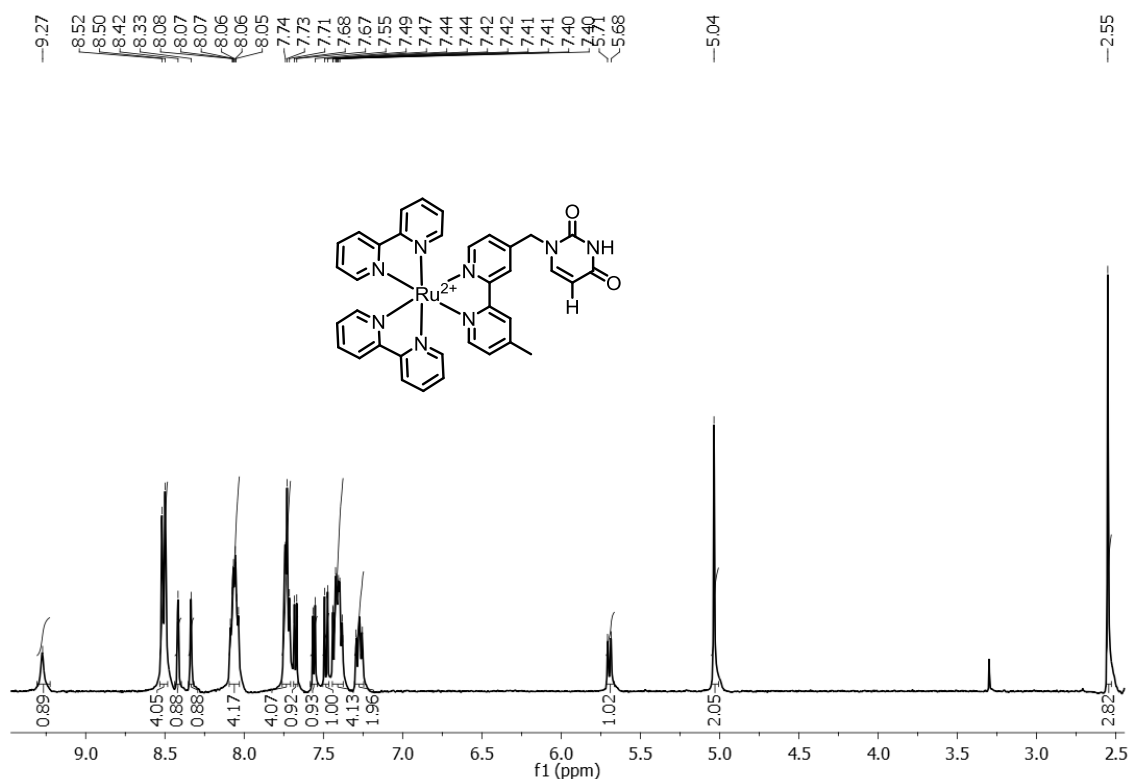


Figure 19. ^1H NMR spectra recorded in acetonitrile-d₃.

Ru-uracil #551 RT: 2.45 AV: 1 NL: 4.96E5
T: FTMS + p ESI Full ms [150.00-1000.00]

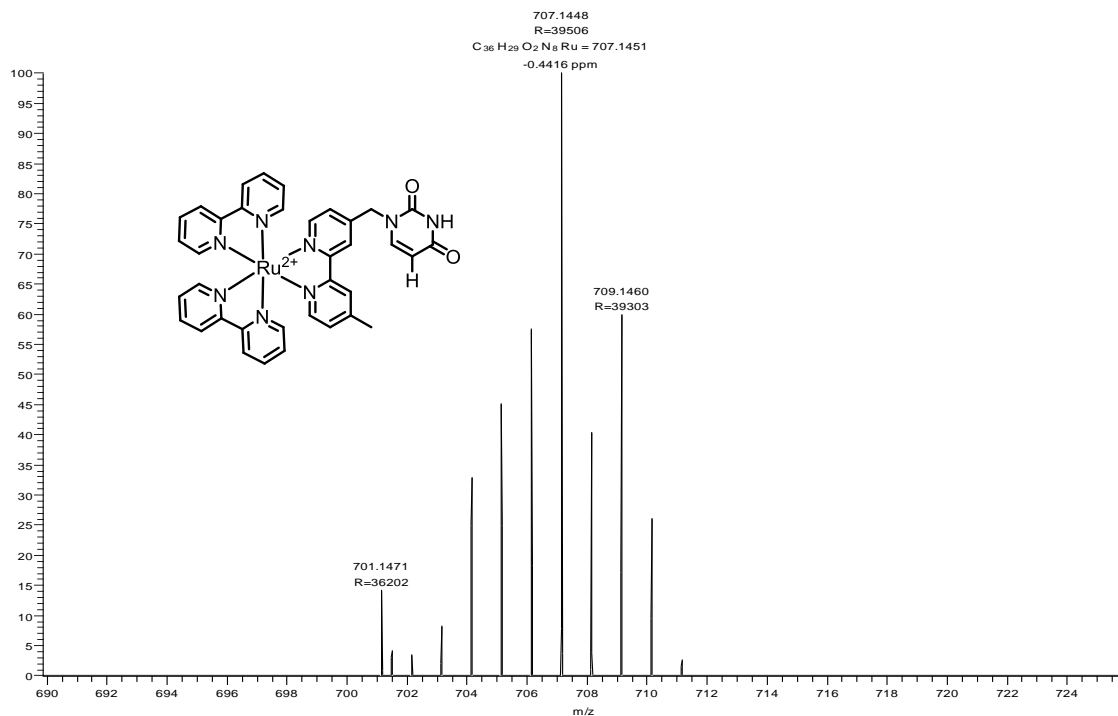


Figure 20. ESI Mass spectra recorded in acetonitrile.

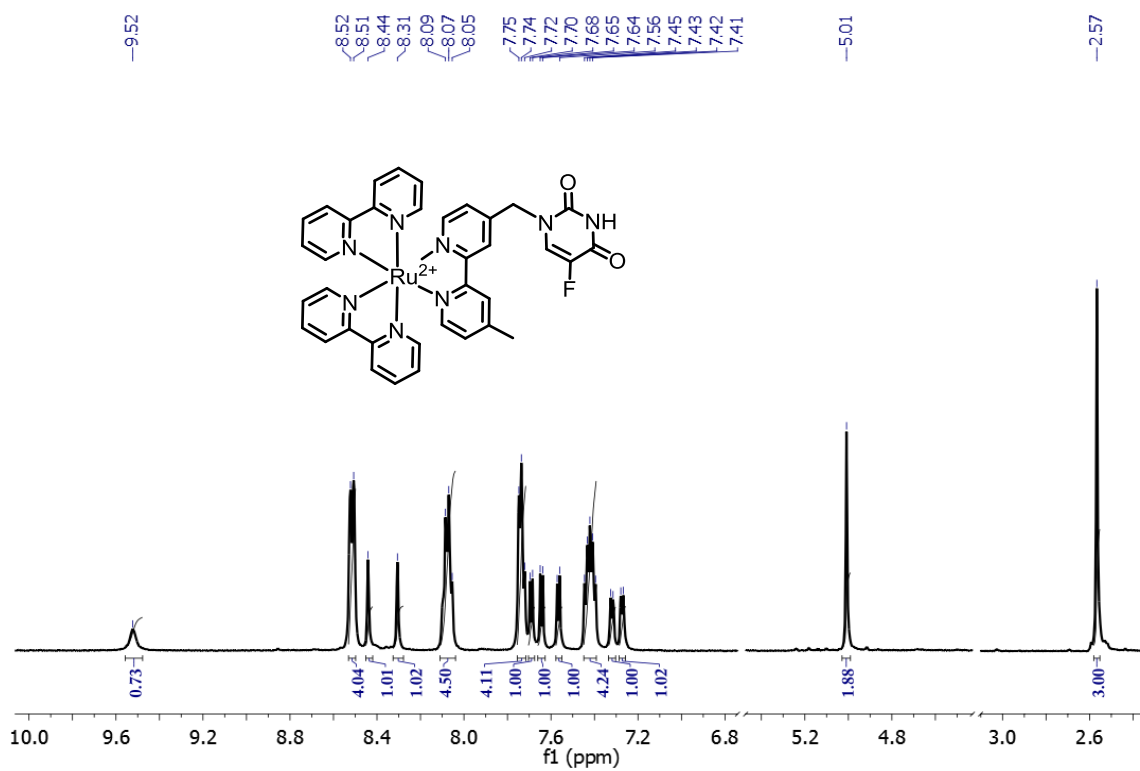


Figure 21. ^1H NMR recorded in acetonitrile- d_3 .

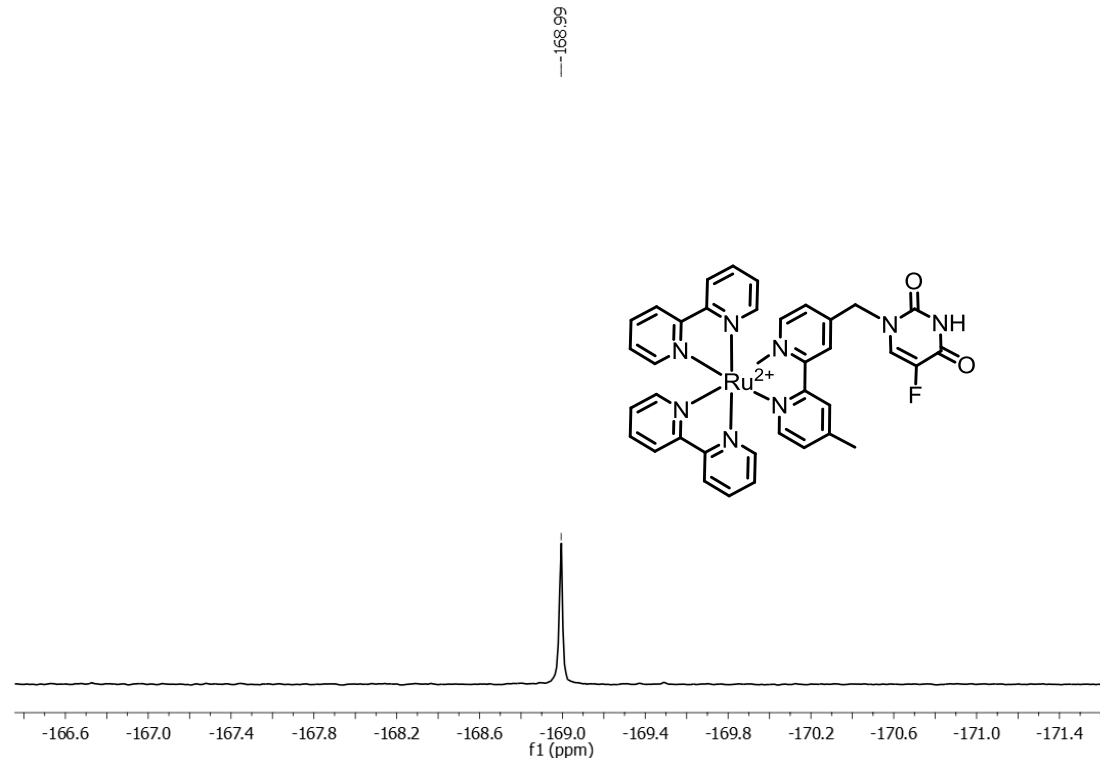


Figure 22. ^{19}F NMR recorded in acetonitrile- d_3 .

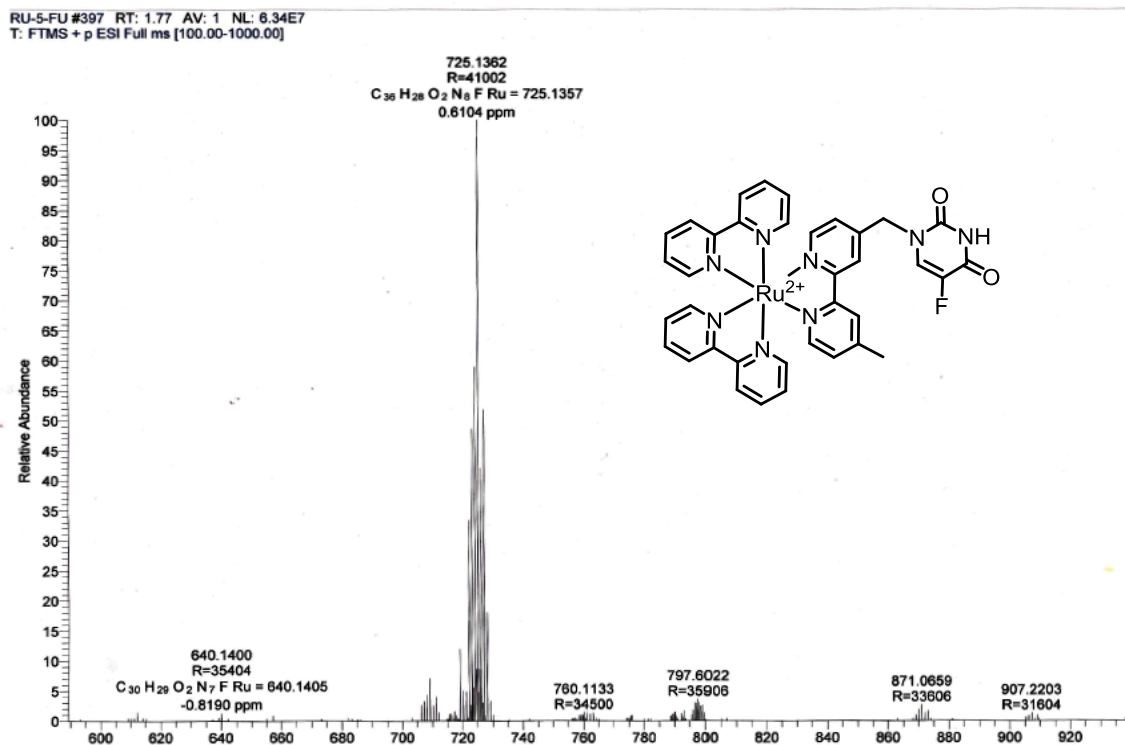


Figure 23. ESI Mass spectra recorded in acetonitrile.

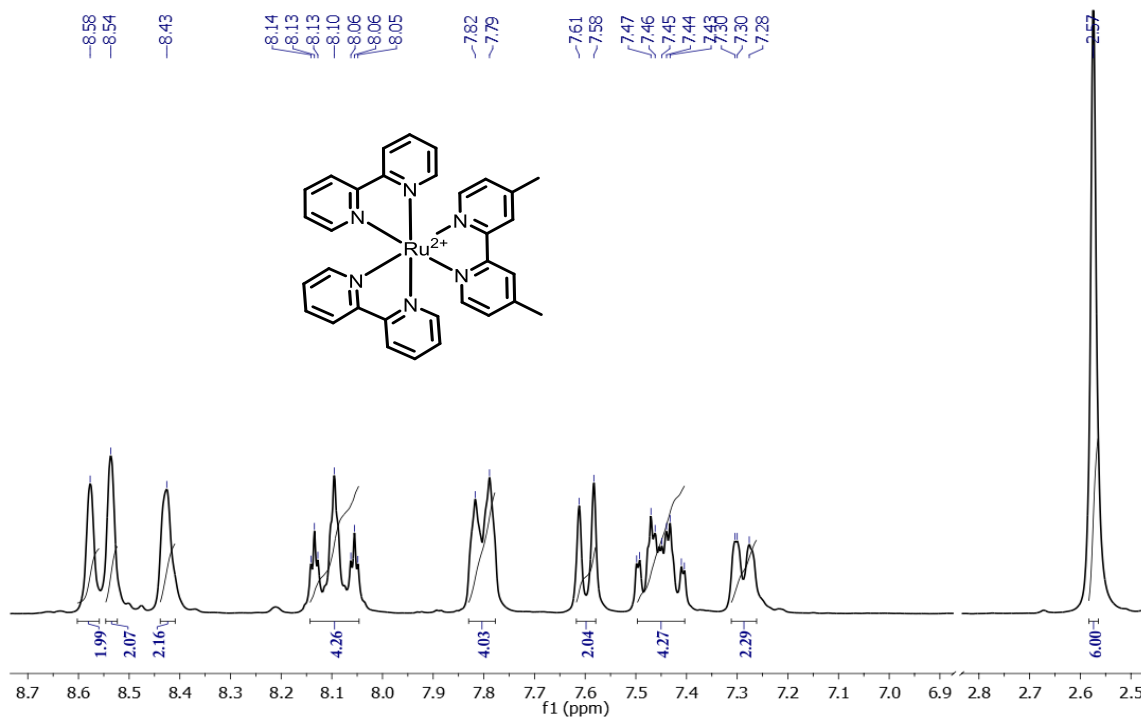


Figure 24. 1H NMR spectra recorded in acetonitrile- d_3 .

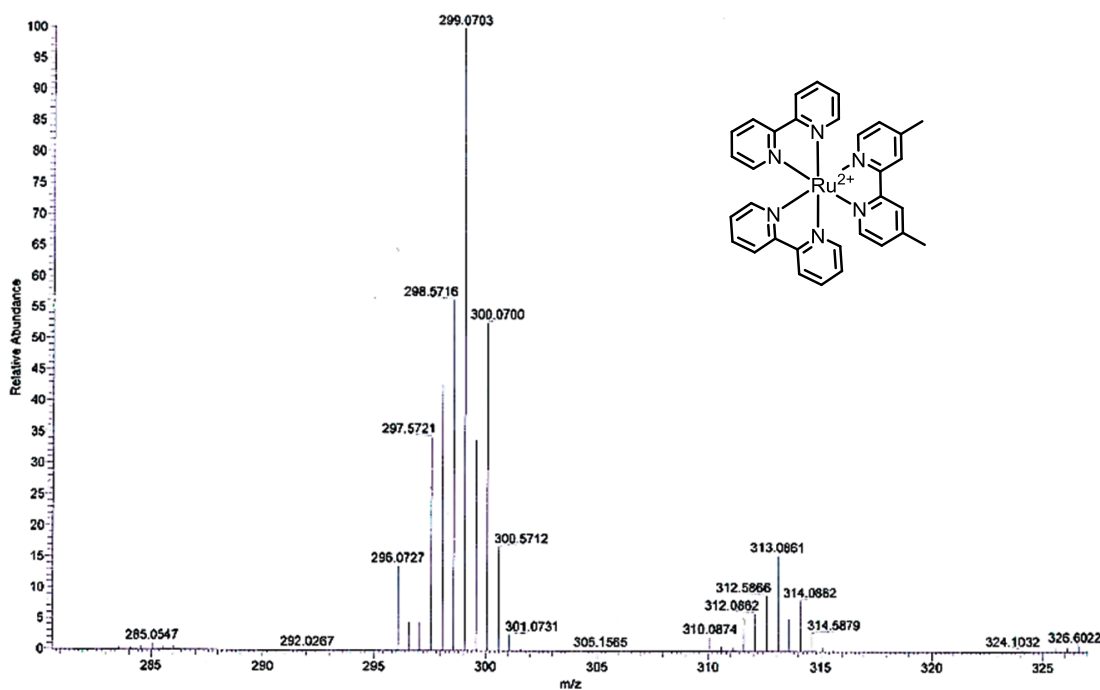


Figure 25. ESI Mass spectra recorded in acetonitrile.

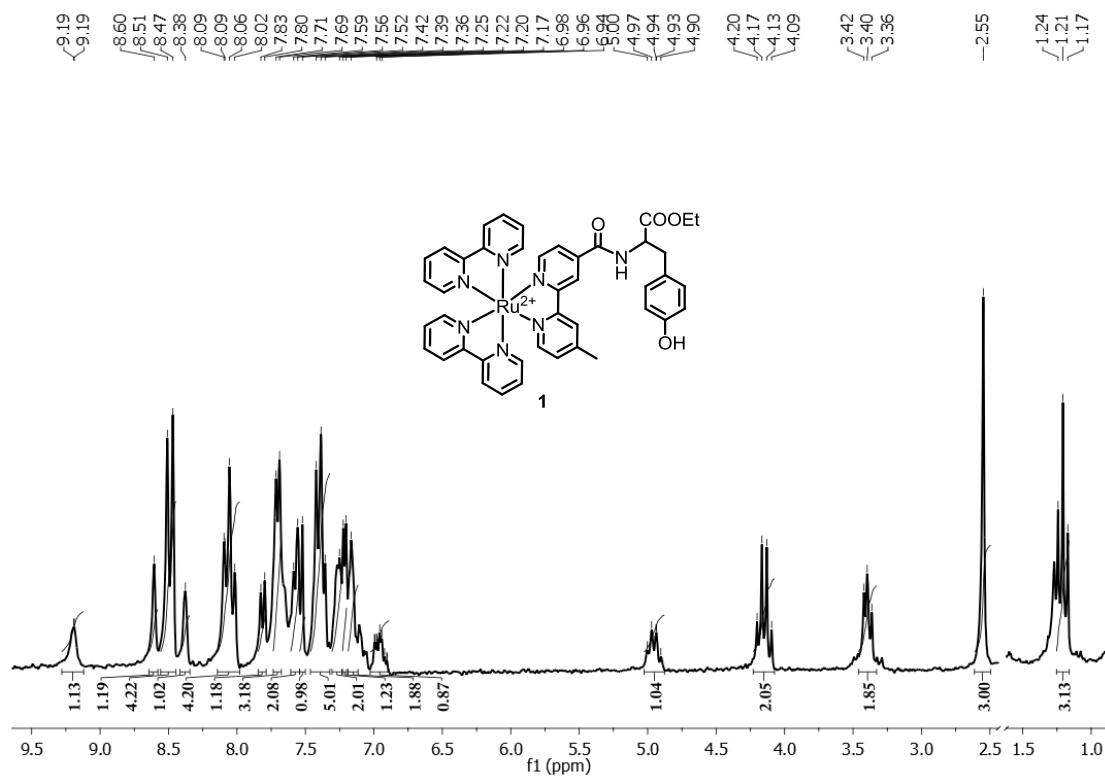


Figure 26. ^1H NMR spectra recorded in acetonitrile- d_3 .

RN-TYRO #150 RT: 0.67 AV: 1 NL: 2.79E6
 T: FTMS + p ESI Full ms [100.00-1500.00]

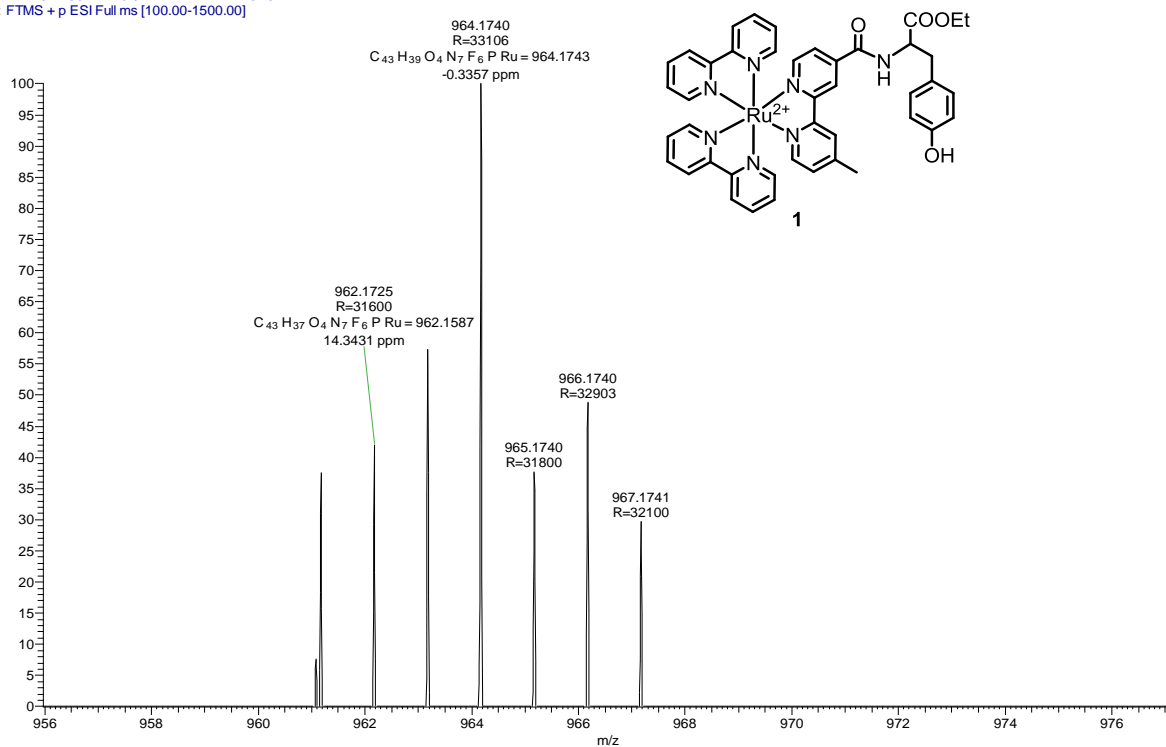


Figure 27. ESI Mass spectra recorded in acetonitrile.

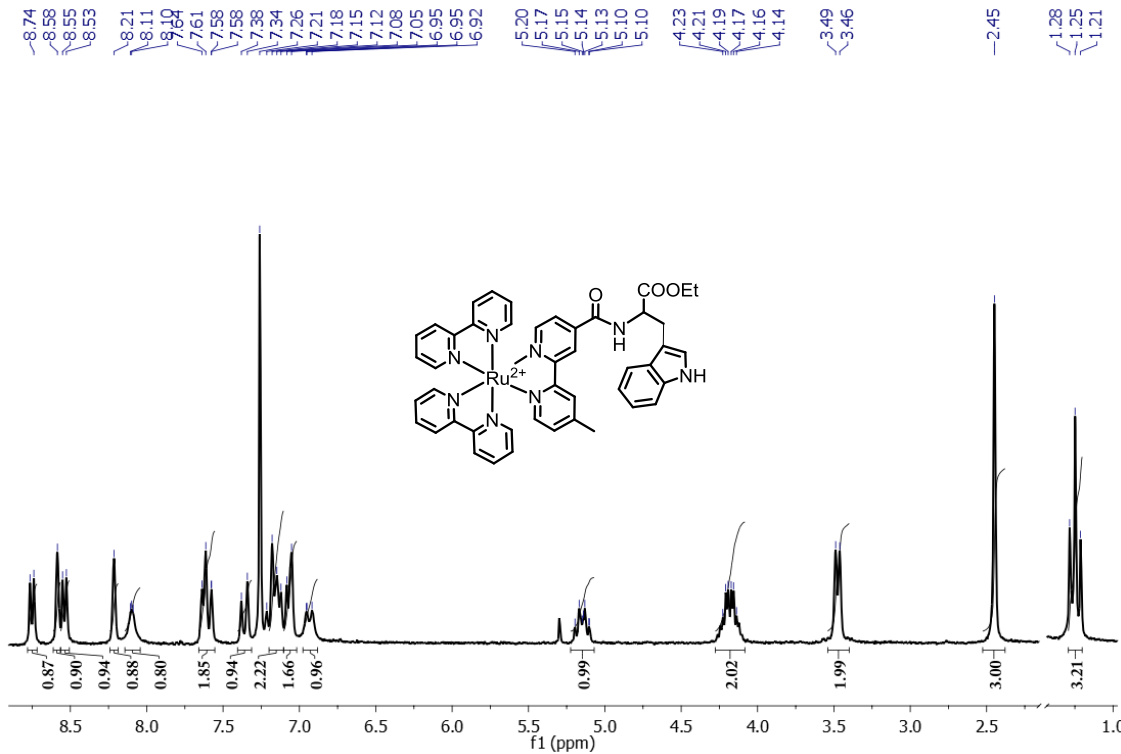


Figure 28. ^1H NMR spectra recorded in acetonitrile- d_3 .

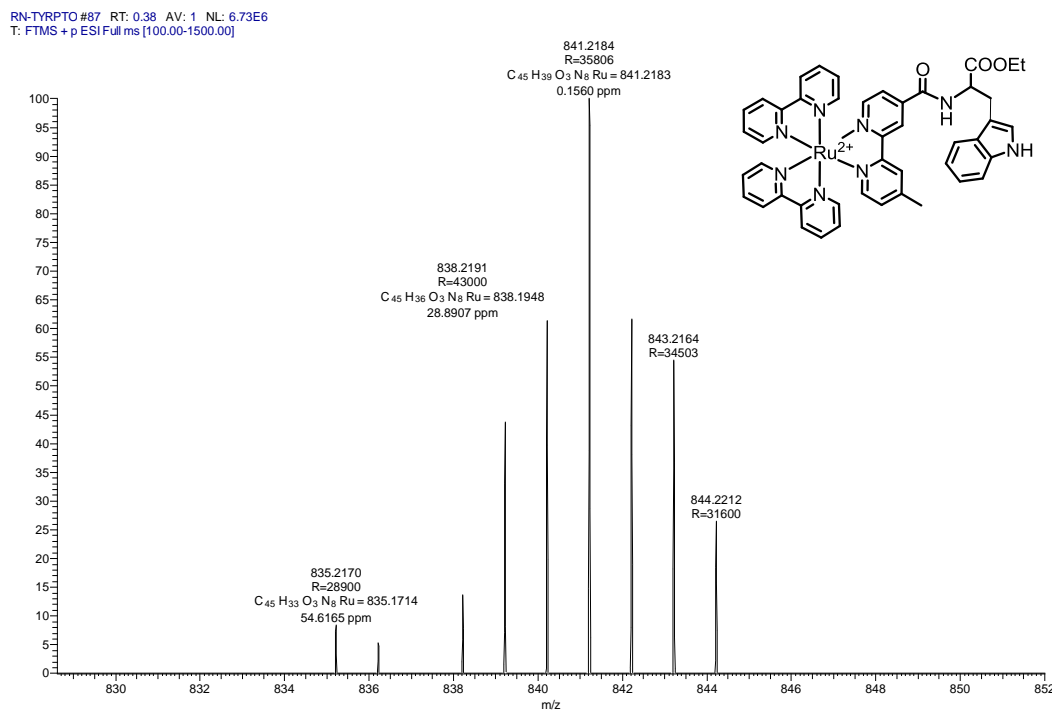


Figure 29. ESI Mass spectra recorded in acetonitrile.

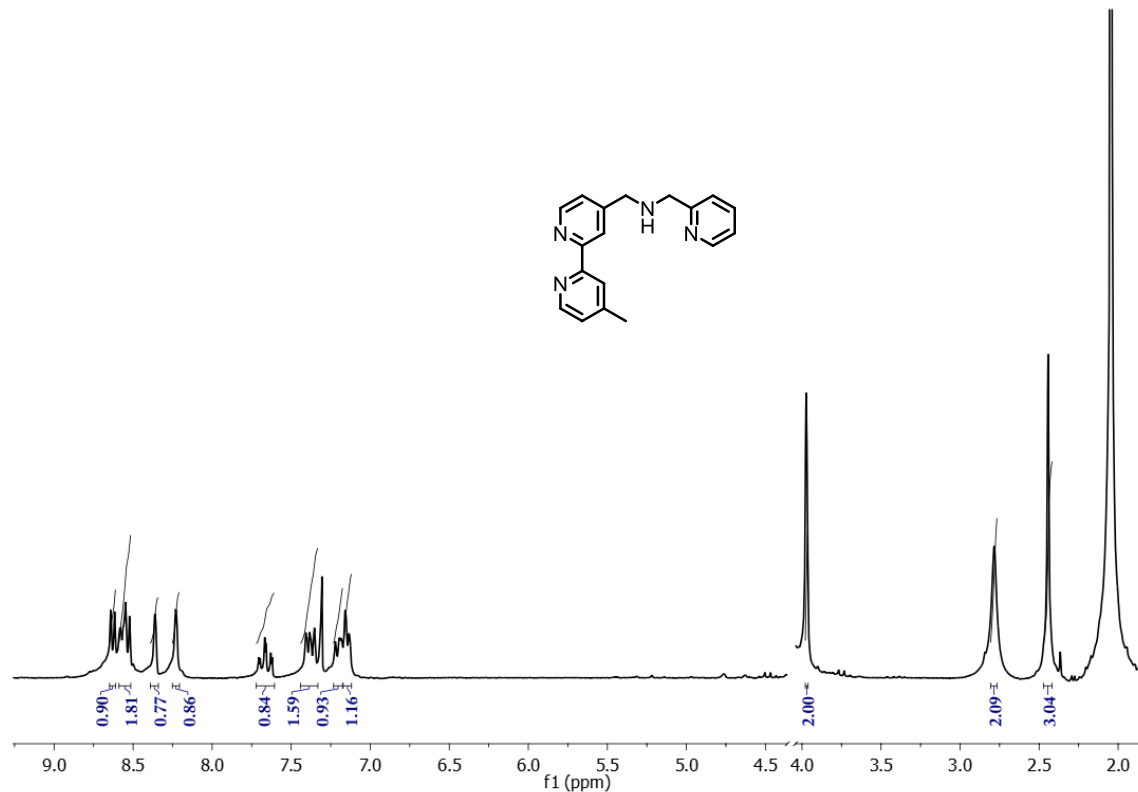


Figure 30. ^1H NMR partial spectra recorded in chloroform- d_3 .

Appendix

D:\Data\BPY-PY

6/3/2015 12:19:57 PM

BPY-PY #314 RT: 1.40 AV: 1 NL: 2.00E6
T: FTMS + p ESI Full ms [66.70-1000.00]

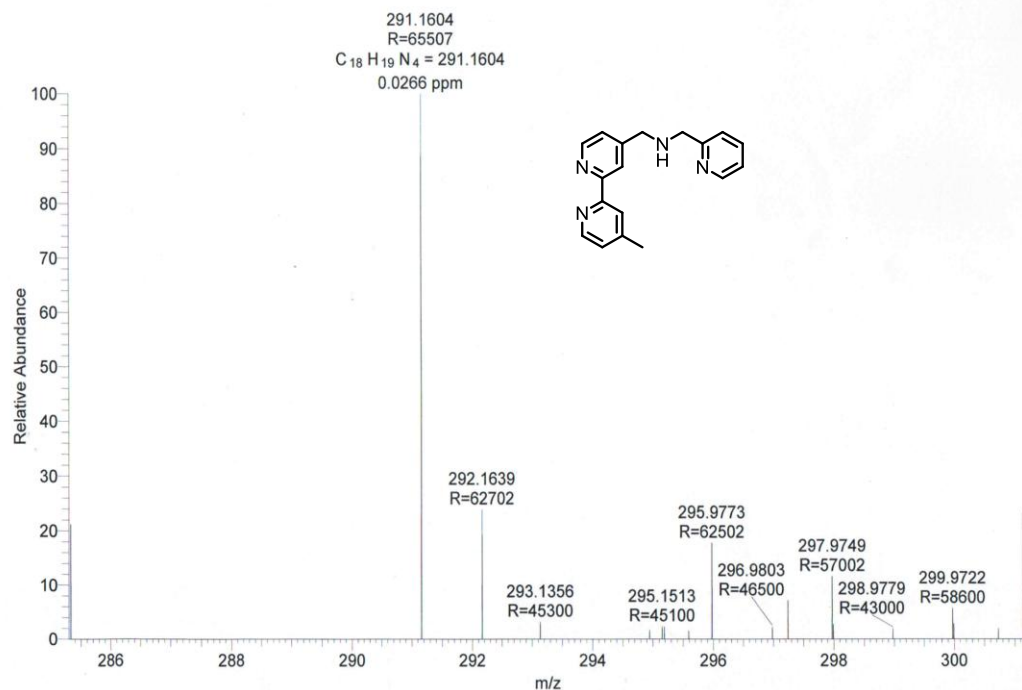


Figure 31. ESI Mass spectra recorded in acetonitrile.

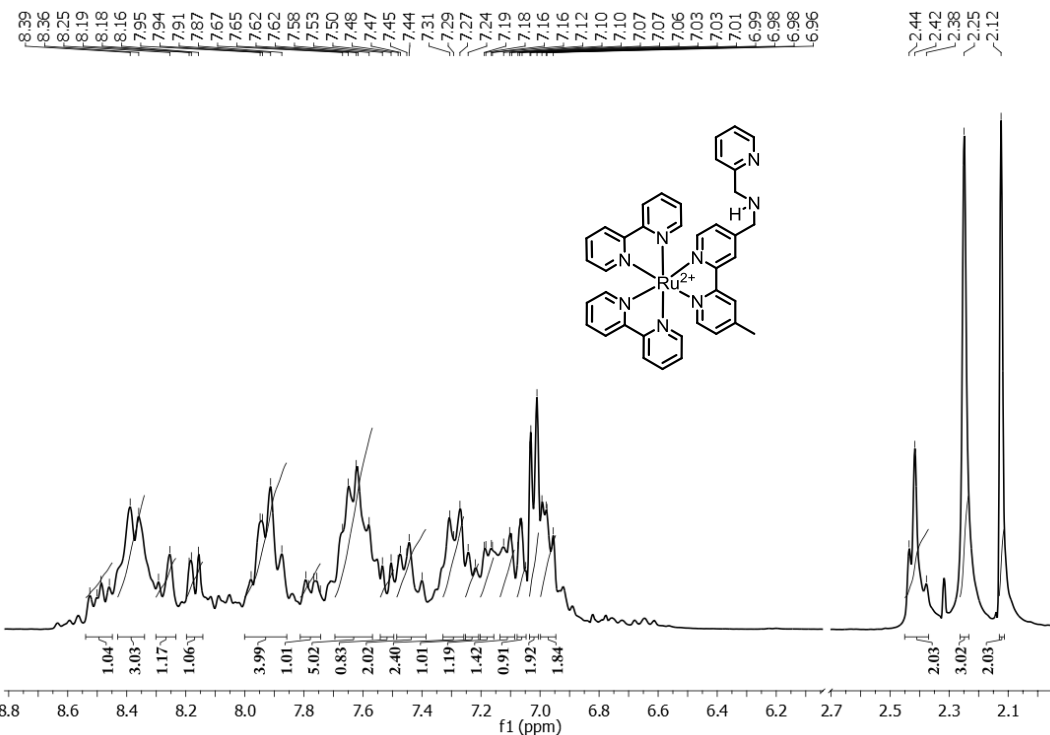


Figure 32. ^1H NMR spectra recorded in acetonitrile- d_3 .

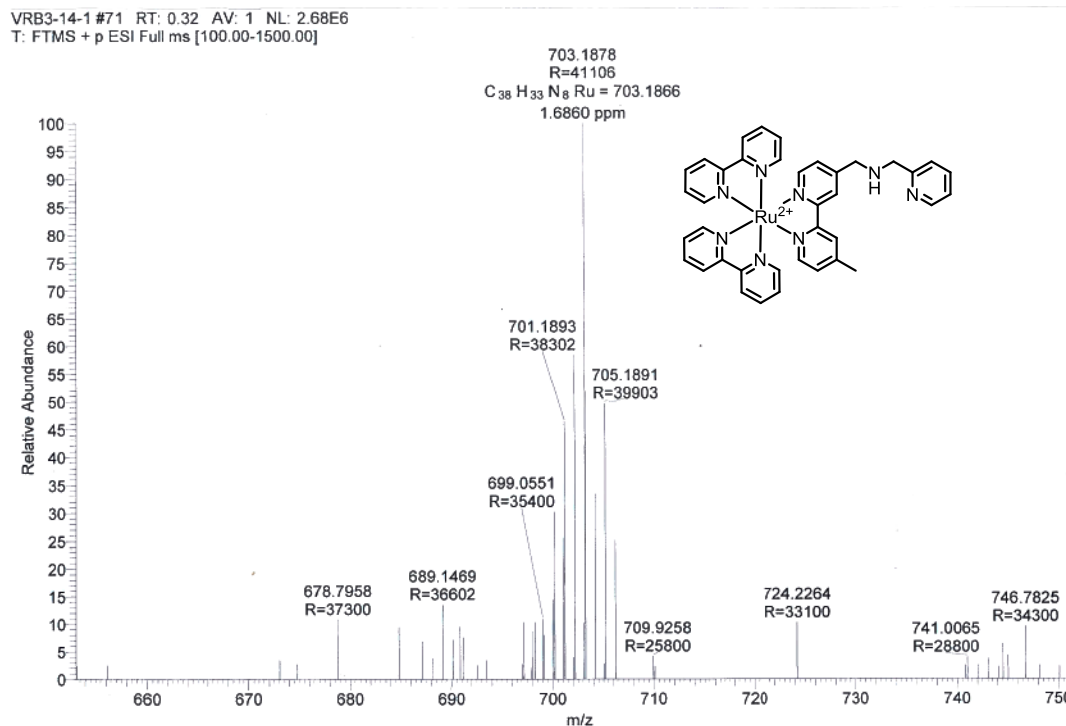


Figure 33. ESI Mass spectra recorded in acetonitrile.

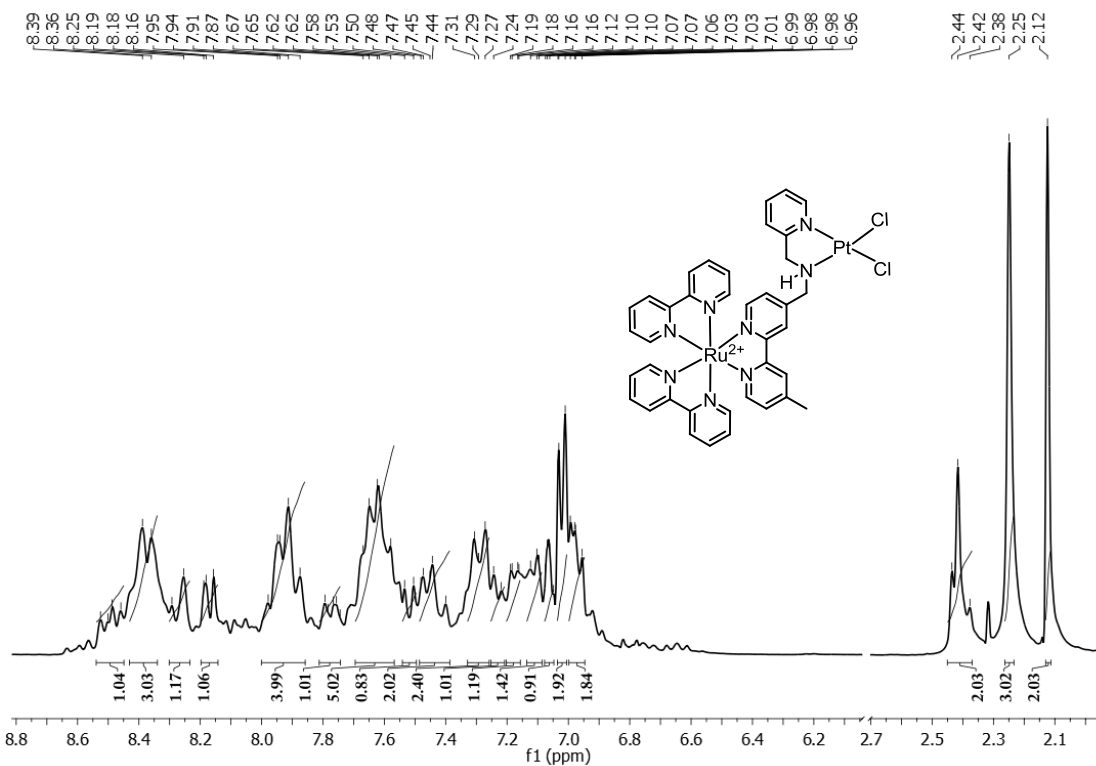


Figure 34. ^1H NMR spectra recorded in acetonitrile- d_3 .

Appendix

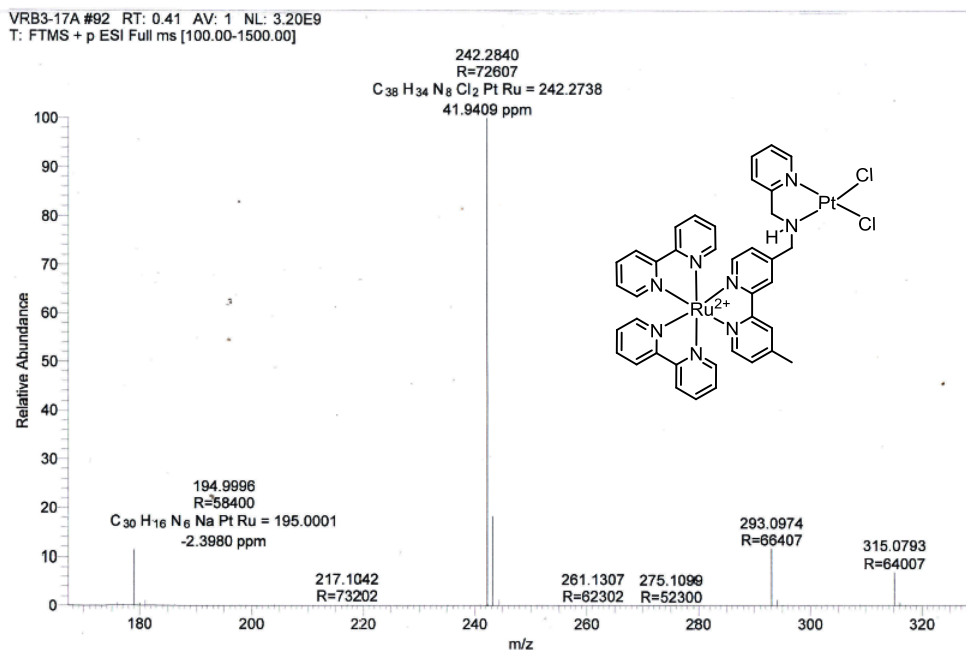


Figure 35. ESI Mass spectra recorded in acetonitrile.

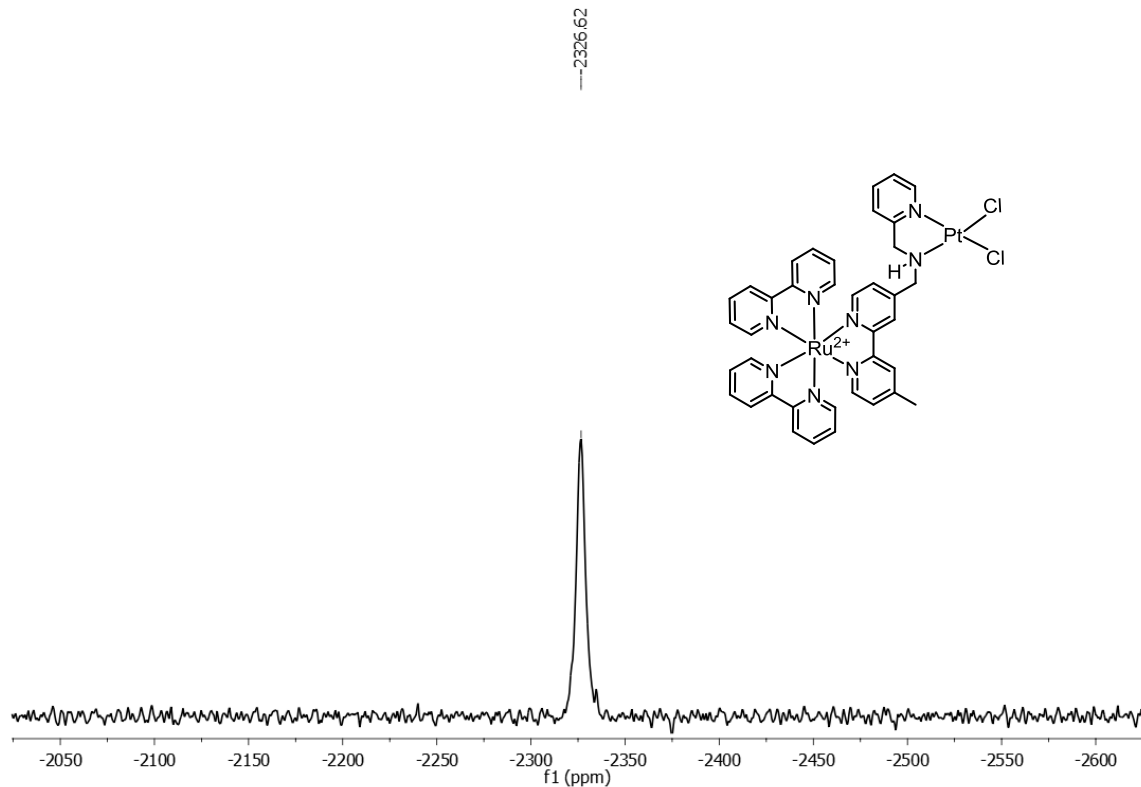


Figure 36. ^{195}Pt NMR spectra recoded in DMF-d_7 .

LIST OF PUBLICATIONS FROM THESIS

1. A Cytostatic Ruthenium(II)-Platinum(II) Bis(terpyridyl) Anticancer Complex That Blocks Entry into S Phase by Up-regulating p27KIP1.
Vadde Ramu, Martin R. Gill, Paul J. Jarman, David Turton, Jim A. Thomas, Carl Smythe and Amitava Das, *Chem. Eur. J.* 2015, 21, 9185-9197.
2. New Imaging Reagents for Lipid Dense Region in Live cells and Nucleus in Fixed MCF-7cells.
Vadde Ramu, Firoj Ali, Nandaraj Taye, Bikash Garai, Aftab Alam and Samit Chattopadhyay, and Amitava Das, *J. Mater. Chem. B*, 2015, 3, 7177-7185. (**Selected as hot article for the year 2015**)
3. Study of Photo Induced Cytotoxicity, Anti-Metastatic behavior of Ruthenium (II)-Polypyridyl Complexes in search of Photodynamic Therapeutic Agents.
Vadde Ramu, Nandaraj Taye, Sunil Aute, Jim A. Thomas, Samit Chattopadhyay, Amitava Das. (**Manuscript to be communicated**).

LIST OF OTHER PUBLICATIONS

4. A specific probe for Hg²⁺ to delineate even H⁺ in pure aqueous buffer/Hct116 colon cancer cells: Hg (II) - η²- arene π-interaction and a TBET-based fluorescence response. Upendar Reddy G, **Vadde Ramu**, Sovan Roy, Nandaraj Taye, Samit Chattopadhyay, Amitava Das. *Chem. Commun.*, 2014, **50**, 14421-14424.
5. Zn^{II}·2, 2': 6, 2"-Terpyridine-Based Complex as Fluorescent Chemosensor for PPi, AMP & ADP. Priyadip Das, Amrita Ghosh, Manoj K. Kesharwani, **Vadde Ramu**, Bishwajit Ganguly, and Amitava Das. *Eur. J. Inorg. Chem.* 2011, 3050–3058.
6. A ratiometric sensor for DNA based on a dual emission Ru (dppz) light switch complex. Michael G. Walker, **Vadde Ramu**, Anthony. J. H. M. Meijer, Amitava Das, and Jim A Thomas. (*To be communicated*).
7. Effective Intracellular Entry of Prodrugs and Concomitant Release of Drug: Probing Intracellular Phenomena by Imaging Studies.
Suman Pal, **Vadde Ramu**, Nandaraj Taye, Srinivasa Reddy, Samit Chattopadhyay, and Amitava Das. (*To be communicated*).

PATENT FROM THE THESIS

1. Novel uracil and 5-fluorouracil conjugated ruthenium (II) polypyridyl complexes as cellular DNA imaging agents. *USA patent application number 14/878,568. Provisional filing date: 10/08/2014.*

List of conferences / workshops attended

1. Poster presented at 6th International conference on Metals in Genetics, Chemical Biology and Therapeutics during 17-20 February 2016 held in IISc Bangalore. (**Awarded a New Journal of chemistry Poster Prize from the Royal Society of Chemistry**).
2. Poster presented in 5th International workshop on Radiation and Photochemistry during 10-12 January, 2016 held in SP Phule Pune University, Pune (**winner of the Photochemical & Photobiological Sciences Poster prize from the Royal Society of Chemistry**).
3. Poster presented at National Conference on Recent Trends in Drug Development during 12-14 march 2016 (**Won the best poster award from SP Phule Pune University**).
4. Poster presented on the occasion of National Science day Celebrations during 25-26th February, 2015 at CSIR-NCL, Pune.
5. Participated in 17th CRSI National symposium in chemistry during 6-8th February, 2015 held at CSIR-NCL, IISER-Pune.
6. Poster presented at Indo-German conference on Bio-Inspired Chemistry during 10-12th September, 2014. Held at IISc Bangalore.
7. Poster presented on the occasion of National Science day Celebrations during 25-26th February, 2014 at CSIR-NCL, Pune.
8. Poster presented in 16th CRSI National symposium in chemistry during 7-9th February, 2014 held at IIT Bombay.
9. Participated in the International conference on structural and Inorganic chemistry during 4-5th December, 2014 held at CSIR-NCL, IISER-Pune.
10. Participated in 2nd National level workshop on Cheminformatics during 7-8th January, 2011 organised by Christ College, Rajkot.

Medicinal Chemistry

A Cytostatic Ruthenium(II)–Platinum(II) Bis(terpyridyl) Anticancer Complex That Blocks Entry into S Phase by Up-regulating p27^{KIP1}

Vadde Ramu,^[a] Martin R. Gill,^[b] Paul J. Jarman,^[c] David Turton,^[b] Jim A. Thomas,*^[c] Amitava Das,*^[a] and Carl Smythe*^[b]

Abstract: Cytostatic agents that interfere with specific cellular components to prevent cancer cell growth offer an attractive alternative, or complement, to traditional cytotoxic chemotherapy. Here, we describe the synthesis and characterization of a new binuclear Ru^{II}–Pt^{II} complex [Ru(tpy)(tpypma)Pt(Cl)(DMSO)]³⁺ (tpy = 2,2':6',2''-terpyridine and tpypma = 4-([2,2':6',2''-terpyridine]-4'-yl)-N-(pyridin-2-ylmethyl)aniline), VR54, which employs the extended terpyridine tpypma ligand to link the two metal centres. In cell-free conditions, VR54 binds DNA by non-intercalative reversible mechanisms ($K_b = 1.3 \times 10^5 \text{ M}^{-1}$) and does not irreversibly bind guanosine. Cellular studies reveal that VR54 suppresses proliferation of A2780 ovarian cancer cells with no cross-re-

sistance in the A2780CIS cisplatin-resistant cell line. Through the preparation of mononuclear Ru^{II} and Pt^{II} structural derivatives it was determined that both metal centres are required for this anti-proliferative activity. In stark contrast to cisplatin, VR54 neither activates the DNA-damage response network nor induces significant levels of cell death. Instead, VR54 is cytostatic and inhibits cell proliferation by up-regulating the cyclin-dependent kinase inhibitor p27^{KIP1} and inhibiting retinoblastoma protein phosphorylation, which blocks entry into S phase and results in G1 cell cycle arrest. Thus, VR54 inhibits cancer cell growth by a gain of function at the G1 restriction point. This is the first metal-coordination compound to demonstrate such activity.

Introduction

Based on the success of cisplatin, platinum-based drugs remain the first line of treatment—either alone or in combination with other anticancer drugs—for a variety of cancers, including head and neck, testicular and ovarian.^[1] One of the targets of cisplatin is DNA, where—following ligand substitution—the molecule binds irreversibly to the nucleobases, typically at N₇ sites of guanine, creating both intra- and interstrand cross-links.^[2] Since the cellular DNA mismatch repair or nucleotide excision repair systems do not process these lesions efficiently, an apoptotic cell death response is induced.^[3] Despite the success of cisplatin, intrinsic or acquired drug resistance combined with toxicity represents a significant challenge for the future of platinum chemotherapy.^[4] Mechanisms that con-

tribute to platinum-based resistance include changes in efficiency of drug accumulation, intracellular thiol levels and DNA adduct repair,^[4] with resistance often being multifactorial. Such resistance requires ever-greater doses of platinum therapeutic, eventually precluding safe use of the drug due to the inherent high toxicity of the molecule.

One strategy to overcome this problem has involved the design of new transition metal-based compounds, which aim to utilise the opportunities afforded by coordination chemistry to explore novel chemical space in cancer biology. Specifically, by employing a variety of metal centres, the effect of ancillary and active ligand(s) on reactivity, cellular uptake and anti-proliferative potency has been explored in detail.^[5] With some exceptions,^[6] work in this area has often focussed on the development of potent, purely cytotoxic systems. However, clinical application of cytotoxic drugs is often restricted by narrow therapeutic windows and inherent off-target tissue toxicity.^[7] This principle may be illustrated by platinum-based drugs themselves: carboplatin, a less potent cisplatin-derivative, was introduced in an attempt to reduce the nephrotoxicity and emetic properties of the parent complex,^[1] while clinical trials of the highly cytotoxic triplatinum agent BBR 3464 ceased due to its severe dose-limiting side-effects.^[8]

As insights into the cell biology of cancer have developed, targeted therapy has emerged as an alternative approach to conventional cytotoxic chemotherapy.^[9] Utilising a detailed understanding of the molecular aetiology of individual tumours, targeted therapies aim to inhibit the growth and spread of cancer either by selectively down-regulating intracellular path-

[a] V. Ramu,* Dr. A. Das
Organic Chemistry Division, CSIR-National Chemical Laboratory
Pune, 411008, Maharashtra (India)
E-mail: a.das@ncl.res.in

[b] Dr. M. R. Gill,* Dr. D. Turton, Prof. C. Smythe
Department of Biomedical Science, University of Sheffield
Sheffield S10 2TN (UK)
E-mail: c.g.w.smythe@sheffield.ac.uk

[c] P. J. Jarman, Prof. J. A. Thomas
Department of Chemistry, University of Sheffield
Sheffield S10 2TN (UK)
E-mail: james.thomas@sheffield.ac.uk

[*] These authors contributed equally to this work.

Supporting information for this article is available on the WWW under <http://dx.doi.org/10.1002/chem.201500561>.



Cite this: *J. Mater. Chem. B*, 2015,
3, 7177

New imaging reagents for lipid dense regions in live cells and the nucleus in fixed MCF-7 cells†

Vadde Ramu,^a Firoj Ali,^a Nandaraj Taye,^b Bikash Garai,^a Aftab Alam,^b Samit Chattopadhyay*^b and Amitava Das*^a

Two new uracil (U) and 5-flurouracil (5-FU) labeled ruthenium(II)-polypyridyl based cellular imaging reagents are reported. Confocal laser scanning microscopic images with live and paraformaldehyde (PFA) fixed MCF-7 cells are examined using these two low-cytotoxic reagents. Experimental results show that these two complexes, appropriately functionalized with U (**1**) and 5-FU (**2**), have specific affinity for the lipid dense regions like the endoplasmic reticulum, cell membrane, and cytoplasmic vacuoles in live MCF-7 cells, and dye internalization in these regions happened following an endocytosis pathway. Interestingly, these two complexes are found to be localized in the nucleus of the PFA fixed cells. For fixed cells, presumably the lipid layer disruption helped in the explicit localization of the complexes **1** and **2** in the cell nucleus through specific interaction with cellular DNA. Poor and non-specific internalization of an analogous model complex **3**, without having a U or 5-FU moiety, reveals the definite influence of U or 5-FU as well as the role of lipophilicity of the respective complex **1** and **2** in the cellular internalization process. Apart from these, a large Stokes shift (~160 nm) and an appreciably long lived $^3\text{MLCT}$ excited state (~320 ns) in aq. buffer medium (pH 7.4) are other key features for complexes **1** and **2**. Unlike the common nuclear DNA staining reagents like DAPI, these low-cytotoxic reagents are found to be highly stable towards photo-bleaching upon irradiation with 455 nm at the MLCT band for these complexes.

Received 2nd July 2015,
Accepted 3rd August 2015

DOI: 10.1039/c5tb01309g

www.rsc.org/MaterialsB

Introduction

The non-invasive imaging approach is generally preferred for observing individual events in cells compared to the traditional biochemical methods that give average results for cells exposed to certain experimental treatment for studying cell functioning, evolution, differentiation, reproduction, and also gene expression in living organisms.¹ Such processes are expected to affect the native intracellular processes while the imaging studies are performed in physiologically authentic environments and have relevance for cell/molecular biology, studying bio-chemical processes, medicine, pharmacology and diagnostics.² Accordingly, visualization of cellular structures by fluorescence microscopy remains a powerful research tool in recent years. There are significant activities in designing appropriate imaging reagents for visualization of specific organelles with organelle-selective

dyes in the membrane-enclosed intracellular structures, as this helps in gaining insight for monitoring important biological processes.^{3,4} Stability towards photo-bleaching, cell membrane permeability, nominal cytotoxicity and luminescence in the longer wavelength following excitation with non-harmful visible light are some of the essential criteria for any such efficient imaging reagent.^{5–8} For imaging application, a target like the ER, a specific organelle in the cells of eukaryotic organisms, is of great significance.^{9,10} Proteins for the secretory pathway are inserted into the membrane of the ER, where they are processed/folded into their native conformation. Misfolded proteins are retained in the ER and transported to the cytosol for ER-associated protein degradation, which has a serious implication in physiology.¹⁰ The ER can be stained with a variety of commercially available lipophilic probes and typical highly ER specific dyes include the lipophilic carbocyanine (DiOC6 or DiOC5 with Stokes shift ($\Delta\lambda_{\text{SS}}$) of ~14 nm) or boron-dipyrromethane (BODIPY) dyes (E34251 or E34250 with $\Delta\lambda_{\text{SS}}$ of ~28 & 7 nm, respectively).¹¹ Such dyes suffer from the limitations of narrow $\Delta\lambda_{\text{SS}}$, photo-bleaching, and partial toxicity.¹² There are only two reports which reveal that the above referred limitations could be addressed for either ER or mitochondria-specific dyes by using dinuclear Ru(II)-polypyridyl based complexes.¹³ Gill *et al.* also showed that the DNA groove-binding dinuclear complex

^a Organic Chemistry Division, National Chemical Laboratory, Pune, 411008, India.
E-mail: a.das@ncl.res.in

^b Chromatin and Disease Laboratory, National Center for Cell Science, Pune, 411007, India. E-mail: samit@nccs.res.in

† Electronic supplementary information (ESI) available: CLSM images for complex **1** & **2**, detailed characterization data for **1**, **2** & **3** and the X-ray structural details of **1**. CCDC 1035338. For ESI and crystallographic data in CIF or other electronic format see DOI: 10.1039/c5tb01309g



Cite this: *Chem. Commun.*, 2014, 50, 14421

Received 27th August 2014,
Accepted 15th September 2014

DOI: 10.1039/c4cc06740a

www.rsc.org/chemcomm

A specific probe for Hg^{2+} to delineate even H^+ in pure aqueous buffer/Hct116 colon cancer cells: $\text{Hg}(\text{II})-\eta^2\text{-arene}$ π -interaction and a TBET-based fluorescence response[†]

Upendar Reddy G.^a Vadde Ramu,^a Sovan Roy,^a Nandaraj Taye,^b Samit Chattopadhyay*^b and Amitava Das*^a

A new molecular probe that demonstrates a distinct TBET process, induced by the $\text{Hg}(\text{II})-\eta^2\text{-arene}$ π -interaction, in pure aqueous medium with a large pseudo-Stokes shift of 200 nm.

Intramolecular triplet-triplet energy transfer is being pursued more recently for developing efficient fluorescence-based receptors, as the average lifetime of the triplet state is much longer than the singlet state.¹ However, such a triplet-triplet energy transfer is spin-forbidden by the dipole-dipole mechanism (Förster-type mechanism) and is only allowed by the electron exchange mechanism (Dexter-type mechanism).¹ Such a triplet-triplet energy transfer requires either an effective orbital overlap or coupling mediated by an appropriate conduit. More importantly, such a through bond energy transfer (TBET) process is not limited by the fact that donor and acceptor fragments ought to have a spectral overlap. This offers the opportunity to achieve a large pseudo-Stokes shift to avoid self-quenching of the donor fluorophore and fluorescence detection errors because of excitation back-scattering effects.² Additionally such an energy transfer dyad also helps in avoiding the problem of photo-bleaching of the probe fluorophore.^{2,3} For fluorophore dyad systems that have an insignificant spectral overlap between the donor emission and acceptor absorption, the FRET process could be operational along with the TBET process. The challenge of demonstrating the TBET process in a small molecule based fluorophore dyad without the complete absence of the spectral overlap has not been met to date, barring one recent example.⁴

Among various fluorophores, acyclic xanthene forms of different rhodamine derivatives have been widely used as imaging reagents because of their high emission quantum yield, cell membrane permeability, non-toxic nature towards live cells and finally the *switch on* fluorescence response upon conversion of a cyclic lactam form to the acyclic one.⁵ However, such reagents generally have a Stokes shift

of about 50 nm and respond to H^+ as well as certain metal ion(s) with a fluorescence on response.⁵ More recently, a much larger Stokes shift was reported for a receptor with TBET-based response on specific binding to Hg^{2+} .⁶ However, there existed a small spectral overlap between the donor and the acceptor fragments and this did not completely exclude the possibility of the FRET-based response along with the predominant TBET process. Thus, examples of TBET-based cassettes for intracellular imaging applications are actually rare.^{3,6}

Among various metal ions, Hg^{2+} is one of the most potent neurotoxins known and its deleterious influences on human as well as plant physiology are well documented in a range of literature reports and the lowest $\text{Hg}(\text{II})$ concentration that is allowed in safe drinking water is 0.2 ppb.^{7–9} Keeping this in mind, it is imperative to develop a reagent that could specifically recognize, detect and quantitatively estimate mercury ion concentration as low as the above referred limit in pure aqueous/buffer medium having physiological pH. Hg^{2+} is known to be an efficient quencher of molecular fluorescence due to a facile spin-orbit coupling process.¹⁰ The solvation enthalpy for Hg^{2+} is also significant (1824 kJ mol^{-1}). Thus, designing an ultrasensitive fluorescence-based specific probe for $\text{Hg}(\text{II})$ with a high Stokes shift is a challenging issue.

In the present communication, we have described a new probe molecule that allowed us to achieve specificity in detecting Hg^{2+} in aqueous buffer medium through formation of a $\text{Hg}(\text{II})-\eta^2\text{-arene}$ complex. This not only allowed us to delineate Hg^{2+} from H^+ based on a distinctly different fluorescence response, but also helped us to achieve a significant pseudo-Stokes shift of ~ 200 nm through a TBET-based response. Such an example is rare in the contemporary literature.

Detailed synthesis of **L**, **R₁** and **R₂** (Scheme 1), their spectral (¹H NMR and ¹³C NMR) and analytical characterization data are provided in the ESI.[†] Reagent **L** showed an intense absorption band at 386 nm for the benzimidazole derivative of the phenanthrene moiety and apart from this, no other absorption band was observed when spectra were recorded for 20 μM solution of **L** in aq. buffer medium (aq. HEPES buffer; 10 mM; pH 7.2) containing 0.4 mM Triton X100 (TX100) (Fig. 1a (inset)). This assignment was based on the observed electronic spectral band for the model compound **R₁** at 375 nm. A biologically benign neutral surfactant (TX100) allowed

^a Organic Chemistry Division, CSIR-National Chemical Laboratory, Pune-411008, India. E-mail: a.das@ncl.res.in; Fax: +91 2025902629; Tel: +91 2025902385

^b Chromatin and Disease Biology Lab, National Centre for Cell Science, Pune-411007, India. E-mail: samit@nccs.res.in

† Electronic supplementary information (ESI) available. See DOI: 10.1039/c4cc06740a

Zn^{II}-2,2':6',2''-Terpyridine-Based Complex as Fluorescent Chemosensor for PPi, AMP and ADP

Priyadip Das,^[a] Amrita Ghosh,^[a] Manoj K. Kesharwani,^[a] Vadde Ramu,^[a] Bishwajit Ganguly,^{*[a]} and Amitava Das^{*[a]}

Keywords: Chemosensors / Zinc / Density functional calculations / Fluorescent probes / Bioinorganic chemistry

A new Zn^{II}-2,2':6',2''-terpyridine complex, derivatized with a coumarin moiety (**L₁Zn**), acts as a fluorescent chemosensor for different biologically important phosphates like PPi, AMP and ADP in mixed aqueous media. Depending on the proportion of the aqueous fraction present in the solvent mixture, **L₁Zn** shows a preference for different phosphate moieties at physiological pH. In an aqueous acetonitrile (2:3, v/v)

medium this reagent shows a preference for AMP as compared to ADP, ATP and PPi. The binding affinities of **L₁Zn** with different phosphate ions and associated shifts in the electronic spectra were rationalized by DFT calculations. Such an example of a receptor that is selective for AMP under physiological conditions is rare in the literature.

Introduction

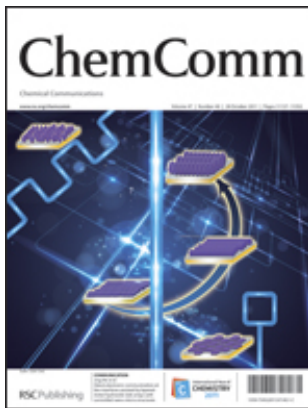
The selective recognition and sensing of biologically important phosphate ions have been the focal point of current research because these ions play crucial role(s) in various metabolic processes.^[1–4] More importantly adenosine triphosphate (ATP) and pyrophosphate (PPi) are involved in energy transduction in organism-controlling metabolic processes by participation in enzymatic reactions, e.g. DNA replication, etc.^[5–7] Furthermore, the detection of PPi is important in real-time DNA sequencing methods,^[8] as well as in cancer research and is formed by the hydrolysis of ATP into adenosine monophosphate (AMP) in cells. AMP and adenosine diphosphate (ADP) are well known to play a crucial role in the energy cycle, as well as in various other biological processes.^[9] Accordingly, detection and discrimination of these phosphates are important for evaluating the generation of each of these ions during various biological processes and clarifying their roles in these processes. Among various methodologies adopted for developing sensor molecules for anionic analytes in aqueous environments, metal ion-anion coordination is recognized as one of the most popular for ions with a high hydration energy, e.g. fluoride, various phosphates, acetate ions. In this regard, the Zn²⁺ complex with vacant coordination sites is significant as the Zn²⁺ ion generally has higher affinity towards phosphate functionality. Higher affinity and stronger Zn^{II}-phosphate binding is expected to be reflected in the more

pronounced influence on the molecular orbital energy levels and thereby on the output spectral response. Besides this, Zn²⁺ does not exhibit any emission quenching effects to fluorophore because of its electronic (3d¹⁰4s⁰) configuration. Thus, examples of the Zn²⁺-based chemosensors for recognition of biological phosphates, which work either in aqueous environments or under physiological conditions, are relatively more common in the literature than those that work on the hydrogen-bonded adduct formation procedure.^[10,11] However, examples of an appropriate receptor that shows preferential binding affinity towards AMP or PPi, compared to other common anions like F[−], Cl[−], Br[−], I[−], NO₃[−], CH₃COO[−], C₆H₅COO[−], SO₄^{2−}, HSO₄[−], H₂PO₄[−] and other biologically important phosphate ions like ATP, CTP, ADP under different mixed aqueous buffer-solvent environments, are scarce in the literature. This promoted us to design and synthesize Zn^{II} complexes as a fluorescent probe for different phosphates like AMP and PPi. Most of the Zn^{II} complexes, which are used as the receptor for phosphate ions, are generally either various derivatives of Zn^{II}-dipicolylamine^[10,11a–11b] or Cu^{II}-dipicolylamine,^[11i,11j] barring one recent reference where Zn^{II}-cyclen (1,4,7,10-tetraazacyclododecane) is reported to show comparable affinity towards ATP and PPi.^[12a] There are only few examples available in the literature where Cu^{II}/Cd^{II}-cyclen derivatives are used as receptors for AMP/PPi.^[12,13a] Though the Cu^{II} complex shows specificity toward PPi, observed binding affinity was not appreciable; while the anion binding response for the Cd^{II}-cyclen derivative works on displacement phenomena and lacks any specificity towards PPi. In a recent report, Gao et al. have shown that a dizinc(II)-cyclen derivative could also be used for specific binding to deoxythymidine and thymidylthymidine.^[13b] In this article we report synthetic methodology, characterization and binding stud-

[a] Central Salt & Marine Chemicals Research Institute (CSIR), Bhavnagar, 364002 Gujarat, India
Fax: +91-278-2567562

E-mail: amitava@csmeri.org
ganguly@csmeri.org

Supporting information for this article is available on the WWW under <http://dx.doi.org/10.1002/ejic.201100125>.

**Title:**

Peptide directed transmembrane transport and nuclear localization of Ru(ii) polypyridyl complexes in mammalian cells

Logged in as:

Vadde Ramu

Account #:
3001025779[LOGOUT](#)**Author:**

Lorraine Blackmore,Roisin Moriarty,Ciaran Dolan,Kellie Adamson,Robert J. Forster,Marc Devocelle,Tia E. Keyes

Publication: Chemical Communications (Cambridge)**Publisher:** Royal Society of Chemistry**Date:** Feb 13, 2013

Copyright © 2013, Royal Society of Chemistry

Order Completed

Thank you for your order.

This Agreement between Vadde Ramu ("You") and Royal Society of Chemistry ("Royal Society of Chemistry") consists of your license details and the terms and conditions provided by Royal Society of Chemistry and Copyright Clearance Center.

Your confirmation email will contain your order number for future reference.

[Get the printable license.](#)

License Number	3872941276846
License date	May 20, 2016
Licensed Content	Royal Society of Chemistry
Publisher	
Licensed Content Publication	Chemical Communications (Cambridge)
Licensed Content Title	Peptide directed transmembrane transport and nuclear localization of Ru(ii) polypyridyl complexes in mammalian cells
Licensed Content Author	Lorraine Blackmore,Roisin Moriarty,Ciaran Dolan,Kellie Adamson,Robert J. Forster,Marc Devocelle,Tia E. Keyes
Licensed Content Date	Feb 13, 2013
Licensed Content Volume	49
Licensed Content Issue	26
Type of Use	Thesis/Dissertation
Requestor type	non-commercial (non-profit)
Portion	figures/tables/images
Number of figures/tables/images	2
Distribution quantity	5
Format	print and electronic
Will you be translating?	no
Order reference number	None
Title of the thesis/dissertation	Design, Synthesis and DNA interaction Studies with Novel Photosensitizer Molecules as Efficient Photodynamic Therapeutic Agents
Expected completion date	Jun 2016
Estimated size	160
Requestor Location	Vadde Ramu Organic Chemistry Division

CSIR-National Chemical Laboratory
Dr. Homi bhabha road, Pashan
Pune, India 400118
Attn: Vadde Ramu

Billing Type Invoice

Billing address Vadde Ramu
Organic Chemistry Division
CSIR-National Chemical Laboratory
Dr. Homi bhabha road, Pashan
Pune, India 400118
Attn: Vadde Ramu

Total 0.00 USD

[ORDER MORE](#)

[CLOSE WINDOW](#)

Copyright © 2016 [Copyright Clearance Center, Inc.](#). All Rights Reserved. [Privacy statement](#). [Terms and Conditions](#).
Comments? We would like to hear from you. E-mail us at customercare@copyright.com

**Title:**Methods to Explore Cellular
Uptake of Ruthenium Complexes

Logged in as:

Vadde Ramu

Author:Cindy A. Puckett, Jacqueline K.
BartonAccount #:
3001025779**Publication:** Journal of the American Chemical
Society**LOGOUT****Publisher:** American Chemical Society**Date:** Jan 1, 2007

Copyright © 2007, American Chemical Society

PERMISSION/LICENSE IS GRANTED FOR YOUR ORDER AT NO CHARGE

This type of permission/license, instead of the standard Terms & Conditions, is sent to you because no fee is being charged for your order. Please note the following:

- Permission is granted for your request in both print and electronic formats, and translations.
- If figures and/or tables were requested, they may be adapted or used in part.
- Please print this page for your records and send a copy of it to your publisher/graduate school.
- Appropriate credit for the requested material should be given as follows: "Reprinted (adapted) with permission from (COMPLETE REFERENCE CITATION). Copyright (YEAR) American Chemical Society." Insert appropriate information in place of the capitalized words.
- One-time permission is granted only for the use specified in your request. No additional uses are granted (such as derivative works or other editions). For any other uses, please submit a new request.

If credit is given to another source for the material you requested, permission must be obtained from that source.

BACK**CLOSE WINDOW**

**Title:**

Cell studies of the DNA bis-intercalator Δ-Δ [μ-C4(cpdppz)2-(phen)4Ru2]4+: toxic effects and properties as a light emitting DNA probe in V79 Chinese hamster cells:

Logged in as:

Vadde Ramu

Account #:

3001025779

[LOGOUT](#)**Author:**

Björn Önfelt, Lovisa Göstring, Per Lincoln, Bengt Nordén, Agneta Önfelt

Publication: Mutagenesis**Publisher:** Oxford University Press**Date:** 07/01/2002

Copyright © 2002, Oxford University Press

Order Completed

Thank you very much for your order.

This is a License Agreement between Vadde Ramu ("You") and Oxford University Press ("Oxford University Press"). The license consists of your order details, the terms and conditions provided by Oxford University Press, and the [payment terms and conditions](#).

[Get the printable license.](#)

License Number	3873030442453
License date	May 20, 2016
Licensed content publisher	Oxford University Press
Licensed content publication	Mutagenesis
Licensed content title	Cell studies of the DNA bis-intercalator Δ-Δ [μ-C4(cpdppz)2-(phen)4Ru2]4+: toxic effects and properties as a light emitting DNA probe in V79 Chinese hamster cells:
Licensed content author	Björn Önfelt, Lovisa Göstring, Per Lincoln, Bengt Nordén, Agneta Önfelt
Licensed content date	07/01/2002
Volume number	17
Issue number	4
Type of Use	Thesis/Dissertation
Requestor type	Academic/Educational institute
Format	Print and electronic
Portion	Figure/table
Number of figures/tables	3
Will you be translating?	No
Author of this OUP article	No
Order reference number	None
Title of your thesis / dissertation	Design, Synthesis and DNA interaction Studies with Novel Photosensitizer Molecules as Efficient Photodynamic Therapeutic Agents
Expected completion date	Jun 2016
Estimated size(pages)	160
Publisher VAT ID	GB 125 5067 30
Total	0.00 USD

[ORDER MORE...](#)[CLOSE WINDOW](#)

Copyright © 2016 [Copyright Clearance Center, Inc.](#). All Rights Reserved. [Privacy statement](#). [Terms and Conditions](#).
Comments? We would like to hear from you. E-mail us at customercare@copyright.com



Title: A ruthenium(II) polypyridyl complex for direct imaging of DNA structure in living cells
Author: Martin R. Gill, Jorge Garcia-Lara, Simon J. Foster, Carl Smythe, Giuseppe Battaglia et al.
Publication: Nature Chemistry
Publisher: Nature Publishing Group
Date: Oct 18, 2009
 Copyright © 2009, Rights Managed by Nature Publishing Group

Logged in as:

Vadde Ramu

Account #:

3001025779

[LOGOUT](#)

Order Completed

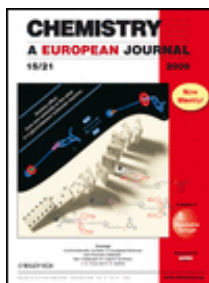
Thank you very much for your order.

This is a License Agreement between Vadde Ramu ("You") and Nature Publishing Group ("Nature Publishing Group"). The license consists of your order details, the terms and conditions provided by Nature Publishing Group, and the [payment terms and conditions](#).

[Get the printable license.](#)

License Number	3872940867457
License date	May 20, 2016
Licensed content publisher	Nature Publishing Group
Licensed content publication	Nature Chemistry
Licensed content title	A ruthenium(II) polypyridyl complex for direct imaging of DNA structure in living cells
Licensed content author	Martin R. Gill, Jorge Garcia-Lara, Simon J. Foster, Carl Smythe, Giuseppe Battaglia et al.
Licensed content date	Oct 18, 2009
Type of Use	reuse in a dissertation / thesis
Volume number	1
Issue number	8
Requestor type	academic/educational
Format	print and electronic
Portion	figures/tables/illustrations
Number of figures/tables/illustrations	2
High-res required	no
Figures	Figure 1.18.
Author of this NPG article	no
Your reference number	22
Title of your thesis / dissertation	Design, Synthesis and DNA interaction Studies with Novel Photosensitizer Molecules as Efficient Photodynamic Therapeutic Agents
Expected completion date	Jun 2016
Estimated size (number of pages)	160
Total	0.00 USD

[ORDER MORE...](#)[CLOSE WINDOW](#)

**Title:**

A Cytostatic Ruthenium(II)-Platinum(II) Bis(terpyridyl) Anticancer Complex That Blocks Entry into S Phase by Up-regulating p27KIP1

Logged in as:

Vadde Ramu

[LOGOUT](#)**Author:**

Vadde Ramu, Martin R. Gill, Paul J. Jarman, David Turton, Jim A. Thomas, Amitava Das, Carl Smythe

Publication: Chemistry - A European Journal**Publisher:** John Wiley and Sons**Date:** May 7, 2015

© 2015 WILEY-VCH Verlag GmbH & Co. KGaA, Weinheim

Order Completed

Thank you for your order.

This Agreement between Vadde Ramu ("You") and John Wiley and Sons ("John Wiley and Sons") consists of your license details and the terms and conditions provided by John Wiley and Sons and Copyright Clearance Center.

Your confirmation email will contain your order number for future reference.

[Get the printable license.](#)

License Number	3862421287198
License date	May 05, 2016
Licensed Content	John Wiley and Sons
Publisher	
Licensed Content Publication	Chemistry - A European Journal
Licensed Content Title	A Cytostatic Ruthenium(II)-Platinum(II) Bis(terpyridyl) Anticancer Complex That Blocks Entry into S Phase by Up-regulating p27KIP1
Licensed Content Author	Vadde Ramu, Martin R. Gill, Paul J. Jarman, David Turton, Jim A. Thomas, Amitava Das, Carl Smythe
Licensed Content Date	May 7, 2015
Licensed Content Pages	13
Type of use	Dissertation/Thesis
Requestor type	Author of this Wiley article
Format	Print and electronic
Portion	Full article
Will you be translating?	No
Title of your thesis / dissertation	Design, Synthesis and DNA interaction Studies with Novel Photosensitizer Molecules as Efficient Photodynamic Therapeutic Agents
Expected completion date	Jun 2016
Expected size (number of pages)	160
Requestor Location	Vadde Ramu Organic Chemistry Division CSIR-National Chemical Laboratory Dr. Homi bhabha road, Pashan Pune, India 400118 Attn: Vadde Ramu
Billing Type	Invoice

Billing address	Vadde Ramu Organic Chemistry Division CSIR-National Chemical Laboratory Dr. Homi bhabha road, Pashan Pune, India 400118 Attn: Vadde Ramu
Total	0.00 USD

Would you like to purchase the full text of this article? If so, please continue on to the content ordering system located here: [Purchase PDF](#)

If you click on the buttons below or close this window, you will not be able to return to the content ordering system.

[CLOSE WINDOW](#)

Copyright © 2016 [Copyright Clearance Center, Inc.](#). All Rights Reserved. [Privacy statement](#). [Terms and Conditions](#).
Comments? We would like to hear from you. E-mail us at customercare@copyright.com